

UC Irvine

UC Irvine Electronic Theses and Dissertations

Title

Control of Spin Waves via Spin-Orbit Coupling in Magnetic Nanostructures

Permalink

<https://escholarship.org/uc/item/6r12r5f7>

Author

Khan, Amanatullah

Publication Date

2022

Supplemental Material

<https://escholarship.org/uc/item/6r12r5f7#supplemental>

Copyright Information

This work is made available under the terms of a Creative Commons Attribution License, available at <https://creativecommons.org/licenses/by/4.0/>

Peer reviewed|Thesis/dissertation

UNIVERSITY OF CALIFORNIA,
IRVINE

Control of Spin Waves via Spin-Orbit Coupling in Magnetic Nanostructures

DISSERTATION

submitted in partial satisfaction of the requirements
for the degree of

DOCTOR OF PHILOSOPHY

in Physics

by

Amanatullah Khan

Dissertation Committee:
Professor Ilya N. Krivorotov, Chair
Assistant Professor Luis A. Jauregui
Assistant Professor Javier D. Sanchez-Yamagishi

2022

DEDICATION

In loving memory of Anthony M. Straus

TABLE OF CONTENTS

	Page
LIST OF FIGURES	vii
ACKNOWLEDGMENTS	ix
VITA	x
ABSTRACT OF THE DISSERTATION	xii
1 Introduction	1
1.1 Preamble	1
1.2 The physical limit of electronics.	2
1.3 Spin orbit coupling, magnonics, & non-reciprocity.	3
2 Background	5
2.1 Magnetism and Magnetization Dynamics	5
2.2 Spin Waves	10
2.2.1 Linearizing the torque equation.	11
2.2.2 Spin waves with exchange and anisotropy fields.	13
2.2.3 Propagating spin waves under exchange.	16
2.2.4 Dispersion Relation of Surface Waves ($\mathbf{M} \perp \mathbf{k}$ in plane)	19
2.3 Spin-Orbit Coupling	22
2.4 Non-reciprocity	23
Part I: Microwave Spectroscopy of Non-Reciprocal Wave Propagation in Magnetic Systems	26
3 Non-Reciprocity in Thin YIG and Pt/YIG Films	28
3.1 Motivation and Introduction	28
3.1.1 Yttrium Iron Garnet	29
3.2 YIG Sample Details	30
3.3 Propagating SW Spectroscopy	32
3.3.1 Damon Eshbach Configuration	33
3.3.2 Spin Wave Antenna Design	34
3.3.3 Nanofabrication on Charging Substrate	35
3.3.4 Nanofabrication Recipe	38

3.3.5	Itemized Nanofabrication Steps	39
3.3.6	Experimental Methods	41
3.4	Results and Analysis for 40nm YIG	45
3.4.1	Interfacial Dzyaloshinskii-Moriya Interaction	50
3.5	Results for GGG/Pt/YIG	51
3.6	Discussion	52
3.7	Additional Notes	55
3.7.1	Comments regarding spin wave antennas	55
4	Spin Flexoelectric Gate on GGG/Pt/YIG	57
4.1	Motivation	57
4.1.1	Spin Flexoelectric Interaction	57
4.2	Device Design and Nanofabrication	60
4.2.1	SW Antennas with Gated Active Region	60
4.2.2	Nanofabrication Procedure	62
4.2.3	Itemized Nanofabrication Steps	63
4.3	Gate Controlled Spin Wave Spectroscopy	66
4.4	Results and Discussion	68
4.5	Additional Notes	71
4.5.1	Low frequency modulation of the electric field gate for high sensitivity detection.	71
4.5.2	Electric field effect in the non-linear regime.	71
5	Wide Band Non-Reciprocity via Magneto-elastic Coupling	72
5.1	Motivation	72
5.1.1	Surface Acoustic Waves	73
5.1.2	Magnetoelastic coupling	75
5.2	Imprinting Non-reciprocity through SW and SAW Interaction	77
5.3	Synthetic Antiferromagnet for Tuneable Dispersion.	78
5.4	SAW Device Design and Nanofabrication	81
5.4.1	Interdigital Transducers	81
5.4.2	Lithium Niobate	83
5.4.3	IDT parameters	84
5.4.4	NR-SAW Device Layout	86
5.4.5	One-Step Nanofabrication	87
5.4.6	Itemized Nanofabrication Recipe	88
5.5	VNA measurements of IDTs on LNO	92
5.6	Preliminary Results and Discussion	94
5.7	Additional Notes	99
5.7.1	Comments regarding lack of IDT signal.	99
5.7.2	Strange growth on samples.	100
5.7.3	Reflection due to thin pads and fingers.	101
5.7.4	Using modulated microwave transmission to detect propagating SAWs.	101

Part II: Micromagnetic Simulations of Electrically Excited Spin Waves in Nanostructures	103
6 Dimensional Crossover in Spin Hall Oscillators	106
6.1 Context and Introduction	106
6.1.1 Spin Transfer Torque	107
6.1.2 Spin Hall Effect	109
6.1.3 Auto Oscillatory Dynamics	110
6.2 Sample and Measurement Details	111
6.3 Experimental Data	113
6.3.1 Emission Data	113
6.3.2 BLS Data	117
6.4 Micromagnetic Simulations	119
6.4.1 Simulation Software and Parameters	119
6.4.2 Simulation with applied spin Hall torque	121
6.4.3 Simulation of Spin Wave Eigenmodes	122
6.4.4 Analysis	123
6.5 Simulation Results	124
6.6 Discussion	127
7 Easy-Plane Spin Hall Oscillator	131
7.1 Context and Introduction	131
7.1.1 Magnetic Anisotropy	133
7.1.2 Sample and Measurement Details	135
7.1.3 Experimental Data	140
7.2 Micromagnetic Simulations	143
7.2.1 Simulation Software and Parameters	143
7.2.2 Simulation Execution and Analysis	145
7.3 Simulation Results	147
7.4 Discussion	149
8 Spin Wave Field Effect Transistor	153
8.1 Context and Introduction	153
8.1.1 Voltage Controlled Magnetic Anisotropy	153
8.1.2 Anomalous Hall Effect	155
8.2 Sample and Measurement Details	156
8.2.1 Hysteresis Loop With Out of Plane Field	156
8.2.2 Electrically Detected FMR	157
8.2.3 Electrically Detected Propagating SW Spectroscopy	158
8.3 Experimental Data	158
8.3.1 Hysteresis Loop Data	158
8.3.2 Electrically Detected FMR Data	159
8.3.3 Electrically Detected Propagating SW Spectroscopy Data	160
8.4 Micromagnetic Simulations	162
8.4.1 Simulation Software and Parameters	162

8.4.2	Simulation Execution and Analysis	163
8.5	Simulation Results	164
8.5.1	Simulated Eigenmode Spectra	164
8.5.2	Simulated Gate Effects on Propagating SW Spectra	165
8.6	Discussion	166
9	Summary and Future Work	168
	Bibliography	171
	Appendix A Appendix	186

LIST OF FIGURES

	Page
2.1 Initial set-up for gyroscopic motion demonstration.	6
2.2 Snapshot of spin waves on a lattice.	10
2.3 Boundary conditions for $M \perp k$ in plane.	19
2.4 Schematic of isolator/circulator.	24
2.5 Cartoon of time reversal symmetry breaking.	25
2.6 Cartoon of spatial inversion symmetry breaking	25
3.1 YIG unit cell and lattice.	29
3.2 Ferromagnetic resonance of Pt/YIG with fit.	31
3.3 Fitting of resonance frequencies and line width for Pt/YIG.	32
3.4 Cartoon depiction of exciting spin waves.	33
3.5 SW antenna types	34
3.6 Colorized micrograph of SW antennas on YIG.	35
3.7 Example of pattern distortion due to charging substrate.	36
3.8 Burned PMMA from ion milling.	37
3.9 Enumerated lithography steps for lift-off on charging substrates.	38
3.10 Experiment set-up diagram (VNA).	43
3.11 Raw spectroscopy data collected with calibrated VNA.	44
3.12 Spectroscopy data after field derivative.	45
3.13 Oscillations in frequency swept trace.	46
3.14 S matrix color plot for YIG on GGG.	47
3.15 Dispersion of Propagating SW in YIG(40nm) on GGG.	48
3.16 Quantifying non-reciprocity of SW at fixed field for GGG/YIG.	49
3.17 Cartoon schematic of iDMI	50
3.18 Dispersion of Propagating SW in GGG/Pt/YIG.	52
3.19 Quantifying non-reciprocity of SW at fixed field for GGG/Pt/YIG.	53
4.1 Effect of flexo-electric interaction on spin wave dispersion.	59
4.2 General schematic of generating perpendicular electric field.	61
4.3 SEM of etched Pt/YIG mesa.	62
4.4 SEM of SFEI devices on PtYIG.	63
4.5 Schematic of SFEI measurement.	67
4.6 VNA traces of SW under $\pm V$ applied to gate.	68
4.7 Fit plots for SFEI constant.	69

5.1	Schematic of a surface acoustic wave.	73
5.2	Cartoon of magnetostriction.	76
5.3	Diagram showing non-reciprocal interaction.	78
5.4	Plot and schematic of SW dispersion in SAF.	79
5.5	Plot of ideal SAF spin wave angle dispersion on LNO.	80
5.6	Diagram of interdigital transducers.	81
5.7	Single finger vs split finger IDTs.	83
5.8	Parameters of IDT design.	85
5.9	Initial NR-SAW device layout.	86
5.10	Illustration of one step fab for NR-SAW devices.	87
5.11	Schematic of characterizing NR-SAWs.	92
5.12	VNA measurement of 4.3 GHz IDTs.	94
5.13	VNA measurement of LNO substrate (no device).	95
5.14	VNA measurement of 7.75 GHz IDTs	96
5.15	VNA measurement of different LNO substrate (no device).	97
5.16	VNA measurement of ‘matched’ split finger IDT.	98
5.17	SEM of ‘dirty’ samples.	100
6.1	Illustration of spin Hall effect.	109
6.2	STT applying anti-damping torque.	111
6.3	Schematic of Pt/Py nanowire.	112
6.4	Emission data from auto oscillations.	113
6.5	Emission power for varying wire widths.	116
6.6	Brillouin light scattering of auto-oscillations in nanowire.	118
6.7	Example of transient state.	122
6.8	Micromagnetic simulations of spin wave spectra in the 1.07 μm wide wire with $H_{\text{Oe}} = 36$ Oe, $H = 470$ Oe and $\theta = 85^\circ$	125
6.9	Micromagnetic simulations of spin wave spatial profiles in the 1.07 μm wide wire.	126
7.1	Spin torque oscillator dynamics.	132
7.2	EP-SHO device schematics and magnetoresistance.	136
7.3	Microwave emission of spin-orbit torque nano-oscillator.	140
7.4	Cartoon of xz-plane energy landscape.	142
7.5	Dynamic to static state transition in simulations of EP-SHO configuration.	146
7.6	Micromagnetic simulation of spin-orbit torque nano-oscillator.	147
7.7	Micromagnetic snapshots of EP-SHO auto oscillations at $I_{\text{dc}} = 2.44\text{mA}$	149
8.1	Spin wave field effect transistor.	157
8.2	Hysteresis under out of plane external field.	159
8.3	Nanowire spin wave eigenmodes.	160
8.4	Propagating spin wave spectroscopy,	161
8.5	Simulated SWFET eigenmode spectra.	164
8.6	Simulated VCMA effect on propagating SW.	165

ACKNOWLEDGMENTS

I would like to express my deepest appreciation first and foremost to my committee chair, Professor Ilya Krivorotov, whose seemingly boundless patience and wisdom has fostered my growth not just as a scientist, but as an ever curious human being. His incredible kindness, intelligence, and empathy has motivated me everyday to become better. I would also like to express my appreciation for how incredibly hard he works to ensure that his students remain funded and that they are well equipped in accomplishing new scientific goals that lie before them. I would also like to thank my committee members Professor Javier Sanchez-Yamagishi and Professor Luis Jauregui, for spending their precious time supporting me through my defense.

I would also like to deeply thank Eric Montoya for being effectively my second advisor and always willing to help me when I asked for support. Whether it be answering any stupid questions I've had, nanofabrication issues, brainstorming new ideas, or the plethora of maintenance labor that we had to do in the lab, his presence and input was always beneficial and enjoyable. Next I would like to thank my predecessors Yu-Jin Chen, Han-Kyu Lee, Alejandro Jara, Jen-Ru Chen, Chris Safranski, and Chengcen Sha who all still gave the time to teach me everything I know while they were working on their dissertations, defenses, and job applications the year I joined. I also thank Andrew Smith, whose thesis has been critical in answering so many important questions during my time in the group. I would like to also thank my current lab mates Mara Mishner, Joshua Yang, Xinyao 'Ada' Pei, Mark Hayward, Emma Frantz, and David Nelson for all their awesome companionship, empathetic support, and fun collaboration. I would also like to thank our collaborators Mingzhong Wu, Tao Liu, Ruslan Salikhov, Igor Barsukov, Jürgen Lindner, Olav Hellwig, Andrei Slavin, Roman Verba, Pat Braganca, and Salvatore Perna. I next would like to give thanks to LEXI and INRF staff for their support and maintenance of critical nanofabrication equipment, especially Qiyin Lin for his expertise and support regarding the SEM and E-beam evaporator.

I would also like to acknowledge all funding sources that have allowed me to continue working as a research assistant and have continued supplying our group with the means to remain competitively equipped for research.

Finally I would like to express my gratitude and love to all my friends and family who have supported me through these 6 years and especially through the ongoing pandemic. Specifically I would like to acknowledge the Lindy Hop community for creating the spaces that I hold so dear to my heart now. Finally, I would like to thank Amylene Grace Cabrera, whose infinite love and support has pulled me through my lowest lows and has elevated my highest highs, without her this endeavor would have not been possible.

VITA

Amanatullah Khan

EDUCATION

Doctor of Philosophy in Physics

University of California, Irvine

2022

Irvine, California

Bachelor of Science in Physics

University of Florida

2016

Gainesville, Florida

RESEARCH EXPERIENCE

Graduate Research Assistant

University of California, Irvine

2017–2022

Irvine, California

TEACHING EXPERIENCE

Teaching Assistant

University of California, Irvine

2016–2017

Irvine, California

REFEREED JOURNAL PUBLICATIONS

Spin wave field effect transistor In preparation.	2022
Easy-plane spin Hall oscillator In preparation.	2022
Dimensional crossover in spin Hall oscillators Phys. Rev. B	2020

REFEREED CONFERENCE PUBLICATIONS

Novel Non-Reciprocal Microwave Spin Wave and Magneto-Elastic Wave Devices for On-Chip Signal Processing International Microwave Symposium	2020
Non-Reciprocity in Ultrathin YIG films Magnetism and Magnetic Materials	2019
Electric Field Control of Spin Wave Propagation and Non-reciprocity in Nanodevices EFRI-2DARE Grantees Meeting Workshop	2018

ABSTRACT OF THE DISSERTATION

Control of Spin Waves via Spin-Orbit Coupling in Magnetic Nanostructures

By

Amanatullah Khan

Doctor of Philosophy in Physics

University of California, Irvine, 2022

Professor Ilya N. Krivorotov, Chair

Manipulation of magnetization dynamics in nanoscale systems is critical for developing energy efficient, fast information processing systems. Spin orbit coupling (SOC), the interaction between an electron's spin and its orbital momentum, produces numerous interesting phenomena that can be used to control these dynamics. This dissertation presents a number of studies utilizing SOC to control spin waves in magnetic nanostructures. First, thin yttrium iron garnet (YIG) films were discovered to carry non-reciprocal spin waves. Characterization of the non-reciprocity reveals that it stems from SOC at the interface between YIG and gadolinium gallium garnet (GGG) substrate. The analysis was repeated in thin GGG/Pt/YIG systems to find that the non-reciprocity increased by 50%. Then, gated devices utilizing the spin flexo-electric interaction (SFEI) on GGG/Pt/YIG were studied. The effect is predicted to yield tuneable non-reciprocity in spin waves. Characterization of propagating spin waves through the electric field gate reveal however that the effect is negligibly small in this system. The phenomenological constant related to SFEI was extracted. In ultra-thin CoFeB nanowire systems, the effects of voltage controlled magnetic anisotropy on propagating spin waves were measured. Specifically, a nanoscale spin wave field effect transistor is realized. In this device, a voltage applied to the gate efficiently modulates the amplitude of spin waves propagating between the source and drain of a ferro-magnetic spin wave channel. Finally, magneto-mechanical nanodevices that allow the study of the effects

of magneto-elastic coupling on propagating surface acoustic waves were developed.

In ferromagnet/non-magnetic heavy metal bilayer nanowires, charge current generates a transverse spin current through SOC (called the spin Hall effect). This spin current can apply a torque that negates the damping in a ferromagnet and drives auto oscillations (AOs) which emit microwave power. This dissertation includes two studies regarding these systems. The dimensional crossover of such nanowire systems between quasi-one-dimensional to quasi-two-dimensional wires was investigated. Analysis of the nanowire AOs show that increasing the wire width results in an increase of the number of excited AO modes accompanied by a decrease of the amplitude and coherence of each mode. Thus revealing that there is an optimal wire width that maximizes power output. This is because the increasing number of modes leads to an increase in non-linear interactions between them which lowers the overall amplitude and phase coherence. Such spin Hall oscillator systems however do not have the ideal configuration for maximum torque because their magnetization is not orthogonal to the spin Hall current polarization. A new nanowire system where the magnetization prefers an easy-plane that is orthogonal to the spin torque is realized. This easy-plane configuration exhibits large angle dynamics and enhanced phase coherence. Micromagnetic simulations reveal that this is achieved through balancing the energy landscape of the nanowire such that there is a near-degeneracy along the wire and out of plane.

Chapter 1

Introduction

1.1 Preamble

When a graduate student successfully defends their dissertation and moves on from the research group, a great deal of critical knowledge pertaining to that lab has moved on with them. Even with careful documentation, lab journaling, log-books, post-it notes, living documents, and fleshed out theses, there is still valuable knowledge that evaporates from the group only to be rediscovered a couple years later, often through an identical process of troubleshooting and development. One of my main motivations behind the structure of this dissertation is to serve as a means to pass on as much useful knowledge as I can to my successors in Professor Ilya Krivorotov's research group. My goal is to provide sufficient detail such that future grad students can spend less time troubleshooting or developing already documented issues/solutions and spend more time tackling newer, more engaging problems. Unfortunately in journal publications, discussions of what methods *don't* work and *why* are not incentivised and thus seldom discussed. I intend to take advantage of the dissertation format to help fill at least a little of that knowledge gap. This tome has

three main parts to it: microwave spectroscopy of non-reciprocal wave propagation in magnetic systems (Chapter 3,4,5), micromagnetic simulations of electrically excited spin waves in nanostructures (Chapter 6,7,8), and the Appendix. In Chapter 3, I design and fabricate spin wave antennas which then I use to measure/characterize non-reciprocity in thin yttrium iron garnet (YIG) films. In Chapter 4, I use the previously developed techniques to fabricate gated YIG on Pt devices to measure the spin flexo-electric phenomenological constant and characterize tuneable non-reciprocity if present. In Chapter 5, I design and fabricate surface acoustic wave devices meant to measure non-reciprocity imprinted onto them via magneto-elastic interaction from a synthetic anti-ferromagnetic interface. In Chapter 6, I simulate auto oscillations in a spin Hall oscillator to understand the origin of the loss of power and coherence of spontaneous microwave emission from wide-based spin Hall oscillators upon the dimensional crossover from one- to two-dimensional active magnetic regions. In Chapter 7, I simulate achieving large angle dynamics in a spin Hall oscillator through the balancing of perpendicular magnetic anisotropy with shape anisotropy to compare to experimental data. Finally, in Chapter 8, I simulate spin wave eigenmode spectra and propagating spin wave spectra under varying perpendicular magnetic anisotropy in the active region of a CoFeB nanowire. The appendix will have all standard operating procedures, extended laboratory notes, and simulation code/scripts. I have written all chapters in a modular and pedagogical fashion. The end of each chapter will have any personal notes or potentially useful information relevant to that particular study.

1.2 The physical limit of electronics.

Moore's Law, which describes the exponential growth of computational power for integrated chips, has notably slowed to a crawl. The main contributor to this is the underlying fact that all electronics rely on charge transport. The current paradigm of designing and packing

smaller electrical components onto an ever shrinking area has faced serious challenges. As long as the industry continues to try and scale down charge based computation components, certain issues worsen and incur more expenses:

- Gate leakage \Rightarrow components are so small they are susceptible atomic scale defects and even quantum tunnelling and thus become unstable.
- Joule heating \Rightarrow scales inversely with the cross sectional area of the conductor, which quadratically rises with decreasing dimensions, increases chances of self-destruction and requires expensive cooling.
- Unsustainable power demand \Rightarrow increased component density dramatically increases the required power to operate, cool, and maintain.
- Economically inefficient \Rightarrow all previously mentioned issues lower the overall reliability of the chips which then require huge amounts of resources to overcome and make consumer friendly.

The current bleeding edge technology leaders are dumping billions of dollars to only achieve marginal improvements in newer generations of devices. Yet these problems will only continue to get worse. While the paradigm was quite effective for scaling down to the micrometer scale, the rapidly growing issues strongly motivates searching for new physics in condensed matter that can address these issues.

1.3 Spin orbit coupling, magnonics, & non-reciprocity.

Spin waves (whose quanta are magnons) are a highly attractive candidates to answer this dilemma. They are information carriers that require no charge transport (eliminates Joule heating), are very easy to excite (energy efficient, $\sim \mu\text{eV}$), have continuous phase (encoding

complexity), can be non-interacting (can be multiplexed or paralleled), and are compatible with today's complementary metal-oxide-semiconductor (CMOS) technology.

In the context of spin waves, the relativistic interaction between the spin and the orbital momentum of an electron (dubbed spin-orbit coupling, SOC) has been the underlying mechanism in numerous useful and interesting phenomena that can be used to manipulate the spin state. Some effects (of which I will cover a number of in this dissertation) include: magneto-crystalline anisotropy, magnetic damping, spin Hall effect, spin orbit torques, magneto-elastic coupling, spin-flexoelectric interaction, Dzyaloshinskii-Moriya interaction, and more [142, 118, 57, 91, 99]. In an effort to advance our understanding of spin wave phenomena and how to harness their properties, it is vital that we investigate these effects in various configurations and circumstances.

Magnonics, the application of spin waves in electronic devices, is an exciting subfield of spintronics which utilizes propagating spin waves for nanoscale transmission and processing of information [25]. Magnonics offer a promising alternate route towards faster, more efficient computational and signal processing hardware. One aspect of pushing the boundaries of magnonics is that of non-reciprocity, where spin waves behave differently when travelling in opposite directions in a magnetic media. Non-reciprocal radio-frequency (GHz band) electronic devices, for example, have yet to be developed at the integrated chip scale (currently they are still bulky components). Spin wave non-reciprocity opens up a huge space of magnonics applications such as logic gates, spin wave transistors, analogue computing, and low noise information busses to name a few [84]. The effects of SOC have already offered us many potential methods of achieving non-reciprocal microwave devices. This thesis explores some of those effects in novel nanofabricated structures and discusses their results.

Chapter 2

Background

2.1 Magnetism and Magnetization Dynamics

The origin of *ferromagnetism*, which is the spontaneous alignment of magnetic moments in a material, lies nearly entirely in the interaction of the *spin* of electrons (through the *exchange* interaction). Spin is angular momentum that all electrons carry with themselves (specifically they are spin $1/2$). The origin of spin however is a *very deep, unresolved* topic and will not be discussed here. Before we discuss further how this angular momentum turns into magnetism, we will take a quick tangent into gyroscopic motion.

There is a popular physics demonstration where a bike wheel is spinning on an axle and one side is hung to a rope (shown in Fig. 2.1). When released, the spinning wheel will keep itself suspended horizontally and begin precessing around the point it is hanging from on the rope.

What's going on here is that the spinning wheel has angular momentum, and has gravity trying to pull the center of mass downward, but because it is fixed on one side, gravity's force on the center of mass is actually applying a *torque* to the spinning wheel. This torque

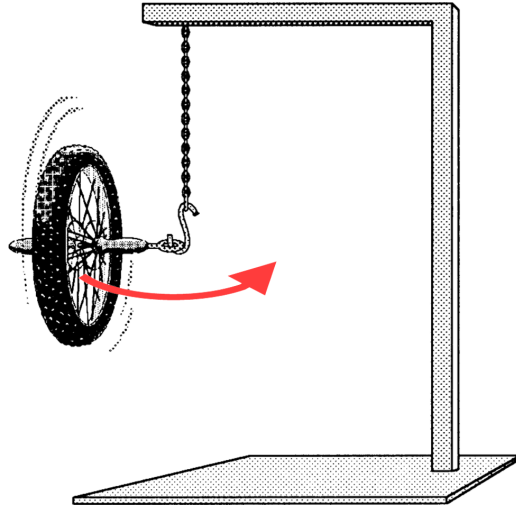


Figure 2.1: **Initial set-up for gyroscopic motion demonstration.** Illustration showing initial configuration to demonstrate gyroscopic motion due to gravity. A wheel is spun up and suspended on one side to a hanging rope as shown. When released, gravity subsequently causes the wheel to precess around the rope (red arrow) instead of hanging straight down as intuitive linear mechanics would naively imply. Image found at <https://www.exploratorium.edu/snacks/bicycle-wheel-gyro>.

actually leads to precessional motion (the revolution around the hanging point):

$$\boldsymbol{\tau} = \mathbf{r} \times \mathbf{F}_g \tag{2.1}$$

where \mathbf{r} is the vector from the fixed point to the center of mass.

Torque is the rate of change of angular momentum ($\mathbf{L}_{classical}$), which looks like:

$$\boldsymbol{\tau} = \frac{d\mathbf{L}_{classical}}{dt} = \mathbf{r} \times \mathbf{F}_g \tag{2.2}$$

A cross product will always result with a vector pointing perpendicular to both vectors involved. If you consider Fig. 2.1, this *torque* is continuously pointing tangentially to the circular path because gravity is constantly downward and \mathbf{r} is constantly rotating. This is also the same mechanism behind why a spinning top precesses as it is tipping over due to

gravity.

Now, torques are fundamental to the dynamics of magnetism. When we go to the atomic scale, the total angular momentum that an electron has is:

$$\mathbf{J} = \mathbf{L} + \mathbf{S} \tag{2.3}$$

where \mathbf{L} is the angular momentum from the electron motion around atoms (orbital) and \mathbf{S} is the intrinsic angular momentum that electrons *simply have* (spin).

We can treat these electrons semi-classically by considering their *orbital* angular momentum as an *electric current* which then generates a magnetic field or *magnetic moment*. This yields:

$$\boldsymbol{\mu} = \gamma_L \mathbf{L} \tag{2.4}$$

$$\gamma_L = \frac{q}{2m_e} \tag{2.5}$$

where γ_L is the *gyromagnetic* ratio, i.e. a conversion factor between (orbital) angular momentum and magnetic moment. Its constituents are the fundamental constants q of electric charge and m_e of electron mass.

The contribution to $\boldsymbol{\mu}$ from spin angular momentum \mathbf{S} requires a quantum mechanical approach [125], but it turns out that it differs from γ_L by a factor of 2. This yields overall:

$$\boldsymbol{\mu} = \gamma_L(\mathbf{L} + 2\mathbf{S}), \tag{2.6}$$

often however the magnetic moment for an electron will be written in this form:

$$\boldsymbol{\mu} = -\frac{\mu_B}{\hbar}(\mathbf{L} + 2\mathbf{S}), \tag{2.7}$$

where μ_B is the *Bohr magneton*, a natural unit for magnetic moment of an electron.

Now, if one wants to *rotate* the magnetic moment of an electron, a torque must be acted on the electron, in this case, a magnetic field \mathbf{H} does this [61]:

$$\boldsymbol{\tau} = \boldsymbol{\mu} \times \mathbf{H}. \quad (2.8)$$

This description however is for a single atom. To promote our equation to something macro scale we use the continuum approach by looking at a *body* of many magnetic moments, summing them up (N), and dividing by the volume V to produce a new parameter \mathbf{M} which is *magnetization*:

$$\mathbf{M} = \frac{N}{V} \boldsymbol{\mu}, \quad (2.9)$$

which now finally yields our gyroscopic analog for magnetism:

$$\frac{\partial \mathbf{M}}{\partial t} = -\gamma \mathbf{M} \times \mathbf{H}. \quad (2.10)$$

Eq. (2.10) is the Landau Lifshitz equation for gyroscopic precession of ferromagnets [74]. Note that this equation has no dissipative term, meaning that the gyroscopic motion would ensue indefinitely. We knew however from simple experiments that when a ferromagnetic material is in a magnetic field the magnetization \mathbf{M} *eventually* becomes parallel to the external field. Therefore there must be an additional torque that pulls \mathbf{M} towards \mathbf{H} . Landau and Lifshitz actually proposed an additional term to achieve this:

$$\frac{\partial \mathbf{M}}{\partial t} = -\gamma \mathbf{M} \times \mathbf{H} + \frac{\gamma \lambda}{M^2} \mathbf{M} \times (\mathbf{M} \times \mathbf{H}). \quad (2.11)$$

Where λ is the dissipation parameter. This description for small damping works, however for infinite damping seems to fail (the torque goes to infinity!). Another theorist T.L. Gilbert

(unaware of this failure actually) proposed that instead the phenomenological term should operate like a *viscous* term (viscous meaning it scales with the rate of change itself, like wind resistance for example) [46]:

$$\frac{\partial \mathbf{M}}{\partial t} = -\gamma \mathbf{M} \times \mathbf{H}_{eff} + \frac{\alpha}{M_S} \mathbf{M} \times \frac{\partial \mathbf{M}}{\partial t}, \quad (2.12)$$

where α is the *Gilbert damping* parameter, M_S is the saturation magnetization (maximum magnetization of the system), and \mathbf{H} has been promoted to \mathbf{H}_{eff} to include all present fields in the system. The viscous term doesn't diverge when damping is high, which resolves the former issue. Thus the *Landau-Lifshitz-Gilbert* (LLG) equation was born. In literature, often the first term is the “field-like” term while the second is “damping-like”. Since the damping-like term in Eq. (2.12) goes to 0 for infinite damping (which intuitively makes sense), it is accepted as more accurate and has been widely used ever since.

Finally, it is important to point out the microscopic origins of magnetic damping. One source of dissipation is due to the interplay between the lattice vibrations (phonons) and the magnetization dynamics (magnons) between atoms. Since magnetic interactions can contribute to the vibrational motion of atoms, energy can be lost in this way. Another source of dissipation is the generation of *eddy currents* from the changing magnetic moments, which generate a reactive magnetic field that mitigates the magnetic dynamics (since nature does not like changing magnetic fluxes). There is also the scattering of magnetization dynamics with itself (two-magnon scattering) [60]. Finally, the combination of spin orbit coupling and electron-lattice scattering leads to the electron energy states changing under the precessing magnetization which then form electron-hole pairs near the fermi surface (hence called the *breathing* Fermi surface) which finally scatter and decay [65]. This is not an exhaustive list of damping sources.

2.2 Spin Waves

Naturally, magnetic atoms (magnetic due to their outer shell electrons) in a lattice will influence each others orientation since they are packed together. In other words, the atoms are magnetically *coupled* to their neighbors. Two main mechanism of coupling are dipole-dipole (long range) and exchange (short range) interactions. If precessional perturbations are generated in one part of the lattice, those perturbations will propagate through the rest. These collective excitations of magnetic moments are called *spin waves*. Fortunately, some of the intuition one may have regarding sound waves or even water waves are transferable to spin waves. Fig. 2.2 shows an instantaneous snapshot of spin waves in a lattice driven by an antenna. If time were to progress, we would observe a literal ‘wavefront’ travelling away from the antenna towards both edges. Although the spins are spatially not moving, information of their orientation is, this is a key attractive feature in that they can transmit information without any ballistic like motion of electrons.

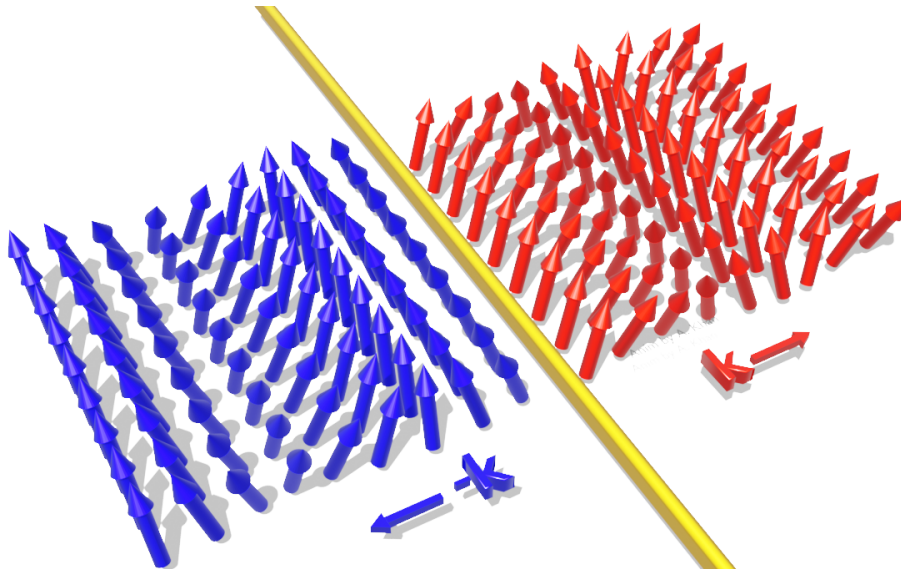


Figure 2.2: **Snapshot of spin waves on a lattice.** An instantaneous snapshot of propagating spin waves. Spins (blue and red arrows) placed in a lattice with a gold antenna at the middle (which drives the precession), each column of spins away from the center is in a progressing *phase* of the spin wave. The distance between two columns of spins oriented in the same direction would be the wavelength of the spin wave. The direction of propagation is labeled by $\pm\mathbf{k}$.

Before we dive into the mathematical derivation, I want to notify the reader that there is a quantum theory that yields the dispersion relation of *magnons*, this is called the method of Holstein and Primakoff, which gives a nice quasi-particle picture of spin waves and their interactions. I will defer this derivation to the reference textbook by Stancil and Prabhakar [125]. In this section we will look at the semi-classical treatment which yields a more direct solution in which we utilize in our experiments.

2.2.1 Linearizing the torque equation.

In our pursuit to understand spin waves under an external source of excitation (like a *spin wave antenna*) we must begin with Eq. (2.10) (*lossless LL equation*) and introduce a small time varying magnetic field.

$$\frac{\partial \mathbf{M}}{\partial t} = \gamma \mu_0 \mathbf{M} \times \mathbf{H}_{\text{eff}} \quad (2.13)$$

where

$$\mathbf{H}_{\text{eff}} = \mathbf{H} + \mathbf{H}_{\text{ex}} + \mathbf{H}_k. \quad (2.14)$$

Here we absorb the minus sign into the γ . The \mathbf{H}_{ex} and \mathbf{H}_k represent the *exchange* field and effective anisotropy field, respectively. Note that $\mathbf{H}_{\text{ex}} = \lambda_{\text{ex}} \nabla^2 \mathbf{M}$. The exchange field actually has a linear \mathbf{M} term but is omitted since $\mathbf{M} \times \mathbf{M} = 0$ in our differential equation.

For now we will actually ignore the exchange and anisotropy terms to make things a little

easier and get a feel for the solution. We introduce the time varying components:

$$\mathbf{M} = \mathbf{M}_0 + \mathbf{m}(t) \quad (2.15)$$

$$\mathbf{H} = \mathbf{H}_0 + \mathbf{h}(t) \quad (2.16)$$

We plug this into Eq. (2.13) to get

$$\frac{d\mathbf{m}}{dt} = \gamma\mu_0[\mathbf{M}_0 \times \mathbf{H}_0 + \mathbf{M}_0 \times \mathbf{h} + \mathbf{m} \times \mathbf{H}_0 + \mathbf{m} \times \mathbf{h}] \quad (2.17)$$

Now we will make some assumptions and *linearize* the equations so it is solvable. In the case of magnetic saturation or *near* saturation, we can throw out the first term since they will be parallel. Next, since \mathbf{h} and \mathbf{m} are *small*, the last term can also be removed (since it is *small squared*). Finally, we will assume the static equilibrium will be along a particular direction –lets say $\hat{\mathbf{z}}$, this then means that its components will have small deviations and $M_0 \approx M_S$. With the time dependence set to look like $e^{(-i\omega t)}$ we get an equation of motion like

$$-i\omega\mathbf{m} = \hat{\mathbf{z}} \times [-\omega_M\mathbf{h} + \omega_0\mathbf{m}] \quad (2.18)$$

with

$$\omega_M \equiv -\gamma\mu_0 M_S \quad (2.19)$$

$$\omega_0 \equiv -\gamma\mu_0 H_0 \quad (2.20)$$

We solve the linearized torque equation Eq. (2.18) for \mathbf{h} ¹:

$$\begin{bmatrix} h_x \\ h_y \end{bmatrix} = \frac{1}{\omega_M} \begin{bmatrix} \omega_0 & i\omega \\ -i\omega & \omega_0 \end{bmatrix} \begin{bmatrix} m_x \\ m_y \end{bmatrix}. \quad (2.21)$$

¹This is presented as a 2×2 matrix since our calculation only cares about the x and y .

This description then can be condensed into:

$$\mathbf{m} = \bar{\chi} \cdot \mathbf{h} \quad (2.22)$$

where $\bar{\chi}$ is known as the *Polder susceptibility* [125] and looks like:

$$\bar{\chi} = \begin{bmatrix} \chi & -i\kappa \\ i\kappa & \chi \end{bmatrix} \quad (2.23)$$

where

$$\chi = \frac{\omega_0 \omega_M}{\omega_0^2 - \omega^2} \quad (2.24)$$

$$\kappa = \frac{\omega \omega_M}{\omega_0^2 - \omega^2} \quad (2.25)$$

The resonance condition presents itself here with the denominator of χ : as ω approaches ω_0 , the susceptibility diverges, which implies that small perturbations of that frequency can lead to a uniform precession. For a lossless system, this kind of result is typical, and to first order the frequency doesn't change when the damping term is included (the shifting is usually on the order of α^2 , which for most spin wave media, where damping is typically low, is negligible).

2.2.2 Spin waves with exchange and anisotropy fields.

Now with the inclusion of exchange and anisotropy the derivation gets a *little* more complicated, but is still doable. The additional complexity is:

$$\mathbf{H}_k = \mathbf{H}_{0k} + \mathbf{h}_k(t) \quad (2.26)$$

$$\mathbf{H}_{ex} = \mathbf{H}_{0ex} + \mathbf{h}_{ex}(t) \quad (2.27)$$

which, like before, can be plugged into Eq. (2.13):

$$\frac{1}{\gamma\mu_0} \frac{d\mathbf{m}}{dt} = \mathbf{M}_0 \times [\mathbf{H}_0 + \mathbf{H}_{0k} + \mathbf{H}_{0ex}] + \mathbf{M}_0 \times [\mathbf{h} + \mathbf{h}_k + \mathbf{h}_{ex}] \quad (2.28)$$

$$+ \mathbf{m} \times [\mathbf{H}_0 + \mathbf{H}_{0k} + \mathbf{H}_{0ex}] + \mathbf{m} \times [\mathbf{h} + \mathbf{h}_k + \mathbf{h}_{ex}] \quad (2.29)$$

We use similar linearizing assumptions like having small perturbations in the time variation, static equilibrium along $\hat{\mathbf{z}}$, \mathbf{M}_0 being uniform and approximately parallel to \mathbf{H}_0 , and finally having $|\mathbf{H}_0| \gg |\mathbf{H}_{0k}|$:

$$i\omega\mathbf{m} = \hat{\mathbf{z}} \times \left[\mathbf{h} + \lambda_{ex} \nabla^2 \mathbf{m} + \bar{\mathbf{N}}^a \cdot \mathbf{m} - (Z_0 + Z_k) \mathbf{m} \right] \quad (2.30)$$

with

$$\Omega = \omega/\omega_M \quad (2.31)$$

$$Z_0 = \mathbf{H}_0/M_S \quad (2.32)$$

$$Z_k = \mathbf{H}_{0k} \cdot \hat{\mathbf{z}}/M_S \quad (2.33)$$

Once again solving for \mathbf{h} and then condensing everything down ²:

$$\mathbf{h} = \bar{\mathbf{A}}_{op} \cdot \mathbf{m} \quad (2.34)$$

where

$$\bar{\mathbf{A}}_{op} = \begin{bmatrix} Z_0 + Z_k - N_{xx}^a - \lambda_{ex} \nabla^2 & i\Omega - N_{xy}^a \\ -i\Omega - N_{yx}^a & Z_0 + Z_k - N_{yy}^a - \lambda_{ex} \nabla^2 \end{bmatrix} \quad (2.35)$$

where the N scripted terms arise from the crystalline anisotropy.

²Here there are higher order terms ignored for Z_k because we are working with small perturbations and everything is pointing along the $\hat{\mathbf{z}}$ axis, if one would like to see *non-linear* effects, those higher order terms can't be ignore and thus the derivation will deviate from here.

If we consider neglecting exchange and inverting the matrix to get our Polder tensor back (now with anisotropy effects included), we get:

$$\bar{\chi} = \frac{1}{D} \begin{bmatrix} Z_0 + Z_k - N_{yy}^a & -i\Omega + N_{xy}^a \\ i\Omega + N_{yx}^a & Z_0 + Z_k - N_{xx}^a \end{bmatrix} \quad (2.36)$$

where

$$D = [Z_0 + Z_k - N_{yy}^a][Z_0 + Z_k - N_{xx}^a] - [i\Omega + N_{yx}^a][-i\Omega + N_{xy}^a] \quad (2.37)$$

Like before, making our susceptibility diverge requires $D = 0$, which gives us our resonance condition. From this we can extract a general uniform precession (wavevector $\mathbf{k} = \mathbf{0}$) resonance frequency. Let's consider an example case, where our external field is along the $\hat{\mathbf{z}}$ axis and the easy axis for the uniaxial anisotropy is along $\hat{\mathbf{x}}$. Then we find:

$$\mathbf{h}_{ku} = H_{ku}m_x/M_X \hat{\mathbf{x}} \quad (2.38)$$

$$N_{xy}^a = N_{yx}^a = N_{yy}^a = Z_k = 0 \quad (2.39)$$

$$N_{xx}^a = H_k/M_S \quad (2.40)$$

and finally our FMR frequency

$$\omega_R = \gamma\mu_0\sqrt{H_0(H_0 - H_k)} \quad (2.41)$$

where

$$H_k = 2K_{u1}/(\mu_0M_S) \quad (2.42)$$

Now, in actuality, we will be neglecting anisotropy in our dispersion relation calculation for

nonzero \mathbf{k} , regardless, I think it is valuable to observe how the crystalline anisotropy *deforms* the susceptibility matrix by having a term present in every index (Eq. (2.37)).

2.2.3 Propagating spin waves under exchange.

Walker's Equation and *Dipolar Spin Waves*.

In order to build upon our formulation, we need to consider Maxwell's equations to constrain our solutions, this will yield magneto-static solutions called *Walker's equations*:

$$\nabla \times \mathbf{h} = 0 \tag{2.43}$$

$$\nabla \cdot \mathbf{b} = 0 \tag{2.44}$$

$$\nabla \times \mathbf{e} = i\omega \mathbf{b} \tag{2.45}$$

Then the relation between \mathbf{b} and \mathbf{h} is

$$\mathbf{b} = \bar{\boldsymbol{\mu}} \cdot \mathbf{h} \tag{2.46}$$

Where $\bar{\boldsymbol{\mu}} = \mu_0(\bar{\mathbf{I}} + \bar{\boldsymbol{\chi}})$ which turns out to be:

$$\bar{\boldsymbol{\mu}} = \mu_0 \begin{bmatrix} 1 + \chi & -i\kappa & 0 \\ i\kappa & 1 + \chi & 0 \\ 0 & 0 & 1 \end{bmatrix} \tag{2.47}$$

This is again based on a bias field along the $\hat{\mathbf{z}}$ direction, but works similarly for any other defined magnetic direction.

Now with $\nabla \times (\nabla\psi) \equiv 0$, we can write under Maxwell's constraints

$$\mathbf{h} = -\nabla\psi \quad (2.48)$$

and

$$\nabla \cdot (\bar{\boldsymbol{\mu}} \cdot \nabla\psi) = 0 \quad (2.49)$$

Finally we can plug in $\bar{\boldsymbol{\mu}}$ and get

$$(1 + \chi) \left[\frac{\partial^2\psi}{\partial x^2} + \frac{\partial^2\psi}{\partial y^2} \right] + \frac{\partial^2\psi}{\partial z^2} = 0 \quad (2.50)$$

Which is our desired Walker's equation. This describes the *magneto-static* modes of the system in a simple ferromagnet (we must be careful since this was done with small time variations of \mathbf{m} and \mathbf{h}). Now calling back to our assumed plane wave solutions we can turn all the second partial derivatives into k 's

$$(1 + \chi)(k_x^2 + k_y^2) + k_z^2 = 0 \quad (2.51)$$

We can use the relative angle between the propagation axis and the external field to add angular dependence

$$k_x^2 + k_y^2 = k^2 \sin^2 \theta \quad (2.52)$$

$$k_z^2 = k^2 \cos^2 \theta \quad (2.53)$$

When substituted in and simplified

$$\chi \sin^2 \theta = -1 \quad (2.54)$$

which finally yields (when placed back into our Eq. (2.24) equation:

$$\omega = [\omega_0(\omega_0 + \omega_M \sin^2 \theta)]^{1/2} \quad (2.55)$$

A couple remarks about this: It is independent of $|k|$ (so the resonance can have any wavelength!), this is because we effectively solved an electromagnetics problem in an unbounded system where the susceptibility was determined by our original derivation for a lossless torque equation without exchange and anisotropy fields, the angular dependence here informs us of the asymptotic solutions for large- k parallel and perpendicular to the external field. The resonances here can be dubbed *dipolar* spin waves as they are the result of merely imposing Maxwell's constraints (which is like imposing long range dipole-dipole interactions). Once we introduce exchange and boundary conditions do these modes get *lifted out of degeneracy* and we observe a $\omega(k)$ dispersion relation.

Exchange Spin Waves

If we take Eq. (2.35) and neglect H_k , we get the form:

$$\bar{\mathbf{A}}_{op} = \frac{1}{\omega_M} \begin{bmatrix} \omega_0 - \omega_M \lambda_{ex} \nabla^2 & i\omega \\ -i\omega & \omega_0 - \omega_M \lambda_{ex} \nabla^2 \quad i\omega \end{bmatrix} \quad (2.56)$$

When we consider plane wave solutions $e^{(i\mathbf{k}\cdot\mathbf{r})}$, the ∇^2 becomes $-k^2$ terms. Since we observe a familiar matrix equation where ω_0 simply has a new additive term attached to it everywhere, we can simply take our previous solution for ω and add that term without going through the whole derivation again!

$$\omega = [(\omega_0 + \omega_M \lambda_{ex} k^2)(\omega_0 + \omega_M(\lambda_{ex} k^2 + \sin^2 \theta))]^{1/2} \quad (2.57)$$

Thus we see the effects of exchange *lifting* the degeneracy of different wavelength modes and observe the shifting of frequency with increasing k . Furthermore, we can see that k can rapidly dominate the dispersion relation when it is sufficiently large. These spin waves are called *exchange* spin waves (since they stem from the exchange term).

2.2.4 Dispersion Relation of Surface Waves ($\mathbf{M} \perp \mathbf{k}$ in plane)

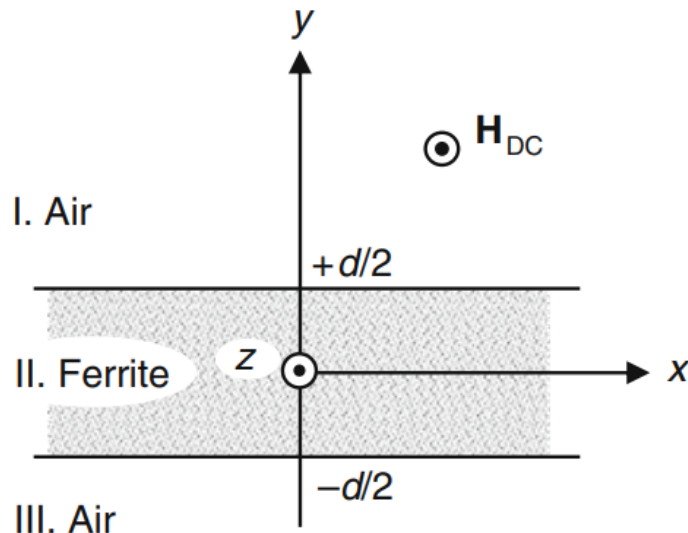


Figure 2.3: **Boundary conditions for $\mathbf{M} \perp \mathbf{k}$ in plane.** Schematic from Stancil and Prabhakar [125] showing boundary conditions for tangentially magnetized ferrite film.

Up to this point, we started with the (linearized) torque dynamics, then added in Maxwell's equations, and finally included exchange interactions, all that remains are the boundary conditions. Since we are studying spin waves in a *thin film*, we need to consider the fact that there are three regions, the air above (I, which is in $+y$), the film itself (II, which is at the origin to $\pm d/2$), and the air below (III, which is in $-y$). Furthermore, we're looking at the configuration of having spin waves propagating perpendicular to an in plane external field, i.e. along the $\pm x$ direction Fig. 2.3. We will first make some assumptions of what the potentials will look like in these regions (remembering standard wave intuition like decaying

at infinity, not diverging anywhere, should be oscillatory everywhere, etc.)

$$\psi_I(\mathbf{r}) = C e^{-ky+i\nu kx} \quad (2.58)$$

$$\psi_{II}(\mathbf{r}) = [\psi_{0+}e^{ky} + \psi_{0-}e^{-ky}] e^{i\nu kx} \quad (2.59)$$

$$\psi_{III}(\mathbf{r}) = D e^{ky+i\nu kx} \quad (2.60)$$

Normally there are component subscripts for the k 's above, but we drop those subscripts because in the magnetic region (II), Eq. (2.51) becomes

$$(1 + \chi)(k_x^2 + k_y^2) = 0 \quad (2.61)$$

whose solutions requires that $k_y^2 = -k_x^2$ (which implies $k_x = |k_y| \equiv k$). This also brings up a point about ψ_{II} , if we want k_x to be real, then k_y must be imaginary, this is the reason why ψ_{II} is a linear combination of exponentials.

Next we consider the boundary conditions at the film interfaces, which requires ψ to be continuous at $y = \pm d/2$ where d is the thickness of the film.

$$C e^{-kd/2} = \psi_{0+} e^{kd/2} + \psi_{0-} e^{-kd/2}, \quad (2.62)$$

$$D e^{-kd/2} = \psi_{0+} e^{-kd/2} + \psi_{0-} e^{kd/2}. \quad (2.63)$$

Finally, we need b_y to be continuous at the interfaces as well, this imposes (from Eq. (2.46):

$$b_y = i\mu_0\kappa h_x + \mu_0(1 + \chi)h_y. \quad (2.64)$$

Which we plug our potentials into

$$C e^{-kd/2} = \nu \kappa [\psi_{0+} e^{kd/2} + \psi_{0-} e^{-kd/2}] - (1 + \chi) [\psi_{0+} e^{kd/2} - \psi_{0-} e^{-kd/2}], \quad (2.65)$$

$$D e^{-kd/2} = -\nu \kappa [\psi_{0+} e^{-kd/2} + \psi_{0-} e^{kd/2}] + (1 + \chi) [\psi_{0+} e^{-kd/2} - \psi_{0-} e^{kd/2}]. \quad (2.66)$$

Apply the previous boundary conditions:

$$\begin{bmatrix} (\chi + 2 - \nu \kappa) e^{kd/2} & -(\chi + \nu \kappa) e^{-kd/2} \\ -(\chi - \nu \kappa) e^{-kd/2} & (\chi + 2 + \nu \kappa) e^{kd/2} \end{bmatrix} \begin{bmatrix} \psi_{0+} \\ \psi_{0-} \end{bmatrix} = 0. \quad (2.67)$$

From this system of equations we can set the determinant = 0 and simplify:

$$e^{-2kd} = \frac{(\chi + 2)^2 - \kappa^2}{\chi^2 - \kappa^2}. \quad (2.68)$$

Observe that the ν has canceled, implying that this dispersion relation is symmetric over flipping the direction of propagation. With a final substitution of χ and κ (from Eq. (2.24) and Eq. (2.25)) and solving for ω^2 we reach our goal:

$$\omega^2 = \omega_0 (\omega_0 + \omega_M) + \frac{\omega_M^2}{4} [1 - e^{-2kd}]. \quad (2.69)$$

This is our dispersion relation for a ferromagnetic film polarized in the plane of the film and perpendicular to the direction of propagation. These spin waves are generally called *magneto-static surface waves* (MSSW) or Damon Eshbach modes.

A remark about our solution, k here is positive definite, and usually for redundancy will be embedded as $|k|$. More importantly, even though ν fell out of the solution, the mode fields still flip when the direction of propagation is the other way. Flipping the direction of propagation leads to the surface waves actually propagating on the *opposite surface*. Which is called *field displacement non-reciprocity*. Finally, our solution decays the further into the

film one goes, hence why these are *surface* spin waves. In our case with sufficiently thin films however, we have the magnetization effectively *pinned* across the thickness, which in principle removes the aforementioned non-reciprocity.

While the derivation is quite lengthy and has many layers, I felt that it was necessary to leave as little out as possible, as most papers (understandably) present only Eq. (2.69) and then cite a paper or reference text. Unfortunately, those references usually have terse derivations or unfamiliar notation that makes them difficult to follow.

2.3 Spin-Orbit Coupling

Maxwell’s unified theory of *electromagnetism* tells us that, depending on your frame of reference, the electromagnetic field will ‘seem’ more electric or more magnetic. The electrons in atomic orbitals are subjected to electric fields primarily from the nucleus, in the rest frame of the moving electron, an effective magnetic field is observed and interacts with the electrons own spin. The interaction between the spin of an electron and its orbital motion is the **spin orbit interaction**. As mentioned before, spin orbit interaction (or spin orbit coupling, SOC) has been the origin of a huge number of phenomena and is one of the central parts of condensed matter physics. The general form of SOC can be written as:

$$H_{SO} = \frac{e\hbar}{4m^2c^2} \hat{\boldsymbol{\sigma}} \cdot [\nabla V(\mathbf{r}) \times \mathbf{p}] \quad (2.70)$$

where e is the electric charge, m is the electron mass, c is the speed of light, $\hat{\boldsymbol{\sigma}}$ is the vector of Pauli spin matrices, \mathbf{p} is the momentum operator, and $V(\mathbf{r})$ is the electric potential. From this we can see that any presence of an electric field $\mathbf{E} = \nabla V(\mathbf{r})$ then leads to a deformation of the energy landscape. By extension then anything that can manipulate/modulate the local effective fields will then contribute to the SOC energy in the total Hamiltonian. This is

why it is responsible for so many effects in condensed matter systems as they generally have to do with orbitals or the nuclei. Recently, however, there has been an explosion of academic effort into studying spin orbit coupling under the added condition of *broken spatial inversion symmetry*, which has fostered all kinds of fascinating results and phenomena, some of which are covered in this dissertation [17].

2.4 Non-reciprocity

A non-reciprocal system is defined as **a system that exhibits different received-transmitted field ratios when its sources and detectors are exchanged** [15]. In other words, when you swap the ports on a non-reciprocal device, you observe different behavior. Note that non-reciprocity however is a *general* description, and can be found in literature of many other topics in physics outside of spintronics.

Non-reciprocity has been critical in the development of numerous electronic components that are ubiquitous in the world today. A diode is a simple example, as it is a one-way current carrier. Isolators and circulators are other popular examples, where the former is similar to a diode but for AC signals (usually microwave), and the latter operates like a traffic roundabout (shown in Fig. 2.4). Many non-reciprocal devices also aim to take advantage of the resulting suppression of reflection/back-action to improve the fidelity of transmission.

A system can exhibit non-reciprocity through a number of means like non-linear materials and movable media [41, 50]. One primary approach is to simultaneously break the time-reversal and spatial inversion symmetry of a system. Time reversal symmetry (TRS) is when a system is identical to itself when time flows in the opposite direction. Mathematically, it does not change under a sign change for all time t 's present in an equation. Fig. 2.5 shows an example of TRS breaking and why magnetism breaks it. The simple case of a loop of

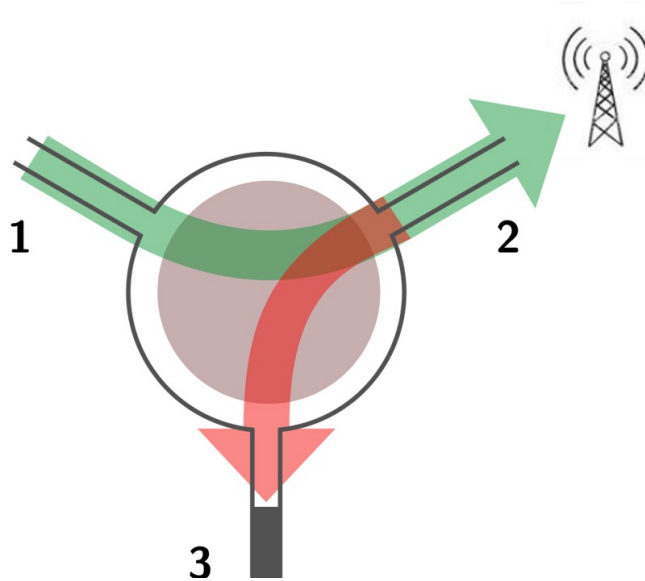


Figure 2.4: **Schematic of isolator/circulator.** Diagram of how a non-reciprocal device like a circulator works. In a circulator signals can only transmit to the adjacent port going clockwise, i.e., $1 \rightarrow 2$, $2 \rightarrow 3$, $3 \rightarrow 1$. If any of the ports are terminated to absorb any signal, then the device becomes the RF analog of a diode (one way of transmission only). Such a device permits the simultaneous transmitting and receiving of information, which wireless communications benefit greatly from.

current generating a magnetic field gets flipped when time is reversed.

Spatial inversion symmetry is when the system looks the same under flipping from a *right-handed* coordinate system to a *left-handed* one (or vice versa). More specifically, the system is inversion symmetric if flipping the sign of any *single* coordinate axis does not change the system. Fig. 2.6 demonstrates an example of breaking spatial inversion symmetry. The generation of *electrical* dipoles break inversion symmetry, this is because under the axis sign flip, the position of positive and negative charges swap, which then flip the polarization vector \mathbf{P} . Breaking spatial inversion symmetry is required for *ferroelectricity*, which is the electric polarization analog of magnetism (where electric dipoles align with electric field).

Inducing broken inversion symmetry can be done through a number of different ways. To achieve a net polarization in the lattice for example, an electric field can be applied (covered in Chapter 4). Another, more general, method that can be employed is by having a

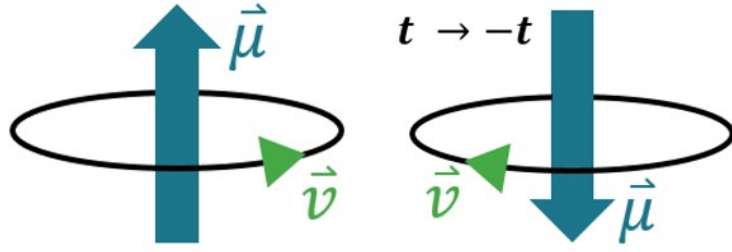


Figure 2.5: **Cartoon of time reversal symmetry breaking.** A loop of current going counter clockwise generates an upwards magnetic field. When time is reversed, the current now flows in the opposite direction, also flipping the field. This is an example of TRS breaking.

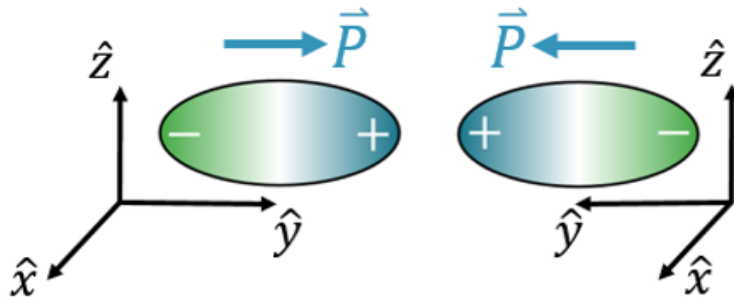


Figure 2.6: **Cartoon of spatial inversion symmetry breaking.**

spatial gradient present in the media. This can be achieved through an interface (this is how interfacial Dzyaloshinskii-Moriya interaction is manifested), spatially varying material parameters (gradient anisotropy or varying superlattice structures), or meta materials (periodic nanoscale structures) [42, 82]. The main idea is that as long as there is an axis that fails the reflection symmetry, the condition is satisfied.

Part I: Microwave Spectroscopy of Non-Reciprocal Wave Propagation in Magnetic Systems

The recent decade has experienced an explosion of interest in studying spin waves for data transmission and wave-based computing. For many practical applications, short wavelength spin waves that are also non-reciprocal are required. Ergo, methods of exciting and characterizing propagating spin waves are highly motivated. In this part of my thesis I present the development of nanodevices that enable microwave spectroscopy of propagating waves and discuss studies carried out with them. Here is a quick overview of these chapters.

Chapter 3 covers the design and fabrication of spin wave antennas used to characterize spin waves in thin yttrium iron garnet (YIG) and Pt/YIG films. Measurements of spin waves in thin YIG reveal that they are non-reciprocal. Characterizing the non-reciprocity revealed that it came from the interfacial Dzyaloshinskii-Moriya interaction (a consequence of spin orbit coupling) between the YIG and substrate gadolinium gallium garnet interface. When the measurements were repeated on Pt/YIG, the non-reciprocity was higher by 50%.

Chapter 4 presents a study of the spin flexo-electric coupling in Pt/YIG systems. The nanofabrication and measurement of gated spin wave devices are discussed. The theory

claims that the perpendicular electric field from the gate breaks inversion symmetry and induces non-reciprocity, where it scales with the strength of the electric field. The measurements however show that this effect is small. The upper bound of the associated phenomenological constant is calculated and discussed.

Lastly, Chapter 5 covers the progress towards achieving non-reciprocal surface acoustic waves (SAWs) through magneto-elastic coupling. The basics of surface acoustic waves are covered along with the critical theory proposed by our collaborators. Design and fabrication of SAW resonators are discussed and preliminary measurements of early devices are presented.

Chapter 3

Non-Reciprocity in Thin YIG and Pt/YIG Films

3.1 Motivation and Introduction

Non-reciprocal spin wave devices are critical in the community effort of exploring scalable microwave signal processing solutions. Some future applications that are possible with non-reciprocal spin waves are integrated chip GHz filters, spin wave logic devices, circulators, and mixers to name a few. Few of these applications have already been developed using conventional semi-conductor approaches, but they are active and require power. While passive non-reciprocal microwave components require large ferromagnetic components and cannot be scaled down (and their bulkiness consumes a lot of valuable real estate in their applications). Therefore, exploring non-reciprocal media opens the floor to explore novel non-reciprocal devices (like a spin wave diode or phase shifter) and is pertinent towards progressing the field. In this chapter, I will cover the surprising result that thin YIG films (one of the best spin wave mediums out there), can be *intrinsically* non-reciprocal.

3.1.1 Yttrium Iron Garnet

The main character of our study is a magnetic oxide that has been used in a plethora of high end microwave equipment since the 50's: $\text{Y}_3\text{Fe}_5\text{O}_{12}$ (YIG). It is a synthetic mineral that is well known for it's exceptionally high quality factor and, more importantly for us, it's ultra low magnetic damping [124]. Its complicated unit cell yields quenched orbital moments (so all of its magnetic moment comes purely from intrinsic spin) and a *ferrimagnetic* lattice (described in Fig. 3.1(c)). YIG's damping coefficient is usually on the order of 10^{-4} and can even reach down to 10^{-5} , because of it's low damping, it can carry spin waves across very long distances (up to millimeters or even centimeters). YIG is also an *insulator*, so pure spin wave studies can be conducted without worrying about shorts or charge transport related issues, furthermore there are no Joule heating losses which makes it highly efficient (and is mainly the reason why it is such low damping since there are no conduction electrons to scatter, i.e. no spin orbit interaction) [86]. This makes YIG a popular media in magnonics research.

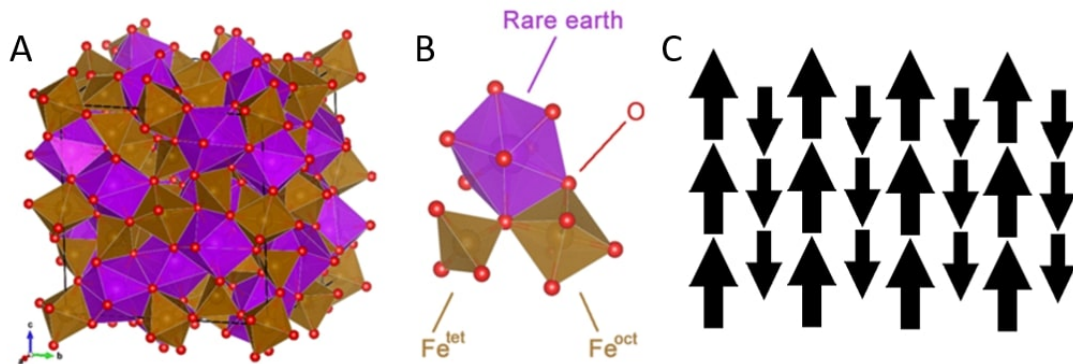


Figure 3.1: **YIG unit cell and lattice.** (A) Yttrium iron garnet unit cell [100]. (B) Sublattice components that form the unit cell. It is believed that the yttrium serves as a ‘Goldilocks’ spacer atom that allows the material to become ferrimagnetic, the orbital moments to be quenched, and have low damping. (C) Diagram showing what a ferrimagnetic lattice looks like. It resembles an anti-ferromagnetic configuration but with a net magnetic moment.

It wasn't until this recent decade that $< \mu\text{m}$ thin film YIG has become accessible. Since

their discovery of low damping and high quality factor resonances, bulk YIG crystals and thick YIG films have been the workhorse media for spin wave research. Thin YIG films however allow magnonics researchers to truly explore prototype applications of spin waves and to better understand the fundamental dynamics of them in a virtually dissipationless environment.

3.2 YIG Sample Details

Our samples were films grown via YIG target magnetron sputtering on gadolinium gallium garnet (GGG) substrates, the reason for the substrate is that it is very closely lattice matched to YIG which promotes proper, single crystalline growth. Our collaborators in Mingzhong Wu's group from Colorado State University grew 40 nm thin YIG on GGG and 40nm YIG on GGG/Pt(10nm) for us to perform this study on [18].

Prior to nanofabrication, we characterized the film via broadband ferromagnetic resonance with field modulation [94]. Which allows us to extract the FMR spectra and subsequently the magnetic properties of our films. An example spectra with the fitting is shown in Fig. 3.2. The use of field modulation with a lock-in amplifier means we are measuring the change in RF absorption, so we fit the derivative of the absorption line shape equation and extract the line width (ΔH) and resonance field (H_{FMR}) at each fixed frequency. The fitting function is as follows [94]:

$$\mathcal{F}(H) = A \left(-\cos(\phi) \frac{2\Delta H (H_0 - H_{FMR})}{((H_0 - H_{FMR})^2 + \Delta H^2)^2} + \sin(\phi) \frac{\Delta H^2 (\Delta H^2 - (H_0 - H_{FMR})^2)}{((H_0 - H_{FMR})^2 + \Delta H^2)^2} \right) \quad (3.1)$$

With a series of resonance fields we can fit their relationship with frequency f to get $4\pi M_{eff}$,

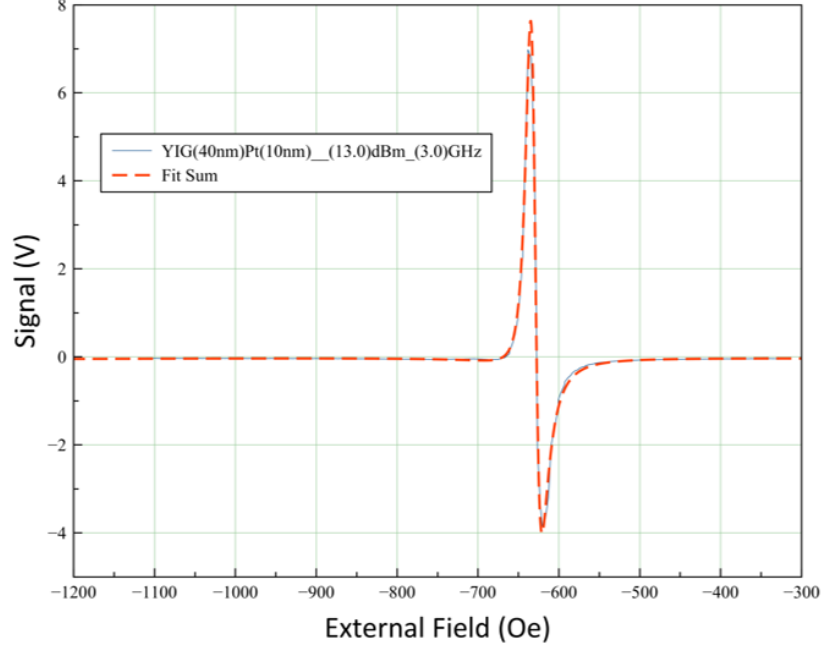


Figure 3.2: **Ferromagnetic resonance of Pt/YIG with fit.** Example film absorption FMR taken for GGG/Pt(10nm)/YIG(40nm) at 3 GHz. The fit (Eq. (3.1)) provides the resonance field and line width. We repeat the fit for a series of fixed frequencies in order to extract $4\pi M_{eff}$, damping parameter α , and g-factor g .

g -factor, and α , this is demonstrated in Fig. 3.3. The linear fit is:

$$\frac{\omega}{\gamma} = \sqrt{H_{FMR}(H_{FMR} + 4\pi M_{eff})} \quad (3.2)$$

where the g factor is embedded within γ . The g factor seldom deviates from 2, so it also serves as a solid sanity check when measuring and fitting data. When there is strong spin orbit coupling or non-zero orbital momentum, then g may sensibly deviate.

Similarly, the damping parameter α can be found using [4]:

$$\Delta H(\omega) = \alpha \frac{\omega}{\gamma} + \Delta H(0) \quad (3.3)$$

where $\Delta H(0)$ is the zero frequency line width intercept. This usually is due to inhomogeneity within the sample (so you can imagine there is a non-zero *spread* of resonance frequencies due

to the variation throughout the magnetic media). The table of values for our two measured films are in the table below.

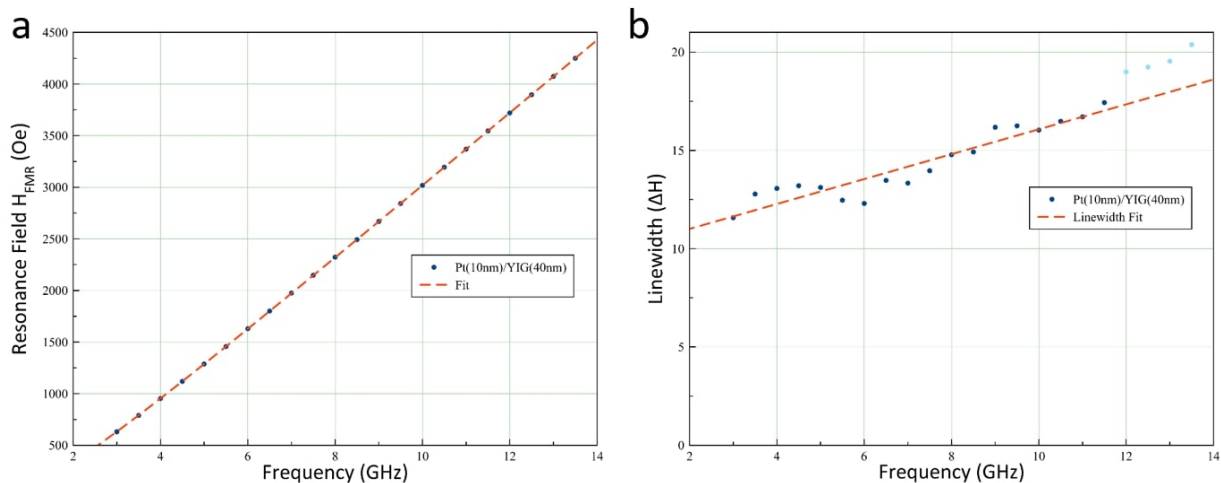


Figure 3.3: **Fitting of resonance frequencies and line width for Pt/YIG.** (a) Using Eq. (3.2) to extract $4\pi M_{eff}$ and g -factor from a series of measured H_{FMR} like in Fig. 3.2. (b) Using Eq. (3.3) to extract the damping parameter of Pt/YIG

GGG/YIG(40)	GGG/Pt(10)/YIG(40)
$4\pi M_{eff} \approx 1700$ kOe	$4\pi M_{eff} \approx 1170$ kOe
$g = 2.020$	$g = 2.010$
$\alpha = 1.2 \times 10^{-3}$	$\alpha = 1.8 \times 10^{-3}$

These values will come in handy when we characterize our propagating spin waves.

3.3 Propagating SW Spectroscopy

Studying non-reciprocity of spin waves requires exciting and characterizing short wavelength spin waves. The reason being that non-reciprocal phenomena generally scale with decreasing wavelength (equivalently increasing \mathbf{k}). Coupling to short wavelength spin waves however requires structures that are of similar scale to the wavelengths themselves. This warrants

nanofabrication of fine features which is a relatively new and challenging approach for spin wave spectroscopy. In this section I will cover the design and fabrication of devices that allow for characterizing propagating spin waves.

3.3.1 Damon Eshbach Configuration

The configuration in which we make our measurements involve the ferromagnetic layer being magnetized *in plane and perpendicular* to the direction of propagation (determined by the antenna structure). This configuration results in magnetostatic surface waves (MSSW) shown by Fig. 3.4, and is also known as the Damon Eshbach Configuration.

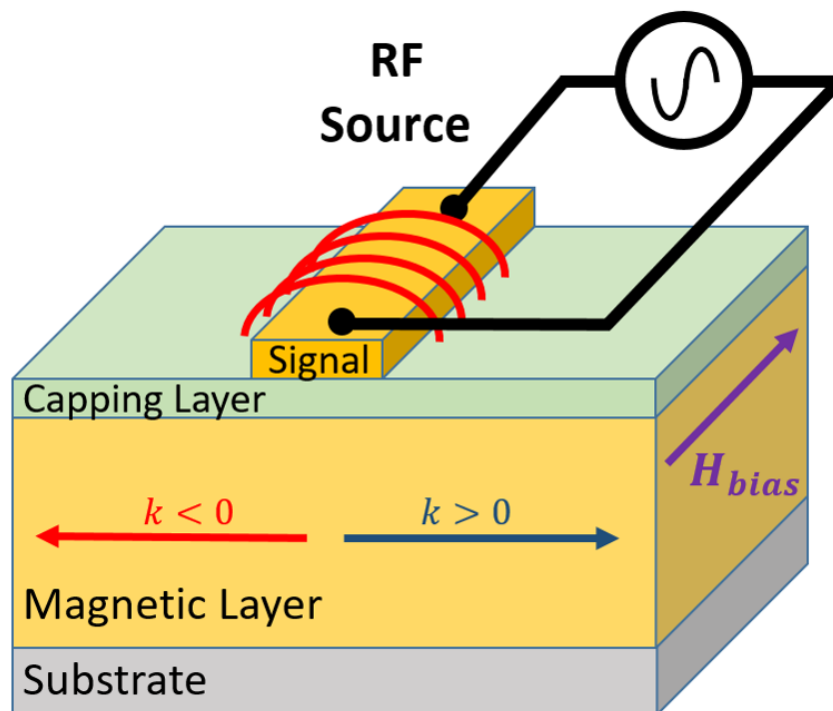


Figure 3.4: **Cartoon depiction of exciting spin waves.** Diagram showing in plane external field H_{bias} magnetizing the film while the fabricated signal line emits an AC driven oscillating field that applies a magnetic torque and excites spin waves in the ferromagnet for both directions of \mathbf{k} .

One detail to note is that short wavelength (where $k \gg 1/d$) surface waves actually will travel on opposite surfaces depending on the direction of \mathbf{k} . In Fig. 3.4, the positive \mathbf{k}

spin waves travel on the top surface, while the negative \mathbf{k} spin waves travel on the bottom. When the ferromagnetic layer is sufficiently thin (< 50 nm), the magnetization dynamics are *exchanged locked* across the thickness, meaning that the MSSW's for highly thin films are expected to be reciprocal.

3.3.2 Spin Wave Antenna Design

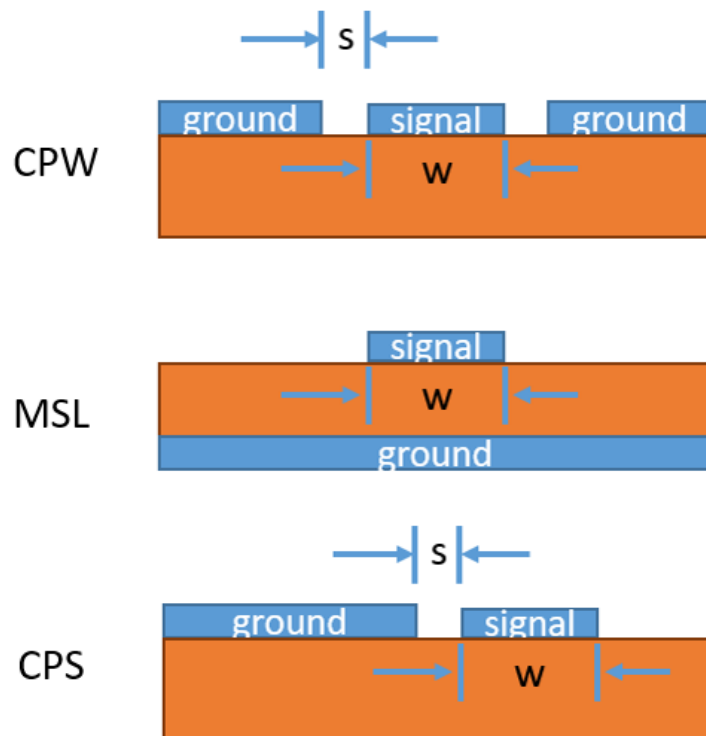


Figure 3.5: **SW antenna types.** Diagram of some antenna types which all have different spectra of excitation, where s is the antenna gap and w is the signal width. The microstripline antenna (MSL) is broadband but less coupling to higher modes. The coplanar waveguide (CPW) will have some bands but will couple more strongly to modes with wavelength closest to it's feature size. Finally the coplanar stripline (CPS) will operate similarly to CPW but with less required space at the expense of less output.

Various antenna designs can be used for exciting spin waves, often the choice is strongly influenced by a mix of fabrication limitations and desired spectra of excitation. Since we aim to excite as short of spin waves as we can, we aim for a form factor that can couple

more efficiently to shorter wavelengths. We choose to go with the coplanar stripline antenna so that we can space the antennas more closely together. If one has access to COMSOL or any antenna design software, taking the spatial fourier transform of the fields emitted by the antennas yields the f vs coupling strength of each design.

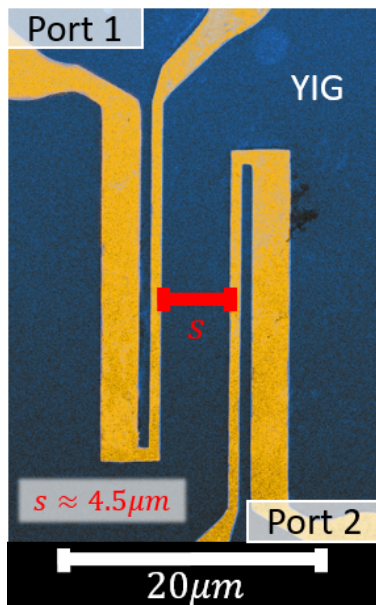


Figure 3.6: **Colorized micrograph of SW antennas on YIG.** Scanning electron microscope image of spin wave antennas (gold) fabricated on top of thin yttrium iron garnet film (blue). The distance s denotes the propagation length.

3.3.3 Nanofabrication on Charging Substrate

Electron beam lithography (EBL) is the method we use to nanopattern devices. It involves using high velocity electrons to hit a special film, called an e-beam resist, to draw out the patterns. The areas exposed in the film have their chemical composition changed (usually through ionization of the resist polymer resulting in cross-linking chains). Depending on the kind of resist, the exposed regions either become soluble or insoluble when placed in their respective developer agent (positive photoresist like PMMA and MMA are soluble when exposed, negative photoresist like ma-N2401 become insoluble). Since a large electron beam is involved in this process, insulating samples become problematic in that they do not allow

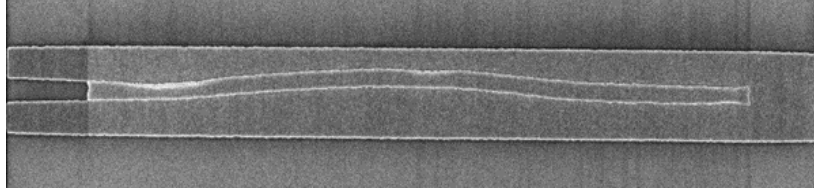


Figure 3.7: **Example of pattern distortion due to charging substrate.**

charge to easily dissipate. The build up of charge leads to a repulsive field that then deflects the e-beam and distorts whatever pattern was being generated.

Fig. 3.7 shows an example of when there is charging on the sample, patterns become deformed and the straight lines become curved and nonuniform. Microwave antennas are sensitive to edge defects so this must be addressed.

Sometimes depositing a thin metal layer on top of the resist prior to EBL can work, but this runs the risk of redepositing on top of your chip when submerged in the developer. Furthermore, the additional surface physics that the metal introduces to the resist can cause issues for high resolution features.

In the past I have tried to use the ion mill to etch the conductive metal off of the resist after exposure but before development, this however does *not* work for thin photo-resists, as the ion beam burns the resist and makes it develop extremely poorly (see Fig. 3.8). Micrometer thick resists on the other hand has shown to work since the resist does not burn all the way through.

The commercial solution to this is to use a special conductive polymer that can be spin coated on top the resist. These special conductive polymers however are quite expensive (can go for thousands of dollars for 100 mL for example).

Fortunately, a cheaper alternative is easily available. Since the issue was getting the conductive layer *off* of the resist after e-beam exposure, we can employ a water soluble ‘sacrificial’ layer like PSSA between the metal and resist. Michael Rooks at Yale informed me of some

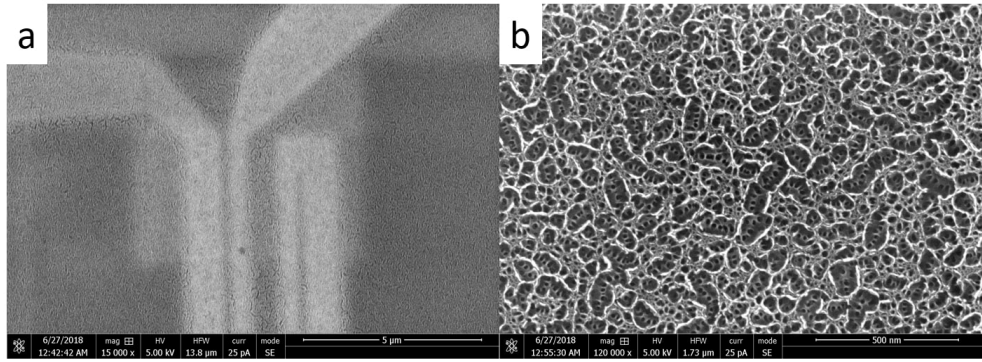


Figure 3.8: **Burned PMMA from ion milling.**

quick steps to make a nice ‘fake e-spacer’ as he calls it (<https://nano.yale.edu/sites/default/files/files/pssa.pdf>):

1. Dilute PSSA from Sigma-Aldrich (part #561223-500G) in 1:1 deionized water to get a 4.5% solution.
2. Add 1% Triton X100 surfactant (by volume)
3. Stir.

The solution is stable at room temperature and is recommended to use a filter syringe when dispensing. The surfactant is critical in making the PSSA properly soluble.

When depositing the conductive layer, it is worth knowing how thick of a layer is required to actually get a electrically continuous surface. I have employed 3 nm Pt or 7 nm Au, depending on whichever is in the sputter chamber at the time, it doesn’t really matter what material you use but you may need to perform some dosage tests to ensure good patterns. Also, if the deposited conductive layer is too thin, it may form nano-clusters or islands and thus remain insulating.

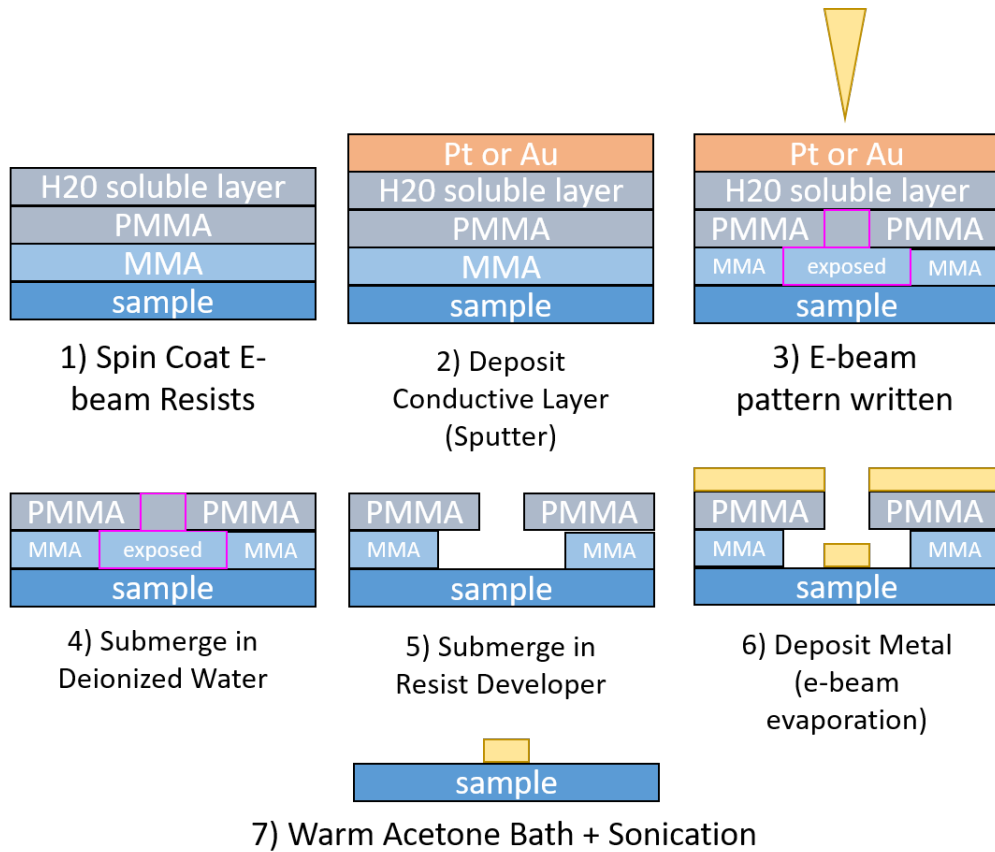


Figure 3.9: Enumerated lithography steps for lift-off on charging substrates.

3.3.4 Nanofabrication Recipe

Making thin width antennas on a charging substrate with non-reductive processes is challenging. These devices were fabricated via a lift-off procedure that involved a bilayer resist undercut and e-beam evaporated deposition. Fig. 3.9 shows the condensed procedure for the fabrication. MMA e-beam resist is more sensitive to exposure than PMMA, thus, the bottom layer forms a nice *undercut* when developed. This undercut is crucial as the metal deposition process becomes considerably less likely to deposit on the side walls and risk ripping off the main features when removed in the final step. Usually for macro-scopic features like leads or contact pads, using a deposition process like magnetron sputtering is fine. For fine features however, side wall deposition becomes a serious issue. In magnetron sputtering, the depositing atoms have a short mean-free path due to the ambient plasma and low vacuum, meaning

that side-wall deposition is statistically much higher. For this reason, e-beam evaporation is employed for the deposition step. This is because e-beam evaporation is performed at high vacuum and has a considerably larger mean-free path for the deposition atoms to land on the substrate as oppose to the side walls, this makes the final step of lifting off the resist + excess metal considerably more likely to be successful.

3.3.5 Itemized Nanofabrication Steps

1. Clean sample in Acetone, sonicate for 3 minutes.
2. Quickly move sample over to IPA, sonicate for 3 more minutes.
3. Dry using N2 gun
 - ⇒ Be sure that liquid does not flow from your tweezers onto the substrate as that accumulates dirt. You can flow the N2 towards the tweezers until dry, be careful to not let the tweezers slip or chip fly away. Visually inspect for dirt or residue using reflection of the surface.
4. Oxygen plasma 'etch' sample at 40W for 3 minutes (can skip this step if you think it doesn't matter or if the sample is sensitive to O_2 plasma).
5. Turn on hot plate, set to 180° C
 - ⇒ If sample permits, can pre-bake to remove ambient moisture before next step (I did not pre-bake).
6. Place sample on spin coater vacuum chuck and turn on vacuum.
7. Spin coat MMA at 4000 rpm for 45 seconds (program 6)
 - ⇒ When dispensing MMA, make sure to not touch the pipette tip, blow out with N2 including towards the inside, squeeze the pipette while N2 cleaning so it doesn't suck

in any dust/dirt, while still squeezed, carry to resist bottle and fill with couple drops of MMA, dispense couple drops onto chip.

8. One finished, release vacuum and post-bake on hot plate at 180° C for 90 seconds.
9. Remove chip from hot plate and let it cool by placing it on the foil covered glass plate in the front of the fume hood. Usually 20-30 seconds is enough time.
10. Spin coat PMMA at 1800 rpm for 45 seconds (program 8).
11. Post-bake on hot plate at 180° C for 90 seconds.
12. Let cool for 20 seconds. Change hot plate temperature to 90° C.
13. Spin coat 'fake e-spacer' (PSSA + Triton X) at 3600 rpm for 45 seconds (program 9).
14. Post-bake on hot plate at 90° C for 3 minutes.

⇒ Keep sample in dark place or wrapped in foil until EBL time, be sure to follow standard fume hood/spin coater SOP to clean up after yourself.
15. Evaporate or Sputter 7 nm Au or 3 nm Pt.
16. Perform EBL

⇒ For GGG/YIG(40nm) 125 $\mu\text{C}/\text{cm}^2$ at 13 pA for fine features seem to work, this will vary from substrate to substrate up to 250 $\mu\text{C}/\text{cm}^2$, higher current can be done for larger features.
17. Submerge in deionized water for 45-60 seconds to remove the PSSA and conductive layer.

⇒ You can visually see the metal peel off, let it do its thing when it happens. Note DI water slightly develops the resist.
18. Develop in MIBK:IPA (1:3) for 20-40 seconds

⇒ Pick a consistent time like 30 seconds for dose testing and development.

19. Rinse with IPA for 45 seconds, can also nozzle squirt the surface.
20. Use optical to inspect resist, can SEM to image progress.
 - ⇒ Can reset fab and start over by doing the initial cleaning steps (Acetone, IPA, O₂ plasma) if the patterns look bad. Be weary your chip is thermally cycling when repeatedly being fabricated on.
 - ⇒ Prior to next step, it has been recommended to do a ‘descumming’ step by doing a short O₂ plasma etch (15-20W for 30 seconds) to remove surface organics and in principle aid in adhesion of the evaporated metal. I found that skipping this step made devices stick better for some reason.
21. E-beam evaporate Ti(5nm) then Au(125nm)
 - ⇒ Use IMRI evaporator for > 15 nm deposition, the ion mill evaporator is **ONLY** for passivation, **not leads or thick structures**.
22. Lift-off with 60° C Acetone for 45 minutes followed by 3-5 second sonication.

Apparently ultra fine features with positive photoresist can be achieved via *cold development*, I was not aware of this during the development of this recipe but it is worth looking into for future recipe development [59].

3.3.6 Experimental Methods

The coplanar stripline antennas fabricated on top of the thin YIG films require a microwave frequency (RF) input at one port to generate spin waves and an RF spectral analyzer at the other port to observe the propagating spin waves. In order to characterize non-reciprocity, we either must swap the port connections, which reverses the direction of \mathbf{k} , or flip the direction of the \mathbf{H}_{ext} , which flips the dispersion relation for \mathbf{k} (but not both). Swapping the port

connections will introduce circuit based artifacts in the spectrum data due to displacement of cables and re-mating of port connectors. Flipping \mathbf{H}_{ext} on the other hand will include artifacts from any error in the field calibration or field controller. Ideally both of these aspects of the experiment should remain fixed and stable during data collection to improve quality of the measurement and uphold quantitative fidelity of the characterization.

A Vector Network Analyzer (VNA) helps to resolve this by measuring both forwards and backwards microwave signals (in our case propagating spin waves) without needing any changing of cables. Internally the port output and inputs are electrically switched, which allows us to observe and characterize non-reciprocity if there is any. The VNA sweeps a designated set of frequencies and measures the reflection and transmission for each frequency (usually in units of dB and phase or in real and imaginary components of voltage). It then electrically swaps the ports and repeats the measurement. Such measurements are assembled into a scattering matrix called an S-matrix, which represents the reflective and transmissive response of a network. For each frequency a 2-port VNA collects this matrix, which looks like:

$$\begin{bmatrix} S_{11} & S_{12} \\ S_{21} & S_{22} \end{bmatrix}, \quad (3.4)$$

where S_{xy} means the response at port x from port y . This data is usually represented either through magnitude (either log or linear scale) and phase, or as real and imaginary parts. If there are n -ports in a network, the S-matrix is an $n \times n$ matrix, where all off diagonal terms represent port to port transmission. When there is a difference between S_{xy} and S_{yx} , there is non-reciprocity in the network.

Fig. 3.10 shows the experimental set-up of our measurement. In order to map our spin wave spectra, we must collect the electrical response for a range of frequencies over a series of set external fields \mathbf{H}_{ext} . To be clear, we fix \mathbf{H}_{ext} , have the VNA collect an S matrix for a series

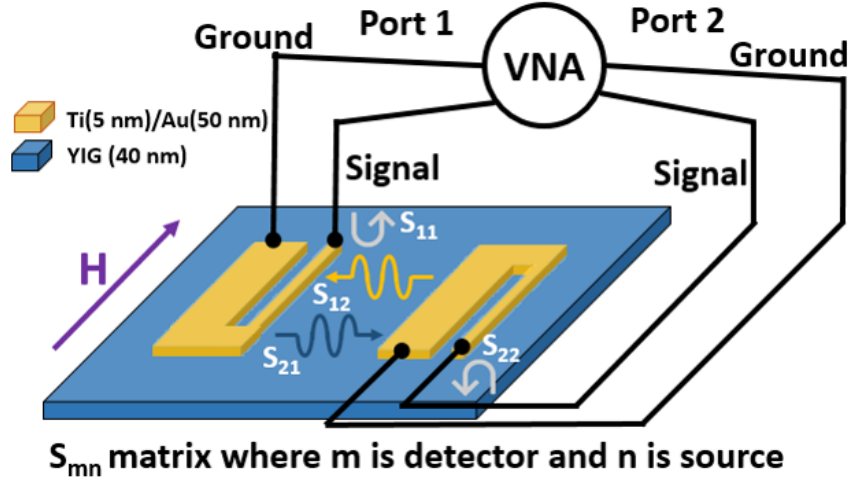


Figure 3.10: **Experiment set-up diagram (VNA)**. Vector network analyzer connected to spin wave antennas. Having the external field parallel to our antennas yields surface spin waves.

of frequencies, then increment \mathbf{H}_{ext} by a small step, and repeat. In doing so we collect a *trace* $S_{xy}(f)$ at every set field. We then can take these traces and compile them together to generate a 2 dimensional plot $S_{xy}(f, H_{\text{ext}})$ for each term in the S-matrix.

It is almost always required to do a calibration of the VNA prior to connecting your sample (calibration procedure is found in Smith [122]). Otherwise, the VNA output will introduce artifacts in your frequency swept traces. In our case however, we employ a measurement (and post-processing) technique that allows one to ignore the need to calibrate, assuming our field steps are sufficiently small (on the order of ≤ 5 Oe).

Fig. 3.11(a) shows a raw frequency vs field colorplot. If you look closely, you can see some systematic features. Due to the large background however, it is quite difficult to see, much less to characterize (indicated by Fig. 3.11(b)). Since we are studying the response to a *magnetic* stimulus, we need only to see the changes with respect to a *changing* magnetic field. This means that we can subtract out a trace measured at high field (where the spin wave frequencies would be outside the frequency range we are measuring) from all other traces. This method is often employed and is quite reliable for quick measurements and

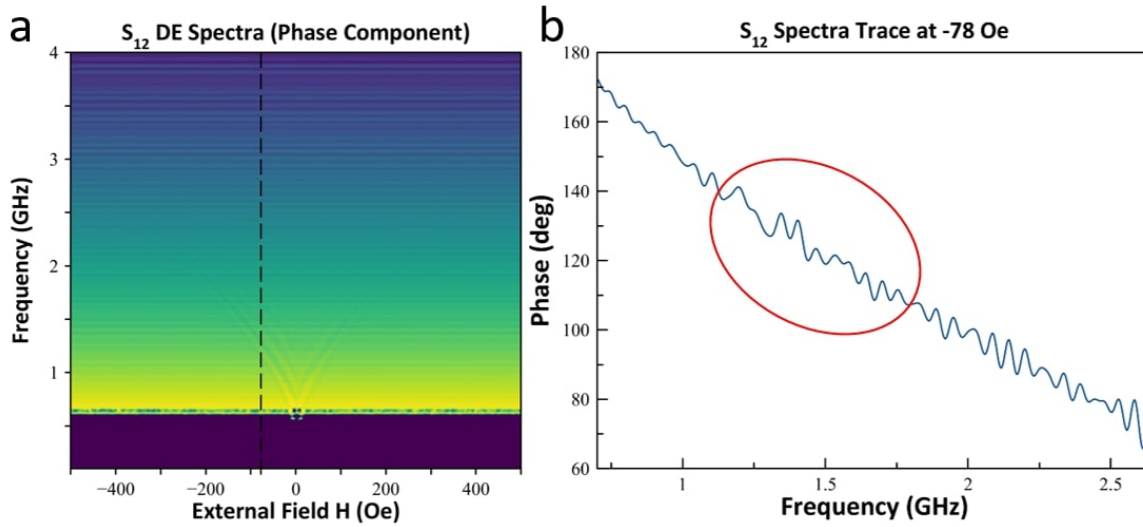


Figure 3.11: **Raw spectroscopy data collected with calibrated VNA.** (a) Colorplot of raw VNA traces collected over a series of H_{ext} , signals are visible near 1 GHz band, but difficult to see, even with calibration of microwave circuit. (b) Shows the trace taken at -78 Oe (cross section of dashed line in (a)), area circled in red is the ‘spin wave’ signal.

stable experimental set-ups. This approach however is still susceptible to any non magnetic drift (such as frequency dependent properties of the microwave circuit) as it will introduce and compound artifacts across the traces. It turns out, with small enough steps in field, one can isolate the magnetic response by taking the *field derivative* of the VNA traces [85]. This has shown to be quite effective in removing significant background as shown in Fig. 3.12, where the ripple pattern and large signal to noise ratio is evident (the non-reciprocity is also quite evident in this case too). In principle this removes the need for any kind of 2-port calibration for the VNA, since our derivative analysis does not require knowledge of the reference plane for the microwave circuit and removes any non-magnetic background.

With the data cleaned out and our signal quite clear, we can now perform quantitative analysis on our spectra. Fig. 3.12(a) has two notable features that we are interested in. One is the striping pattern, which when looked at via taking a cross section (VNA trace) like in Fig. 3.12(b), we observe that there is a systematic amplitude oscillation of the frequency swept trace across a small band of frequencies. This is indicative of propagating spin waves.

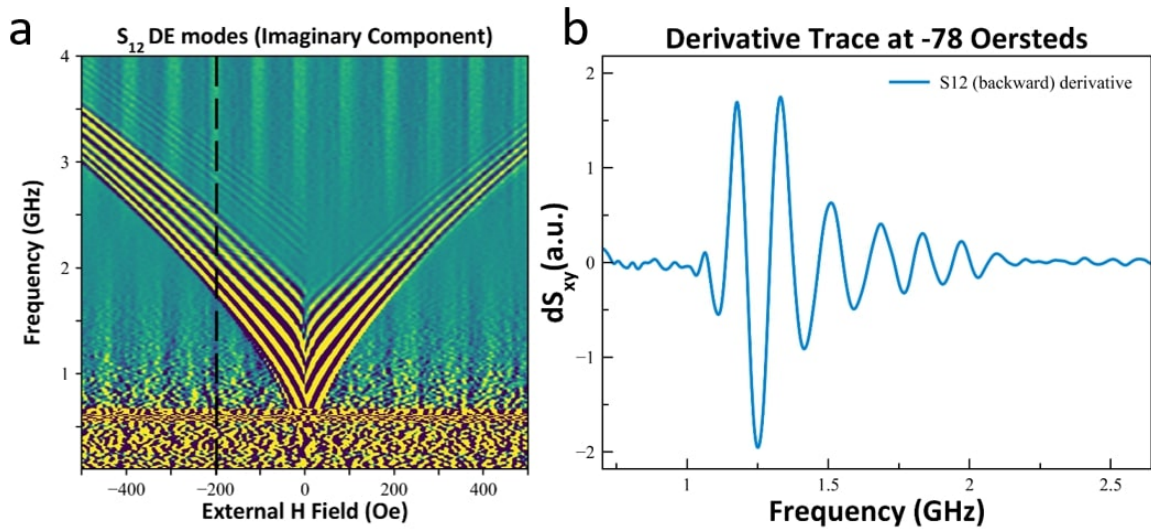


Figure 3.12: **Spectroscopy data after field derivative.** (a) Data in Fig. 3.11 after taking field derivative (note we switched to real and imaginary components, but the signal improvement was the same for phase data). Signal to noise ratio is considerably better. (b) Trace taken at -78 Oe. Signal is good enough to characterize.

As the detection antenna is inductively coupling to spin waves of increasing \mathbf{k} (equivalently shorter and shorter wavelengths). The amplitude will cycle continuously through 2π phase, which are the oscillations in the measured trace. Fig. 3.13 illustrates this effect.

The other feature is the clear asymmetry across $H_{ext} = 0$, this is indicative of non-reciprocity since flipping the external field flips the dispersion relation for the same sign of \mathbf{k} . We will show that for quantitative analysis however it is more reliable to compare across S_{12} and S_{21} for the same field, as the two data sets are collected one after another (whereas for opposite fields the measurement can introduce magnet control related artifacts or any possible temporal drift in data).

3.4 Results and Analysis for 40nm YIG

Fig. 3.14 Shows the f vs H color plot for each part of the S-matrix measured on GGG/YIG(40nm). The embedded cartoon shows physically which signal it represents. The S_{11}

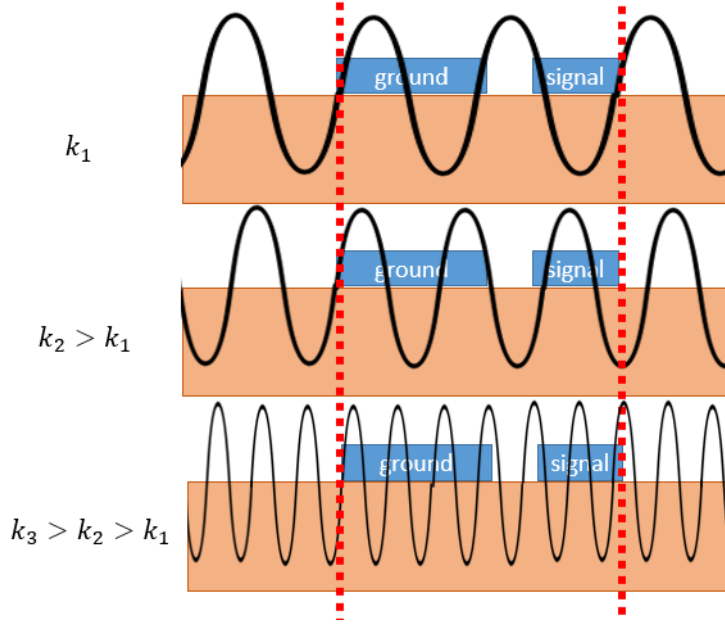


Figure 3.13: **Oscillations in frequency swept trace.** Coupling to shorter and shorter wavelength spin waves leads to a continuous cycling through 2π for signal amplitude. The region between the dashed lines shows how varying the wavelength will vary the phase of inductive pickup. This cartoon also illustrates why smaller geometry is needed in order to detect shorter wavelength spin waves. When the SW wavelength is below a certain length (like k_3), the effective pickup drops precipitously due to excessive oscillations within the coupling region. This is similar to when aliasing occurs in signal processing systems in general.

and S_{22} represents the *reflection* observed at the each port. In other words, it informs us at which frequencies there are power losses, usually in the form of being absorbed or radiated by an element in the network. The quasiuniform mode (a.k.a. the FMR or $\mathbf{k} = 0$ mode), is most notably visible in these spectra. There are more (considerably fainter) modes visible, which are likely due to some spin waves returning to the source antenna. The signals shown indicate that the antenna is *radiating* energy via excitation of spin waves. The S_{11} and S_{22} data in this context can be considered very similar to the standard absorptive FMR techniques used, where in this case the radio frequency source is on the micrometer scale. The S_{12} and S_{21} plots represent our *transmission* spectra. Here we observe any spin waves that are excited from one antenna and detected at the other. It is important to note that if there is any RF leakage (like cross talk or capacitive shunting), it will show up in these

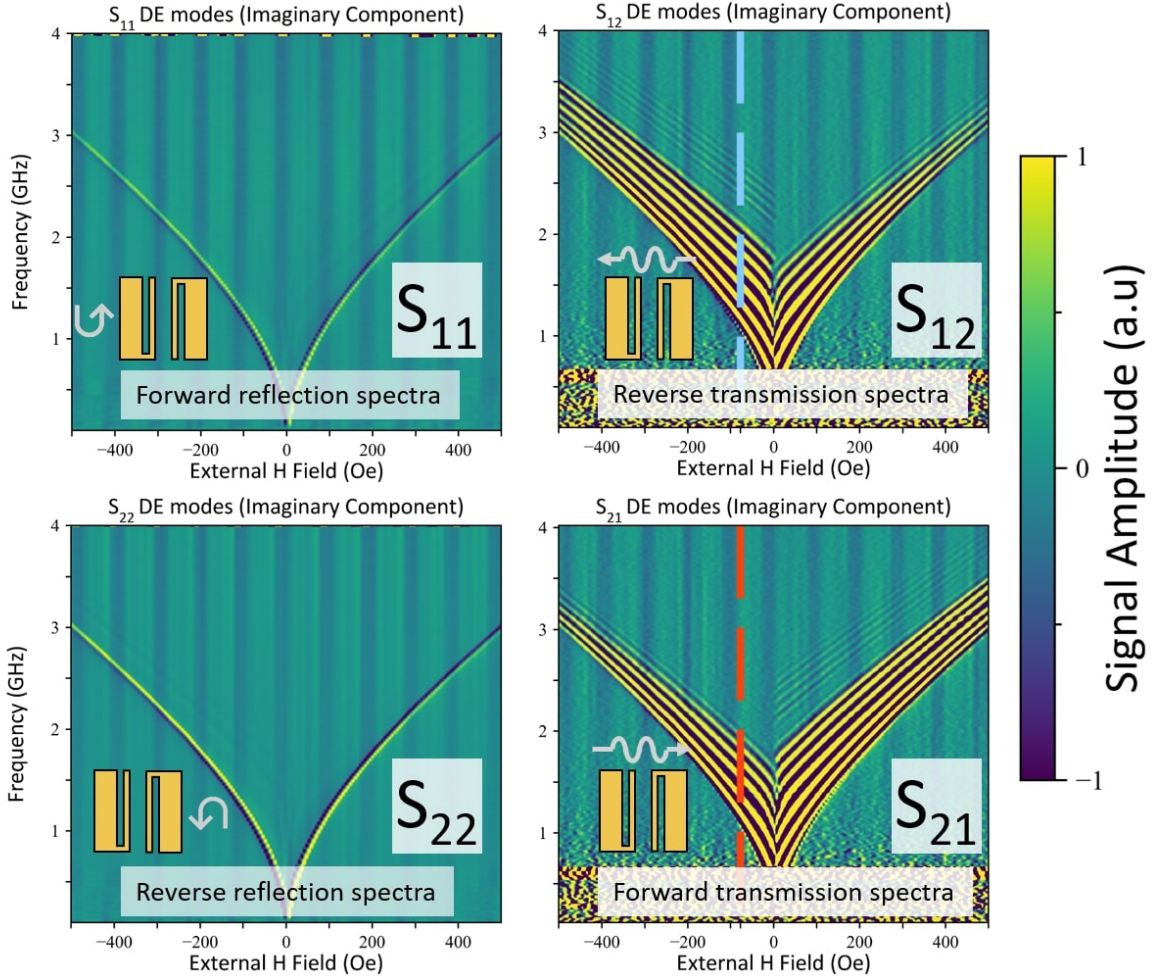


Figure 3.14: **S** matrix color plot for YIG on GGG. VNA traces measured across varying \mathbf{H}_{ext} compiled together to form colorplots. Inset cartoons clarify which antenna response the colorplot measures. The vertical dashed lines indicate the slices used in the trace comparison plot in Fig. 3.16.

VNA measurements (our field derivative approach however mitigates this).

As mentioned before, we observe nice oscillations which are indicative of exciting high wave number propagating spin waves. We also observe for the same field significant visual asymmetry (i.e. non-reciprocity) at higher order modes. We can take the film parameters we extracted from doing film level absorption FMR prior to nanofabrication and overlay the expected dispersion relation on our S_{21} color plot. The Eq. (2.69) is shown here again for

convenience:

$$f(H, k) = \frac{\gamma}{2\pi} \sqrt{(H + Dk^2)(H + Dk^2 + 4\pi M_{eff}) + \left(\frac{4\pi M_S}{2}\right)^2 (1 - \exp(-2|k|d))}$$

Fig. 3.15 shows this equation plotted over the colorplot, and serves as a sanity check on the legitimacy of the results (validation of FMR mode agreement). It also tells us how short the wavelengths are for our highest order detectable modes (about 400 nm). Which makes sense considering the dimensions of our antennas.

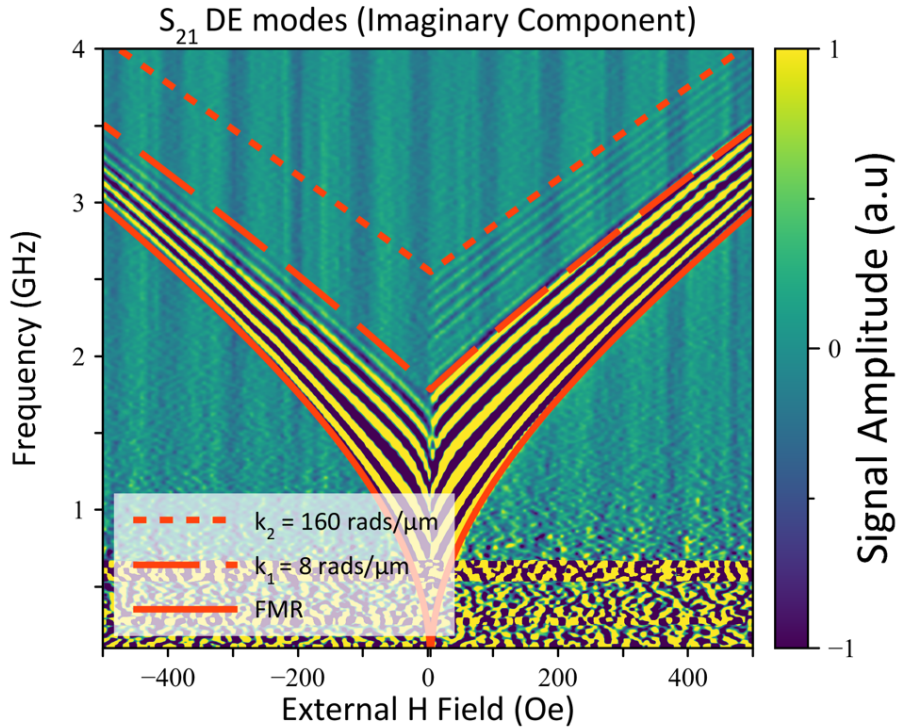


Figure 3.15: **Dispersion of Propagating SW in YIG(40nm) on GGG.** Spin wave dispersion relation for various \mathbf{k} overlaid on S_{21} color plot. We use $4\pi M_{eff} = 1.7$ kOe, $g = 2.02$, and assumed exchange stiffness $D = 5.2 \times 10^{-8}$ Oe cm² with thickness $d = 4 \times 10^{-8}$ m. The FMR curve is with $\mathbf{k} = 0$, while the dashed curves are with $\mathbf{k} \neq 0$. We confirm we can detect spin waves down to roughly 400 nm in wavelength.

In order to quantify the non-reciprocity we see, we compare the group velocity for forwards and backwards propagating SW. This is extracted from the frequency separation Δf between

two adjacent peaks of oscillations and plugged into this relation:

$$v_g = \frac{\partial \omega}{\partial k} \approx \frac{2\pi \Delta f}{\frac{2\pi}{s}} = \Delta f \cdot s \quad (3.5)$$

Where s is the propagation length. We demonstrate this comparison in Fig. 3.16.

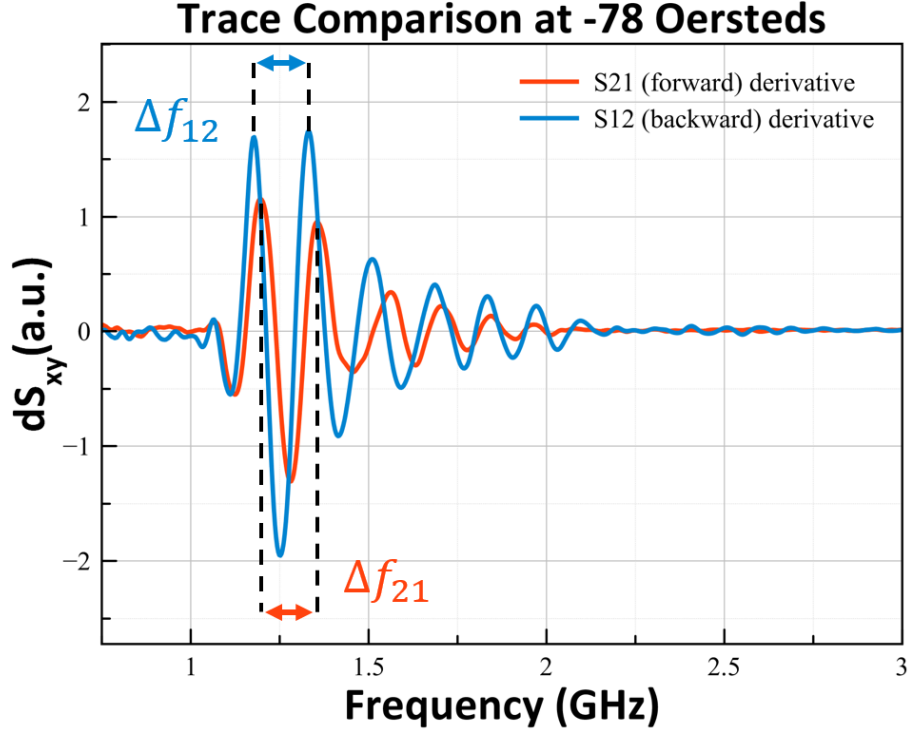


Figure 3.16: **Quantifying non-reciprocity of SW at fixed field for GGG/YIG.** VNA traces for S_{21} and S_{12} at -78 Oe which represents the signal for forwards and backwards propagating SW, respectively. The dashed lines in Fig. 3.14 correspond the fields that these traces were pulled from. We observe an amplitude non-reciprocity factor of $2/3$ and δv_g of 26 ± 5 m/s.

We calculate $v_{g(S_{12})} \approx 725 \pm 3$ m/s and $v_{g(S_{21})} \approx 699 \pm 3$ m/s, giving us a nonreciprocity δv_g of 26 ± 5 m/s, about a $4 \pm 1\%$ difference.

This result is actually quite surprising, as the system of GGG/YIG(40nm) does not have any particularly obvious indicators of being non-reciprocal. The ferrimagnet is sufficiently thin to be exchange locked and thus uniform along the thickness, there is no active region with any modulation of features, and the device configurations are symmetrical.

3.4.1 Interfacial Dzyaloshinskii-Moriya Interaction

We propose that perhaps the reason behind the non-reciprocity is that the interface with the GGG can actually introduce an effect called the interfacial Dzyaloshinskii-Moriya Interaction (iDMI)[36, 98, 99]. This effect occurs when there is an interface with a high spin orbit coupling material. The fundamental idea behind iDMI is that the presence of spatial inversion symmetry breaking (like an interface) with spin orbit coupling leads to anti-symmetric exchange interaction terms that favors neighboring magnetic spins to be *canted*. The strength of the interaction was calculated with super-exchange and strong spin orbit coupling [98]. Fig. 3.17 shows a nice schematic of iDMI from [38]. The energy term is:

$$\mathbf{D}_{12} \cdot (\mathbf{S}_1 \times \mathbf{S}_2), \quad (3.6)$$

where \mathbf{D}_{12} is the DMI vector relating to the coupling between the neighboring spins and the large SOC interfacial atom. One can see that Eq. (3.6) is minimized when two spins (\mathbf{S}_1 and \mathbf{S}_2) are perpendicular to each other (hence favoring canted magnetic textures).

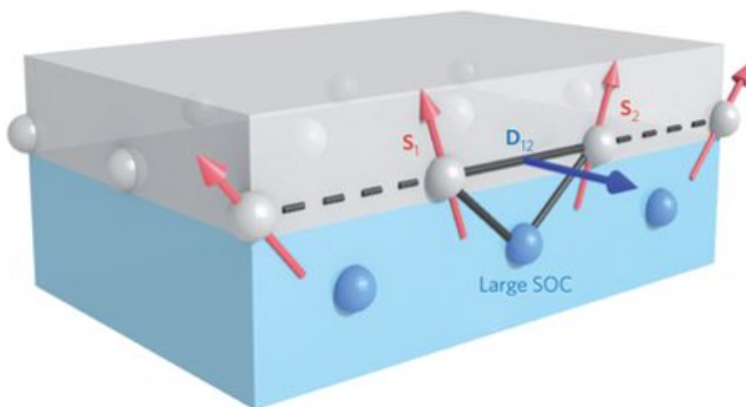


Figure 3.17: **Cartoon schematic of iDMI.** The two spins (gray) become coupled through the heavy metal (blue) in the interfacial layer. Cartoon is from Fert et al. [38].

In context of this chapter, the effects of iDMI lead to a *linear* term in the dispersion relation,

which means that the difference in group velocity with respect to iDMI looks like:

$$\delta v_g = \left[\left(\hat{\mathbf{n}} \times \hat{\mathbf{H}} \right) \cdot \hat{\mathbf{k}} \right] \frac{\gamma}{M_S} D_{iDMI} \quad (3.7)$$

Where $\hat{\mathbf{n}}$ is the direction normal to the interface, $\hat{\mathbf{H}}$ is the external field direction, $\hat{\mathbf{k}}$ is the wave vector, γ is the gyromagnetic ratio, M_S is the saturation magnetization, and finally D_{iDMI} is the phenomenological constant accounting for the strength of iDMI in the system.

Plugging in δv_g and our previously measured $M_S = 140 \text{ kA m}^{-1}$, we have determined that $D_{iDMI} = 5.17 \mu\text{J m}^{-2}$ in our GGG/YIG system. We can take this idea and ask whether we can enhance this effect by inserting a known heavy metal layer like Pt between the YIG and GGG.

3.5 Results for GGG/Pt/YIG

Fig. 3.18 Shows the propagating spin wave spectra for GGG/Pt(10nm)/YIG(40nm). Due to the Pt enhancing the damping in the system (since it is an effective spin sink) [93], there is some loss of resolution for the spectroscopy measurement, regardless, we are able to resolve spin waves down to $1.4 \mu\text{m}$ in wavelength.

We repeat the analysis procedure and compare the forwards (S_{21}) and backwards (S_{12}) propagating spin wave VNA traces for the same fixed field of $\sim 78 \text{ Oe}$. Fig. 3.19 shows this comparison. We observe a larger amplitude non-reciprocity factor of 5 and extract the calculated group velocities to be $v_{g(S_{12})} \approx 822 \pm 4 \text{ m/s}$ and $v_{g(S_{21})} \approx 775 \pm 4 \text{ m/s}$. Which yielded a δv_g of $47 \pm 6 \text{ m/s}$, which yields a nonreciprocity of $6 \pm 1\%$. If we attribute this non-reciprocity to iDMI, we calculate the constant to be $D_{iDMI} = 8.01 \mu\text{J m}^{-2}$

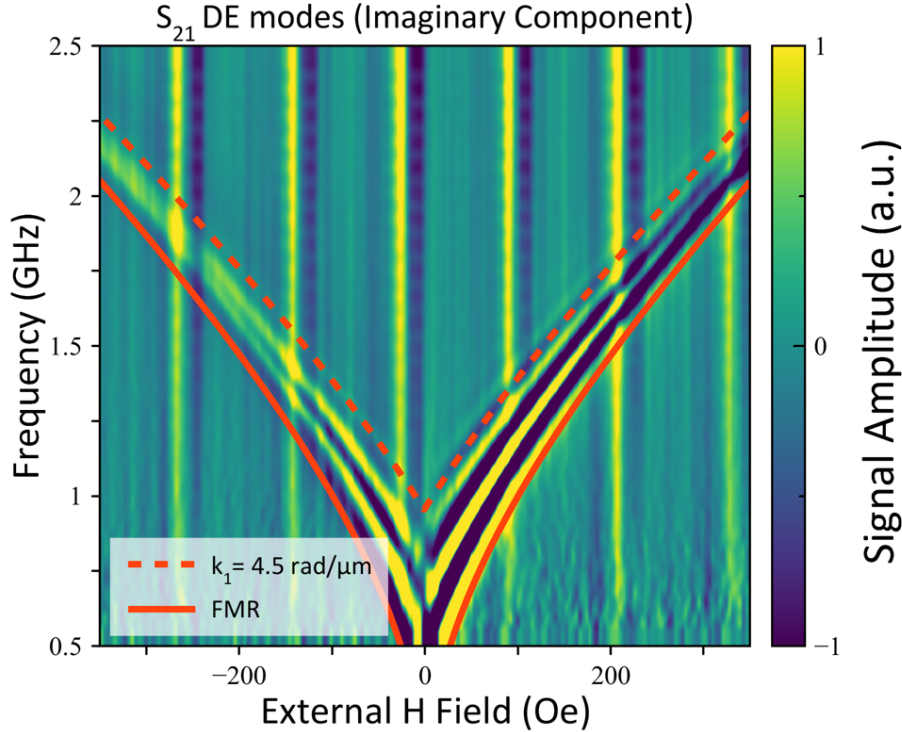


Figure 3.18: **Dispersion of Propagating SW in GGG/Pt/YIG.** We observe similar qualitative features to Fig. 3.15, but with less wavelength resolution. We use $4\pi M_{eff} = 1.2$ kOe, $4\pi M_S = 1.5$ kOe, $g = 2.01$, and assumed exchange stiffness $D = 5.2 \times 10^{-8}$ Oe cm² with thickness $d = 4 \times 10^{-8}$ m. The FMR curve is with $\mathbf{k} = 0$, while the dashed curves are with $\mathbf{k} \neq 0$.

3.6 Discussion

We have shown that the field derivative technique works for propagating spin waves in a VNA measurement, the significantly enhanced signal to noise ratio (from Fig. 3.11 to Fig. 3.12) allows us to not require VNA calibration and quantitatively characterize spin waves.

The amplitude non-reciprocity in our results is well understood as it has to do with the proximity of the spin wave antenna to the surface of propagation. Mentioned at the end of Section 2.2.4, field displacement non-reciprocity points to the fact that there will always be a *non-zero* difference in coupling of the spin wave antenna to the surface directly interfacing it and the surface on the other side of the film thickness. This actually has some implication that perhaps our films were not thick enough to be *truly* exchange locked.

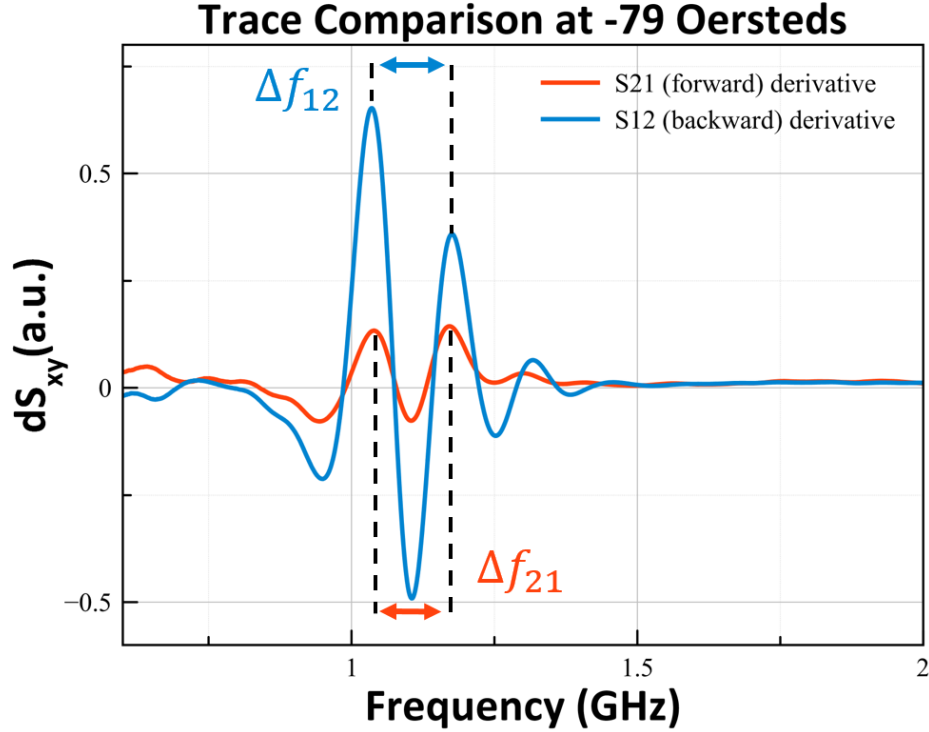


Figure 3.19: **Quantifying non-reciprocity of SW at fixed field for GGG/Pt/YIG.** VNA traces for S_{21} and S_{12} at -78 Oe. We observe an amplitude non-reciprocity factor of $1/5$ and δv_g of 47 ± 6 m/s.

As mentioned in Section 3.4.1, we propose that the dispersion non-reciprocity we see may be due to the GGG substrate introducing interfacial DMI to our system. It is argued that the GGG and YIG interface induces a *Rashba* effect (splitting of bands due to the interaction between momentum and spin) which then is manifested as a DMI-like term in the dispersion relation [7]. This work motivates looking more deeply into Rashba induced non-reciprocity in other films, as it may have potential in engineering highly non-reciprocal media.

Alternatively, the dispersion non-reciprocity in GGG/YIG may be attributed to some specific sources, one may be that the difference in surface anisotropy between the GGG and air interfaces. Since our configuration excites surface spin waves (Eq. (2.69)), the different interfacial anisotropies will shift the dispersion relation asymmetrically by some constant value. Additionally, it has been shown in literature that YIG films can have a *magnetically dead* layer [62], which can vary the surface anisotropy or even the damping. In other words,

even though the film is thin, it may not be thin enough to be treated as a homogeneous magnetic material throughout. This means that the Damon Eshbach surface waves can be thought of as travelling in *two different mediums* for their corresponding directions.

By repeating the measurement in GGG/Pt/YIG, we have observed an enhancement of the dispersion non-reciprocity. The comparison is shown in the table below. We see the group velocity difference is doubled from bare YIG to Pt/YIG, we also see that the non-reciprocity was raised from $\sim 4\%$ to $\sim 6\%$, which is a 50% increase. This supports our working theory that the non-reciprocity is stemming from iDMI.

GGG/YIG(40)	GGG/Pt(10)/YIG(40)
$\delta v_g \approx 26 \pm 5 \text{ m/s}$	$\delta v_g \approx 47 \pm 6 \text{ m/s}$
$M_S \approx 140 \text{ kA/m}$	$M_S \approx 120 \text{ kA/m}$
$D_{iDMI} = 5.17 \mu\text{J/m}^2$	$D_{iDMI} = 8.01 \mu\text{J/m}^2$

Despite our iDMI factors being quite small (many materials with characterized iDMI are on the order of mJ or hundreds of μJ [42]), we discover a very clear effect in our system. The fact that it is clearly visible in our low damping, single crystal system is promising for future spin wave research and applications.

It would be interesting to see the effects of other underlayers on the non-reciprocity of YIG, in our case, we have observed considerably enhanced damping due to the Pt, which required challenging fabrication to make measurable. With improved nanofabrication techniques however, characterization of non-reciprocal spin waves in higher damped systems will become accessible. Such systems may have other attractive features that are not present in low damping systems like YIG. With non-reciprocity induced by the media itself, passive non-reciprocal magnonic devices can be explored.

3.7 Additional Notes

3.7.1 Comments regarding spin wave antennas

Spin wave antennas

When designing spin wave antennas it is a good idea to make sure the impedance of the structures do not deviate from 50 Ohms, several COMSOL like softwares can do these calculations for your exact geometry. Alternatively can do a preliminary check with the length and cross sectional area of the signal line in the antenna and the material (usually gold) it is made of, as the signal line will be the most resistive part of the circuit. The simulation suggestion is nice though if you want the RF related values of your design.

Antenna Health

The spin wave antennas have been pretty robust to electrostatic discharge, I've only had one device 'explode' ever. Prior to hooking up the sample to the VNA, I did some quick DC resistance measurements on the ports. To do so, I connected SMA to banana adapters on the sample holder ports and used banana cables to check each permutation of port connections.

For a two port sample this means:

- (After wirebonding only the signal lines to the antennas)
Port 1 signal \Rightarrow Port 2 signal (should be open, if there is resistance then there is a short somewhere).
- Port 1 signal \Rightarrow Port 1 ground (ideally 50 ohms)
- Port 2 signal \Rightarrow Port 2 ground (ideally 50 ohms)

- Port 1 signal \Rightarrow Port 2 signal (should be sum of above resistances since it routes through both)
- Port 1 ground \Rightarrow Port 2 ground (~ 1 ohms)

Chapter 4

Spin Flexoelectric Gate on GGG/Pt/YIG

4.1 Motivation

Most of Chapter 3 was accomplished as a means of developing fabrication and measurement techniques toward this study, where the goal is not only to achieve non-reciprocity but to be able to *tune* it via external control like voltage. In this study we aimed to use the *spin flexo-electric interaction* (SFEI) to create a spin wave device where the applied voltage can change the non-reciprocity. Such an effect would open many new application routes like spin wave logic gates, multiplexed spin wave busses, and more [63].

4.1.1 Spin Flexoelectric Interaction

One of the ways in which non-reciprocity can be manifested is through simultaneous breaking of time reversal and spatial inversion symmetry. This warrants studying electric fields in

ferromagnetic media, as the electric field breaks inversion symmetry and the ferromagnetism breaks time reversal symmetry. The electric field results in a nonzero electric polarization of the media, which then leads to a *Doppler*-like shift in the spin wave spectra. In other words, the electric field couples to the gradient of magnetization and modulates the spin wave dispersion relation through a new energy term.

The mathematical representation of this effect is as follows: we construct the ‘flexo-electric’ induced field term, append it as a modulation of the base Hamiltonian H_0 , which already contains the exchange, anisotropy, and dipole interaction terms, and proceed to solve the system of torques and boundary conditions using linearization and perturbative approximations. I will only present the mathematical starting point to present the intuition and the end result to provide the quantitative motivation.

The spin flexoelectric interaction manifests itself as a coupling like [91]:

$$V_E^{(1)} = b_1 \int d^3r [\mathbf{E} \cdot \mathbf{M}(\mathbf{r})] [\nabla \cdot \mathbf{M}(\mathbf{r})] \quad (4.1)$$

and

$$V_E^{(2)} = b_2 \int d^3r \mathbf{E} \cdot \{\mathbf{M}(\mathbf{r}) \times [\nabla \times \mathbf{M}(\mathbf{r})]\} \quad (4.2)$$

where b_1 and b_2 are phenomenological constants associated with the effect. These terms result in an overall combined effective energy V_E that gets included in the complete Hamiltonian $H = H_0 + V_E$ in calculation. Through linearization and some simple assumptions (similar to Section 2.2.4), the resulting dispersion with their vector relationships intact is:

$$\omega_E(\mathbf{k}) = \omega_0(\mathbf{k}) - \gamma b \mathbf{k} \cdot [\mathbf{E} \times \mathbf{M}_S], \quad (4.3)$$

where ω_0 is the non-electric field portion of the dispersion relation (includes exchange, ap-

plied, and anisotropy fields), and b is the combined phenomenological constant (which is our goal to measure).

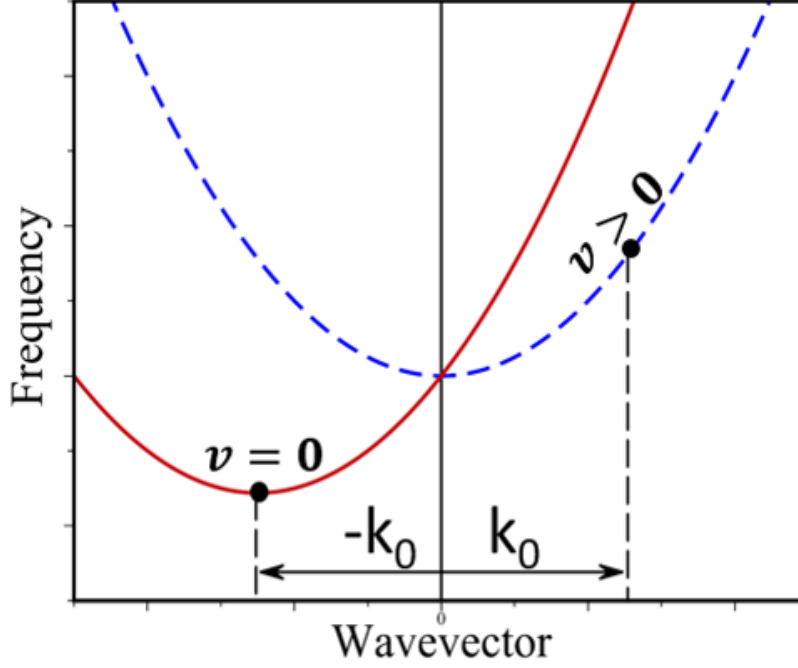


Figure 4.1: **Effect of flexo-electric interaction on spin wave dispersion.** The blue dashed curve is the reciprocal spin wave dispersion relation when $E = 0$, which has a symmetric parabolic shape. When a linear term is introduced, the curve is *canted* (red solid curve), leading to non-reciprocity. Measuring spin wave group velocity in opposite directions informs us whether there is non-reciprocity, as shown by the slope of the dispersion curve for equal and opposite k_0 .

Note that when \mathbf{E} is \perp to both \mathbf{M}_S and \mathbf{k} , we get:

$$\omega_E(\mathbf{k}) = \omega_0(\mathbf{k}) + \gamma b E_{\perp} M_S k_x, \quad (4.4)$$

where x is the axis of spin wave propagation. Here we have shown that the introduction of an electric field leads to a linear shift in the the dispersion relation, it is important to see here that it depends on the sign of k and E . So for a fixed electric field, our dispersion relation would experience a linear shift like in Fig. 4.1.

The critical quantitative feature that we will utilize is the group velocity $\frac{d\omega}{dk}$:

$$v_g(E) = \frac{d\omega}{dk} = v_{g0} + -\gamma b M_S E_{\perp} \quad (4.5)$$

Where v_{g0} is the base group velocity without SFEI present. This informs us that for a fixed applied field, we can change the electric field and measure the variation in spin wave group velocity, this is our objective.

4.2 Device Design and Nanofabrication

Like in Chapter 3, we are performing spin wave spectroscopy measurements. In this project we have one additional complication: inclusion of a *gated* active region. So everything covered in there is relevant here. Furthermore, the GGG/Pt/YIG samples measured in Chapter 3 were used for this study as well.

4.2.1 SW Antennas with Gated Active Region

The spin wave antennas will follow the same coplanar stripline design used in Chapter 3. Since SFEI and it's calculated non-reciprocity scales with increasing \mathbf{k} (shorter wavelengths), we must still aim for fine width antennas so that we can couple to these higher wave vectors and see a more pronounced effect.

The spin wave non-reciprocity from SFEI requires an electric field perpendicular to the plane of the ferromagnetic film. This is why we are fabricating on top of GGG/Pt/YIG. Since YIG is insulating, a deposited Au gate on top of film surface would then form a parallel plate capacitor between the Au and Pt, generating the desired electric field configuration when a voltage is applied across the Au gate and the Pt underlayer. Fig. 4.2 shows a general

schematic for the electric field gate, where the metallic underlayer serves as the back plate for our effective parallel plate capacitor.

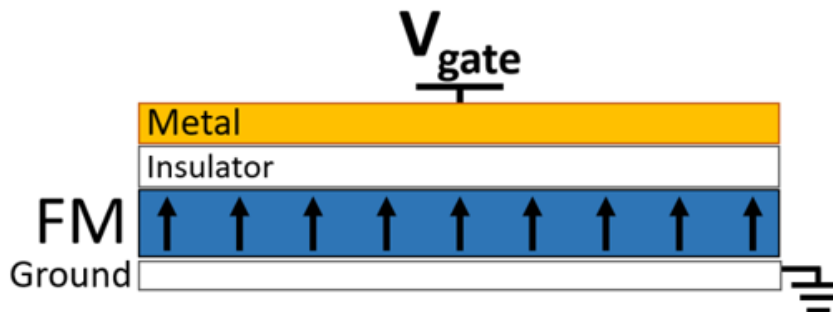


Figure 4.2: **General schematic of generating perpendicular electric field.**

Top gate metal and back plate generate an out of plane electric field (black arrows) through the ferromagnet. If \mathbf{M} is into or out of the page, and \mathbf{k} is pointing perpendicular to both \mathbf{M} and \mathbf{E} , then then Eq. (4.4) describes the resulting effect on the dispersion relation. In our case, since the FM is insulating in our system, we do not require an insulating layer between the top gate and FM.

Since the Pt is everywhere underneath the YIG film, we must pattern a working area in which we do not have to worry about any electrical shorting across the Pt underlayer for the antenna leads. This is achieved by patterning and etching a trapezoid that is $100 \times \sim 400 \mu\text{m}$ with 45° angled edges to absorb any spin waves travelling to the ends (shown in Fig. 4.3). Our leads are patterned off of the Pt/YIG trapezoid so that wire bonds only land on Au pads. The mesa size is also deliberately large such that one wire bond can land on the edge, puncture through the thin YIG into the Pt, and ground it to become back plate of the electric field gate.

The Pt underlayer however also increases the magnetic damping in adjacent films, which means that shorter wavelength spin waves may be harder to detect and thus the group velocity characterization may be more difficult. Ideally growing YIG on top of a non-heavy spin orbit coupling material like Au would improve measurement fidelity.

Two spin wave antennas are fabricated down the center of the mesa, with a large ‘gated’ area between the spin wave antennas. Fig. 4.4 shows an SEM of the device up close.

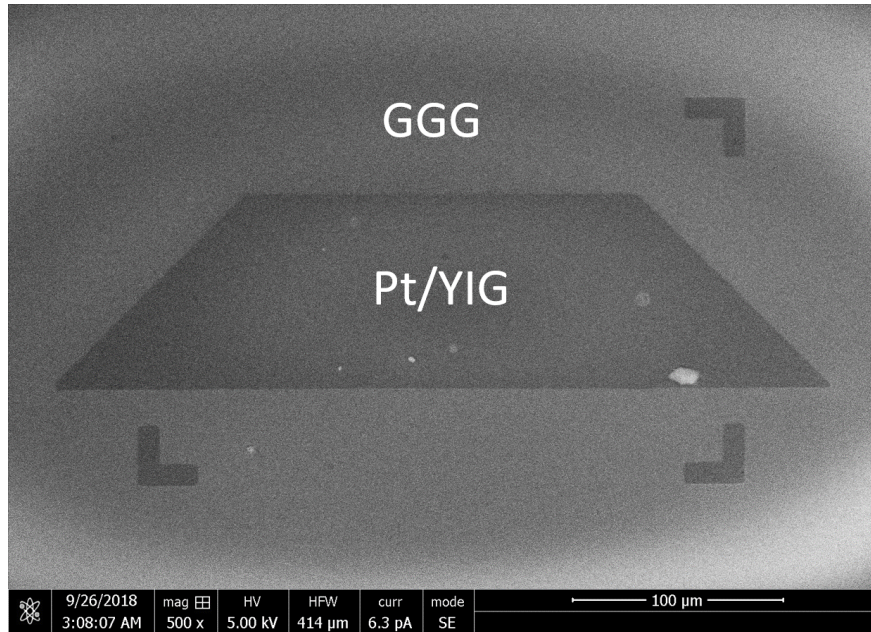


Figure 4.3: **SEM of etched Pt/YIG mesa.** Scanning electron micrograph image of etched trapezoid of Pt/YIG, the edges are angled to be 45° to absorb spin waves. Spin wave antennas and gates are then fabricated such that the wire bond pads are off of this area. The mesa is large so that one wire bond can land on one of the edges, puncture the thin YIG, and connect the Pt under layer to ground.

4.2.2 Nanofabrication Procedure

The fabrication procedure is similar to that of Section 3.3.5 but with some minor modifications. Since the antenna leads must be off of the mesa, there is a small chance of shorting to the Pt underlayer near the edges, to prevent this, an insulating layer must be deposited prior to deposition of the antennas. Otherwise most of the process is the same, I will list the steps in a more concise manner with additional comments specific to this fabrication.

One thing worth stressing is that since the spin wave antenna patterning step is non-destructive (everywhere but the exposed area is still protected), fabrication can be repeated over the same chip *from one mesa to mesa*. This is extremely useful if you have a limited number of films to nanofabricate on. As long as the film is not susceptible to repeated thermal cycling to 180°C , a lot can be done on a single film.

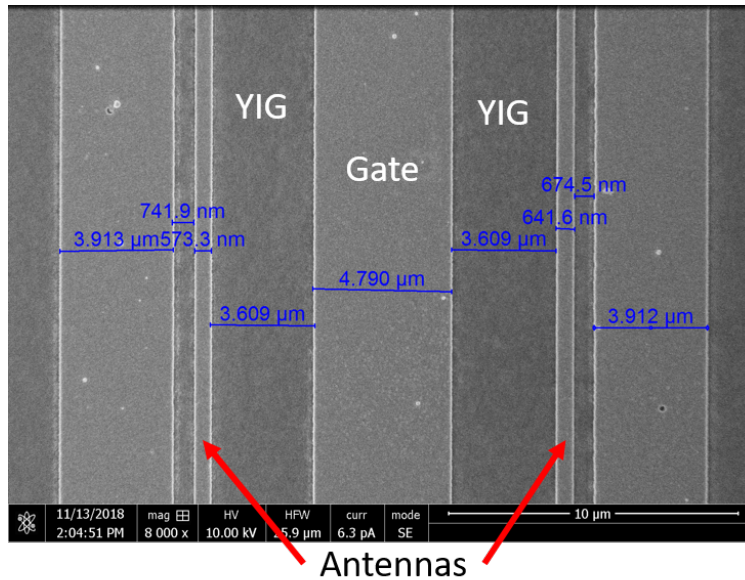


Figure 4.4: **SEM of SFEI devices on PtYIG.** Scanning electron micrograph image of spin wave antennas with electric field gate in the center, dimensions are measured and displayed.

4.2.3 Itemized Nanofabrication Steps

Refer to Section 3.3.5 for additional commentary on the bilayer lift-off section of fabrication.

Etching the Pt/YIG mesa.

1. Acetone clean, 3 min sonication.
2. IPA clean, 3 min sonication.
3. N₂ Dry
4. Spin coat ma-N24xx negative photoresist at 3500 rpm for 45 seconds (program 5)
 ⇒ The thicker the hard mask the better, YIG etches pretty slowly, so the mask must survive the entire etching time.
5. Post-bake at 90° C for 60 seconds.
6. Protect sample from natural lighting until EBL (wrap in foil or keep in drawer).

7. EBL sample

⇒ About $300 \mu\text{C}/\text{cm}^2$ should be sufficient, the more mesas on a chip the better, exposed ma-N24xx is difficult to remove though so this is a semi-permanent step.

8. Develop in maD-525 for 60 seconds, then rinse in DI water for 3 minutes.

9. See in optical for confirmation of structures.

10. Etch in ion mill all the way down to the substrate GGG

⇒ For GGG/Pt(10nm)/YIG(40nm), total etch time was 16 minutes at 65 degrees with 25% duty cycle (ion mill program 5)

⇒ (YIG etches at 3.7 nm/min at 65 degrees, Pt etches at 9 nm/min)

Bilayer Lift-off of SW Antennas and Gate

1. Clean sample in Acetone, sonicate for 3 minutes.

2. Quickly move sample over to IPA, sonicate for 3 more minutes.

3. Dry using N2 gun

⇒ Be sure that liquid does not flow from your tweezers onto the substrate as that accumulates dirt. You can flow the N2 towards the tweezers until dry, be careful to not let the tweezers slip or chip fly away. Visually inspect for dirt or residue using reflection of the surface.

4. Spin coat MMA at 4000 rpm for 45 seconds (program 6)

⇒ When dispensing MMA, make sure to not touch the pipette tip, blow out with N2 including towards the inside, squeeze the pipette while N2 cleaning so it doesn't suck in any dust/dirt, while still squeezed, carry to resist bottle and fill with couple drops of MMA, dispense couple drops onto chip.

5. Post-bake on hot plate at 180° C for 90 seconds.
6. Cool for 20 seconds
7. Spin coat PMMA at 1800 rpm for 45 seconds (program 8).
8. Post-bake on hot plate at 180° C for 90 seconds.
9. Let cool for 20 seconds. Change hot plate temperature to 90° C.
10. Spin coat ‘fake e-spacer’ (PSSA + Triton X) at 3600 rpm for 45 seconds (program 9).
11. Post-bake on hot plate at 90° C for 3 minutes.
⇒ Keep sample in dark place or wrapped in foil until EBL time, be sure to follow standard fume hood/spin coater SOP to clean up after yourself.
12. Evaporate or Sputter 7 nm Au or 3 nm Pt.
13. Perform EBL, you can use alignment steps or execute the proper Δx and Δy for the specific mesa.
⇒ For GGG/YIG(40nm) 125 $\mu\text{C}/\text{cm}^2$ at 13 pA for fine features seem to work, this will vary from substrate to substrate up to 250 $\mu\text{C}/\text{cm}^2$, higher current can be done for larger features.
14. Submerge in deionized water for 45-60 seconds to remove the PSSA and conductive layer.
⇒ You can visually see the metal peel off, let it do its thing when it happens. Note DI water slightly develops the resist. Can sonicate if necessary.
15. Develop in MIBK:IPA (1:3) for 20-40 seconds
⇒ Pick a consistent time like 30 seconds for dose testing and development. Can do 15 second increments to gauge progression of features.

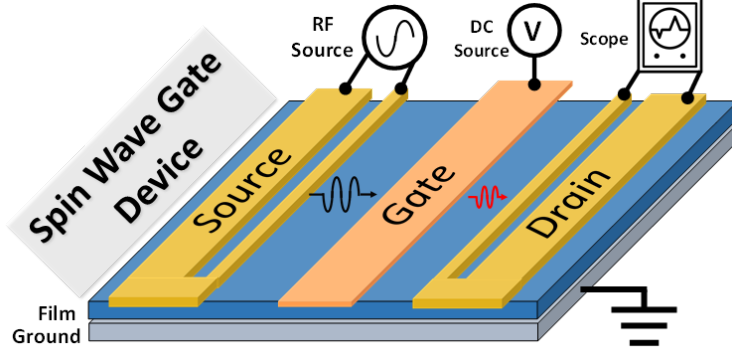


Figure 4.5: **Schematic of SFEI measurement.** Diagram showing how to measure SFEI on a gated spin wave device. We use a VNA to serve as an oscilloscope and microwave source simultaneously with the added benefit of being able to measure forwards vs backwards spin waves.

which generates our electric field E :

$$E = \frac{V}{d} \quad (4.6)$$

We perform the measurements first by mapping the entire SW spectra when the gate is disconnected ($V = 0$, methods discussed in Chapter 3), then choose a fixed field where the propagating spin wave oscillations are clearest. Next, we take VNA traces for one direction of spin waves under varying gate voltages. From the traces measured we extract the group velocities by measuring the frequency separation between adjacent peaks (just like in Chapter 3):

$$v_g = \frac{\partial \omega}{\partial k} \approx \frac{2\pi \Delta f}{\frac{2\pi}{s}} = \Delta f \cdot s \quad (4.7)$$

where s is the propagation length, and see if any variation has resulted. In order to average out any temporal drifting as the set voltage is changed, we measure traces with the gate voltage steps alternating from positive to negative. We also average the group velocity measurement for each set gate voltage over multiple measurements.

Finally, to map the results to the phenomenological constant b we measure the group velocity for different gate voltages relative to when the gate is off. Assuming that the shifting is linear, we can combine Eq. (4.6) and Eq. (4.5) to form

$$v_g(E) = v_{g0} + -\gamma b M_S \frac{V}{d} \quad (4.8)$$

and fit for b .

4.4 Results and Discussion

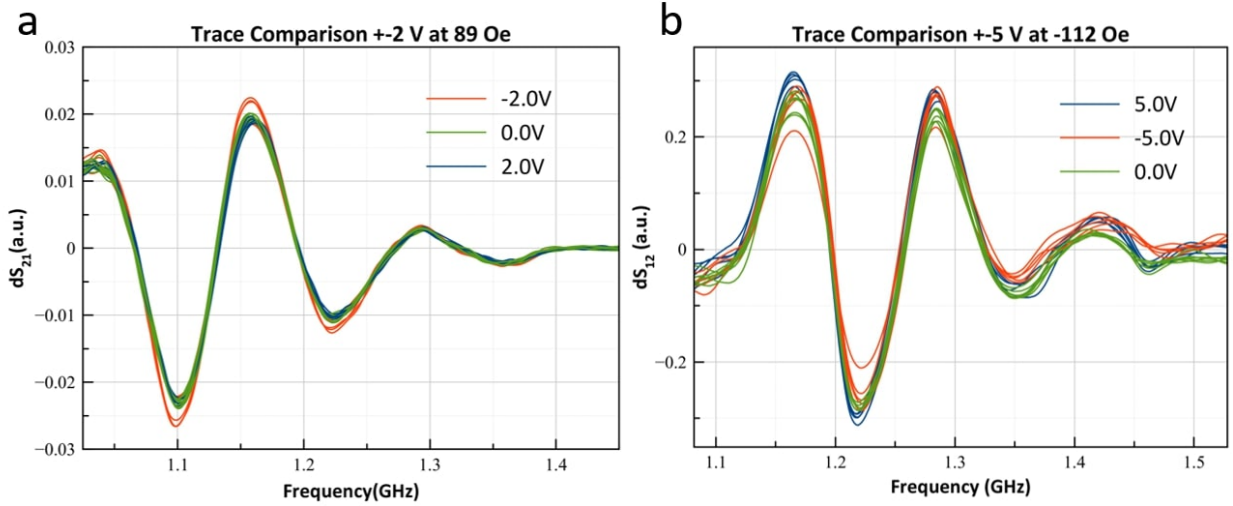


Figure 4.6: **VNA traces of SW under $\pm V$ applied to gate.** Measurements of propagating spin waves under different gate voltages for 2 devices. Qualitatively an effect seems visible, but almost within noise. **(a)** Device measured under 89 Oe at ± 2 V, where $\overline{\Delta v_{g2+}} = +3$ m/s and $\overline{\Delta v_{g2-}} = -3$ m/s. **(b)** Device measured under -112 Oe at ± 5 V, where $\overline{\Delta v_{g5+}} = -12$ m/s and $\overline{\Delta v_{g5-}} = -0.7$ m/s. Fitting of the data is shown in Fig. 4.7.

Fig. 4.6 shows the results of two devices under different gate voltages. We observe little variation in the peak to peak separation of our spin wave signal oscillations, indicating that the effect is very small. Qualitatively, we visually see some nonzero effect. Fig. 4.6(a) shows a device that yields a shift of $+3 \pm 5$ m/s for 2 V and -3 ± 3 m/s for -2 V over multiple measurements. We fit our group velocities as a function of voltage using Eq. (4.5) and

Eq. (4.6) with $\gamma = 2.8 \text{ MHz/Oe}$, $M_S = 120 \text{ kA/m}$, and $d = 40 \text{ nm}$. The fitting is shown in Fig. 4.7(a). This yields us an upper bound for the phenomenological constant value of $b \leq 1.54 \times 10^{-17} \text{ m}^2/\text{V}$.

The process was repeated for a different device (Fig. 4.6(b)) for $\pm 5 \text{ V}$. In this measurement, we measure and calculate $\overline{\Delta v_{g+}} = -12 \pm 4 \text{ m/s}$ and $\overline{\Delta v_{g-}} = -0.7 \pm 5 \text{ m/s}$ which were averaged across numerous traces. The lack of shifting direction for opposite voltages does not meet our expectations and is not understood. Regardless, when fitted for (shown in Fig. 4.7(b)), we obtain an upper bound $b \leq 1.30 \times 10^{-17} \text{ m}^2/\text{V}$.

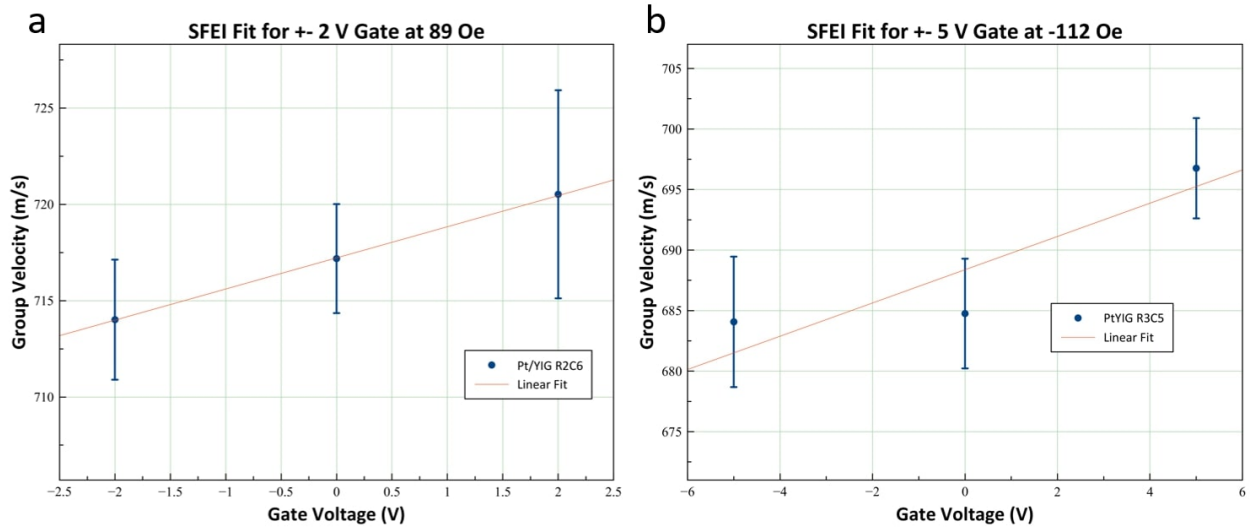


Figure 4.7: **Fit plots for SFEI constant.** Fitting of average group velocities extracted from peak to peak separation in Fig. 4.6. The data points for nonzero gate voltages are averaged across 5 measurements, the zero voltage data point was averaged across 10. (a) Fitting for $\pm 2 \text{ V}$ applied at the gate yields $b \leq 1.54 \times 10^{-17} \text{ m}^2/\text{V}$. (b) Fitting for $\pm 5 \text{ V}$ applied at the gate $b \leq 1.30 \times 10^{-17} \text{ m}^2/\text{V}$.

The lack of significant effect is consistent across multiple devices. Even with high averaging ($\times 100$ per point in Fig. 4.6) and repeated measurements, the variation (Fig. 4.7) in the extracted group velocities under an active gate was on the order of the variation with no gate voltage. Due to this, it was difficult to quantify, especially due to the enhanced damping and non-reciprocity from the Pt. While qualitatively an effect *seems* visible, the standard error

from our measurements (shown in Fig. 4.7) places it fairly close to within noise. Zhang et al. [141] measured a similar set-up but on a 30 mm scale that calculated $b = 1.095 \times 10^{-16} \text{ m}^2/\text{V}$, which is almost an order of magnitude larger than our fitted upper bound. When their value is used to calculate the expected shifts for our devices, we expect a shifted group velocity of $\sim 23 \text{ m/s}$ for 2 V and $\sim 58 \text{ m/s}$ for 5 V. It is surprising to not see a significant shift as their measurements exhibited a clear effect even with smaller wave vector (60 cm^{-1} compared to our $1.5 \mu\text{m}^{-1}$) and electric field ($\sim 10^6 \text{ V/m}$ compared to our $\sim 10^8$). According to that measurement and the theory, our experiment should have yielded largely tuneable non-reciprocity because we are operating at two orders of magnitude larger for both k and E . We suspect that perhaps something else is at play for their observable effect, since it involves long wavelength spin waves, huge propagation distances (30 mm), kV range voltages applied to the top and bottom of the entire chip (0.5 mm thickness), and thick YIG samples ($5 \mu\text{m}$).

Using the developed nanofabrication and microwave spectroscopy techniques, we have measured and extract an upper bound for the SFEI constant in thin Pt/YIG systems. We find that the effect on group velocity, specifically the induced non-reciprocity, is negligibly small. We believe this is because YIG is a centrosymmetric material, which means its unit cell (which has cubic symmetry) strongly suppresses polarization from the electric field and thus does not sufficiently break spatial inversion symmetry required for significant induced non-reciprocity [8]. This then motivates future studies in using the techniques in measurement and nanofabrication to investigate SFEI in non-centrosymmetric films like LiFe_5O_8 [44], Cu_2OSeO_3 [126, 116], or thickness gradient ferrites like $\text{MgAl}_x\text{Fe}_{2-x}\text{O}_4$ [37] to name a few.

4.5 Additional Notes

4.5.1 Low frequency modulation of the electric field gate for high sensitivity detection.

To enhance signal quality it may be worth trying to apply a < 20 kHz modulation frequency onto the electric gate and use a lock-in amplifier to pick up the detector signal amplitude after it is converted to DC through a microwave diode. If there is any electric field effect, the modulation should allow the transmitted spin waves to be filtered out of the background. This requires testing however.

4.5.2 Electric field effect in the non-linear regime.

It may also be interesting to see the electric field effects when pushed into the non-linear regime, this however will require utilizing a set-up similar to the previous section with an RF generator that can sweep frequency continuously (to characterize the fold-over).

Chapter 5

Wide Band Non-Reciprocity via Magneto-elastic Coupling

5.1 Motivation

The application of surface acoustic waves (SAWs) have already been implemented in a number of signal processing devices like sensors and filters [16, 97]. SAWs have been very attractive to technologists due to features like low losses in the MHz to GHz range, high efficiency in excitation, and considerably shorter wavelengths compared to electromagnetic radiation which make them scalable. SAWs however are intrinsically reciprocal, this is because the mechanical origin, i.e. the vibrational Hamiltonian, is time-reversal symmetric. Development of non-reciprocal SAWs would accelerate its evolution into critical scalable on-chip communication components such as microwave valves, circulators, and isolators. Achieving non-reciprocity for SAWs however is difficult, and have found success under conditions that require moving media or power dependent non-linearities [56, 41], both of which are not all that practical for scalable solutions. SAWs however can interact with spin waves through

another spin orbit coupling mediated effect called magneto-elastic interaction. With this interaction, the non-reciprocity of spin waves can be *imprinted* onto SAWs and thus make them also non-reciprocal by proxy. In this chapter, I present the theory of achieving non-reciprocal SAWs (specifically wide-band, unidirectional non-reciprocity) developed by collaborators Verba et al. [133] and discuss some nanofabrication and measurements already done towards accomplishing this goal.

5.1.1 Surface Acoustic Waves

Surface acoustic waves are *Rayleigh waves*, which are visually presented by Fig. 5.1. The

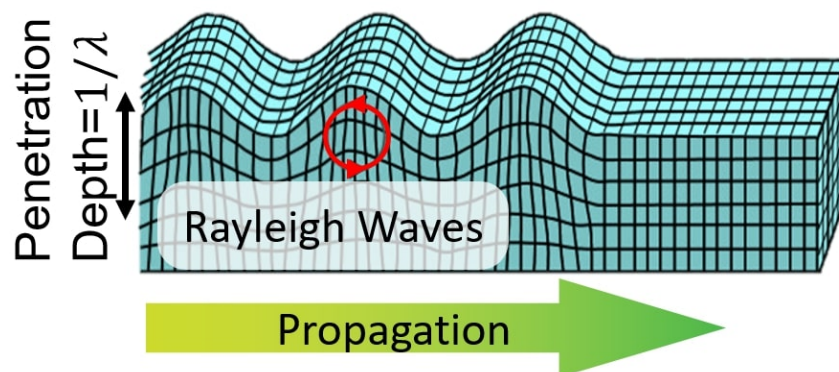


Figure 5.1: **Schematic of a surface acoustic wave.** Oscillatory deformations in the media leads to a propagating *surface wave*. The red arrows indicate how the lattice itself oscillates. SAWs have the majority of their energy on the surface and decay rapidly into the bulk.

general starting point for the mathematical description of SAWs starts with the elastic deformation of a non-piezoelectric media, this is the generalized Hooke's law ¹:

$$T_{ij} = c_{ijkl} S_{kl} \tag{5.1}$$

¹Repeated indices are implied summations

where T_{ij} is the stress tensor and S_{kl} is the strain component represented by

$$S_{kl} = \frac{1}{2} \left(\frac{\partial u_k}{\partial x_l} + \frac{\partial u_l}{\partial x_k} \right) \quad (5.2)$$

where u_k is the particle displacement in the k direction and x_l is the l th position coordinate. Finally, c_{ijkl} is the *elastic stiffness* tensor for a medium.

However, since we *are* interested in a *piezoelectric* media (which couples the electric field to the mechanical strain), additional coupling terms must be included and Eq. (5.1) is modified:

$$T_{ij} = c_{ijkl}S_{kl} - e_{ijm}E_m \quad (5.3)$$

$$D_n = e_{nkl}S_{kl} + \epsilon_{nm}E_m \quad (5.4)$$

where e_{ijm} are elements of the piezoelectric tensor, E_m is the electric field, D_n is the electric displacement, and ϵ_{nm} is the dielectric permittivity tensor. When these equations are applied to Newton's Law, we get:

$$\rho \ddot{u}_i = e_{kij} \partial_j \partial_k \vartheta + c_{ijkl} \partial_j \partial_k u_l \quad (5.5)$$

where $\mathbf{E} = -\nabla \vartheta$, and ϑ being the scalar potential.

With the imposition of surface boundary conditions, the stress tensor simplifies $T_{xz} = T_{yz} = T_{zz} = 0|_{z=0}$. Further imposing that the substrate is an insulator (no free charges) gives $\nabla \cdot \mathbf{D} = 0$ and grants another constraint [103]:

$$\epsilon_{ij} \vartheta + e_{ijk} \partial_i \partial_j u_k = 0 \quad (5.6)$$

It is important to note that piezoelectric media are inherently anisotropic, which renders much derivation beyond this point only feasible via numerical methods. Still, the intuition

behind the formation of these 4 coupled differential equations (Eq. (5.3), Eq. (5.4), Eq. (5.5), Eq. (5.6)) are present. The rest of the derivation is deferred to Oliner [103]. The punchline is that the surface wave solutions turn out to be a linear combination of four partial waves that all decay exponentially into the bulk, furthermore, its relative group velocity is slower than the bulk wave group velocities (meaning, combined with the linearity of the dispersion relations, they are excited at lower frequencies). Generally though, the spectrum for SAWs turn out to be simply (which can be extracted from solving Eq. (5.5) for an isotropic media and assuming plane wave solutions):

$$\omega_{SAW} = c_{SAW}|k| \tag{5.7}$$

which is linear, gapless, and reciprocal.

5.1.2 Magnetoelastic coupling

Since the lattice of a ferromagnet is intrinsically tied to the orbitals of the atoms that make it up, deformations in the lattice can induce deformations of orbitals. If there is spin orbit coupling present in the system, then deformations in the lattice modify the spin energies via SOC and induce magnetic dynamics (magnetoelastic coupling, MEC). Conversely, the lattice can deform in response to the magnetization changing (magnetostriction). Fig. 5.2 shows the latter at work, where the changing external field reorients the magnetization in the 1-D lattice, but this as a result changes the overall length of the chain.

MEC can manifest itself as an energy term that relates the strain of a system to the magnetization (as the name suggests), similar to the SAW calculation, the introduction of MEC

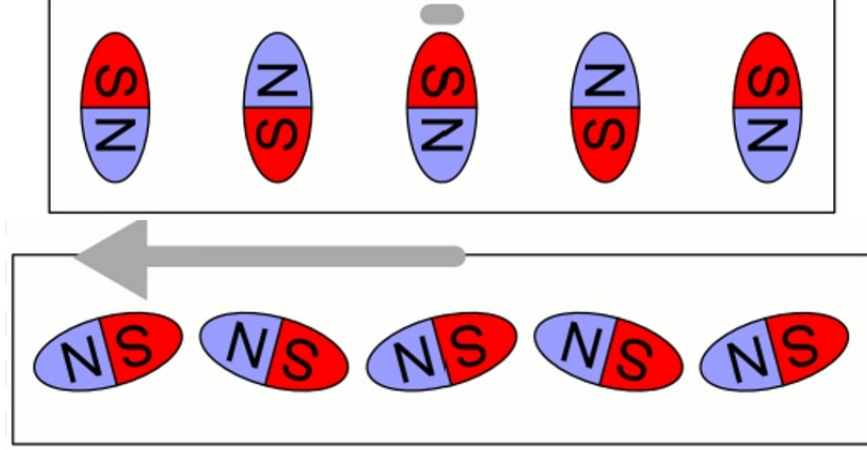


Figure 5.2: **Cartoon of magnetostriction.** One dimensional lattice under an external field. When the field is zero (top) the length of the chain is shorter. When the external field pulls the spins along a direction (bottom), the changing magnetization elongates (i.e. deforms) the chain.

modifies Eq. (5.5):

$$\rho \ddot{u}_i - c_{ijkl} \partial_j \partial_k u_l = f_{me} \quad (5.8)$$

$$\frac{1}{\gamma} \hat{\mathbf{J}} \cdot \dot{\mathbf{m}} - \int \hat{\mathbf{\Omega}} \cdot \mathbf{m}' dr' = \mathbf{b}^{me} \quad (5.9)$$

where \mathbf{m} is the time dependent (normalized) deviation of magnetization from equilibrium, $\mathbf{J} = \mathbf{e} \cdot \boldsymbol{\mu}$ is the angular momentum operator (which involves the Levi-Civita antisymmetric tensor \mathbf{e} and the unit vector pointing along static magnetization $\boldsymbol{\mu}$), and $\hat{\mathbf{\Omega}}$ is the operator of magnetic interactions. The dependence on position and time were removed to de-clutter the equations. The RHS of the first equation is the effective force that stems from the effective magnetic field \mathbf{b}^{me} arising from deformations in the lattice. The strain S_{kl} then becomes coupled with the magnetic field through a *magnetostriction* tensor which is present in the magnetoelastic energy density:

$$W^{me} = \frac{1}{M_S^2} b_{ijkl} S_{ij} M_l M_n \quad (5.10)$$

From this energy density the effective field $b = \partial_{\mathbf{M}} W$ and the effective force $f = \partial_{x_i} \partial_{S_{ij}} W$

are extracted through linearization. Further explicit derivation is deferred to Verba et al. [132]. I present the theory up to this point to mainly illustrate how the magnetoelastic effect is modeled mathematically.

5.2 Imprinting Non-reciprocity through SW and SAW Interaction

When the dispersion relation of two quasi-particles cross, i.e., they have the same energy, then the particles interact resonantly (with conservation of energy and momentum), leading to the (excitation) hybridization of the interacting particles, this is a general phenomenon. In the context of SAWs and spin waves (SWs), one can imagine that propagating SAWs along a surface that is interfaced with a ferromagnet can scatter into SWs at the right frequency. This new magnon will either scatter back to a phonon or decay in the ferromagnet. When the dispersion relation for magnons in the interfacing layer is *canted* (i.e. non-reciprocal), the crossing points between the two dispersion relations have become asymmetric (Fig. 5.3(b)) with respect to $k = 0$. The imprinting of non-reciprocity for SAWs arises because the resonant interaction frequency is now different for forwards and backwards propagating SAWs. The predicted narrow band non-reciprocity for SAWs has already been accomplished using non-reciprocal ferromagnetic layers with iDMI [112]. Due to the non-reciprocity being fixed in ferromagnets with iDMI at growth, the band of interaction is severely constrained by both the group velocity of the piezoelectric and the group velocity of these spin waves near the resonant interaction band. This motivates seeking alternative materials where the (non-reciprocal) spin wave group velocity (i.e. the crossing point between dispersion relations) can be manipulated in situ. Additionally, one can question whether there exists a non-reciprocal ferromagnetic material that has its dispersion relation *overlap* with the dispersion relation of SAWs, leading to a wider band of frequencies in which they interact and thus achieve

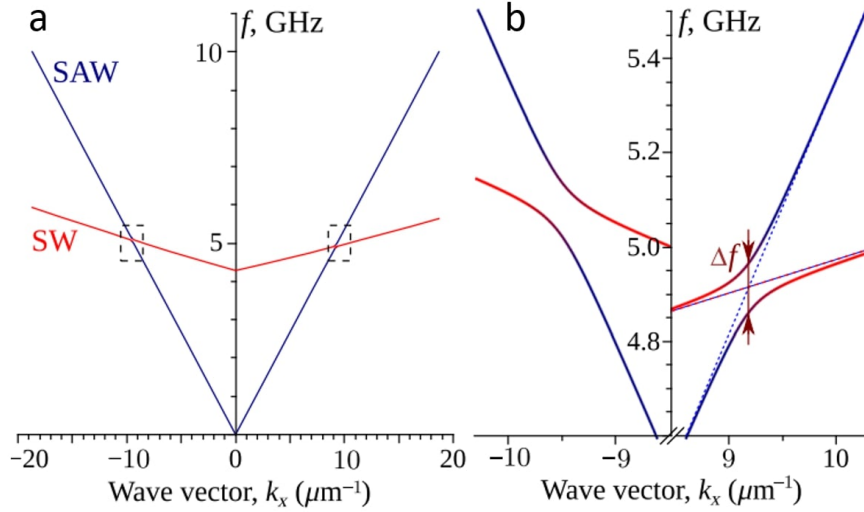


Figure 5.3: **Diagram showing non-reciprocal interaction.** (a) Zoomed out view of the spin wave (red curve, SW) and surface acoustic wave (blue curve, SAW) dispersion relations. Their intersections are points of interest. (b) Zooms into the points of interest, the non-reciprocal feature of the spin wave dispersion relation is now apparent, the interaction ‘frequency’ is now different for forwards and backwards propagating waves, diagram is from Verba et al. [132].

wide-band non-reciprocity.

5.3 Synthetic Antiferromagnet for Tuneable Dispersion.

In order to achieve our goal, we require a ferromagnetic structure that is non-reciprocal, gapless, and linear. Collaborators Verba et al. [133] have presented that *synthetic antiferromagnets* (SAFs) satisfies these requirements. An SAF is a pair of ferromagnetic layers with a nonmagnetic *spacer* layer of precise thickness in between that stabilizes the anti-ferromagnetic coupling between the two layers (hence being synthetic). The mechanism that enables the anti-ferromagnetic coupling is called the Ruderman-Kittel-Kasuya-Yoshida (RKKY) interaction, which arises from the interaction of itinerant, conduction electrons and localized magnetic moments [110]. The exchange coupling that arises from this interaction

oscillates in sign with increasing spacer thickness (hence it must be of a certain thickness for it to be anti-ferromagnetic).

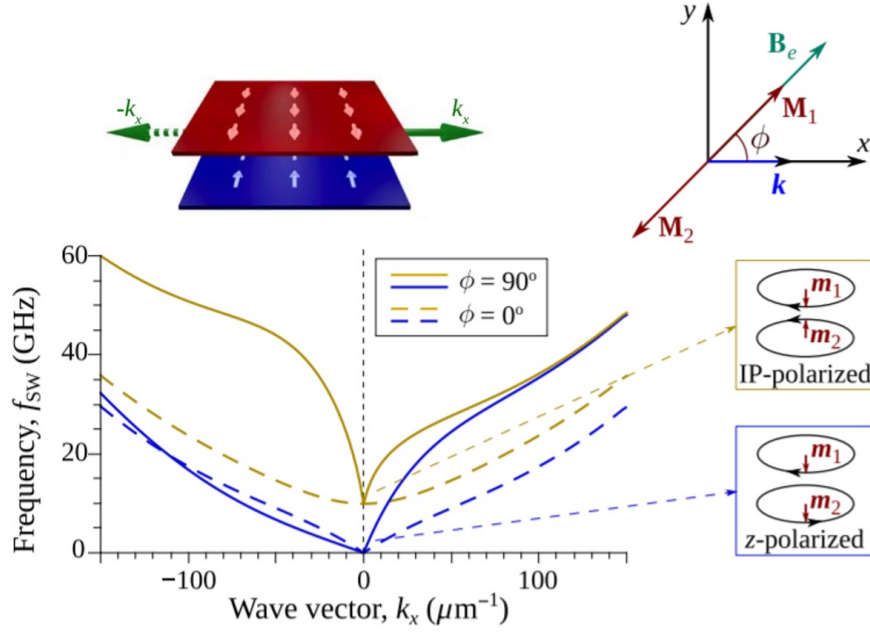


Figure 5.4: **Plot and schematic of SW dispersion in SAF.** Plot showing the different SW dispersions for different orientations of the SAF structure. The solid curves ($\phi = 90^\circ$) exhibit maximum non-reciprocity. With a weak external field, \mathbf{M}_1 and \mathbf{M}_2 can be rotated and thus the non-reciprocity is tuned.

SAFs have strong non-reciprocity when the relative angle ϕ between the direction of \mathbf{k} and the SAF magnetization (which will be collinear with external field) is nonzero. Furthermore, varying ϕ modulates the SW dispersion relation. Fig. 5.4 shows a plot of the SW dispersion relation for an SAF under different angles of relative propagation. In other words, we can actively change the SW group velocity by rotating the external field.

The SAF structure our collaborators Verba et al. [133] calculated the spectra for is Co(15nm)/Ru(0.9nm)/Co(15nm). They have derived the SW dispersion as a function of ϕ :

$$\omega_{\mathbf{k}} = \omega_M t_{FM} \left[\sqrt{\frac{l^2}{t_{FM}^2} + \frac{1}{3} \sin^2 \phi + \frac{1}{2} \sin \phi \text{sign } k} \right] |k| \quad (5.11)$$

where $\omega_M = \gamma \mu_0 M_S$, M_S is the saturation magnetization, $t_{FM} = t_1 = t_2$ is the thickness of

the ferromagnetic layers, and l is the exchange length, which is the characteristic distance associated with the relative strength of exchange and self-magnetostatic energies. From this relation we can mathematically see that the dispersion is non-reciprocal (dependent on sign k and ϕ), gapless (when $k = 0$, $\omega = 0$), and linear ($\omega_{\mathbf{k}} = c_{\phi}|k|$). Fig. 5.5 shows the dispersion relation for $\phi = 36^\circ$ when considering SAWs propagating in Y -cut Lithium Niobate (LNO) along the Z axis.

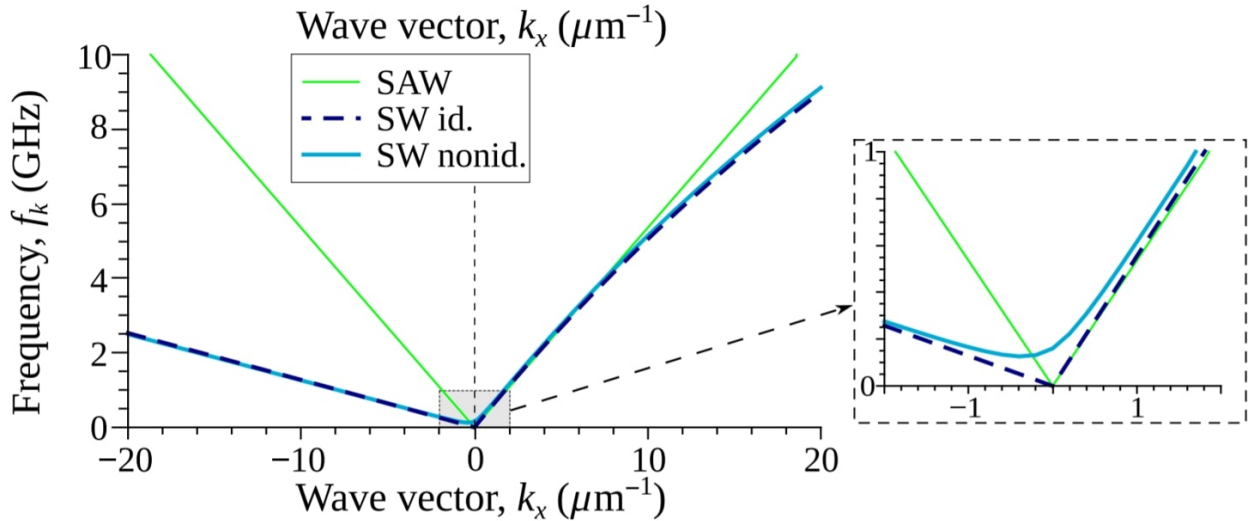


Figure 5.5: **Plot of ideal SAF spin wave angle dispersion on LNO.** Plot showing the dispersion relation for Co(15nm)/Ru(0.9nm)/Co(15nm) with $\phi = 36^\circ$. There is huge overlap between spin waves and SAWs on Y -cut, Z direction LNO for positive k_x . This implies wide band interaction and thus wide band non-reciprocity. Figure from Verba et al. [133].

One final thing to note is unbalanced vs balanced films. The balanced films (where both ferromagnetic layers are same thickness), while gapless (Fig. 5.5 dashed dark blue curve), will be vulnerable to thermal noise and thus ϕ will be not be homogeneous throughout the propagation area. The unbalanced films, with a moderately small external field, remedy this issue as the imbalanced magnetization under the external field leads to quasi-uniform, stable alignment across the sample. This however comes at the cost of a gap opening up in the dispersion relation (Fig. 5.5 solid light blue curve), this however is not an issue if the SAWs excited are above the gap frequency.

Fortunately, we have access to LNO/Ta(5)/Co(15/16)/Ru(0.9)/Co(15)/Ta(5) SAF films

(layers are in units of nm) grown by our collaborators R. Salikhov and co-workers at the Institute of Ion Beam Physics and Materials Research in Helmholtz-Zentrum Dresden-Rossendorf, Germany. We will perform our nanofabrication and measurements on these.

5.4 SAW Device Design and Nanofabrication

5.4.1 Interdigital Transducers

In order to drive surface acoustic waves, there must be a source of mechanical oscillations in the media. Since piezoelectric materials respond to applied electric fields by mechanically flexing, we can employ nanofabrication techniques to create periodic structures that, when applied with AC signals, provide the mechanical oscillations and excite SAWs.

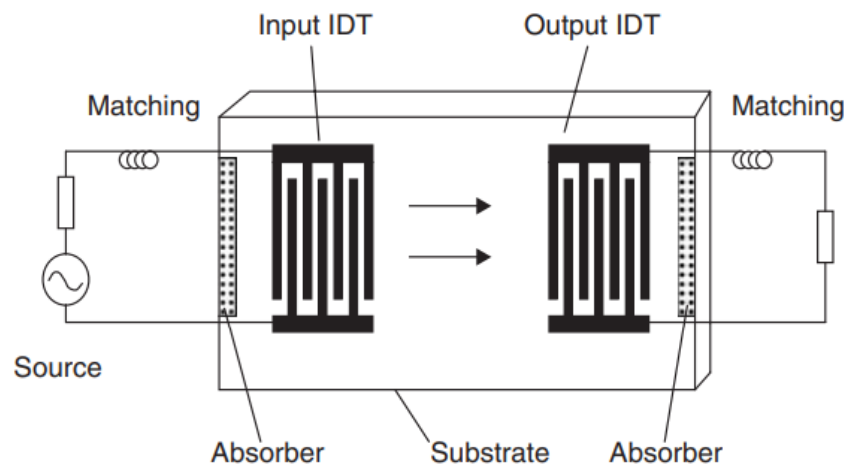


Figure 5.6: **Diagram of interdigital transducers.** Single finger IDTs (left) reflect incident SAWs in phase, distorting the received signal. When split fingers are employed (right), the reflected SAWs are out of phase and cancel themselves, mitigating the distortion. Note the required increase in feature resolution (p is reduced by half) for the split finger design. Figure is from Morgan [97].

Fig. 5.6 shows an example pair of structures that can drive SAWs, these are called *interdigital transducers* (IDTs). The structure involves two combs with their *fingers* alternating between

each other with no electrical shorting. When an AC signal is applied to the IDT, the alternating fingers (a.k.a. electrodes) generate a periodic electric field, which then results in a periodic elastic strain. Reciprocally, mechanical oscillations will generate an AC signal in the transducer, so IDTs also work as a SAW detector.

The pitch separation of the fingers determine the wavelength λ_0 of SAWs that the IDT will couple most to. So it is imperative to design the IDTs such that they will operate within the desired frequency band $f_0 \propto 1/\lambda_0$ (because IDTs behave like bandpass filters). Furthermore, impedance mismatching will reduce the efficiency of exciting SAWs. IDTs are also bidirectional, meaning that half of the power transmitted will go in each direction so there is an inherent 3dB loss. This is also the same for detecting SAWs, so a total insertion loss of a 2 port IDT system will be at least -6dB. This motivates careful design of the IDT to ensure that there is appreciable signal within the desired band.

There is also the issue of *internal* reflection, the standard ‘single finger’ (or single-electrode) IDT design will reflect SAWs in phase, which is undesirable for detecting SAWs as the reflected waves then distort the initial signal. One way to address this is to employ a ‘split’ finger design, where there are a pair of fingers for each alternating electrode. Fig. 5.7 from Morgan [97] illustrates the designs and concept. The drawback for using the split finger design is that the pitch length p must be halved to operate at the same frequency. This then makes the fabrication more challenging and may reduce the overall yield.

The reflection however can be utilized in the form of *Bragg* reflectors on the far ends of the device (shown in Fig. 5.8). The idea is to reflect the SAWs propagating in the wrong direction to reflect back in phase with the SAWs going in the correct direction. This then can aid in mitigating the minimum -6dB loss mentioned earlier.

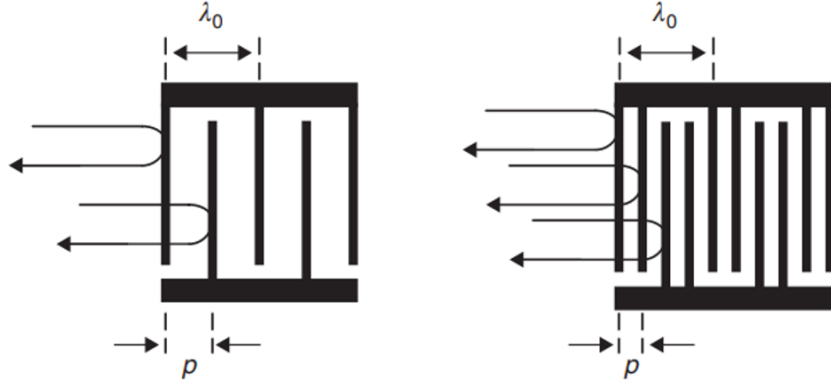


Figure 5.7: **Single finger vs split finger IDTs.** Figure is from Morgan [97].

5.4.2 Lithium Niobate

The efficiency of exciting SAWs also highly depends on the piezoelectric material itself, in particular, the relative surface velocities for a metallized and free surface (v_m and v_f) characterizes the piezoelectric coupling to the wave. Normally, a coupling constant K^2 is defined such that:

$$\frac{(v_f - v_m)}{v_f} \equiv \frac{K^2}{2} \quad (5.12)$$

It turns out that this coupling coefficient can also be defined:

$$K^2 = \frac{e^2}{c\epsilon} \quad (5.13)$$

where e is the piezoelectric coefficient, c is the stiffness coefficient, and ϵ is the dielectric permittivity. The anisotropic nature of piezoelectrics implies that K^2 will vary based on the crystallographic cut that the SAWs propagate on. One of the more popular piezoelectrics used for SAW applications is lithium niobate (LiNbO_3 or LNO), which is among the higher K^2 materials. The table below shows some notable piezoelectric substrates.

Material	Crystal Cut	SAW Axis	Velocity (m/s)	K^2 (%)
Quartz	ST	X	3158	0.11
LiNbO ₃	Y	Z	3488	4.5
LiNbO ₃	128°	X	3992	5.3
Bi ₁₂ GeO ₂₀	110	001	1681	1.4
LiTaO ₃	Y	Z	3230	0.72
GaAs	⟨001⟩	(110)	<2841	<0.06

In this study we use Y -cut LiNbO₃ and fabricate our IDTs such that the propagation axis is along Z . With the SAW velocity, our SAW frequency relationship is as follows,

$$f_0 = \frac{v_{SAW}}{\lambda_0} \quad (5.14)$$

For example, if we wish to excite SAWs of 3.488 GHz on our substrate ($\lambda_0 = 1\mu\text{m}$), our single finger pitch length must be 500 nm. If using split finger, then it must be 250 nm. The pitch also includes the finger width and spacing between them, meaning that the finger and spacer width would be 250 nm and 125 nm respectfully. With conventional nanofabrication means of lift-off (like in Section 3.3.5), this is quite challenging. Most SAW resonators actually are fabricated to operate in the sub-GHz bands. Through our developed method (which we will cover later), we can easily fabricate devices well above this into 1-10 GHz band (down to sub 100 nm pitch and finger widths).

5.4.3 IDT parameters

The points that should be considered in designing IDTs are as follows, some parameters are in reference to Fig. 5.8 [137]:

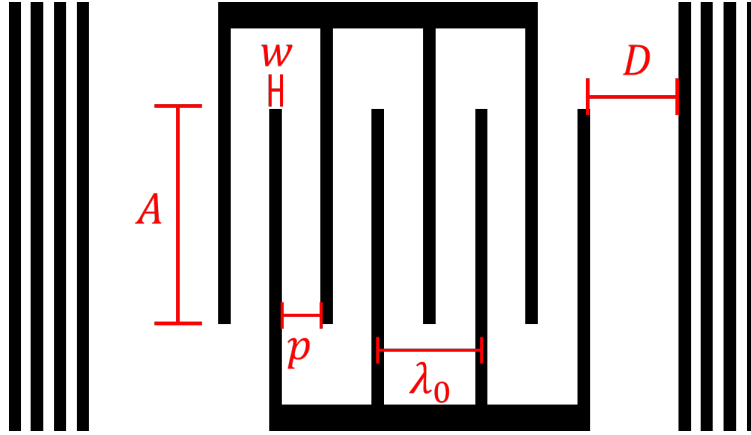


Figure 5.8: **Parameters of IDT design.** Parameters of single finger IDT structure. Where w is the finger width, p is the electrode pitch length, λ_0 is the coupling SAW wavelength, A is the aperture, and D is the reflector separation.

- Shorter wavelength \Rightarrow higher frequency.
- Higher transmission efficiency \Rightarrow better signal to noise ratio.
- Smaller total pattern exposure area \Rightarrow shorter write times per device which allows more devices to be patterned (increased yield).
- Finer features \Rightarrow increased chance of failed devices (reduces yield).
- Higher yield \Rightarrow more measurable devices and data to collect.
- Single finger width (assuming gaps are same width) $w_{1f} = \lambda_0/4$
- Split finger width (assuming gaps are same width) $w_{2f} = \lambda_0/8$
- Finger width and pitch $w + p = n \frac{\lambda_0}{2}$ where n is the number of fingers per alternating electrode (e.g. $n = 1$ for single finger and $n = 2$ for split).
- Length of finger overlap (aperture A) increases performance of resonator, should be about $50\lambda_0$ to $100\lambda_0$
- If using reflectors, make sure they receive the SAWs at the peak $D = (n - \frac{1}{2}) \frac{\lambda_0}{2}$
- The number of fingers (total) increases the quality factor of the resonators.

- The thickness of the electrodes have an impact on the excitation frequency (mass loading effect), heavier electrode materials will downshift the frequency [27].

5.4.4 NR-SAW Device Layout



Figure 5.9: **Initial NR-SAW device layout.** Where $A = 24 \mu\text{m}$, $p = 125 \text{ nm}$, $w = 125 \text{ nm}$, $\lambda_0 = 450 \text{ nm}$, off- Z angle $\theta = 35^\circ$, and IDT separation $d = 12 \mu\text{m}$. The lower left inset shows the center zoomed in with the active region SAF included and the top right inset shows the center zoomed in without the SAF. The device was rotated 35° to try and observe the effect with little rotation needed for the chip.

Fig. 5.9 shows one of the lithographic layouts that I used to for our initial set of devices. Half were fabricated with the SAF in the center and half without. The pad structure was designed so that the chip can be rotated and still allow the microwave probes to connect to the device. The IDT parameters are as follows: $A = 24 \mu\text{m}$, $p = 125 \text{ nm}$, $w = 100 \text{ nm}$, $\lambda_0 = 450 \text{ nm}$, off- Z angle $\theta = 35^\circ$, and IDT separation $d = 12 \mu\text{m}$. The slightly smaller w is to account for bloating of the resist patterns. This results in an $f_0 = 3488 \frac{\text{m}}{\text{s}}/450 \text{ nm} \approx 7.75 \text{ GHz}$

5.4.5 One-Step Nanofabrication

Since fabrication of many fine features ≤ 100 nm is required for high frequency (> 5 GHz) resonators, it was clear that application of high resolution *hydrogen silsesquioxane* (HSQ) electron-beam resist would be beneficial in this project. Since HSQ is a negative resist (e-beam exposure hardens and makes insoluble, forming a mask) however, it often requires a reductive process like ion beam milling to utilize it. Furthermore, the SAF films grown on LNO will require ion milling anyways to create the active region SAFs and not short the entire chip. Finally, patterning lift-off structures (which is standard for SAW resonators) on bare LNO can be challenging due to its insulating nature, even with the developed charge mitigation techniques discussed in Chapter 3. This warrants patterning the IDT, landing pads, and SAF active region all in one step. A diagram of the process is shown in Fig. 5.10. Since the SAF is metallic, etching them into IDTs is a viable strategy, we believe that the magnetic properties of the metals in the IDTs will not interfere with the excitation of SAWs. There is still, however, some mass loading that will occur since Co and Ta are heavier than say, Al (which is commonly used for IDTs), but this effect is not expected to be significant since the Co multilayer is fairly thin (about 30 nm).

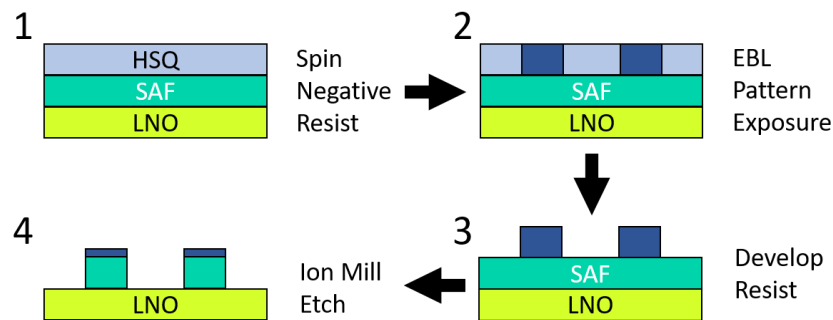


Figure 5.10: **Illustration of one step fab for NR-SAW devices.** Procedure is *one-step* because it involves performing e-beam lithography (EBL) only once. Beneficial as EBL can be quite volatile in its behavior.

By including the entire structure into a single EBL session and using HSQ which requires high dosage, the total writing time becomes a limiting factor in the amount of devices that can

be written. Using a dosage of $1700 \mu\text{C}/\text{cm}^2$ at 50 pA for example takes $0.34 \mu\text{s}/\text{nm}^2$. HSQ must be developed within 2 hours of spin coating (longer times have not really been tested, but the data sheet says this), this maximum time limit, plus the usual 20 to 30 minutes it takes to prep the EBL, gives usually a total writing time of 60 minutes. This yields a total writing area of roughly $8,823 \mu\text{m}^2$ if writing entirely with 50 pA current. Increasing the current linearly reduces the time it takes, at the risk of excessive proximity exposure and bloating (but this can be dose tested for). For the larger features like the pads, I use the 12.6 nA beam to quickly write them, since they are not writing any fine features, bloating is not an issue.

5.4.6 Itemized Nanofabrication Recipe

This recipe is written in context of UC Irvine's Krivorotov Group Laboratory, it is recommended that you begin the process roughly 40 minutes before your scheduled EBL time. Prior to even booking make sure that you have HSQ, MF-319, both salty developers, HPLC water, and a non-empty nitrogen tank connected to the spin-coater. The crux of the procedure is that the sample must be 'primed' by being cleaned in MF-319 and HPLC water before spin coating. After EBL, a 3-step development process is necessary to prevent ripping off fine resist structures, this procedure should work for any HSQ related step in general. It seems that developing with the least aggressive developer (MF-319) first removes a large amount of the excess resist without attacking the fine features, this allows the subsequent developers (MIT salty developer [138]) to dissolve the finer features without a huge volume of disruptive chemistry (since only the smaller areas remain) displacing the sensitive features.

Caution: MF-319 is highly toxic and should be handled with care, make sure you are wearing appropriate PPE and are properly trained.

1. Clean SAF chip with acetone then IPA, ultra-sonicate for 3 minutes while in each. O2

plasma cleaning at 45W for 3 minutes can be done if there seems to be persistent crap on the surface (check with optical).

2. Dry with N₂, often dirt from the tweezer will collect on the chip surface, once dried while holding on corner of the chip, use the dry tweezer to grab the opposite corner and dip into the IPA (making sure the tweezer stays dry), then N₂ dry once more. It is important that **no dirt gets on the chip**. Visually inspect after drying.
3. Take HSQ out from the fridge to warm up ~20 minutes before spin coating, time this so that when you spin the HSQ it is about 5 to 10 minutes before your EBL session.
4. Turn on the hot plate in the fume hood (labeled HP2) and set to 105 C.
5. Take out 3 plastic developer beakers and 1 large chemical waste beaker (for MF-319 + DI water), label glass cover for the waste beaker, be sure to include your initial and the date.
6. Clean the plastic beakers using IPA and a Kim wipe. Designate 1 beaker for MF-319, one for the MIT salty developer, and one for HPLC water rinsing.
7. After cleaning the MF-319 dedicated beaker, fill it with some HPLC water and swirl to wet the inside, dump it into the waste beaker.
8. Next fill the same beaker with a little bit of MF-319 developer and swirl it around to 'prime' the beaker, dump it into the waste beaker and repeat again. Fill it up a third time with enough to clean your chip (the dipper is not necessary for this).
9. Place chip in MF-319, swirl aggressively.
10. Remove chip and immediately submerge into HPLC water, follow it with a nozzle rinse of HPLC water, dry with N₂. Be weary of the water that sticks to your tweezer, its surface tension can easily draw dirt to the surface of the chip. I make an effort to flow

- N₂ *towards* my tweezer, being careful to not let the chip slip or fly off. You can use contact with the beta wipe to also absorb water away from the chip and tweezer.
11. After drying, pre-bake at 105 C on the hot plate for 60 second. I make sure to place it in the middle of the hot plate.
 12. Mount chip onto spin-coater and spin at 2500 rpm for 45s (program 12) ⇒ Roughly 70 nm thick HSQ. Note current the time this spinning step is completed.
 13. post-bake at 105 C for 3 minutes and 20 seconds, use this time to do standard spin-coater/hot-plate clean-up procedures. You can also empty the smaller MF-319 and water beakers into the waste beaker.
 14. EBL using 1700 $\mu\text{C}/\text{cm}^2$, this is 0.34 $\mu\text{s}/\text{nm}^2$ at 50pA. Note you must develop your sample within two hours of spin coating HSQ.
 15. AFTER EBL post-bake at 80C for 60s.
 16. Prep teflon dipper by cleaning with IPA, HPLC water, N₂ dry.
 17. Fill MF-319 beaker, swirl, empty into waste, fill again for development, make sure enough is filled for full submersion of chip with teflon dipper.
 18. Develop chip in MF-319 for 70s with the dipper, can fill HPLC water plastic beaker meanwhile so the chip is ready to dunk.
 19. Stop development by submerging the dipper into HPLC water for 45 seconds, use squirt nozzle to rinse the chip afterwards, I do this with the chip still in the dipper because I don't like my tweezers touching water and the chip.
 20. Rinse the salty developer plastic beaker with HPLC water, can empty it into the waste beaker. This can be done during the previous step.
 21. N₂ dry the dipper and chip, can be done without removing chip.

22. Fill salty developer beaker with the 'gentle' salty developer (0.1% NaCl and 0.58% NaOH by weight).
23. Develop in 'gentle' salty developer for 120 seconds.
24. Repeat HPLC rinsing process (45 seconds in HPLC with nozzle rinse).
25. Discard salty developer in its disposal container (I just carry it to the chemical waste cabinet in B118).
26. Fill salty developer beaker with '2x diluted' (1% NaCl and 0.5% NaOH by weight) salty developer.
27. Developer in '2x diluted' salty developer for 60 seconds.
28. Dunk and rinse in HPLC water for 45 seconds and N2 dry
29. Inspect under optical to see results, you should be able to see down to roughly 200 nm structures. Discard chemicals appropriately when finished. Be careful not to splash DI water from the tap when rinsing the MF-319 beakers, I normally place it at the bottom of the sink and then turn on the tap, dumping it when it fills up.
30. Can (and should) SEM the resist patterns to confirm they came out proper, even AFM (tapping mode) is helpful to ensure good IDT profile.
31. If ready to etch, mount the sample on a dummy SiO_x chip with vacuum grease as the adhesive and load it into the ion mill chamber. Be sure to follow ion mill SOP for etching + evaporation.
32. High vacuum ($\sim 5 \times 10^{-8}$ Torr) is recommended for etching, this takes a couple hours, normally I load it and pump down over night, check with your lab mates before doing this.

33. Etch for 6 minutes and 45 seconds at 80 degrees incidence (program 8), duty cycle is 30s/30s. (Maximum etch for 70 nm HSQ is roughly 7 minutes and 20 seconds).
34. After etching, e-beam evaporate 7-10 nm AlO_x at 45 deg angle on sample to protect it.
35. Remove sample, it is ready to characterize. Note that it may be difficult to image since LNO is insulating.

5.5 VNA measurements of IDTs on LNO

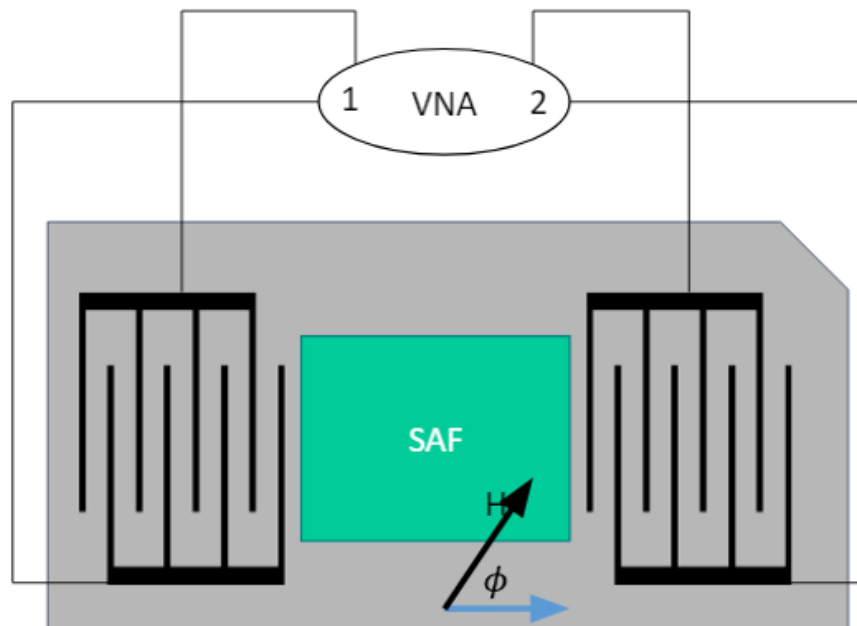


Figure 5.11: **Schematic of characterizing NR-SAWs.** Sample is connected to VNA through microwave landing probes. Measurement procedure is similar to Chapter 3. Prior to measurement, landing probes must be planarized and the VNA calibrated through them (calibration is by Smith [122] and probe handling is discussed by Chen [20]).

Fig. 5.11 shows a simplified schematic of the measurement set-up. It is very similar to that of Chapter 3 and Chapter 4. The main difference here is that microwave landing probes are used to connect to the device. This is because it makes measuring multiple devices quite easy

as no wire bonding is required. In this measurement, the S-matrix of the device is collected for a fixed field. We are mainly looking at the transmission data S_{21} and S_{12} for each device under a small or zero field. We first want to characterize the IDTs without the SAF present, and then measure with the SAF in the center to see any significant changes in the transmission spectra. We can use the reflection data S_{11} and S_{22} to check if we are efficiently exciting SAWs (if at all). Because we are not doing any field sweeping measurements, the field derivative method is not applicable here. As a result, the VNA circuit up to the probes must be calibrated out via following the standard microwave probe calibration procedure (which are covered in the theses by Smith [122] and Chen [20]). It is worth stressing that microwave probes are expensive and have large lead times for repair, so extra care must be taken to handle them, fortunately the aforementioned theses are comprehensive in their standard operating procedures for probe handling, maintenance, and calibration. Before calibration, make sure that your intended calibration range will cover the IDT's designated frequency and that the frequency steps of the VNA are smaller than the bandwidth of the IDT, the Anritsu 37369c is limited to 1601 frequency points between the set start frequency and set end frequency, if the resolution must be increased for your measurement, then you must recalibrate the VNA using a smaller separation between the start frequency and end frequency. After calibrating the probes, it is recommended to 'measure' the calibration substrate to ensure that the reflection and transmission backgrounds are flat.

Looking at the reflection data for each port, we expect that there is a significant loss near the frequency in which the IDTs were designed for, since the transducers should be *radiating* energy at this frequency, ideally through generation of SAWs. It should be noted however that leaky-SAWs and bulk acoustic waves can also be excited, this is not ideal as it can interfere with the fidelity of our measurements. Alternatively the measurement can be performed using a microwave generator and a spectrum analyzer or a microwave generator, lock-in amplifier, and microwave diode, these alternative approaches may need to be employed in the future.

For the transmission spectra, we expect a peak near the designated frequency of IDTs. This would indicate that there are acoustic waves inducing an AC signal through to the other port. A number of factors can reduce the overall surface acoustic wave velocity in the sample (propagating off the Z -axis, mass loading, surface damage) so the operating frequency may be lower than expected.

Finally, electromagnetic cross talk may introduce noise to the measurement, this is usually mitigated by using a time gate, since SAWs are much slower than light. Our VNA however is not equipped to perform time gating, which may warrant repeating measurements using the aforementioned signal generator and lock-in/spectrum analyzer combo.

5.6 Preliminary Results and Discussion

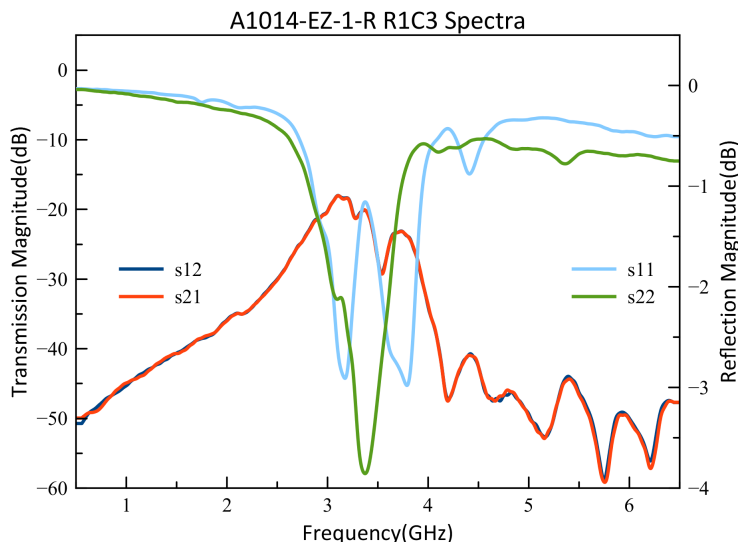


Figure 5.12: **VNA measurement of 4.3 GHz IDTs.** Sample measurement of IDTs with $\lambda_0 = 800$ nm. There is no applied field $\mathbf{H}_{\text{ext}} = 0$. Reflection measurements (light blue and green) correspond to right side axis. Transmission measurements (dark blue and red) correspond to the left.

Fig. 5.12 shows the spectra measurements made on IDTs with pitch length $p = 200$ nm, finger width $w = 190$ nm, wavelength $\lambda_0 = 800$ nm, Aperture $A = 44 \mu\text{m}$, and separation

$d = 40 \mu\text{m}$. Assuming $v_{\text{SAW}} = 3488 \text{ m/s}$, we get $f_0 = 4.3 \text{ GHz}$. We see a large reflection loss at 3.4 GHz, along with some minor dips at other frequencies. Strangely, one of the ports has a peak where the other port has maximum reflection loss (-4 dB). This could be that there is either some intrinsic rejection band in one of the IDTs, since the ports and probes were calibrated. The transmission spectra has an abnormally wide band $> -30 \text{ dB}$, this is not understood as the transmission and reflection features we expect should all be around 4.3 GHz and fairly narrow. If the prominent features we see are due to acoustic wave excitations, then this means the something along the way (growth, mass loading, or nanofabrication related) shifted $v_{\text{SAW}} \approx 2700 \text{ m/s}$, a significant reduction.

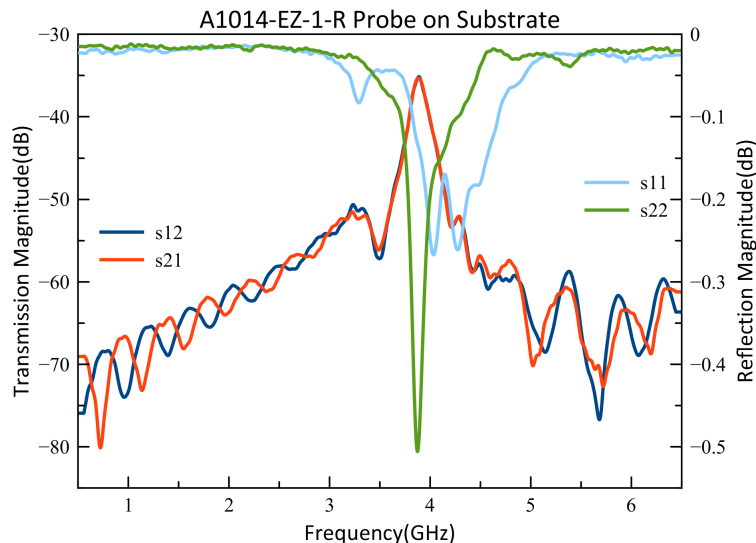


Figure 5.13: **VNA measurement of LNO substrate (no device)**. Sample measurement of probes landing on slightly etched LNO. Reflection measurements (light blue and green) correspond to right side axis. Transmission measurements (dark blue and red) correspond to the left. Note the two different scales for the y -axis.

To vet our results, we can take VNA measurements on the (slightly etched) LNO substrate itself, Fig. 5.13 shows this data. We observe significant transmission peak ($\sim -45 \text{ dB}$) at 4 GHz and some minor reflection loss ($\sim 0.5 \text{ dB}$) at the same frequency. The probes were landed on the substrate similar to how they are landed on device pads. This measurement informs us that the average transmission noise ‘floor’ for LNO is around -60 dB . Furthermore, it informs us that there isn’t significant shunting between the probes without IDTs

(if the chip was not etched all the way through for example, then there would be electrical continuity and thus a higher noise floor). It is interesting to see transmission at 4 GHz, with corresponding reflection loss around the same frequency, this may be due to some electro-magnetic resonance in the substrate or in the probes. Note that the reflection y -axis is quite small ($\sim 1/2$ dB).

The substrate measurement results informs us that there is a resonance background near 3 to 4 GHz that should be avoided until we gain a better understanding of our devices. The results presented in Fig. 5.12 seem suspicious and inconclusive unfortunately, the spectra was similarly seen across a number of devices on the same chip and after multiple recalibrations.

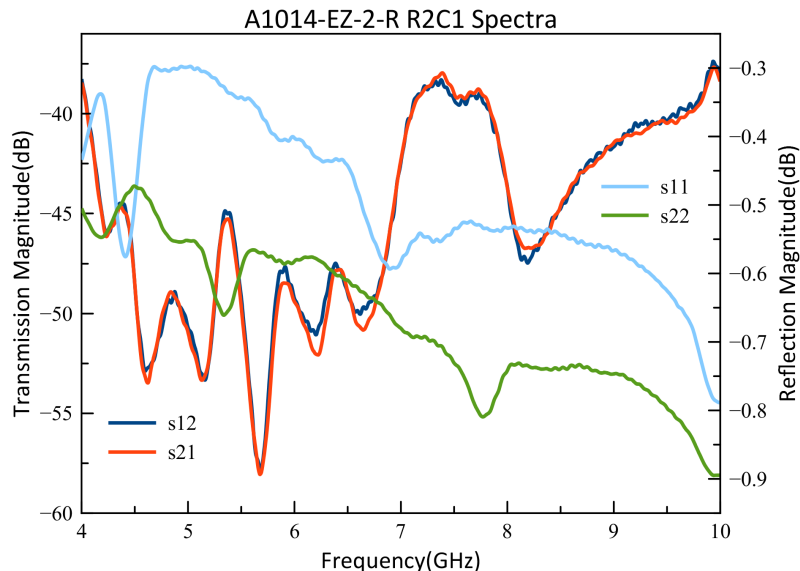


Figure 5.14: **VNA measurement of 7.75 GHz IDTs** Sample measurement of IDTs with $\lambda_0 = 450$ nm. Reflection measurements (light blue and green) correspond to right side axis. Transmission measurements (dark blue and red) correspond to the left.

Next, Fig. 5.14 shows the spectra measurements on a different set of IDTs with pitch length $p = 125$ nm, finger width $w = 100$ nm, wavelength $\lambda_0 = 450$ nm, Aperture $A = 24 \mu\text{m}$, Bragg reflector distance $D = 340$ nm, and separation $d = 5.5 \mu\text{m}$. Assuming $v_{\text{SAW}} = 3488$ m/s, we get $f_0 = 7.75$ GHz. We observe minimal reflection loss (all < 1 dB loss) across the entire measurement band, which implies poor excitation of SAWs, this could be due to a

number things, one of which is poor impedance matching between the VNA and the IDTs. Decreasing the finger width and pitch dimensions and increasing the number of fingers (from the design used in Fig. 5.12) may have shifted the microwave impedance considerably, leading to significant reflection. Near the expected operational frequency, we do see what looks like a peak in the transmission, and corresponding dips in the probe reflection. Also strange is that there is a continued increase in transmission beyond 8 GHz, which corresponds to the continually dipping reflection in the same range. This is not understood.

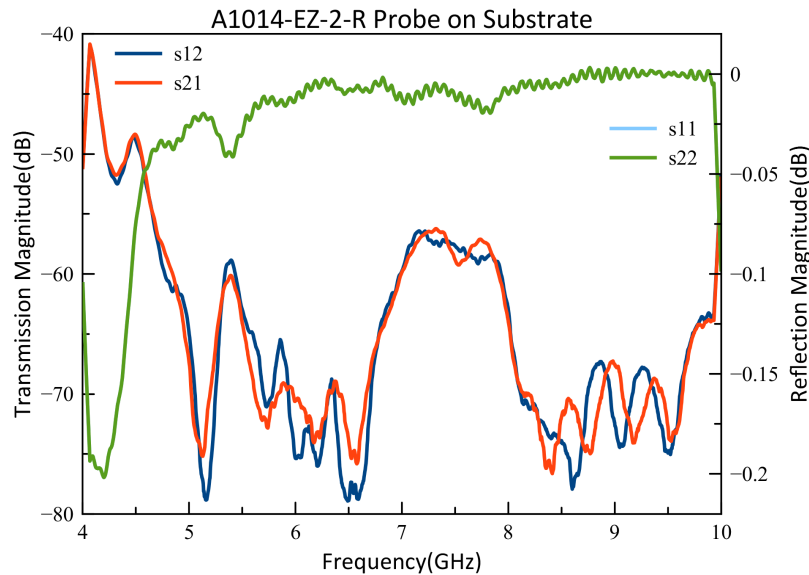


Figure 5.15: **VNA measurement of different LNO substrate (no device).** Sample measurement of probes landing on slightly etched LNO. Reflection measurements (light blue and green) correspond to right side axis. Transmission measurements (dark blue and red) correspond to the left. Note the two different scales for the y -axis.

We similarly check the probe measurement on the substrate of this sample as well. Fig. 5.15 shows this, unfortunately, we see very similar qualitative features in our substrate ‘background’, which seems to imply that what we saw in Fig. 5.14 may not be associated with propagating SAWs through the sample and may be due to some other phenomena independent of the IDTs.

Finally, we used a split finger IDT design that was calculated to be impedance matched to 50 Ohms to try and ensure that design parameters are not interfering with the experiment

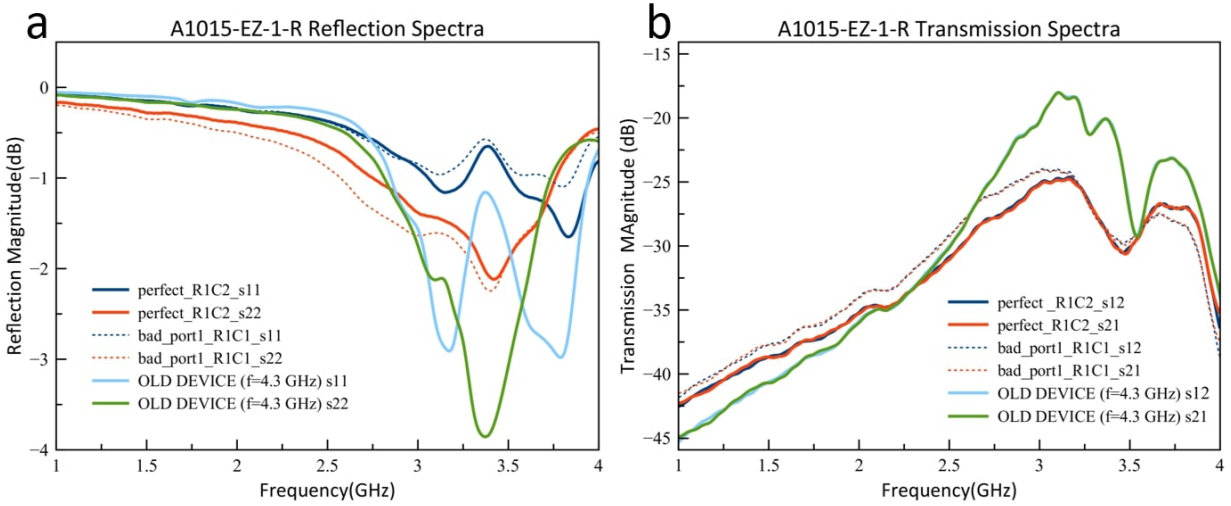


Figure 5.16: VNA measurement of ‘matched’ split finger IDT.

[12]. Fig. 5.16 displays these with the devices from Fig. 5.12 included for comparison. The parameters are pitch length $p = 250$ nm, finger width $w = 250$ nm, wavelength $\lambda_0 = 2 \mu\text{m}$, Aperture $A = 80 \mu\text{m}$, and separation $d = 8.25 \mu\text{m}$. Assuming $v_{\text{saw}} = 3488$ m/s, we get $f_0 = 1.74$ GHz. We see the same 3 to 4 GHz reflection loss in our new devices, even with the ‘bad’ device (which have defects/shorts). This further confirms that there is some characteristic absorption going on in this frequency range that is independent of the IDTs design. In the transmission spectra the new devices also show the same qualitative feature of a gradual increasing transmission towards 3.25 GHz. Near f_0 for both plots, we can barely make out any semblance of signal. Lastly, the spectra between our ‘bad’ device and ‘perfect’ device is marginal, especially near f_0 .

The fabrication recipe for dense high resolution devices has been developed and reliably produces good looking devices (as long as the chip is clean and free of dirt). Unfortunately, the VNA measurements of these devices show little to no SAW excitation/detection. What we have observed is that there are two frequencies that seem to have good transmission independent of the design of IDTs and seem characteristic of either the probes or the substrate. It is possible that the ion mill etching slightly into the LNO can be modifying its

SAW mediating properties. There are articles however that show ion mill etching LNO does degrade the surface but is negligible for our propagation distances [51, 117]. It is clear that future device design would benefit from have their electrical impedance numerically calculated through finite element analysis (like using COMSOL for example). Furthermore, their SAW frequency should probably avoid the 3-4 and 7-8 GHz ranges.

5.7 Additional Notes

5.7.1 Comments regarding lack of IDT signal.

To put to rest the concern of major SAW suppression due to etching of the surface, one could etch into the lower Ta layer and stop before it is all gone to keep the LNO surface unperturbed. Measurements of the IDT while the chip is in this state should still generate the necessary electric fields between fingers since the thin Ta should be highly resistive. Alternatively, the remaining Ta can be removed via wet etching (using some solution that attacks the thin Ta but not LNO). Care must be taken as the capping Ta on top of the SAF will also be attacked, so the timing is critical.

We also have bare, untouched Y-cut polished LNO substrates, some additional fabrication testing can be performed there to study the effects of Ar etching on LNO SAW propagation, for example, one could do lift-off deposition for low resolution IDT's (ideally with a MHz range design based on a paper that shows good results) with Al/AlO_x deposited as the IDT material, perform the measurements, then ion mill the sample and measure again. This actually would be a nice paper since there was little to no literature on the effects of dry etching on LNO.

Finally, there is no time-gating involved in this measurement, so crosstalk signals can intro-

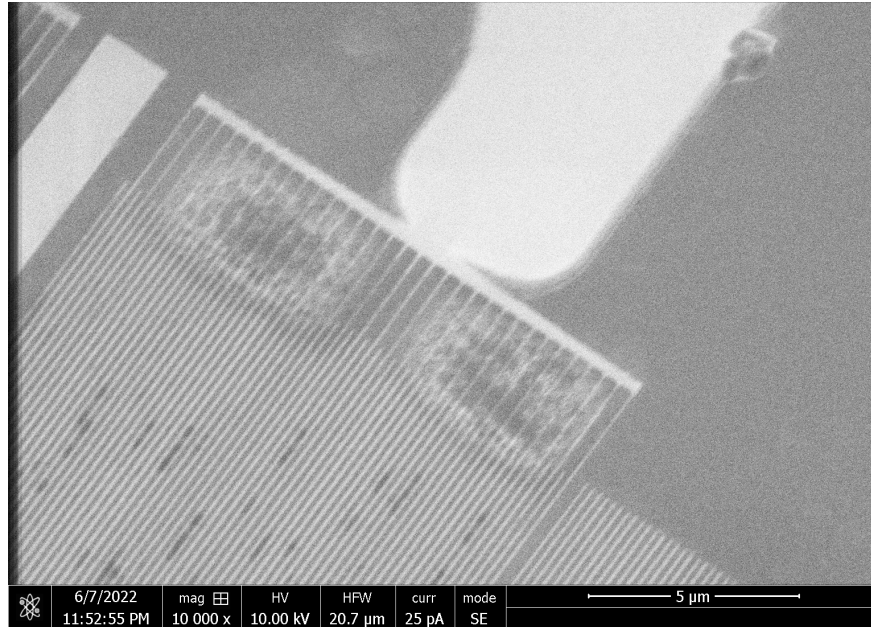


Figure 5.17: **SEM of ‘dirty’ samples.** SEM of chip with strange growth, it doesn’t seem organic, and did not change the VNA trace measurements by much.

duce a large background if the antennas are close enough (which is the case). Our VNA does not have time gating capabilities, but we may be able to

5.7.2 Strange growth on samples.

I have observed some kind of growth on all samples after a couple days, it was unclear as to where it was coming from. It was first observed on a chip that was left out uncovered for a couple weeks (due to COVID quarantine). It was later discovered that it happened to devices left in their container too. Fig. 5.17 shows an SEM image of the crap. Surprisingly, measurements when the devices were fresh vs after the growth showed little variation. **This warrants evaporating 7-10 nm AlOx or spin coating resist (like MMA or PMMA at low rpm) after etching to protect the surface.** My guess is that something about the fine fingers are allowing ambient moisture from the air to collect onto the structures, the residue doesn’t really appear on the larger features.

5.7.3 Reflection due to thin pads and fingers.

The approach of using the SAF to achieve one step fab introduces an issue that the leads are also thin Co (~ 30 nm) that results in large microwave reflection preventing sufficient power output at the antennas. One thing we can try is to maybe deposit 120 nm of Au or Al on top of the magnetic film prior to the one-step fabrication. That way we have thick pads, where the thick Au should not interfere with the spin wave dispersion of the SAF in the active region. Alternatively, the leads can be fabricated through lift-off (Section 3.3.5) immediately after etching the IDT's.

5.7.4 Using modulated microwave transmission to detect propagating SAWs.

An alternative method of measurement that can be used to maybe characterize the SAWs spectrum is through either a field modulated or amplitude modulate microwave transmission measurement. This involves a set-up very similar to the standard field modulated FMR measurement [48], where microwave is input at one antenna and the other antenna is fed into a microwave diode to convert into a DC output. Lock-in techniques can be applied through amplitude modulation of the swept frequency, which most microwave generators will have the option available. The amplitude modulation frequency is then fed to the lock-in's input reference oscillator. If there is a ferromagnetic region in between the antennas, field modulation may be applied instead, which usually gives higher quality signals. This is done through the lock-in amplifier outputting a reference oscillation to modulation coils surrounding the sample. The lock-in detected signal from the micro-wave diode then would be our S_{21} . By rotating the sample in small steps through the 'magic' angle, the change in S_{21} can be measured. It should be noted that the field modulation in principle would only work if there is a ferromagnetic region between the antennas as it must modulate the

spin wave interaction with the SAWs. The amplitude modulation approach should work for all devices at the cost of possible frequency dependent noise. One advantage is that RF generators can output much higher power than the VNA, which can get more power through to the antennas. Finally, a microwave amplifier could be used to boost the signal pick-up at the detector antenna prior to the microwave diode, be careful to check the resulting output using a power meter and checking the spec sheet of the diode to prevent any damage.

Part II: Micromagnetic Simulations of Electrically Excited Spin Waves in Nanostructures

When it comes to many experiments, the data is often collected through some (relatively) long time averaging or spatially macroscopic means of measurement. Ideally, we would like to directly observe the various interesting physics at the atomistic length and ultra-fast time scales. Unfortunately, without access to a synchrotron or similar massive measurement tools, there are little means of directly peering at the magnetic grains or atoms and observing what they are doing at the nanosecond or picosecond timescales during an experiment. What we can do however, is try and *recreate* the experimental results by computationally setting up a system of magnetic *cells* similar in structure to our real system, coupling them via our well proven analytical micromagnetic descriptions (i.e. LLG), and time evolving the system through finite-difference discretization. This is known as micromagnetic simulations. It is a powerful tool in that it allows us to use our full spatial and temporal access of the micromagnetic cells to gain insight as to what may be physically happening in our experiment at the grain or even atomic level. Micromagnetic simulations can also work in reverse, one may want to simulate various parameters to find the ideal conditions to generate desired results or to even to *predict* experimental results, which is useful in publications that

propose a novel effect or conceptual device. The following chapters showcase how powerful micromagnetic simulations are in better understanding experimental data and discovering key dynamics that are not obvious from that data.

Chapter 6 covers bilayer nanowire spin Hall oscillators and how their auto-oscillatory dynamics vary with increasing wire widths. The study revealed that there was an ideal width for maximum power output between the crossover from one-dimensional to two-dimensional nanowires. Wider wires exhibited more auto-oscillatory modes, but also increased non-linear interactions among the modes. The increased non-linear interactions lead to an overall reduction of mode amplitudes and phase coherence, thus, lower power output. This study motivated employing simulations to better understand the auto-oscillatory spectra and spatial profiles, which elucidated the non-linear phenomena among the modes. The simulations also reconciled the discrepancies observed in two different kinds of measurements made on the nanowire. Mainly that electrical detection of auto-oscillations was sensitive to phase cancellations and Brillouin light scattering was sensitive to total population of magnons.

Chapter 7 presents a new nanowire spin Hall oscillator that achieves large angle dynamics when auto-oscillating. This is due to the energy landscape of the nanowire achieving an *easy*-plane anisotropy that is orthogonal to the polarization of the spin Hall current. The configuration enables maximum torque from the spin current and thus large angle dynamics. Simulations of the system revealed that the easy plane was achieved through balancing the energy for magnetization pointing along the wire and out of plane perpendicular.

Finally, Chapter 8 demonstrates using voltage controlled magnetic anisotropy to influence propagating spin waves travelling in a nanowire. In other words, a spin wave field effect transistor was realized. In the device, a voltage applied at the field effect gate modulated the amplitude of spin waves travelling through. Micromagnetic simulations elucidated the spin wave mode structure. They also show that the modulation of perpendicular magnetic anisotropy in the ‘gated’ region bares a similar effect, validating the theory.

These chapters have been written in a kind of modular form, so there may be some redundancy across the chapters when talking about certain concepts or ideas. Finally I want to clarify that my contribution to these studies have been through micromagnetic simulations, all sample nanofabrication and data collection were done by my predecessors.

Chapter 6

Dimensional Crossover in Spin Hall Oscillators

6.1 Context and Introduction

Spin torque oscillators (STO's) are actively researched in industry and academia as they have many useful applications and rich physics to offer. Some examples being nanoscale microwave sources [129, 111], spin wave generators and amplifiers for nanomagnonic applications [83, 130, 47, 2], sensors and magnetic field amplifiers in magnetic recording [14] and core building blocks of artificial neural networks for neuromorphic computing, image processing and pattern recognition [79, 106, 128]. In this project we explore how the width of spin Hall driven nanowire STO's (called spin Hall oscillators (SHO)) have an impact on the auto oscillatory dynamics, specifically, why the emitted power drops precipitously in wider wires, and how the emission spectra shifts from quasi-1D active region nanowires to 2D active regions. I will cover first the core physical concepts involved (like spin transfer torque and spin Hall effect), and then some experimental data collected. I will be focusing mostly

on the micromagnetics aspect of the project, as that was my primary contribution.

6.1.1 Spin Transfer Torque

When spin current is injected into a ferromagnet (usually via flowing electrons), the itinerant spins interact with the spins in the ferromagnet (like conductive electrons interacting with the local d shell electrons) and leads to a mutual exchange of angular momentum, i.e. *spin torque*. This leads to the ferromagnet being tilted out of equilibrium and a filtration of spin current that are polarized along the same direction as the ferromagnet through to the other side. This interaction alone has opened a plethora of new avenues of research. A popular application of this effect involves using a pinned *reference* ferromagnetic layer to filter the spins (i.e. serve as a *spin polarizer*) flowing through so that they can apply spin torque to a target, often called *free* layer for switching of magnetic states, these are commonly called *spin valves* and are actively used and researched in hard drive and random access memory technology.

The introduction of spin transfer torque (STT) into a system adds two new terms to the LLG equation (called Slonczewski terms) [121]:

$$\frac{\partial \mathbf{M}}{\partial t} = -\gamma[\mathbf{M} \times \mathbf{H}_{\text{eff}}] + \frac{\alpha}{M_S} \left[\mathbf{M} \times \frac{\partial \mathbf{M}}{\partial t} \right] - \frac{\gamma a}{M_S} (\mathbf{M} \times [\mathbf{M} \times \mathbf{P}]) - \gamma b (\mathbf{M} \times \mathbf{P}) \quad (6.1)$$

where a and b are constants that scale with the amount of spin current injection, we can take this and apply some simplification and grouping of terms, and unpack the a constant to give more insight in the torque strength,

$$\frac{\partial \mathbf{m}}{\partial t} = -\gamma[\mathbf{m} \times \mathbf{H}_{\text{eff}} + \alpha \mathbf{m} \times \mathbf{m} \times \mathbf{H}_{\text{eff}} - \beta \mathbf{m} \times \mathbf{m} \times \mathbf{p} - \beta' \mathbf{m} \times \mathbf{p}] \quad (6.2)$$

$$\beta = \left| \frac{\hbar}{\mu_o e} \right| \frac{J}{d M_S} \frac{P \Lambda^2}{(\Lambda^2 + 1) + (\Lambda^2 - 1)(\mathbf{m} \cdot \mathbf{p})} \quad \beta' = C \cdot \beta \quad (6.3)$$

where \hbar is the reduced Planck constant, μ_o is the free space permeability constant, e is the electron charge, J is the current density, d is the ferromagnet thickness, M_S is the saturation magnetization, P is the spin current polarization, Λ is the spin torque asymmetry parameter, \mathbf{m} is the magnetization unit vector \mathbf{M}/M_S , \mathbf{p} is the spin current polarization unit vector, and C is the ratio factor between the two Slonczewski torques.

The two additional torques are normally described as *field-like* and *damping-like* due to their resembling nature to the original LLG field and damping terms. Usually the field-like Slonczewski term (β') is not significant in most systems and is usually omitted. We can think of STT as electrons *kicking* the ferromagnet into the direction of the electron's polarization, this means that with enough electrons all polarized in tandem, the ferromagnet would be kicked continuously in that direction as long as the current flows. If the current is unpolarized however, then the kicking direction averages out to zero and so the ferromagnet remains relatively unperturbed in long time scales (milliseconds).

A note about STT

The β term across literature has many different forms depending on what kind of system is considered and what underlying principles are utilized, but they all depend on the current density in some way. This P and Λ dependence considers the overall homogeneity of spin current polarization plus the reflection of charge current at the interfaces (which then leads to a *backflow* which mitigates the overall torque), and in our case is the form used in our simulation software.

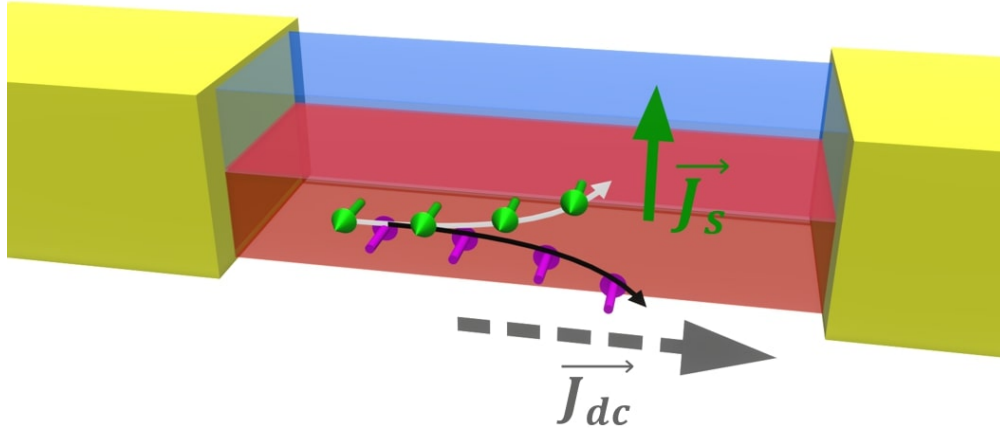


Figure 6.1: **Illustration of spin Hall effect.** Schematic showing the charge current \mathbf{J}_{dc} flowing through the heavy metal (red layer) and through spin-orbit effects yields a transverse *spin* current \mathbf{J}_s of particular polarization (green arrows) that flows into the ferromagnet (blue layer) from below.

6.1.2 Spin Hall Effect

There are several approaches to delivering spin current to a ferromagnet. One common method already mentioned involves having a spin *polarizer* filter the spins carried in flowing charge current and driving that current directly through the ferromagnet. This format however is not ideal for many geometries such as nanowires. In such cases, utilizing the spin Hall effect (SHE) becomes critical. Fig. 6.1 illustrates this effect. It turns out that when charge flows through a heavy, non magnetic metal (like Pt), the spins' interaction with the nucleus leads to a splitting in energy levels between up and down spin electrons (spin orbit coupling). On the scale of a lattice, this takes the electron conduction band and splits it into spin dependent bands (i.e. the degeneracy was lifted due to the Zeeman field). This leads to a transverse *spin* current (i.e. spin up deflects in one direction and spin down deflects in the opposite) that yields a net angular momentum transfer at the boundaries. This kind of *spin orbit* interaction can be formalized as an energy term in the Hamiltonian:

$$H_{SO,int} = -\frac{1}{2}\boldsymbol{\sigma}\cdot\mathbf{B}(\mathbf{k}) \quad (6.4)$$

Where $\mathbf{B}(\mathbf{k})$ is an effective \mathbf{k} -dependent magnetic field for the electron band considered. This *shifting* of \mathbf{k} within the material and from defects/impurities leads to a net, *transverse* spin current and is generally referred to as the *intrinsic* contribution to SHE. The key thing here is that these intrinsic contributions involve changing the *momentum direction* or *band structure* of spin carriers.

The inclusion of impurities also introduces two more contributions to the SHE, which are normally called the *side-jump* and *skew-scattering* mechanisms. Both of these mechanisms are quite similar, but have a subtle difference. In skew-scattering, electrons will spatially deflect at an angle (let's say θ) of off defects/impurities. The sign of the angle however depends on the spin species (i.e. up spins deflect by θ and down spins by $-\theta$). In side-jump, itinerant spins spatially shift depending on their spin orientation when scattering off of defects/impurities (e.g. if electrons are travelling along x in an xy -plane, they will scatter Δy or $-\Delta y$ depending on spin, which also results in a perpendicular flow of spin current through repeated scattering). These mechanisms are considered *extrinsic*, since their effects depend spatially on the moving electrons (i.e. they are physically scattering) and their momentum remains unchanged.

6.1.3 Auto Oscillatory Dynamics

An important feature of the β term in Eq. (6.3) is that it can flip sign based on the polarized current. It is called a *damping-like* term because it can be used to tune the damping of a system. Fig. 6.2 illustrates a simple, but key, STT configuration. With sufficient current density and polarization that is anti-parallel to the magnetic field, this term can *cancel* the damping term entirely (hence *anti-damping*) and allow the ferromagnet to freely precess under the field torques along a constant energy path. This phenomenon is the core mechanism behind STO's. A feature of STO's worth highlighting is that you need only input DC to get

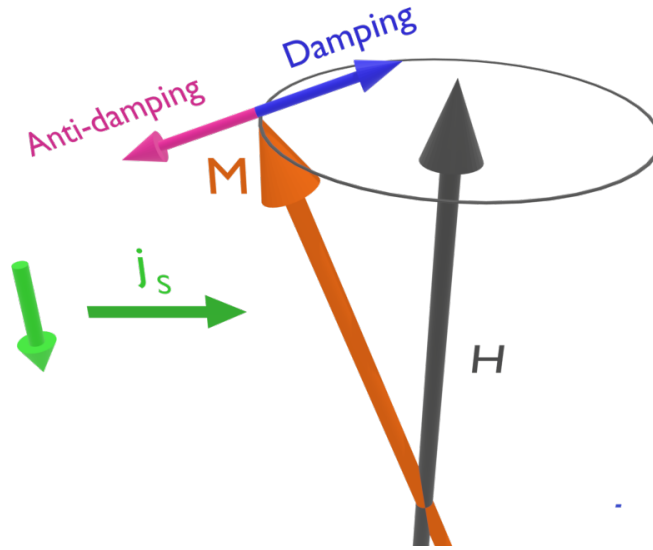


Figure 6.2: **STT applying anti-damping torque.** Spin current \mathbf{j}_s polarized such that the resulting torque pulls the magnetization \mathbf{M} away from equilibrium. This is directly anti-parallel to the damping torque and hence is called *anti-damping* torque.

AC dynamics, which is a large part of why they are so attractive for research.

One configuration to feasibly study and develop STO's is with a ferromagnetic metal (FM) and heavy, non-magnetic metal (NM) bilayer patterned into a nanowire. This allows for the sufficient current density and, through the SHE, the correct polarization to apply anti-damping torque and thus achieve a one-dimensional oscillator. It turns out that as the nanowire width increases, the auto-oscillatory dynamics become suppressed. This study aims to better understand the transition from 1D to 2D spin Hall oscillators (SHO's).

6.2 Sample and Measurement Details

The studied samples were nanowires of platinum and permalloy (nickel and iron alloy) bilayers with an aluminum oxide capping layer. The layers were Pt(6nm)/Py(5nm)/AlOx(2nm) grown on a *c*-plane sapphire substrate. The nanowires had widths ranging from 0.17 μm up to 2.11 μm . The active region (area between leads, where the current density is highest),

was $1.9 \mu\text{m}$ long. Fig. 6.3 illustrates the sample.

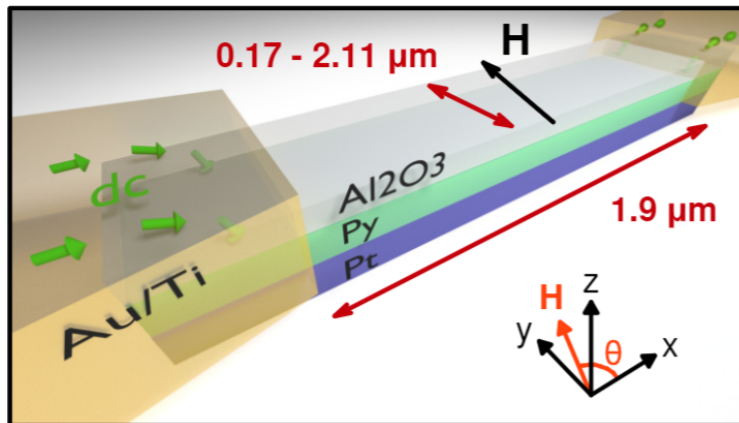


Figure 6.3: **Schematic of Pt/Py nanowire.** Sapphire/Pt(6nm)/Py(5nm)/AlOx(2nm) stack with dimensions and coordinate axes defined. The green arrows depict the flow of electrons.

Samples were characterized mainly through magneto-resistance measurements and Brillouin Light Scattering (BLS). The former mainly involved electrical detection through the emitted voltage oscillations while the sample was auto-oscillating. The microwave voltage $V_{ac} \sim I_{dc}\delta R_{ac}$ is generated by the AMR resistance oscillations δR_{ac} arising from the magnetization auto-oscillations of the Py layer [78]. The latter involves scattering photons off of the sample while under operation and using the scattered photon's energies to calculate what spin wave frequencies are being excited while auto-oscillating. BLS also yields spatial information of where certain frequencies are heavily excited. Finally some electrical detection measurements were made at low T. Since I took little part in the physical data collection and sample preparation, I will defer those details to the publication and Andrew Smith's thesis.

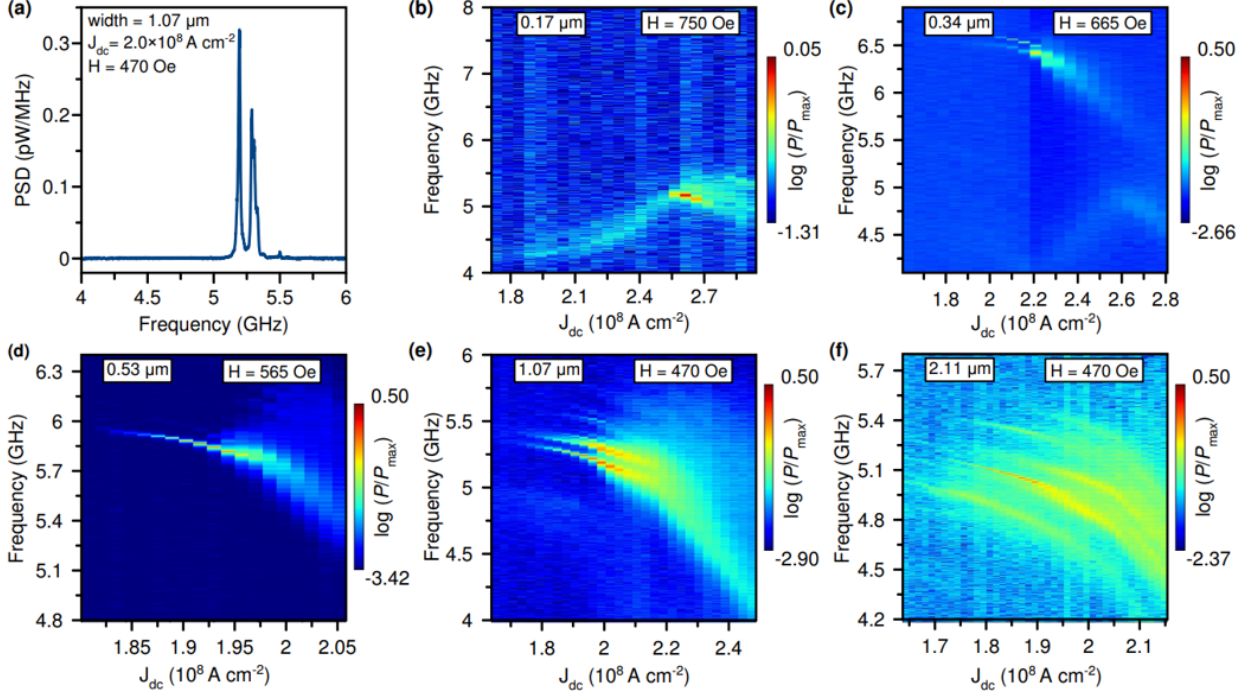


Figure 6.4: **Emission data from auto oscillations.** (a) Power spectral density (PSD) of the microwave signal generated by the $1.07 \mu\text{m}$ wide Pt/Py/ AlO_x wire SHO at the bias current density $J_{\text{dc}} = 2.0 \times 10^8 \text{ A cm}^{-2}$, bath temperature $T = 4.2 \text{ K}$ and magnetic field $H = 470 \text{ Oe}$ applied at 5° from y -axis ($\theta = 85^\circ$). Three auto-oscillatory modes are excited. The non-Lorentzian peak lineshapes are mainly due to standing waves in the microwave circuit. (b–f) Microwave emission spectra versus J_{dc} for five wires of different widths measured in fields exceeding H_{sat} by approximately 100 Oe and applied at $\theta = 85^\circ$. The logarithmic color scale represents the emitted power normalized to the maximum power P_{max} . The wire widths and the applied field values are shown in the figures. The low frequency edge mode is seen for narrower wires ($0.17 \mu\text{m}$ and $0.34 \mu\text{m}$ wide). The higher frequency bulk modes are observed in wider wires ($0.34 \mu\text{m}$, $0.53 \mu\text{m}$, $1.07 \mu\text{m}$ and $2.11 \mu\text{m}$ wide).

6.3 Experimental Data

6.3.1 Emission Data

Fig. 6.4 illustrates the spectral properties of the microwave signals generated by the Pt/Py wire devices as a function of direct electric current density J_{dc} applied to the wire at the sample bath temperature $T = 4.2 \text{ K}$ and $\theta = 85^\circ$. Here the charge current density J_{dc} is defined as direct current bias I_{dc} divided by the cross-sectional area of the Pt/Py bilayer

wire. To facilitate direct comparison among the wires of different widths, the measurements in Fig. 6.4 are made at magnetic field values exceeding the width-dependent saturation field $H_{\text{sat}}(w)$ by approximately 100 Oe. This ensures approximate spatial uniformity of the wire's saturation magnetization and similarity of the internal magnetic fields among the wires of different widths [32]. Fig. 6.4(a) shows a typical microwave emission spectrum measured for the $1.07 \mu\text{m}$ wide wire device at $J_{\text{dc}} = 2.0 \times 10^8 \text{ A cm}^{-2}$ and $H = 470 \text{ Oe}$. The spectrum shows multiple peaks, which demonstrates that auto-oscillations of several spin wave modes of the device are excited at this value of J_{dc} . Such coexistence of multiple spin wave modes has been the focus of recent research [33, 140]. Quantitative analysis of the spectral linewidth and lineshape of these peaks is complicated by the presence of standing waves in the microwave circuitry, which manifest themselves as oscillatory modulation of the spectral peak amplitude seen for the peak at 5.3 GHz. Figs. 6.4(b)–6.4(f) show the microwave emission spectra generated by five Pt/Py wire devices with different wire widths as a function of J_{dc} . For the $0.17 \mu\text{m}$ wide wire (Fig. 6.4(b)), a single low-frequency mode is observed. The frequency of this mode first increases and then decreases with current [35], and the spectral line of this mode is relatively broad. Previous studies of the Pt/Py nanowire SHOs [31] revealed that this low-frequency mode is the *edge mode* (EM) whose amplitude is maximum at the wire edge. This mode is created by a spatially inhomogeneous demagnetizing field, which creates magnetic potential wells for spin waves near the edges of a transversely magnetized wire [32, 104, 10, 30]. Since this mode is confined to a relatively small volume near the wire edges, random thermal torques are expected to significantly increase the spectral linewidth of this mode [119] compared to the bulk modes that occupy the entire active region. The wire edge roughness and the magnetic material inhomogeneities caused by ion mill damage and oxidation of the edge may also contribute to the line broadening of the EM [89].

The EM auto-oscillations are also excited in the $0.34 \mu\text{m}$ wide wire (Fig. 6.4(c)) but this mode generates less microwave power in comparison to the $0.17 \mu\text{m}$ wire. This can be explained by the smaller volume fraction occupied by the EM in the $0.34 \mu\text{m}$ wire, and does

not imply that the amplitude of the EM auto-oscillations in the wider wire is lower than that in the narrower wire. In addition to the EM, two higher frequency auto-oscillatory modes are excited in the $0.34 \mu\text{m}$ wire. Such high frequency modes with narrow spectral linewidths have been previously identified as *bulk* spin wave modes (BM), whose amplitudes are maximum near the center of the wire [31, 32]. The existence of multiple BM with a discrete set of eigenfrequencies [52] is a result of geometric confinement of the magnetic oscillations to the SHO active region. The confinement along the wire width is provided by the geometric edges of the wire. The confinement along the wire length may arise from two sources: (i) a current-induced Oersted field that opposes the applied field for the current polarity generating anti-damping ST in the Pt/Py system [31] and (ii) a step-wise change of the effective magnetic damping at the boundaries between the active region and the electric leads. All observed BMs exhibit red frequency shifts with increasing current that arises from several factors: (i) reduction of the Py saturation magnetization via ohmic heating and short-wavelength magnon generation by ST [24], (ii) Oersted field from the electric current in the Pt layer and (iii) nonlinear frequency shift due to increase of the mode amplitude with increasing current [119, 72, 13].

For the $0.53 \mu\text{m}$ wire (Fig. 6.4(d)), auto-oscillatory dynamics of the the EM are no longer detected. This, however, does not imply that the EM is not excited. As the volume fraction of the active region occupied by the EM becomes smaller, more of the applied current flowing in the ferromagnet shunts through the bulk of the wire and the microwave signal generated by magnetization oscillations at the wire edge falls below the detection threshold of our measurement setup. It is interesting to note that for this wire width, auto-oscillations of the lowest frequency BM are excited with large amplitude while the amplitude of the higher frequency BMs is negligibly small compared to that of the lowest frequency BM. At this wire width, the Pt/Py wire SHO behaves nearly as a single-mode microwave signal generator. As we discuss below, this single-mode behavior gives rise to the highest microwave power generated among all SHOs studied in this project.

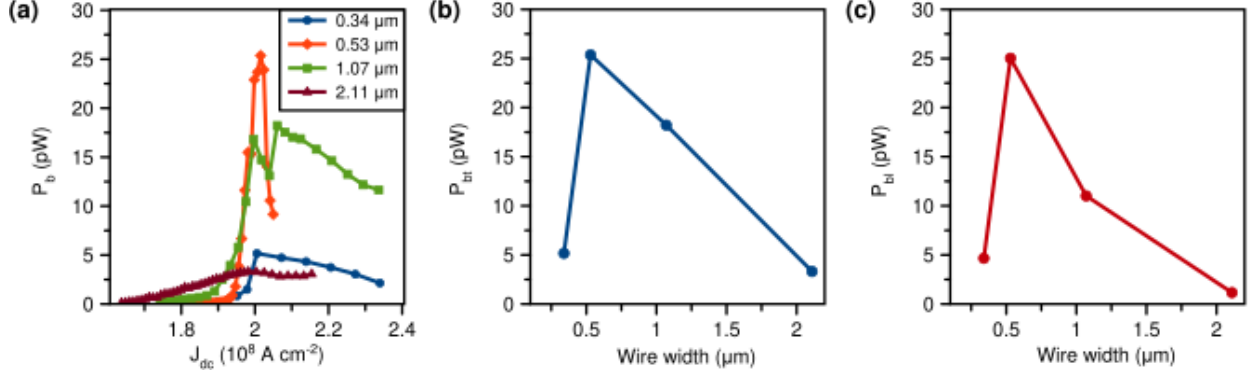


Figure 6.5: **Emission power for varying wire widths.** (a) Integrated microwave power emitted by all bulk modes of the wire P_b versus bias current density J_{dc} . The data is shown for all four wires exhibiting bulk mode auto-oscillations. (b) Maximum value of the integrated microwave power emitted by all bulk modes of the wire P_{bt} as a function of the wire width. (c) Maximum integrated power of the largest-amplitude bulk mode P_{bt} as a function of the wire width.

Further increase of the Pt/Py wire width results in excitation of the auto-oscillatory dynamics of multiple BMs. The number of the excited BM increases with increasing wire width, as illustrated in Fig. 6.4(e) for the $1.07 \mu\text{m}$ wide wire and Fig. 6.4(f) for the $2.11 \mu\text{m}$ wide wire, while the amplitude of auto-oscillations of each mode decreases. The precipitous decrease of the auto-oscillation amplitude with increasing wire width is illustrated in Fig. 6.5, which shows integrated microwave power generated by the auto-oscillatory modes. Fig. 6.5(a) shows the total integrated power in all BMs of a wire P_b as a function of the applied current density J_{dc} . This figure demonstrates that the critical current for the excitation of the auto-oscillatory dynamics $J_c \approx 2 \times 10^8 \text{ A cm}^{-2}$ is nearly independent on the wire width. For all wires, the integrated microwave power first increases with increasing current above J_c and then decreases after reaching a maximum at a current density J_{max} . Fig. 6.5(a) also shows that the onset of the auto-oscillations becomes softer as the wire width increases. Indeed, the current interval between J_c and J_{max} is $\approx 0.5 \times 10^7 \text{ A cm}^{-2}$ for the $0.34 \mu\text{m}$ wide wire while it is $\approx 2.5 \times 10^7 \text{ A cm}^{-2}$ for the $2.11 \mu\text{m}$ wide wire.

We also find that the maximum integrated microwave power generated by the wire is a non-monotonic function of the wire width. Fig. 6.5(b) shows the maximum total integrated

power generated by all BMs of a wire P_{bt} as a function of the wire width. The power first increases with the wire width reaching the value of 26 pW for the 0.53 μm wide wire and then rather precipitously decreases with increasing width. Comparison of this figure with Fig. 6.4 clearly shows that the maximum power is achieved in the 0.53 μm wide wire that exhibits single-mode auto-oscillatory dynamics. Fig. 6.5(c) illustrates that the power generated by the largest-amplitude BM P_{bl} shows a similar trend to that in Fig. 6.5(b). However the decrease of the largest-amplitude BM power with increasing wire width is even more rapid than that in Fig. 6.5(b).

The data in Fig. 6.4 and Fig. 6.5 clearly show that coherent auto-oscillatory dynamics of magnetization are rapidly suppressed as the wire width increases into the micrometer-scale range. The data demonstrate that the crossover between coherent large-amplitude auto-oscillatory dynamics in 1D nanowires and incoherent small-amplitude dynamics in 2D microwires proceeds via a gradual increase of the number of spin wave modes participating in the auto-oscillatory dynamics accompanied by a rapid decrease of the maximum amplitude of auto-oscillations achievable by each of these modes.

6.3.2 BLS Data

We employ micro-Brillouin light scattering (BLS) [95] to directly measure the spatial profiles of the auto-oscillatory modes at room temperature ($T = 300\text{ K}$). Fig. 6.6(a) shows optical micrograph of the 1.07 μm wide wire device. The Pt/Py wire and the Ti/Au leads are marked in this image. The image also shows the laser beam of the BLS setup focused on one edge of the wire active region. Fig. 6.6(b) shows the BLS spectrum measured at this laser beam position. The frequency resolution of the BLS apparatus is $\sim 0.1\text{ GHz}$. The data are taken at a current density $J_{dc} = 9.77 \times 10^7\text{ A cm}^{-2}$ exceeding the critical density for excitation of the auto-oscillatory dynamics at room temperature. The measurement is

made in 495 Oe magnetic field applied in the plane of the sample nearly perpendicular to the wire axis ($\theta = 87^\circ$). Two peaks are visible in the spectrum. Spectral mapping of the BLS signal intensity at center frequencies of these peaks allows us to determine the spatial profiles of the excited auto-oscillatory modes.

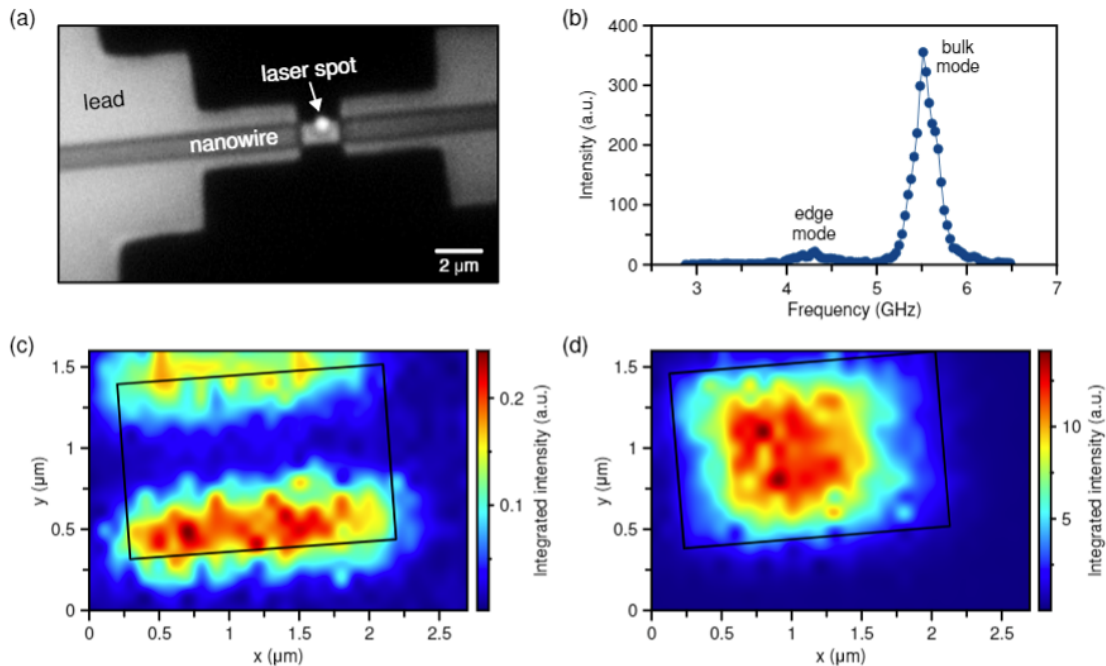


Figure 6.6: **Brillouin light scattering of auto-oscillations in nanowire.** Brillouin light scattering characterization of auto-oscillatory modes of the $1.07 \mu\text{m}$ wide wire device at room temperature ($T = 300 \text{ K}$). (a) Optical micrograph of the devices showing Pt/Py wire, Ti/Au leads and laser spot of the BLS apparatus focused on one edge of the active region of the device. (b) BLS spectrum measured at the laser beam position at the edge of the active region shown in (a) for $J_{\text{dc}} = 9.77 \times 10^7 \text{ A cm}^{-2}$ and $H = 495 \text{ Oe}$ applied at $\theta = 87^\circ$. Spatially resolved BLS allows to reveal the origin of the excitations: (c) Spatial profile of the BLS signal intensity at $f = 4.3 \text{ GHz}$ – the center frequency of the low-frequency peak (edge mode). The rectangle denotes the approximate location of the active region of the device. This BLS spectral mapping reveals that this auto-oscillatory mode is an edge spin wave mode of the wire. (d) Spatial profile of the BLS signal intensity at $f = 5.6 \text{ GHz}$ – the center frequency of the high-frequency peak (bulk mode). This BLS spectral mapping reveals that this auto-oscillatory mode is a bulk spin wave mode of the wire.

Fig. 6.6(c) shows the BLS signal intensity measured at the center frequency of the low-frequency peak $f = 4.3 \text{ GHz}$ as a function of the laser beam position. The rectangular frame on this figure outlines the contour of the active region of the device. It is clear from

Fig. 6.6(c) that the low-frequency auto-oscillatory mode is the edge mode of the sample (labeled as edge mode in Fig. 6.6(b)). It is interesting to note that the amplitude of this mode at one edge exceeds that at the other edge. This symmetry breaking may result from different edge roughness of the two edges [89]. Fig. 6.6(d) shows the BLS signal intensity measured at the center frequency of the high-frequency peak $f = 5.6$ GHz as a function of the laser beam position. This figure reveals that the high frequency mode is the bulk mode of the wire (labeled as bulk mode in Fig. 6.6(b)).

6.4 Micromagnetic Simulations

In order to gain a clearer picture of the auto-oscillatory dynamics we observed experimentally in this study, we turn to using micromagnetic simulations. One *strong motivator* for the sims was the discrepancy between the electrical emission spectra (Fig. 6.4(a)) and the BLS spectra (Fig. 6.6(b)), which is discussed in depth in Section 6.6. We also wanted to confirm the eigenmode spectra and spatial profile of the auto-oscillatory modes from experimentally determined parameters, as agreement between simulations and experiment strengthens the study and its claims.

6.4.1 Simulation Software and Parameters

We perform micromagnetic simulations of such dynamics via the Object Oriented Micromagnetic Framework (OOMMF) [29]. We performed simulations of the $1.07 \mu\text{m}$ wide wire with zero temperature ($T = 0$ K). The system is primarily set with experimentally determined magnetic parameters for Py on a Pt underlayer [31, 30]: saturation magnetization $M_s = 620 \text{ emu cm}^{-3}$, exchange constant $A_{\text{ex}} = 5 \times 10^{-12} \text{ J m}^{-1}$. We assume a Gilbert damping constant $\alpha = 0.01$.

The system emulates the auto-oscillatory dynamics through applying a spin transfer torque within the active region of the Pt/Py wire geometry. The polarization and strength of spin transfer is set to resemble spin Hall driven anti-damping torque. We store the spatial and time dependence of the normalized magnetization component along the wire axis $m_x(t)$ over the active region. These simulations were repeated for several different initial directions of magnetizations to confirm our results to be consistent. Micromagnetic simulations can be highly sensitive to the starting configuration depending on the complexity of the system, so an easy way to vet the robustness of our calculations is to change up the initial conditions and see if the results are the expected and consistent.

The Py wire geometry is 4 μm total length, 1.07 μm width, 5 nm thickness, and 1.9 μm active region in the center. The wire is divided into $5 \times 5 \times 5 \text{ nm}^3$ micromagnetic cells. The cell size should be close to or below the exchange length of the system, which is determined by:

$$\frac{2A_{\text{ex}}}{\mu_0 M_s^2}. \tag{6.5}$$

Simulations with cell sizes too large no longer accurately represent the real system. Computational load and times however dramatically increases for smaller cell sizes (which increases the total number of cells to calculate), note that one must balance these two aspects to achieve efficient and reliable calculations. In this simulation the Pt under layer (which is nonmagnetic) contributes only two main complexities to the Py layer: (1) the delivery of spin transfer torque, (2) the Oersted field generated by the current flowing through it. For this reason the simulation involves only the Py layer and the effects of the Pt are covered via the aforementioned spin transfer torque parameter and a fixed applied field within the active region. Following the appropriate right hand rule we apply an in-plane Oersted field $H_{\text{Oe}} = 36 \text{ Oe}$ parallel the y -axis, which corresponds to a room-temperature critical current density in the Pt layer of $J_c^{\text{Pt}} = 9.5 \times 10^7 \text{ A cm}^{-2}$ [135]. This Oersted field actually opposes

the applied external magnetic field and creates a potential well for spin waves, resulting in the auto-oscillatory dynamics being mostly localized within the active region. Finally there is an external in-plane field of $H = 470$ Oe applied 5° from the y -axis ($\theta = 85^\circ$). The small deviation is pertinent in that high symmetry configurations can actually be sensitive to bit noise and result in inconsistent results.

6.4.2 Simulation with applied spin Hall torque

In the active region we apply the spin Hall torque with spin Hall angle θ_{SH} which parametrizes the conversion of charge current in the Pt to the transverse spin current injected into the Py layer. We vary the spin Hall angle until we observe clear emergence of auto oscillatory behavior. This critical threshold value was found to be $\theta_{\text{SH}}^c = 0.044$. Our simulations are carried out just above this critical value ($\theta_{\text{SH}} = 0.045 > \theta_{\text{SH}}^c$) to analyze the auto-oscillatory behavior at a current density exceeding the critical current density by approximately 2%.

Micromagnetic simulations are calculated out over relatively short physical timescales (usually 100s of picoseconds or $1 \mu\text{s}$), for that reason we must be mindful of transient dynamics after changing some parameter in the system (like turning on the spin Hall torque). The transient dynamics in these simulations lasts for $0.1 \mu\text{s}$ after turning on the spin Hall current (see Fig. 6.7). Following this period the simulation achieves a quasi-steady-state, where a consistent set of auto-oscillatory modes are excited. It however turns out that the relative amplitudes of these modes continue to fluctuate with time. We attribute this to zero-temperature deterministic chaos which can arise in a system like this where there are a large number of degrees of freedom (the huge number of cells in this case).

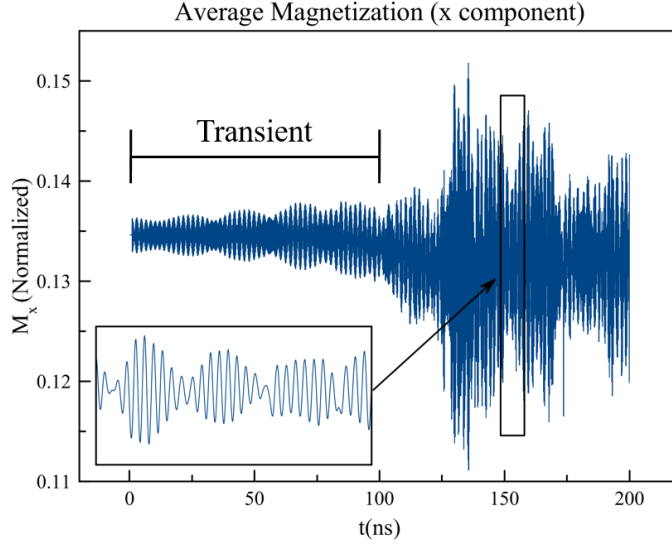


Figure 6.7: **Example of transient state.** Magnetization (x -component) vs time plot which shows an initial transient period prior to exhibiting auto-oscillatory behavior. Inset shows a zoom in of the magnetization dynamics at 150 ns, well within the *quasi-steady-state*. When performing analysis on micromagnetic simulations, these transient regimes are recommended to be removed when trying to emulate experimental data (which would measure for relatively long time scales and thus neglect any transients).

6.4.3 Simulation of Spin Wave Eigenmodes

We want to compare the auto-oscillatory modes to the intrinsic eigenmodes of the nanowire system. In these simulations, we apply the same Oersted field in the active region, but keep the spin Hall torque turned off, which effectively keeps the system the same but with no anti-damping torque. An out-of-plane "tickle" field of small amplitude is applied, which has amplitude $h_{\text{sinc}} = 5$ Oe and has a time-dependent profile described by the function:

$$h_{\text{sinc}}\text{sinc}(t) = h_{\text{sinc}} \sin(2\pi f_c t) / (2\pi f_c t) \quad (6.6)$$

This is known within our group as applying a 'sinc pulse', which excites all modes of the system under the cutoff frequency $f_c = 20$ GHz (can be thought of similarly to striking

a tuning fork or plucking a guitar string). This gives valuable insight into the intrinsic magnetic resonant frequencies of our system and is a standard approach to understanding experimental data.

6.4.4 Analysis

The spectra of auto-oscillatory dynamics are calculated via fast Fourier transforms (FFT) of the x -component of the dynamic magnetization $m_x(t)$ in the active region. The FFT spectra and spatial profiles are calculated from simulation results using a $0.2 \mu\text{s} - 2.0 \mu\text{s}$ time interval after the start of the simulations.

In order to compare the simulated spectra with the microwave emission and BLS experiments, we must consider that the two measurements are sensitive to $m_x(t)$ in different ways. For the electrically detected emission experiment, the spin Hall oscillator output power P_{SHO} is proportional to the square of the dynamic magnetoresistance oscillations δR_{ac} , which are approximately proportional to the average $m_x(t)$ in the active region [31],

$$P_{\text{SHO}} \propto \delta R_{\text{ac}}^2 \propto \langle m_x \rangle^2. \quad (6.7)$$

Therefore to simulate the emission spectra, we first take the *global average* of $m_x(t)$ in the active region and then take the square of the FFT spectra. Out-of-phase magnetization dynamics in different regions of SHO contribute destructively to δR_{ac} , and thus $P_{\text{SHO}} = 0$ does not prove the absence of auto-oscillations. The BLS experiment, on the other hand, is sensitive to the total magnon population and the BLS signal is proportional to the square of the dynamic magnetization. Therefore to emulate the BLS spectra, we calculate the square of the FFT spectra for each micromagnetic region *cell-by-cell* and then take the average; in

this manner we simulate the BLS peak intensity,

$$I_{\text{BLS}} \propto \langle m_x^2 \rangle. \quad (6.8)$$

We note that Eq.(6.8) is only a qualitative estimate because the BLS peak intensity also depends on the wave vector of the spin wave and drops to zero above a critical value of the wave vector [115].

We extract the spatial profile of modes by FFTing each individual magnetic cell's $m_x(t)$ and then plotting the amplitude of a set frequency for every 'pixel' of space. This yields the information of where certain modes of oscillation are localized. In literature often times modes are described with terms such as 'bulk' or 'edge' modes, as in, they are mostly excited in the bulk of the wire or in the edge. This is precisely the analysis one can use to compare directly to BLS measurements for example.

6.5 Simulation Results

Fig. 6.8 shows the micromagnetic simulation spectrum for the 1.07 μm wide wire in an external in-plane field of $H = 470$ Oe applied 5° from the y -axis ($\theta = 85^\circ$). Fig. 6.8(a) shows the global average spectrum simulating the microwave emission experiment and reveals that two clusters of large amplitude peaks, one just above 4.5 GHz and one just above 5.0 GHz, are simultaneously excited above the critical current. Fig. 6.8(b) shows the cell-by-cell average spectrum to be compared to the BLS data.

Figs. 6.9(a)–6.9(f) show the amplitude and phase spatial profiles of the modes labeled a – d in Fig. 6.8(a) and e – f in Fig. 6.8(b). The amplitude spatial profiles of the modes lack mirror symmetry due to the 5° misalignment of the applied field with the in-plane normal to the wire. Notably, all these modes are localized within the active region of the wire. For the

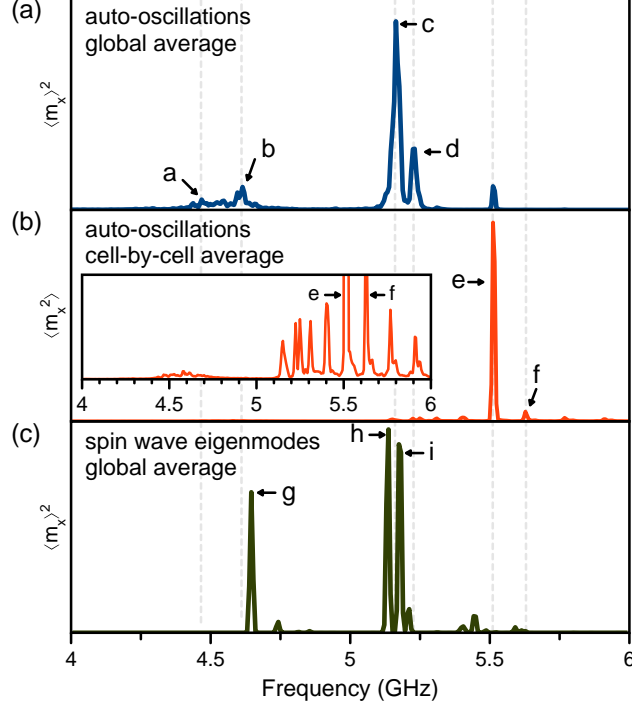


Figure 6.8: **Micromagnetic simulations of spin wave spectra in the $1.07 \mu\text{m}$ wide wire with $H_{Oe} = 36 \text{ Oe}$, $H = 470 \text{ Oe}$ and $\theta = 85^\circ$.** (a) Simulated spin Hall oscillator microwave emission spectra at $\theta_{\text{SH}} = 0.045$ (global average FFT) (b) Simulated cell-by-cell FFT spectra $\langle m_x^2 \rangle$ at $\theta_{\text{SH}} = 0.045$ to be compared to BLS data. Note the scale of (b) is $2500\times$ the scale of (a). Inset shows a zoom of $50\times$ in amplitude. (c) Simulated spin wave eigenmode spectra (global average FFT).

peak cluster just above 4.5 GHz, the spatial profiles reveal the largest amplitude peaks, labeled *a* and *b*, correspond to edge modes. Spatial profiles reveal that the peaks above 5 GHz, labeled *c*–*f*, correspond to bulk modes [32]. Note that the amplitude scale is set equal for Figs. 6.9(a)–6.9(c), while the scale for Figs. 6.9(d), 6.9(e), and 6.9(f) are $2\times$, $100\times$, and $10\times$ larger respectively. Owing to the large FFT amplitude occupying a significant area of the active region, one might expect modes *e* and *f* to have a larger amplitude relative to peaks *a*–*d* in the emission spectrum shown in Fig. 6.8(a). However, as shown in the corresponding phase profiles, alternating anti-nodes have dynamics that are out of phase which significantly reduces contribution to the global average of the dynamic magnetization. The simulated $\langle m_x^2 \rangle$ spectrum, being insensitive to phase, does indeed show that the largest amplitude peak is mode *e*, which is followed in amplitude by mode *f*.

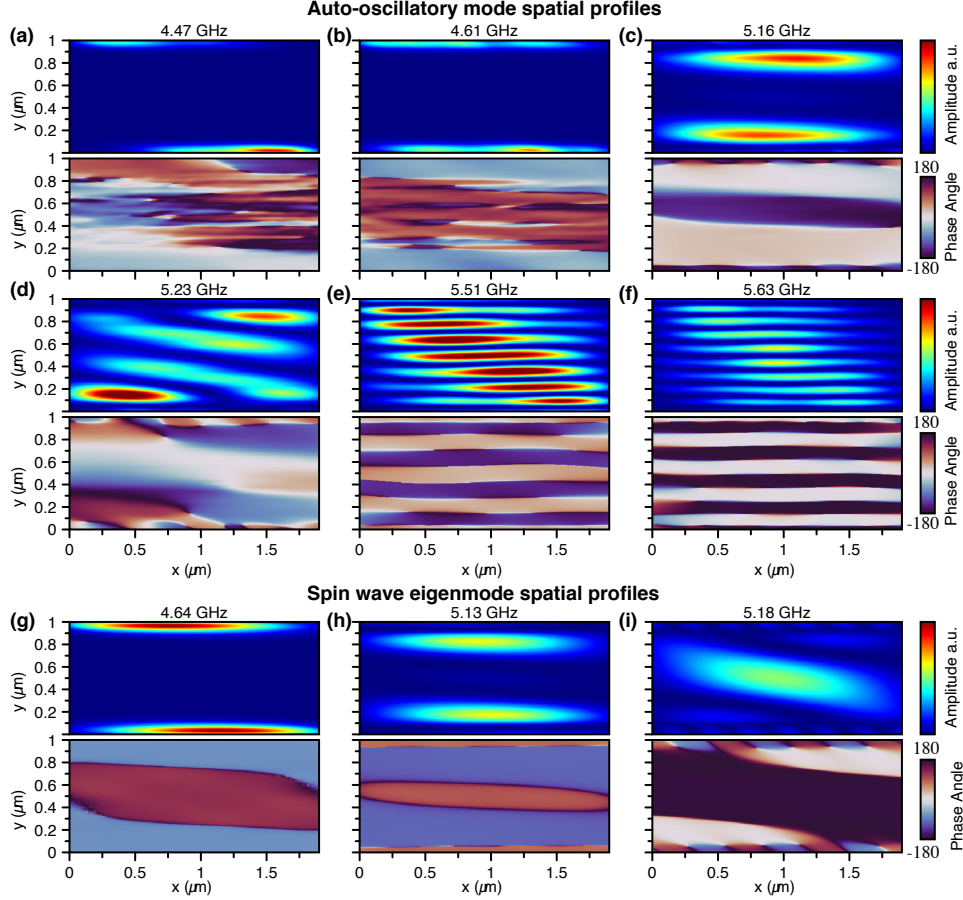


Figure 6.9: **Micromagnetic simulations of spin wave spatial profiles in the $1.07 \mu\text{m}$ wide wire.** Micromagnetic simulations of spin wave spatial profiles in the $1.07 \mu\text{m}$ wide wire. Amplitude (top) and phase (bottom) spatial profiles are shown for the auto-oscillatory modes with frequencies: (a) 4.47, (b) 4.61, (c) 5.16, (d) 5.23, (e) 5.51, and (f) 5.63. The amplitude scales for (a)–(c), are the same, while the scales for (d), (e), and (f) are $2\times$, $100\times$, and $10\times$ larger respectively. Amplitude (top) and phase (bottom) spatial profiles for spin wave eigenmodes with frequencies: (g) 4.64, (h) 5.13, and (i) 5.18 GHz. Individual panel labels correspond to the peaks labeled a – i in Fig. 6.8.

Finally, fig. 6.8(c) reveals a similar grouping of spin wave eigenmodes into two clusters at similar frequencies as the auto-oscillatory modes shown in Fig. 6.8(a). The amplitude spatial profiles of the largest amplitude peaks g – i are shown in Figs. 6.9(g)–6.9(i). The near 4.5 GHz edge mode profiles of auto-oscillatory modes a and b are similar to that of spin wave eigenmode g . We observe a similar match with the 5 GHz auto-oscillatory bulk mode c to that of spin wave eigenmode h . However, we do not observe an auto-oscillatory mode that matches with the bulk spin wave eigenmode i .

6.6 Discussion

Comparing the spin wave eigenmodes and auto-oscillatory modes predicted by micromagnetic simulations to the experimental data provided by electrically detected microwave emission and Brillouin light scattering, we find both qualitative agreement and apparent discrepancies for the $1.07\ \mu\text{m}$ wire. In both the micromagnetic simulations and BLS data, we observe edge modes near 4.5 GHz. In both spectra, edge mode amplitudes are smaller than the dominant modes above 5 GHz. In the microwave emission measurements, however, we do not clearly detect modes near 4.5 GHz. As stated before, this discrepancy may be attributed to the fraction of the active region occupied by the edge mode being too small to generate microwave signal above our instrument's noise floor. This is supported by the data for narrower wires, where edge modes occupying a larger volume fraction of the active region are clearly observed in the microwave emission spectra near 4.5 GHz. Additionally, edge roughness or damage may lead to varying edge anisotropy and/or current distributions that significantly affect the mode profile and excitation, which is not assumed in micromagnetic simulation [89]. The amplitude asymmetry of the 4.5 GHz edge mode as detected by BLS (Fig. 6.6(c)) indicates that the two edges of the nanowire are in fact not identical.

All the data show large excitation of magnetization dynamics at frequencies above 5 GHz. Electrically detected emission measurements (Fig. 6.4(a)) and global-average auto-oscillatory micromagnetic simulations (Fig. 6.8(a)) exhibit a similar grouping of peaks just above 5 GHz. In the BLS experiment (Fig. 6.6(b)) one peak centered around 5.6 GHz is detected, which is expected from the cell-by-cell average micromagnetic simulations (Fig. 6.8(b)). Spatial profiles from both micromagnetic simulations and BLS indicate these modes above 5 GHz are bulk modes.

The micromagnetic simulations indicate that the bulk mode making dominant contribution to the microwave emission exhibits maximum amplitude relatively far from the middle of the

wire, while the BLS data indicate that the majority of the bulk of the nanowire is excited by spin Hall torque. To understand this apparent discrepancy, we must consider that BLS is sensitive to the total population of magnons. We find that higher-order bulk modes, which lead to small-to-negligible amplitude in microwave emission due to phase cancellations, can lead to large amplitude in BLS spectra. Simulations predict that higher frequency modes should actually dominate the BLS spectra compared to the emission spectra, see Figs. 6.8(a) and 6.8(b). In fact this is what we observe experimentally; the BLS spectrum in Fig. 6.6(b) appears shifted to higher frequency compared to the emission spectrum in Fig. 6.4(a).

We note that the microwave emission and BLS experiments were performed with slightly different external fields (470 Oe for emission and 495 Oe for BLS) and at different temperatures (4.2 K for emission and 300 K for BLS). Therefore care must be taken when comparing mode frequencies between the two experiments. As Py is a low anisotropy material, only two temperature dependent magnetic parameters influence the frequency of the modes: saturation magnetization M_s and exchange stiffness constant A_{ex} . Assuming $A_{\text{ex}} \propto M_s^2$ and a decrease in M_s of 7% upon increasing temperature from 4.2 K to 300 K [81], our micromagnetic simulations predict a frequency shift of $\Delta f \approx -0.20$ GHz for bulk eigenmodes near 5.5 GHz. The 25 Oe increase in applied field for the BLS measurements shifts the bulk eigenmode frequency by $\Delta f \approx +0.15$ GHz. Therefore the temperature-induced decrease of mode frequency is nearly compensated by the field-induced increase of frequency for BLS measurements. Thus we expect the frequencies of the modes measured in our room temperature BLS experiment in Fig. 6.6(b) to be similar to those measured in the microwave emission measurements at 4.2 K in Fig. 6.4(a).

The micromagnetic simulations yield reasonable insight into the observed discrepancies between the spectra for microwave emission and BLS experiments. We find that the two experiments have different sensitivity to different auto-oscillatory modes. The microwave emission measurement is sensitive to phase cancellations and we find that in-phase bulk

modes localized away from the wire center are the dominant source of the generated microwave signal. BLS is sensitive to the number of excited magnons and, therefore, bulk modes excited with large amplitude dominate the BLS signal.

It may come as a surprise that the higher order bulk modes e and f are excited with large amplitude while lower order bulk modes are not. We propose an explanation of this effect via nonlinear mode damping. In our measurements, the external field is applied nearly perpendicular to the nanowire. Therefore, the observed bulk modes arise from geometric confinement of backward volume dipole-exchange modes in a 2D film [53], for which the longest wavelength modes do not have the lowest frequency. In fact, we find that the first few bulk modes are closer to each other in frequency, see inset of Fig. 6.8(b), consistent with a local minima of the dispersion relation at a non-zero wave vector expected for backward volume spin waves. The near degeneracy of these modes enhances coupling among them and thus increases nonlinear damping of each mode [90, 120, 9]. Enhanced nonlinear damping impedes excitation of the auto-oscillations and limits their amplitude [119]. On the other hand, higher order modes have weaker nonlinear damping due to more sparse mode spectrum at higher frequencies; thus, these modes may be easier to excite into the auto-oscillatory regime. A quantitative theory will be necessary to fully explain this effect observed in the numerical simulations.

It is instructive to estimate the characteristic wire width of the 1D to 2D dimensional crossover in our experiments. A rough estimate of the crossover width can be obtained from the backward volume spin wave dispersion relation for a given thickness of the ferromagnetic film [53]. Due to the non-monotonic dependence of the backward volume spin wave frequency on wave number, the uniform $\mathbf{k} = 0$ mode can undergo energy- and momentum-conserving four-magnon scattering into backward volume spin wave modes with a non-zero wave vector \mathbf{k}_4 [53]. In the wire geometry, the backward volume spin wave mode spectrum becomes quantized and the four-magnon scattering channel is suppressed when the width is

reduced below $\sim \pi k_4^{-1}$ [31]. The suppression of such nonlinear magnon scattering processes allows for large amplitude auto-oscillatory modes to be excited and sustained above the critical current. In fact, Duan et al. [31] calculated the dispersion for 5 nm thick Py, like that used in the present study, and found that $\pi k_4^{-1} \approx 0.5 \mu\text{m}$. This is consistent with our data in Fig. 6.4 and Fig. 6.5 showing a strong decrease in the emitted microwave power from bulk modes and multi-mode auto-oscillatory dynamics for wires significantly wider than $0.5 \mu\text{m}$.

As a guiding principle in the design of wire spin torque oscillators, one should aim to suppress the nonlinear magnon scattering channels that lead to enhanced nonlinear damping. Our work demonstrates that reduction of the wire width below a characteristic crossover width is a viable approach to this task. It is clear that the characteristic crossover width increases with increasing exchange and decreases with increasing saturation magnetization. Another interesting approach leading to suppression of nonlinear damping has been recently reported by Divinskiy et al. [28]. In this approach, nonlinear mode coupling and nonlinear damping are suppressed via cancellation of magnetic shape anisotropy in a ferromagnetic film by perpendicular magnetic anisotropy. This cancellation strongly reduces spin wave ellipticity, which results in weak nonlinear damping [25].

Chapter 7

Easy-Plane Spin Hall Oscillator

7.1 Context and Introduction

Efficient electric manipulation of magnetization by spin-orbit torques (SOTs) forms the basis of several promising spintronic technologies such as spin-orbit torque memory (SOT-MRAM) [92, 76, 114], spin-orbit torque oscillators (SOTOs) [76, 111, 54], neuromorphic computing devices [49, 55, 80, 139], and SOT-based magnonic logic [25]. Additionally, SOTOs are a great test bed for fundamental studies of strongly nonlinear magnetization dynamics.

The simplest type of SOTO, known as a spin Hall oscillator (SHO) [26, 31, 47, 123], is based on a bilayer of a ferromagnet (FM) and a non-magnetic heavy metal (HM), as illustrated in Fig. 7.1(a). As discussed in Section 6.1.2, a direct electric charge current in the plane of the HM layer propagating in the x -direction leads to a transverse spin current j_s propagating in the z -direction (grey dashed arrow) with polarization in the y -direction (green spin arrows). The component of the spin Hall current polarization anti-parallel to the equilibrium direction of the FM magnetization M , defined here by external applied magnetic field H applied in $-y$ -direction, exerts a spin torque τ_{st} that counters the Gilbert-like damping τ_g of the FM. Above

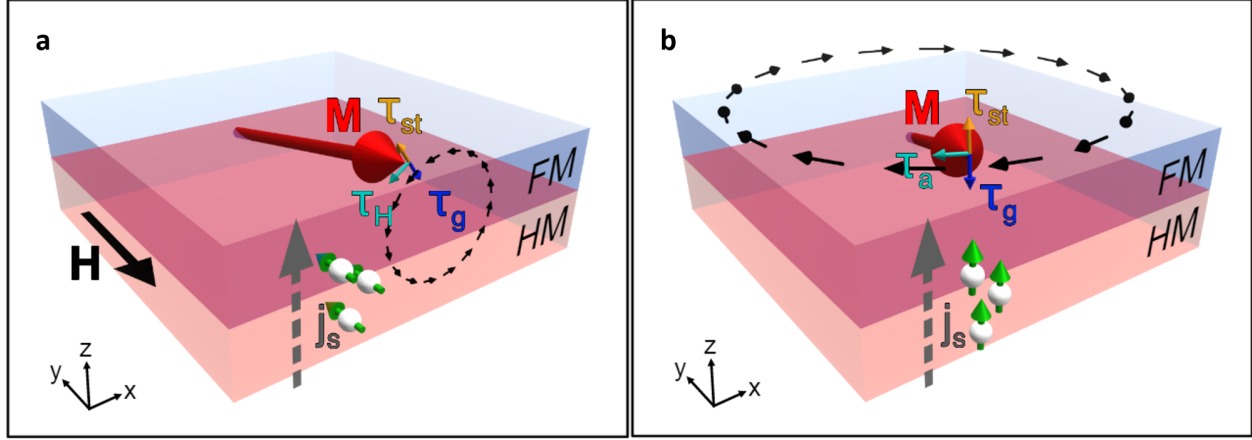


Figure 7.1: **Spin torque oscillator dynamics.** (a) Anti-damping dynamics of a traditional spin Hall oscillator. The spin current j_s (gray dashed arrow) from heavy metal (HM) applies a torque τ_{st} (orange arrow) that compensates the Gilbert damping torque τ_g (dark blue arrow) and drives precessional motion (black dashed arrows) of the FM magnetization \mathbf{M} (red arrow). The spin current is polarized in plane (green arrows) and an external field \mathbf{H} is applied (large black arrow), leading to small angle precessional torque τ_H (turquoise arrow) around the effective field. (b) Easy-plane spin torque oscillator dynamics. Here, FM exhibits natural easy-plane magnetic anisotropy in the FM plane. Perpendicular-to-plane polarized spin current leads to spin torque τ_{st} that pulls \mathbf{M} out of the film plane. The anisotropy field drives a precessional torque τ_a (turquoise arrow) around the film normal, exhibiting large angle dynamics.

a critical current value, τ_{st} overcomes the natural damping τ_g and excites persistent auto-oscillatory magnetization precession (indicated by by small black arrows) due to the torque from the magnetic field τ_H . For currents just above the critical value, a small-amplitude precession around the equilibrium direction of the FM magnetization is excited [119]. The current-driven auto-oscillations of the magnetization generate microwave voltage due to the magnetoresistance of the FM, and thus SHOs are electrically-tunable sources of microwave signals [119].

SHOs generating large-amplitude microwave signals with low phase noise are desired for applications, which can be achieved via excitation of large-amplitude magnetization precession. Large-amplitude dynamics can be efficiently excited in FMs with easy-plane magnetic anisotropy upon injection of spin current polarized normal to the easy-plane [66, 136, 109]. In contrast to the conventional antidamping auto-oscillatory dynamics described in the previous

paragraph, the easy-plane precessional dynamics is excited with large amplitude immediately above the critical current [66]. Figure 7.1(b) illustrates easy-plane dynamics excited by spin torque. Here a natural easy-plane exists in the FM film plane (xy -plane as illustrated). A spin current j_s is injected into FM with polarization in the z -direction (green arrows). The magnetization is forced out of the easy-plane by the spin torque τ_{st} whereupon it precesses with large amplitude driven by the torque τ_a due to the out-of-plane shape anisotropy field [39]. The critical current for these dynamics is defined by the magnitude of a smaller magnetic anisotropy present within the dominant easy-plane anisotropy rather than by the FM Gilbert damping [66, 136, 109].

Exploring a geometry like Figure 7.1(b) has yet to be done in SOT devices like a SHO. Typically the HM/FM bilayer nanowire SHO geometry has the natural easy-plane within the film plane which is not compatible with the spin Hall polarized current to achieve large angle dynamics. In this chapter we present a SHO nanowire where we *engineered* the easy-plane to be along the film normal which enables large angle dynamics and high power output.

7.1.1 Magnetic Anisotropy

If a magnet has a preferred axis to be oriented along when there are no external fields, it has *anisotropy*. Magnetic anisotropy is what breaks the symmetry of magnetization. Generally it can be described as an energy term arising from spin orbit interaction that has a dependence on the direction of the magnetization. There are numerous kinds of magnetic anisotropy such as magnetocrystalline anisotropy (from the crystal unit cell aligning along a direction), shape anisotropy (physical shape), interlayer exchange anisotropy (interfaces of different materials), and magnetoelastic anisotropy (mechanical strain).

Shape Anisotropy

Shape-anisotropy comes from the surface magnetic charges generated from the magnetization pointing normal to the surface. The charges create a dipolar field, called the demagnetization (demag) field, that cancels the internal dipolar fields that originate from the local magnetic moment. In principle, the separation of the surface charges and the saturation magnetization determine the strength of this *demag* field and thus is dependent on the *shape*. The general form of the demag field looks like:

$$\mathbf{H}_{\text{demag}} = -\overleftrightarrow{\mathbf{D}} \cdot \mathbf{M} \quad (7.1)$$

where $\mathbf{H}_{\text{demag}}$ is the demag field vector, $\overleftrightarrow{\mathbf{D}}$ is the *demag tensor* which is determined by the shape of the material, and finally \mathbf{M} is the magnetization. From this the description the demag field becomes maximum along the shortest length, i.e. strongest at the edges and weakest at the center of a ferromagnet. This results in an energy landscape that *usually* prefers \mathbf{M} to be **pointed along the longest axis**.

To break it down further, when considering an *ellipsoid* shape, the demag tensor $\overleftrightarrow{\mathbf{D}}$ becomes symmetric and diagonal in the axes coinciding with the ellipsoid. This yields *demag* factors D_x , D_y , and D_z , which scale depending on the shape of the ellipsoid and are constrained by the sum:

$$D_x + D_y + D_z = 4\pi \quad (7.2)$$

Sometimes the 4π is normalized out and visible in the demag field themselves.

Surface Anisotropy and Perpendicular Magnetic Anisotropy

The surface of a magnetic element will lack atomic bonds or have bonds different from that of the bulk, this will intuitively change the local magnetic energy landscape at the surface and lead to anisotropy. This kind of anisotropy will be more significant the thinner the material is, as its effects do not penetrate that deeply into the bulk. In our case we are particularly interested in an interfacial magnetic anisotropy that favors orientation *out-of-plane*, which is called *perpendicular magnetic anisotropy* (PMA). With the correct material at the surface, the deformation of orbitals leads to enhanced spin orbit interaction, which yields an effective field \mathbf{H}_{SO} that lowers the energy when the magnetization is perpendicular to the surface. With careful control one can create magnetic samples whose PMA is considerably stronger than the in plane shape and crystalline anisotropies. We take advantage of some known materials with strong PMA to help manufacture our perpendicular easy-plane to achieve large angle dynamics.

7.1.2 Sample and Measurement Details

Figure 7.2(a) shows a schematic of the easy-plane spin Hall oscillator (EP-SHO) device along with the coordinate system used in this article. An applied direct electric current flowing in HM Pt along the length of the nanowire (x -direction) leads to a transverse spin Hall current flowing in the z -direction that is polarized in the $-y$ -direction. When injected into the FM, the spin Hall current applies torque to the FM magnetization [11, 121] that can drive auto-oscillatory dynamics [77].

The EP-SHO nanowires studied here were patterned from substrate||seed|HM|FM|cap films deposited by magnetron sputtering. We employed Pt(7 nm) for the HM layer and a [Co(0.98 nm)|Ni(1.46 nm)]₂|Co(0.98 nm) superlattice as the effective FM layer. The Co|Ni superlattice was selected for its large anisotropic magnetoresistance (AMR) [88] and tunabil-

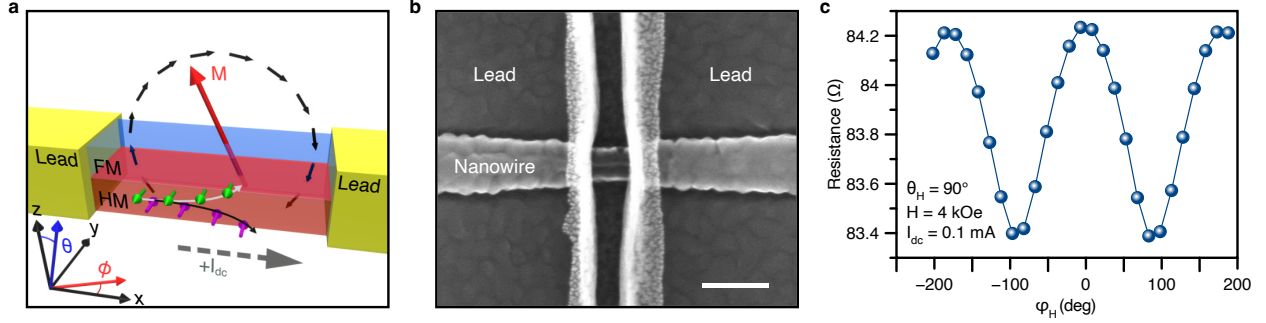


Figure 7.2: **EP-SHO device schematics and magnetoresistance.** Schematic of easy-plane spin Hall oscillator (EP-SHO) that consists of a bilayer of a heavy metal (HM=Pt) and a ferromagnetic metal (FM=Co/Ni superlattice) and coordinate system used in article. Application of positive bias current $+I_{dc}$ (gray dashed arrow) leads to a spin current polarized in the $-y$ -direction (green arrows) impinging on FM which pulls the magnetization vector \mathbf{M} (red arrow) out of the easy xz -plane where it begins to precess about the easy-plane anisotropy field as indicated by black arrows. (b) Scanning electron micrograph of an EP-SHO with 100 nm scale bar. (c) In-plane magnetoresistance of the EP-SHO measured at $T = 4.2$ K with $H = 4.0$ kOe.

ity of perpendicular magnetic anisotropy [5]. Highly resistive Ta is employed for the seed (3 nm) and capping (4 nm) layers [96]. Electron beam lithography and Ar^+ ion milling were used to define 50 nm wide, 40 μm long nanowires from the film stack. Electric leads consisting of Ta(5 nm)|Au(40 nm)|Ta(5 nm) were attached to the nanowire with spacings of 50-450 nm in order to apply electric bias current I_{dc} . The spacing between leads defines the active region of the nanowire where achievable conventional current density j_c in HM can be large enough to create sufficient spin current density j_s to drive auto-oscillations. Figure 7.2(b) shows a scanning electron micrograph of a typical EP-SHO device.

In this study, we explore two distinct types of nanowire auto-oscillatory dynamics: the standard spin Hall oscillator configuration (SHO), as described in Fig. 7.1(a), and our new type of easy-plane spin Hall oscillator (EP-SHO) configuration. In the standard SHO configuration, the auto-oscillatory dynamics are driven by the antidamping spin Hall torque which can compensate the intrinsic magnetic damping of the system. The strength of the antidamping spin Hall torque is proportional to the projection of the spin current polarization and the magnetization vector. In the nanowire geometry, the current flows along the length of the

nanowire and for in-plane field the spin Hall torque is proportional to $\sin(\phi_M)$. For positive applied current, the spin current impinging on the above FM in our structure is polarized in the $-y$ -direction and thus the spin Hall torque is maximized for $\phi_M = 90^\circ$ [58]. This condition is satisfied when moderate magnetic field is applied along the y -axis such that the spin Hall current is polarized opposite to the magnetization. However, the maximum efficiency of converting magnetization oscillations to anisotropic magnetoresistance (AMR) oscillations occurs at $\phi_H = 45^\circ$; therefore, the external field is typically applied between $\phi_H = 45^\circ$ and $\phi_H = 90^\circ$ as a compromise [19]. In the SHO configuration at moderate applied field (compared to y -axis demagnetization field), the magnetization precesses primarily about the applied field.

In the EP-SHO configuration, the energy landscape is dominated by internal fields: shape anisotropy and PMA. The goal is to artificially manufacture an easy-plane in the xz -plane, such that spin Hall current from the Pt underlayer is polarized orthogonal to the easy-plane. In this case, the spin Hall torque pushes the magnetization out of the easy-plane where it precesses about the effective easy-plane field, as shown in Fig. 7.2(a). Shape anisotropy leads to demagnetization fields along the three principle axis: $H_{D_x} = 4\pi D_x M_x$, $H_{D_y} = 4\pi D_y M_y$, and $H_{D_z} = 4\pi D_z M_z$, where D_i are the demagnetization factors and M_i are the magnetization components in the $i = x, y, z$ -directions. The saturation magnetization is $M_s \approx 997 \text{ emu cm}^{-3}$. For our nanowire geometry, analytic solution leads to $D_x = 1.4 \times 10^{-4}$, $D_y = 0.121$, and $D_z = 0.879$. Upon patterning the nanowire, the y -axis becomes a hard magnetic axis with a maximum demagnetization field of $H_{D_y} \approx 1.5 \text{ kOe}$, while the x -axis has a maximum demagnetization field of only a few Oe. The demagnetization field in the perpendicular direction remains quite large, $H_{D_z} \approx 11 \text{ kOe}$. Therefore to achieve near easy- xz -plane, we require a perpendicular anisotropy field of $H_{K_\perp} \approx 11 \text{ kOe}$ to compensate the demagnetization field along the z -axis.

Through film absorption FMR, we characterized film level magnetic anisotropy and choose

stack thicknesses such that the PMA is just under the threshold value that compensates the out of plane demagnetization. We also observe that the PMA increases by 13% when cooled from 295 K to 4.2 K. Upon patterning into nanowires, the devices at 4.2 K have a hard y -axis with an easy- z -axis perturbing the xz easy plane anisotropy. Through localized heating we can then tune the anisotropy until we have full compensation and achieve an easy-plane anisotropy in between. We use Joule heating (originating from the current flow within the nanowire) in this study to tune the PMA.

All device-level measurements in this article are taken from an EP-SHO device with an active region length of $l = 145$ nm that were performed in a continuous flow ^4He cryostat at a bath temperature $T = 4.2$ K. Figure 7.2(c) shows the resistance of the EP-SHO device as a function of in-plane angle ϕ_H ($\theta_H = 90^\circ$) of applied magnetic field $H = 4$ kOe and a small probe current of $I_{\text{dc}} = 0.1$ mA. From measurements of a similar device, we find the magnetoresistance to be due to both AMR and spin Hall magnetoresistance (SMR) [101, 69] with approximately equal contributions.

Microwave Emission

We measured generation of microwave emission signal by the device using a microwave spectrum analyzer [70]. Auto-oscillatory magnetization dynamic states are achieved by applying sufficiently large direct current bias I_{dc} to sample through the DC port of a bias tee. Above a critical current I_c , the spin Hall torque [3] becomes sufficient to excite magnetic self-oscillations. Due to the presence of magnetoresistance in the system, these magnetic self-oscillations convert to resistance oscillations which yields a microwave emission signal $V_{\text{ac}} \sim I_{\text{dc}}\delta R_{\text{ac}}$. The microwave port of the tee was connected to a low noise microwave amplifier with a gain of 45 dB, and the signal was recorded by the spectrum analyzer. All microwave emission experiments were performed in a He flow cryostat at a bath temperature of $T = 4.2$ K.

Standard SHO Microwave Emission

In the standard SHO configuration, we applied a modest in-plane external field ($\theta_H = 90^\circ$) with magnitude $H = 2200$ Oe at an angle of $\phi_H = 68^\circ$.

Easy Plane SHO Microwave Emission

In the easy plane SHO configuration, we measure the same device but only very small external field is applied $H = -140$ Oe at small angle to the x -axis ($\phi_H = 8^\circ$). In the EP-SHO configuration, the energy landscape is dominated by internal fields and shape anisotropy.

7.1.3 Experimental Data

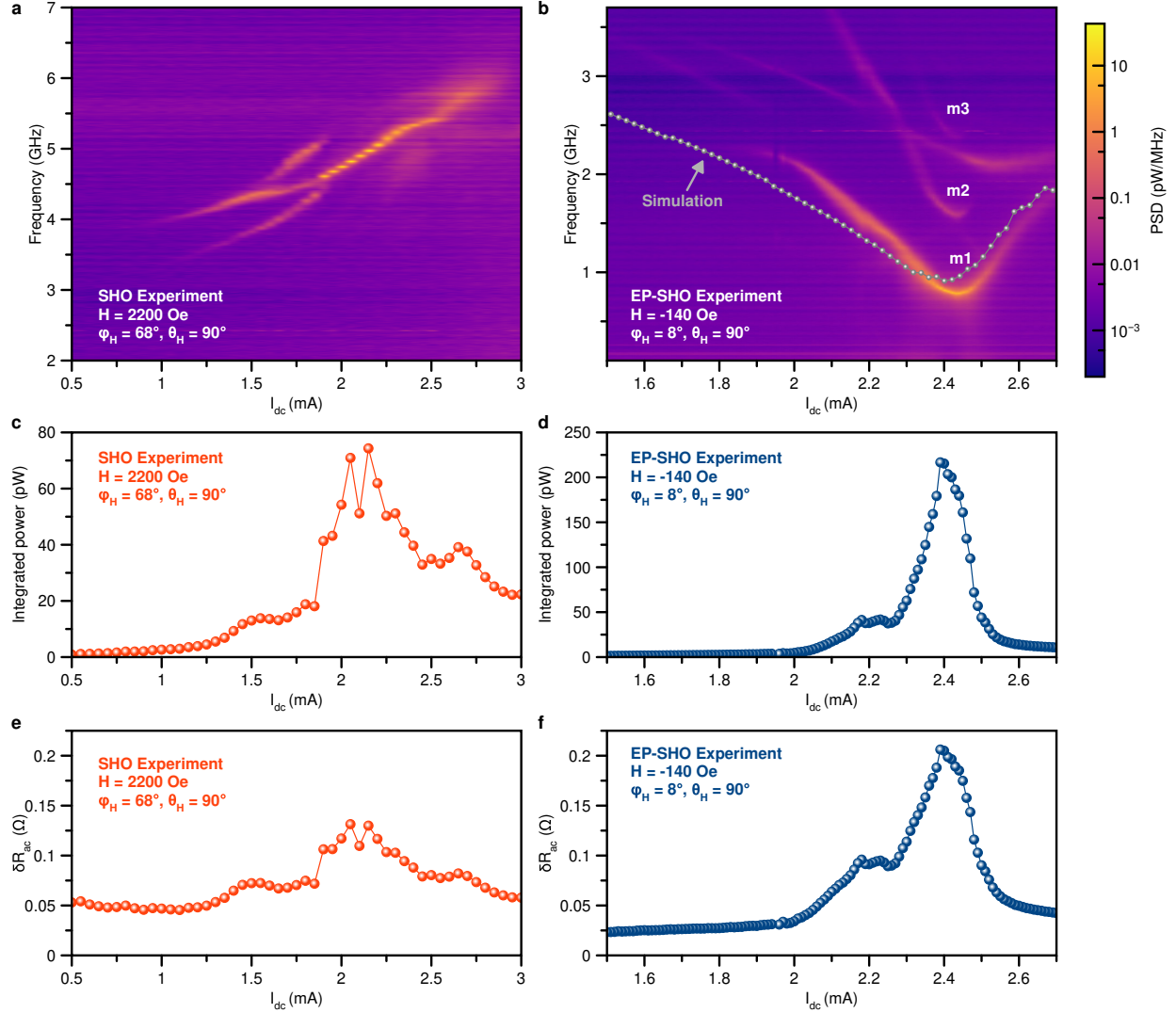


Figure 7.3: **Microwave emission of spin-orbit torque nano-oscillator.** Power spectral density (PSD) of microwave signal generated for the (a) high-field standard-SHO configuration and (b) low-field EP-SHO configuration. Integrated emission power for the (c) standard-SHO and (d) EP-SHO. Power quoted is power available to a 50Ω load. Estimated amplitude of magnetoresistance oscillations for the (e) standard-SHO and (f) EP-SHO.

Standard SHO Emission Data

Figure 7.3(a) shows measured power spectral density (PSD) in the SHO configuration as a function of I_{dc} . The auto-oscillatory state is induced beginning near $I_{dc} = 1$ mA. The frequency of microwave emission is blue-shifted with increasing I_{dc} . We attribute this behavior to the predominantly easy-plane anisotropy with its plane perpendicular to the applied field direction [71]. Figure 7.3(c) shows the total integrated power generated by the auto-oscillatory modes as a function of I_{dc} . The power output is non-monotonic and peaks at $P = 74$ pW near $I_{dc} \approx 2.15$ mA. Note that powers P are quoted as available to a standard 50Ω load [105].

EP-SHO Emission Data

Figure 7.3(b) shows measured PSD in the EP-SHO configuration as a function of I_{dc} . A low frequency mode labelled m1 begins to be excited near $I_{dc} = 2$ mA at a frequency of $f = 2.2$ GHz. In contrast to the standard-SHO, the frequency of emission is at first red-shifted with increasing I_{dc} until $I_{dc} \approx 2.44$ mA, where the output frequency reaches a minimum frequency $f = 0.78$ GHz. Then with further increasing I_{dc} , the emission frequency is blue-shifted. Figure 7.3(d) shows the total integrated power of the EP-SHO as a function of I_{dc} . Again, we observe a non-monotonic dependence of microwave emission power; however, we find that the maximum integrated power of 217 pW occurs at $I_{dc} = 2.39$ mA, near the frequency minimum. We also observe 2nd and 3rd order harmonics of mode m1, labelled as m2 and m3 in Fig. 7.3(b). Another higher order mode can be observed between m2 and m3.

We attribute the EP-SHO frequency dependence on I_{dc} to the tuning of the internal PMA field by Joule heating which alters the energy landscape in the xz -plane as shown in Fig. 7.4. With increasing temperature, the interfacial perpendicular anisotropy is reduced. For $I_{dc} <$

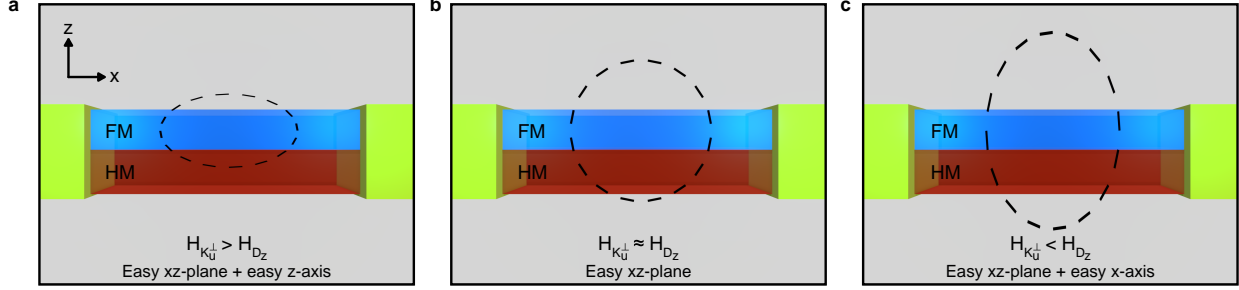


Figure 7.4: **Cartoon of xz -plane energy landscape.** Figures show xz -plane side profile of nanowire device. Dashed ellipsoids indicate energy in the xz -plane (a) When the perpendicular anisotropy field $H_{K_{\perp}}$ is larger than the demagnetization field H_{D_z} , the z -axis is lower energy than the x -axis and the system can be thought of as easy xz -plane + easy z -axis. (b) When $H_{K_{\perp}} \approx H_{D_z}$, the system has nearly easy xz -plane. (c) For $H_{K_{\perp}} < H_{D_z}$, the x -axis is lower energy than the z -axis. The system can be interpreted as easy xz -plane + easy x -axis.

2.4 mA, the perpendicular anisotropy field dominates the z -axis demagnetization field $H_{K_{\perp}} > H_{D_z}$ and the energy landscape can be thought of as easy- xz -plane + easy z -axis, as shown in Fig. 7.4(a). For $I_{dc} > 2.5$ mA the reduced perpendicular anisotropy field can no longer compensate H_{D_z} , and the energy landscape becomes easy- xz -plane + easy x -axis, as shown in Fig. 7.4(c). In between, the energy landscape transitions from easy xz -plane + easy z -axis \Rightarrow easy- xz -plane \Rightarrow easy- xz -plane + easy x -axis with increasing temperature. The easy xz -plane as shown in Fig. 7.4(b), is achieved when $H_{K_{\perp}} \approx H_{D_z}$. We find that the power emitted in the region near balanced easy-plane anisotropy is significantly enhanced compared to the standard-SHO configuration, with the EP-SHO outputting a maximum power of $P = 217$ pW to the standard-SHO maximum of $P = 74$ pW.

The estimated amplitude of magnetoresistance self-oscillations δR_{ac} are shown in Figs. 7.3 (e) and (f) for the standard-SHO and EP-SHO respectively. We estimate the amplitude using the relation [31],

$$\delta R_{ac} = \frac{R(I_{dc}) + R_{50}}{|I_{dc}|} \left(\frac{2P}{R_{50}} \right)^{\frac{1}{2}}, \quad (7.3)$$

where $R_{50} = 50 \Omega$ and $R(I_{dc})$ is the resistance of the nanowire at current I_{dc} .

7.2 Micromagnetic Simulations

Like in Chapter 6 we aim to use simulations to gain insight on the micromagnetic dynamics in our physical system. Thanks to access to new, faster resources (like UCI's High Performance Community Computing Cluster a.k.a. HPC3) we utilized MuMax3 this time around, which is a Graphics Processing Unit (GPU) based simulation software (OOMMF is Central Processing Unit (CPU) based). This allows for utilizing parallel computation which considerably speeds up simulation calculation time. Furthermore, by having access to multiple GPU's on the cluster, one can vary simulation parameters and run them in parallel. In this study, the theory already tells us what dynamics should be going on (the out of plane large angle oscillations along the *easy-plane*), so our motivation is to confirm whether the dynamics we expect are indeed happening (and why or why not).

7.2.1 Simulation Software and Parameters

Our simulations are carried out in Mumax3 [131] at zero temperature ($T = 0$ K) with experimentally determined material parameters: saturation magnetization $M_s = 997 \text{ emu cm}^{-3}$, Gilbert damping $\alpha = 0.027$, and Landé g-factor $g = 2.18$. We assume an exchange constant $A_{\text{ex}} = 1 \times 10^{-6} \text{ erg/cm}$.

The simulation geometry consists of $4 \mu\text{m}$ total length wire of 50 nm width with active region of 145 nm and thickness of 5.85 nm . The micromagnetic system is composed of $2048 \times 16 \times 1$ cells, yielding cell sizes of $1.95 \times 3.13 \times 5.85 \text{ nm}^3$. At the lengthwise ends of the wire we have implemented absorbing boundary conditions via ramping up the damping parameter. We conducted preliminary relaxation simulations with varying $K_{u,s}^{\perp}$ to determine the value

in which the nanowire easy axis transitions to out of plane. We found that the relaxed magnetization of the entire nanowire undergoes transition from in plane to out of plane from 2.895 to 3.050 erg/cm², which agreed well with our experimental results. The perpendicular magnetic anisotropy outside and within the active region at zero bias current is set to be $K_{u,s}^\perp = 3.4$ erg/cm², resulting in an easy- z -axis similar to the experiment. We study current driven auto-oscillations via application of spin Hall torque to the active region of the SHO device. The spin torque resulting from the charge current flowing in the heavy metal Pt layer is calculated using the Slonczewski spin torque solver available within the Mumax3 software. Note that like in Section 6.4.1, the Pt layer is not explicitly involved in the simulation. Since Pt is non-magnetic, it has little effect on the magnetization dynamics of the system, only it's current carrying effects are involved via the Oersted field and Slonczewski spin torque. The spin Hall torque is calculated with fixed spin Hall angle $\theta_{\text{SH}} = 0.07$ and estimated fractional current density flowing in Pt.

We account for current induced effects of Oersted field and Joule heating. The Oersted field is parallel to the $-y$ axis and scales with the nominal charge current. The Oersted field present in the FM layer is calculated by treating the charge current density in the Pt underlayer as a thin ribbon which is described by [45],

$$H_{Oe}(z) = -\frac{\mu J z}{2\pi|z|} \left[\tan^{-1} \left(\frac{w/2}{|z|} \right) + \tan^{-1} \left(\frac{w/2}{|z|} \right) \right] \quad (7.4)$$

where H_{Oe} is the total Oersted field generated in the y direction from the current density J at a vertical distance z from the ribbon of width w . We determined the Oersted field to scale as 0.00478 Oe per A/m. From the temperature dependent anisotropy and resistivity data we determined that $K_{u,s}^\perp$ shifts by -0.1438 erg/cm² per mA for applied bias current in the vicinity of achieving the magnetic easy-plane anisotropy. Stepping the nominal charge current in turn varies $K_{u,s}^\perp$ and Oersted field of the system within the active region. As mentioned, we fix $K_{u,s}^\perp = 3.4$ erg/cm² in the wire outside of the active region, resulting in

an easy z -axis perturbing the easy- xy -plane as in the experiment. The combination of the Oersted field and shifting $K_{u,s}^\perp$ in the active region creates a magnetic potential well for spin waves, resulting in the localization of auto-oscillations inside the active region.

7.2.2 Simulation Execution and Analysis

The standard-SHO simulation has in-plane external field applied $H = 2200$ Oe at angles of $\phi_H = 68^\circ$ and $\theta_H = 89.9^\circ$, where we have tilted the external field slightly out of plane to break symmetry in the simulation. The system is initialized to uniform magnetization along ϕ_H and relaxed to minimum energy prior to turning on the spin Hall torque. We conducted a series of simulations with stepped nominal charge current from 0.5 mA to 3.0 mA. We allow the system to evolve for 200 ns to achieve quasi-steady state dynamics. We use the x and y components of magnetization (averaged over the cells in the active region) to calculate the resistance,

$$R_{ac}(t) = \Delta R_{MR} (\langle m_x(t) \rangle^2 - \langle m_y(t) \rangle^2), \quad (7.5)$$

where $\Delta R_{MR} = 0.4 \Omega$ is the experimentally determined magnetoresistance (we assume AMR and SMR contribute equally to the varying resistance). We take the fast Fourier transform (FFT) of ΔR_{MR} in order to study the auto-oscillatory modes at each current. The EP-SHO simulation has in-plane external field applied $H = -140$ Oe nearly along the x -axis ($\phi_H = 8^\circ$, $\theta_H = 89.9^\circ$). Here we also include a small out of plane component to break symmetry. The system similarly is initialized to uniform magnetization along ϕ_H and relaxed prior to turning on the spin Hall torque. We observed that at some fixed currents the system will switch from large angle dynamic state to static state equilibrium (shown in 7.5). This warrants using time domain analysis of the dynamic state resistance oscillations as opposed to FFT like in the standard-SHO configuration. We also intentionally include the temporal

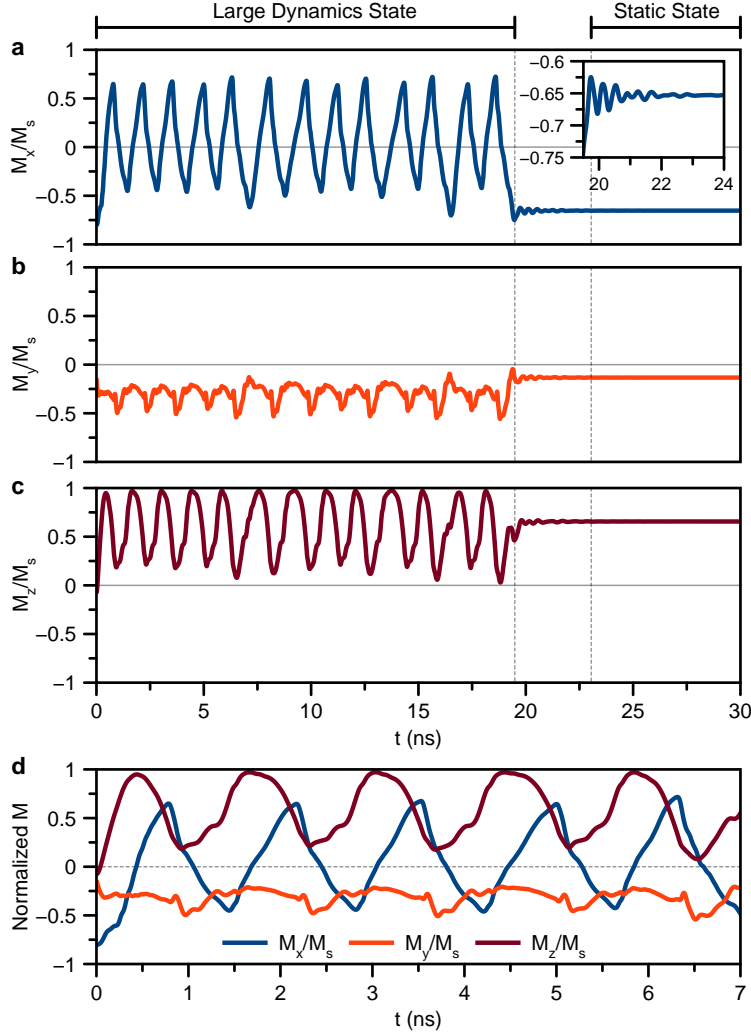


Figure 7.5: **Dynamic to static state transition in simulations of EP-SHO configuration.** Normalized, averaged components (a) m_x , (b) m_y , and (c) m_z of EP-SHO configuration in time domain at $I_{dc} = 2.484\text{mA}$. We observe the large angle dynamics leading up to 20 ns, which then rings down towards static equilibrium. (b) All components are overlaid to showcase their relative dynamics over a shorter time scale.

transient regime in order to capture the shifting frequency modes with increasing current.

The system is evolved for 75 ns. In both simulations, we extracted the average amplitude of resistance oscillations of ΔR_{MR} , which yields the effective power output at each set current.

In this study, it was especially useful to see the dynamics in actual motion. So a video of the averaged magnetization within the active region, with all planar projections simultaneously plotted, was generated from $\mathbf{m}(t)$ fed via Python scripting into Blender. The scripts

themselves will be included in the appendix. Some adjustments may be required for it to operate correctly depending on the computer and Blender version.

7.3 Simulation Results

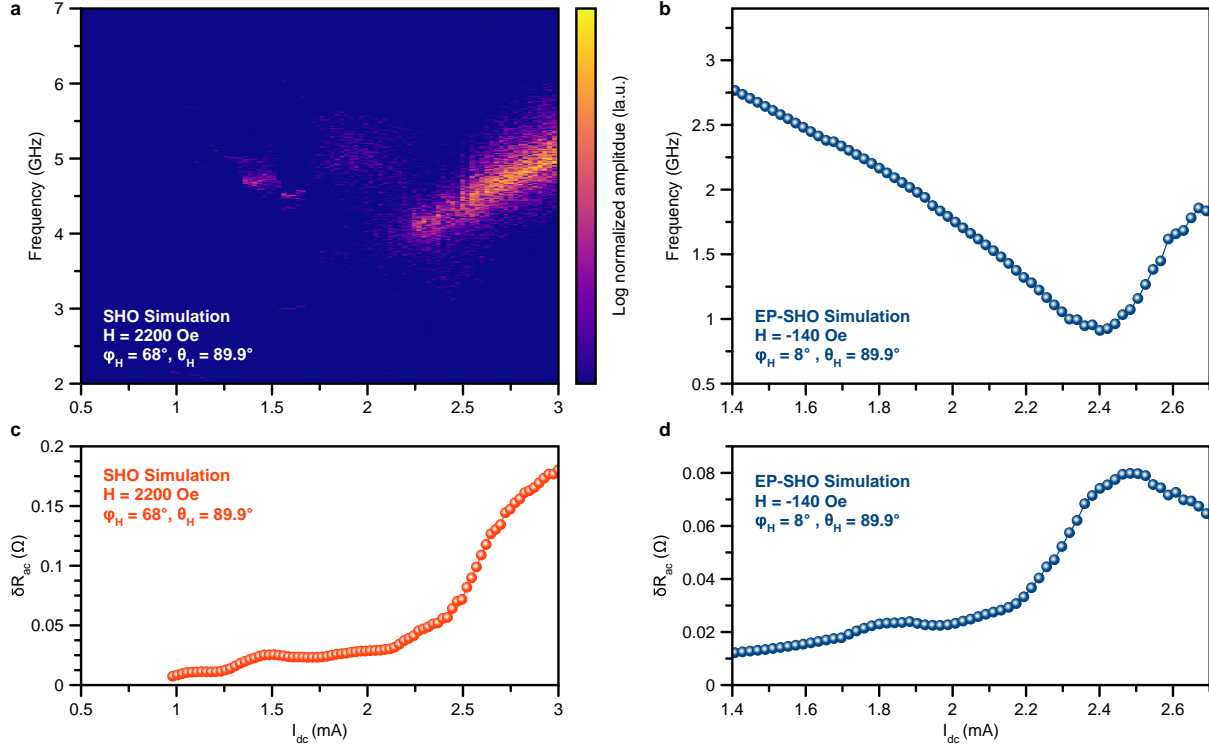


Figure 7.6: **Micromagnetic simulation of spin-orbit torque nano-oscillator.** Figures show analysis of micromagnetic simulation data of resistance auto oscillations at each current (a) for high field standard-SHO configuration (via FFT) (b) for low field EP-SHO configuration (via time domain analysis). Calculated amplitudes of resistance oscillations for (c) high field standard-SHO and (d) low field EP-SHO.

Figure 7.6(a) shows the spectra of auto-oscillatory dynamics calculated via FFT of $R_{ac}(t)$ and highlights the emergence of auto-oscillatory modes above 1.5 mA which then begin to rapidly grow in intensity around 2.0 mA. We also see a consistent blue shifting (increasing frequency) of the main auto oscillatory mode starting from 3.5 GHz at 2.0 mA to 5.0 GHz at 3.0 mA. Figure 7.6(c) shows the average amplitude of resistance oscillations at each current and shows the effective power output of the simulated spin Hall oscillator. Below 1 mA the

oscillation amplitudes were negligible and thus were omitted.

Figure 7.6(b) shows the oscillation frequency determined from the dynamic state at each current. The figure highlights the transition of the nanowire easy axis from $+z$ (red shifting) to $+x$ (blue shifting), where the lowest frequency is when the energy landscape is balanced between the two axes and the system becomes an easy plane oscillator. Figure 7.6(d) shows the average resistance oscillation amplitude determined from the same data.

We observe that in fact the power output is at a maximum near the point where frequency is lowest, indicating that the precession amplitude of the auto oscillation increases as it approaches the easy plane configuration (lower frequency and higher resistance oscillations) and then decreases once again as it goes towards the $+x$ easy axis (higher frequency and smaller resistance oscillations).

Figure 7.7(a)-(c) show snapshots of the magnetization dynamics. Figure 7.7(a) shows the active region at $t = 20.18$ ns after application of spin Hall torque; the magnetization in the active region points predominantly in the $+z$ -direction. The bulk magnetization precesses from here towards the $+x$ -direction, as shown in Fig. 7.7(b) at $t = 20.69$ ns. Instead of precessing from here towards the $-z$ -direction, the magnetization rotates towards the $-y$ -direction, as shown in Fig. 7.7(c) at $t = 20.93$ ns. From here, the magnetization precesses towards the $-x$ -direction before returning to the $+z$ -direction, completing one period of oscillation. Figure 7.7(d) shows a snapshot of the path traced by the averaged magnetization vector with its plane projections for two complete periods. In Fig. 7.7(d), we see the expected large cone angle dynamics emerging from the easy-plane configuration. Furthermore the plane projections in the video reveal (the red and green projections in Fig. 7.7) that the dynamics are confined in the $+z$ half planes. This departure from our cartoon description is due to the area outside of the active region remaining in the $+z$ direction, which through

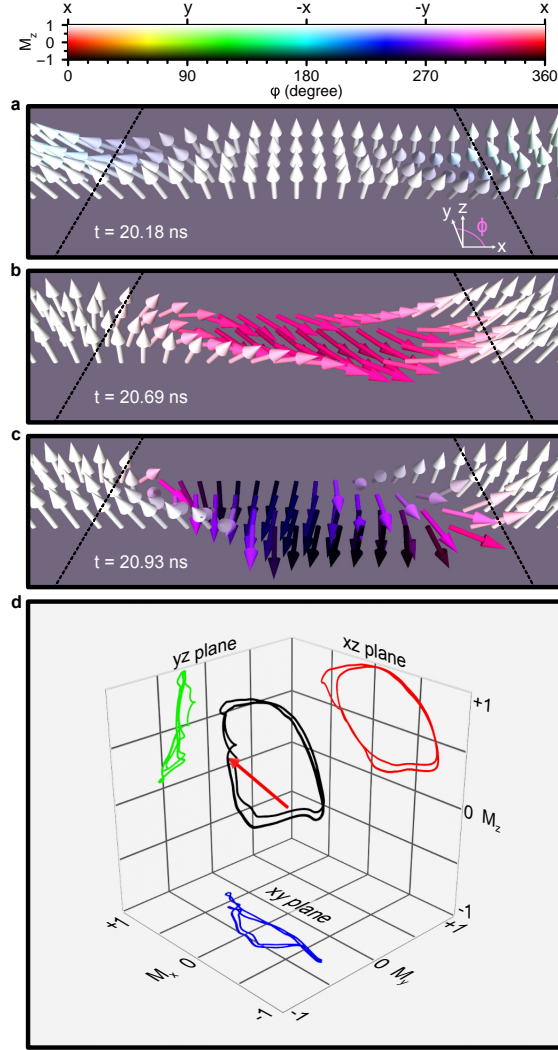


Figure 7.7: **Micromagnetic snapshots of EP-SHO auto oscillations at $I_{dc} = 2.44$ mA** Configuration of subsampled individual micromagnetic cells when the averaged M is: (a) mostly in $+z$, (b) mostly in $+x$, (c) and mostly in plane and $-y$. Black dashed lines indicate boundary of the active region. (d) Average magnetization of active region traced over two periods of oscillation.

dipolar interactions apply an energy pressure to the active region.

7.4 Discussion

We observe experimentally that the EP-SHO configuration yields almost $3\times$ larger power output than the standard SHO configuration in the same device. We find qualitative and

quantitative agreement between the EP-SHO experimental results and simulations. The frequency dependence of emission from the simulations (Fig. 7.6(b)) is overlaid on the experimental results in Fig. 7.3 (b). The emission frequency in both experiment and simulations follows the same red-shift \Rightarrow minimum \Rightarrow blue-shift dependence with increase bias current. The simulations confirm that this frequency dependence is due to the transition from easy- xz -plane + easy- z -axis to easy- xz -plane to easy- xz -plane + easy- x -axis. The resistance oscillations δR_{ac} also show a similar dependence on I_{dc} , with a maximum value achieved near the easy-plane conditions in both experiment and simulations. The maximum emitted power in the EP-SHO is observed when the red shifting approaches its maximum, i.e., the Joule heating from the direct current has reduced the PMA such that the easy-plane energy landscape is achieved. We therefore conclude that the maximum output power is reached when the artificial easy-plane magnetic anisotropy conditions are satisfied.

We find qualitative agreement between the standard-SHO experimental results and simulations. In both cases, the frequency of the dominant emission mode is only blue-shifted with increasing I_{dc} . However, the frequency in the simulation is always lower than in the experiment. The difference in frequency may be due to magnetic edge dilution of the physical nanowire from the nanofabrication process which reduces the demagnetization along the y -axis [89, 31], leading to higher emission frequency in the experiment. In the simulations, δR_{ac}^{sim} generally increases with increasing I_{dc} , whereas in the experiment δR_{ac}^{exp} increases with increasing current bias for $I_{dc} < 2.15$ mA and then upon further increase in I_{dc} the amplitude of oscillation significantly decreases. The experimentally observed dependence is consistent with previous spin-orbit torque oscillator studies [77, 19]. The decrease in oscillation amplitude can be explained by an enhanced thermal magnon population due to high current densities and Joule heating that results in strong nonlinear magnon scattering [24]. The simulations do not account for thermally excited magnons and thus the oscillation amplitude continues to increase. It is important to stress that, in this case, the zero temperature simulations increasingly deviate from reality with increasing bias current as thermal

magnons begin to dominate the dynamics; in reality, one cannot simply keep increasing the bias current to reach larger emission power in real spin Hall oscillator devices. This in stark contrast to the simulations for the EP-SHO, where the oscillation amplitude peaks when the artificial easy-plane anisotropy is achieved and reduction of amplitude is due to tuning away from easy-plane anisotropy. In other words, the zero temperature simulations capture the EP-SHO behavior which indicates the EP-SHO is more robust to parasitic mode conversion by scattering into thermal magnons.

It is interesting that scattering to thermal magnons does not impact the EP-SHO very much, especially compared to the standard-SHO. It has been demonstrated that nonlinear magnon scattering in standard-SHOs increases with increasing ellipticity of the modes [28]. The EP-SHO supports only the large-amplitude mode that cannot be described as a linear spin wave mode. Our experimental results indicate that the nonlinear magnon scattering of this large-amplitude mode is rather small.

Other pathways have been explored to enhance the microwave power output from spin torque and spin Hall oscillator output that fall broadly into two approaches: (i) increase conversion efficiency of magnetic oscillations into electric microwave signals and (ii) increase the amplitude of self-oscillations of magnetization. An approach to increase the conversion efficiency of magnetic oscillations into electric microwave signals is to add additional layers to the structure to enhance its magnetoresistance and thus increase the microwave output power. One example is to use a 3-terminal device, where an MTJ is embedded on the spin Hall material [77, 64]. The spin Hall torque is generated by passing current-in-plane through the spin Hall material. Rather than using anisotropic magnetoresistance, current is passed perpendicular-to-plane to make use of the much larger tunneling magnetoresistance to convert magnetization self-oscillation to microwave voltage. Another approach recently demonstrated involves adding a non-magnetic metallic spacer and second fixed ferromagnetic layer to the simple bilayer nanowire structure in order to use current-in-plane giant

magnetoresistance to enhance power output in a 2-terminal device [19]. Here it was shown that further enhancement was made by matching the symmetry of the spin Hall torque to the symmetry of giant magnetoresistance.

Our EP-SHO aims to increase the amplitude of self-oscillation. In fact, perfect easy-plane oscillations would maximize this amplitude. A common method of increasing the amplitude of magnetic oscillations is vortex oscillators driven by spin transfer torque; however, spin Hall driven vortex oscillators have not been realized due to wrong direction of the current polarization for a vortex in the film plane. At zero temperature, the amplitude of self oscillations for the standard SHO monotonically increases with increasing bias current. However, as described above, due to Joule heating the amplitude of the lowest energy mode is diminished by scattering into thermal magnon modes at large bias currents. Recently, a spin Hall oscillator system based on Pt|Co|Ni structures was used to control nonlinear magnetic damping in spin Hall nano-devices [28]. It was demonstrated in extended disc spin Hall devices ($0.5 \mu\text{m}$ diameter) that nonlinear damping at finite temperature due to non-resonant parametric pumping into thermal magnon modes was efficiently suppressed by minimizing the ellipticity of magnetization precession. Similar to our work, this was achieved by balancing perpendicular-to-plane dipolar shape anisotropy with the perpendicular magnetic anisotropy; however, the extended disc geometry does not support the artificial easy-plane demonstrated in our work.

In conclusion, our experiments and micromagnetic simulations demonstrate that large cone angle magnetization precession is supported in nanowire spin Hall oscillators with artificial easy-plane anisotropy. By balancing dipolar shape anisotropy and perpendicular-magnetic-anisotropy, we can create an artificial easy-plane that is orthogonal to the spin Hall polarization, thus maximizing spin Hall torque. Furthermore, we demonstrate that the easy-plane anisotropy is tunable by electric current and that maximum microwave emission power occurs near the easy-plane conditions.

Chapter 8

Spin Wave Field Effect Transistor

8.1 Context and Introduction

Spin waves are an excellent candidate for low energy information transport in an integrated chip setting [68, 34]. There have been numerous experimental realizations of using magnons as a means of encoding information and logic operations [67, 40, 134, 22, 23, 73, 75, 21]. One of the main challenges however is the energy-efficient manipulation of magnons. In this study we realize a nanoscale spin wave field effect transistor (SW-FET) where we use a gate voltage to modulate the local magnetic anisotropy [87, 43, 102, 143] and thus modulate the amplitude of spin waves propagating between the source and drain of a nanowire spin wave channel.

8.1.1 Voltage Controlled Magnetic Anisotropy

Since magnetic anisotropy was already covered in Section 7.1.1, this section will focus on a method of modulating magnetic anisotropy through application of voltage at the interface.

This is an interfacial magneto-electric effect called voltage controlled magnetic anisotropy (VCMA). The effect originates from the modulation of the filling rates of d-shell electron bands at an interface in response to an electric field applied perpendicular to the surface. Specifically in a Fe/MgO interface, the perpendicular electric field yields a change to the uniaxial PMA at the interface.

To elaborate more on the microscopic origin, at the interface between Fe and an oxide, the $2p_z$ -orbitals of the O atoms bond strongly with the $3d_z^2$ -orbitals in Fe resulting in enhanced PMA (can think of the orbital deforming to favor out of plane magnetization). When electric field is applied at the FM/oxide interface, the number of electrons in the out of plane $3d$ -orbitals of Fe is changed with respect to the in plane orbitals, which then affects the bonding strength between $3d$ - and $2p$ -orbitals which results in a change in the PMA. The modulation of the filling of these orbitals either weakens or strengthens the effective field at the surface and thus modulates the local magnetic anisotropy. Since this is an interfacial effect, it naturally is only significant for ultra-thin FM/oxide systems (on the order of nm thick FMs).

For the sake of mathematical clarity, VCMA manifests as an anisotropy term in the effective field of LLG:

$$\epsilon = K_{u1} \sin^2(\theta) = K_{u1}(1 - (\mathbf{m} \cdot \mathbf{u})^2) \quad (8.1)$$

where K_{u1} is the uniaxial anisotropy constant, $\mathbf{m} = \mathbf{M}/M_s$ is the normalized magnetization, and \mathbf{u} is the symmetry axis of the uniaxial anisotropy.

The effective field due to VCMA then becomes:

$$\mathbf{H}_{\text{VCMA}} = -\frac{1}{M_s} \frac{\partial \epsilon}{\partial \mathbf{m}} = \frac{2K_{u1}}{M_s} (\mathbf{m} \cdot \mathbf{u}) \mathbf{u} \quad (8.2)$$

$$K_{u1} = K_0 + \beta E \quad (8.3)$$

Where β is the VCMA coefficient that relates how much the anisotropy shifts with electric field [107].

8.1.2 Anomalous Hall Effect

The anomalous hall effect (AHE) describes when a transverse charge current is generated from flowing charge through a ferromagnetic metal (FM) wire. The contributors to this effect are quite similar to those of the spin Hall effect (Section 6.1.2): skew scattering and side-jump. The difference here is that in a FM the flow of up spins and down spins will be imbalanced which then results in a net accumulation of transverse charge.

The skew-scattering contribution for transverse conductivity $\sigma_{AH} = j_{cy}/E_x$:

$$\sigma_{AH}^{SS} = -(2\pi/3) \left[\left(\frac{n_{\uparrow} - n_{\downarrow}}{n_{\uparrow} + n_{\downarrow}} \right) + \left(\frac{\sigma_{\uparrow} - \sigma_{\downarrow}}{\sigma_{\uparrow} + \sigma_{\downarrow}} \right) \right] \bar{\eta}_{SO} u_{imp} N_{eff}(0) \sigma_{xx} \quad (8.4)$$

where $N_{eff}(0) = (m/4\pi^2\hbar^2)(k_F^{\uparrow 3} + k_F^{\downarrow 3})/\bar{k}_F^2$ is the effective density of states and

$\bar{k}_F = (k_F^{\uparrow} + k_F^{\downarrow})/2$, this contribution depends on the spin polarizations of electron density and electrical conductivity. Whereas the side jump contribution is:

$$\sigma_{AH}^{SJ} = \frac{e^2}{\hbar} \eta_{SO} n_e \left(\frac{n_{\uparrow} - n_{\downarrow}}{n_{\uparrow} + n_{\downarrow}} \right) \quad (8.5)$$

where $n_e = n_{\uparrow} + n_{\downarrow}$. It is important to note that since magnetization $M_z = \mu_B(n_{\uparrow} - n_{\downarrow})$, the side jump contribution scales with M_z , $\sigma_{AH}^{SJ} \propto M_z$. So dynamics like spin waves where the average M_z has changed should result in an observable change in transverse voltage [1].

8.2 Sample and Measurement Details

The nanowire devices are made from a:

(substrate) | Ta(5 nm) | $\text{Co}_{45}\text{Fe}_{35}\text{B}_{20}$ (1.2 nm) | MgO(2 nm) | TaO_x (3 nm)

multilayer deposited by magnetron sputtering onto thermally oxidized Si substrate, where TaO_x (3 nm) is a 3 nm thick Ta film naturally oxidized in air. Using e-beam lithography and ion mill etching, the multilayer is patterned into a nanoscale Hall bar schematically shown in Fig. 8.1(a) along with Cartesian coordinate system employed in this report. The Hall bar consists of the magnetic multilayer patterned into a nanowire with four non-magnetic voltage leads (labeled 1 through 4) formed by the Ta bottom layer. An AlO_x |Au top gate labeled 5 is placed atop the central section of the Hall bar, where the AlO_x dielectric layer is used to ensure zero leakage current between the Au gate metal and the $\text{Co}_{45}\text{Fe}_{35}\text{B}_{20}$ nanowire. We fabricated and tested devices with the $\text{Co}_{45}\text{Fe}_{35}\text{B}_{20}$ nanowire width w_n ranging from 50 nm to 70 nm, gate width w_g from 200 nm to 600 nm and separation between two Hall crosses w_s from 200 nm to 600 nm as shown in Fig. 8.1(a). Fig. 8.1(b) shows scanning electron micrograph (SEM) of a SW-FET device with $w_n = 50$ nm, $w_g = 200$ nm and $w_s = 400$ nm.

8.2.1 Hysteresis Loop With Out of Plane Field

We characterize magnetic state of the $\text{Co}_{45}\text{Fe}_{35}\text{B}_{20}$ nanowire via AHE measurements. For these measurements, we apply a direct bias current $I_{\text{dc}} = 40 \mu\text{A}$ to the nanowire between leads 6 and 7 and measure Hall voltage V_{xy} between leads 1 and 2 as illustrated in Fig. 8.1(a). All measurements in this study are made at room temperature ($T = 295$ K).

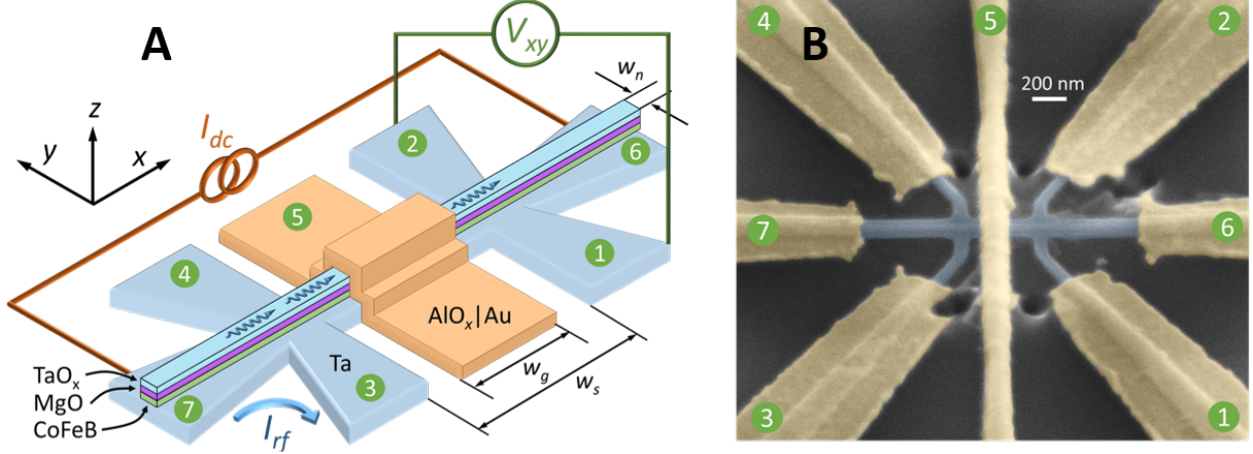


Figure 8.1: **Spin wave field effect transistor.** (A) Schematic of spin wave field effect transistor (SW-FET). The device consists of a $\text{Co}_{45}\text{Fe}_{35}\text{B}_{20} | \text{MgO} | \text{TaO}_x$ nanowire of width w_n on top of a nanoscale Ta Hall bar. Radio frequency current I_{rf} flowing between leads 3 and 7 applies spin-orbit torque to the $\text{Co}_{45}\text{Fe}_{35}\text{B}_{20}$ magnetization and excites spin waves in the left cross of the bar (SW-FET source). Spin waves propagating under the gate of width w_g are detected at the right cross (SW-FET drain) via variation of anomalous Hall voltage V_{xy} measured between leads 1 and 2. Direct current I_{dc} is applied to the wire between leads 6 and 7 to generate V_{xy} . Application of gate voltage V_g to the $\text{AlO}_x | \text{Au}$ top gate 5 modifies magnetic anisotropy of $\text{Co}_{45}\text{Fe}_{35}\text{B}_{20}$ under the gate and thereby controls the amplitude of spin waves propagating distance w_s between the source and drain. (B) SEM image of a SW-FET device with $w_n = 50$ nm, $w_g = 200$ nm and $w_s = 400$ nm.

8.2.2 Electrically Detected FMR

We characterize the spectrum of low-frequency spin waves in SW-FET devices by using electrically detected ferromagnetic resonance (FMR). For these measurements, a radio frequency (RF) current I_{rf} and direct bias current I_{dc} are applied between leads 6 and 7. A fraction of I_{rf} flows in the Ta layer and applies RF spin-orbit torque (SOT) to magnetization of the $\text{Co}_{45}\text{Fe}_{35}\text{B}_{20}$ nanowire. This spatially uniform SOT drive efficiently couples to spin wave eigenmodes with zero wave vector (quasi-uniform) along the wire ($k_x = 0$) and leads to resonant spin wave excitation when the frequency of the RF drive f coincides with the frequency of a $k_x = 0$ eigenmode of the $\text{Co}_{45}\text{Fe}_{35}\text{B}_{20}$ nanowire. Excitation of spin waves reduces time-averaged $|M_z|$ and thereby decreases $|V_{xy}|$, leading to a series of resonances in $V_{xy}(f)$ at spin wave eigenfrequencies. To increase sensitivity of this method, we pulse-modulate the

amplitude of I_{rf} and measure the resulting variation of anomalous Hall voltage ΔV_{xy} at the modulation frequency using lock-in detection.

8.2.3 Electrically Detected Propagating SW Spectroscopy

We next employ electrically detected propagating spin wave spectroscopy to study spin wave transport between two Hall crosses of the device. In these measurements, spin waves are excited at one cross of the Hall bar using giant spin Hall torque of Ta [76] and their arrival to the other cross is detected via AHE. As illustrated in Fig. 8.1(a), we excite spin waves at the left Hall cross by applying RF current I_{rf} between leads 3 and 7. These spin waves propagate in the $\text{Co}_{45}\text{Fe}_{35}\text{B}_{20}$ nanowire under the gate and arrive to the right Hall cross where they are detected via measurement of ΔV_{xy} between leads 1 and 2. Arrival of spin waves to the right Hall cross reduces time-averaged $|M_z|$ at the cross and thereby results in a decrease of $|V_{\text{xy}}|$. Measurements of ΔV_{xy} as a function of the RF drive frequency and direct voltage V_g applied to the gate lead 5 let us determine the frequency of spin waves that propagate under the gate and the effect of V_g on the amplitude of these waves.

8.3 Experimental Data

8.3.1 Hysteresis Loop Data

Fig. 8.2 shows V_{xy} measured as a function of magnetic field H_z applied perpendicular to the sample plane for a sample with $w_n = 70$ nm and $w_g = w_s = 600$ nm. All measurements in this report are made at room temperature ($T = 295$ K). The $V_{\text{AH}}(H_z)$ curve saturates at a field $H_s < 1$ kOe indicating that moderate magnetic field is sufficient to rotate magnetization of the wire from the sample plane to the out-of-plane orientation. The smallness

of H_s compared to the out-of-plane magnetic shape anisotropy field $4\pi M_s \approx 19$ kOe, where $M_s \approx 1500$ emu/cm³ is the Co₄₅Fe₃₅B₂₀ film saturation magnetization, arises from interfacial perpendicular magnetic anisotropy (PMA) of the Ta | Co₄₅Fe₃₅B₂₀ | MgO trilayer [113].

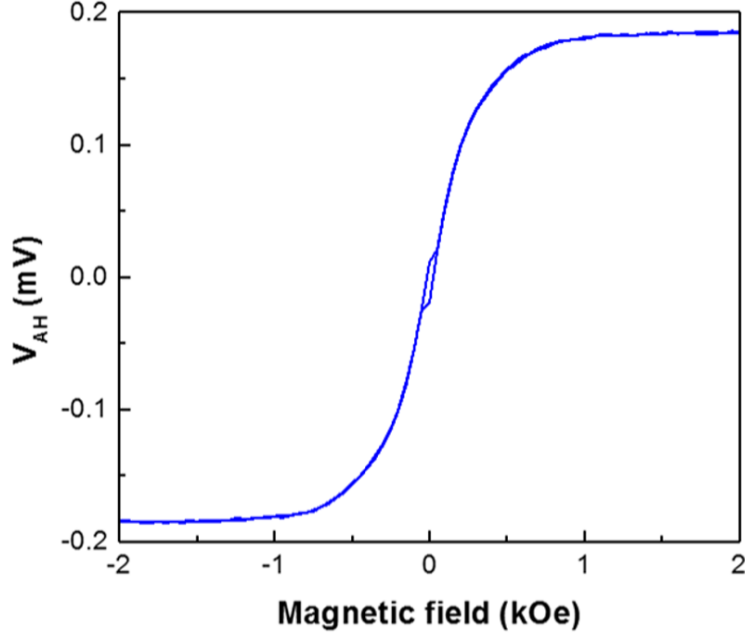


Figure 8.2: **Hysteresis under out of plane external field.** V_{xy} versus out-of-plane magnetic field H_z measured for a SW-FET with $w_n = 70$ nm and $w_g = w_s = 600$ nm at $I_{dc} = 40$ μ A.

8.3.2 Electrically Detected FMR Data

Fig. 8.3 shows ΔV_{xy} measured for the device in Fig. 8.1(b) as a function of f and H_z at $I_{dc} = 60$ μ A and root-mean-square $I_{rf} = 276$ μ A (corresponding to applied RF power of -6 dBm). The data reveals two low-frequency spin wave eigenmodes in this device exhibiting non-monotonic dependence of eigenfrequencies on H_z . We observe what seems to be two modes in our eigenmode spectra, which each have their own saturation field. We suspect that the lower frequency mode is the edge mode while the higher frequency one is the bulk mode.

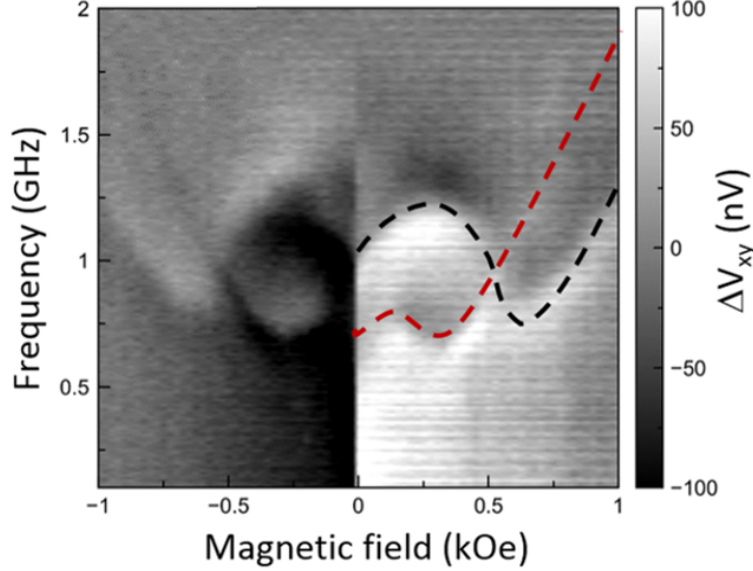


Figure 8.3: **Nanowire spin wave eigenmodes.** Variation of anomalous Hall voltage ΔV_{xy} arising from excitation of spin waves by RF current applied between leads 6 and 7, measured as a function of the RF current frequency and H_z for the device in Fig. 8.2. In this measurement, direct current $I_{dc} = 60 \mu\text{A}$ and RF power of -6 dBm are applied between leads 6 and 7. Dashed lines are guides to the eye showing frequencies of the edge (red) and bulk (black) spin wave eigenmodes of the nanowire.

8.3.3 Electrically Detected Propagating SW Spectroscopy Data

Fig. 8.4(a) shows the propagating spin wave signal $\Delta V_{xy}(f, H_z)$ measured for the device in Fig. 8.1. These data illustrate that both the bulk and the edge spin waves traverse the 600 nm section of the $\text{Co}_{45}\text{Fe}_{35}\text{B}_{20}$ nanowire between the source and drain of the SW-FET device. Fig. 8.4(b) illustrates the effect of V_g on propagation of the edge mode under the gate measured at $H_z = 225 \text{ Oe}$. For this value of H_z , equilibrium magnetization of the wire edge is saturated out of the sample plane. Fig. 8.4(b) shows the difference between $\Delta V_{xy}(V_g)$ measured at a non-zero value of V_g and $\Delta V_{xy}(0)$ measured at $V_g = 0$: $\delta V_{xy}(V_g) = \Delta V_{xy}(V_g) - \Delta V_{xy}(0)$. Negative values of V_g increase magnetic anisotropy of the $\text{Co}_{45}\text{Fe}_{35}\text{B}_{20}$ nanowire directly under the gate due to voltage-controlled magnetic anisotropy (VCMA) at the $\text{MgO}/\text{Co}_{45}\text{Fe}_{35}\text{B}_{20}$ interface [87, 102, 143]. This creates magnetic energy barrier for the propagating edge wave, which gives rise to partial wave reflection and thereby decreases

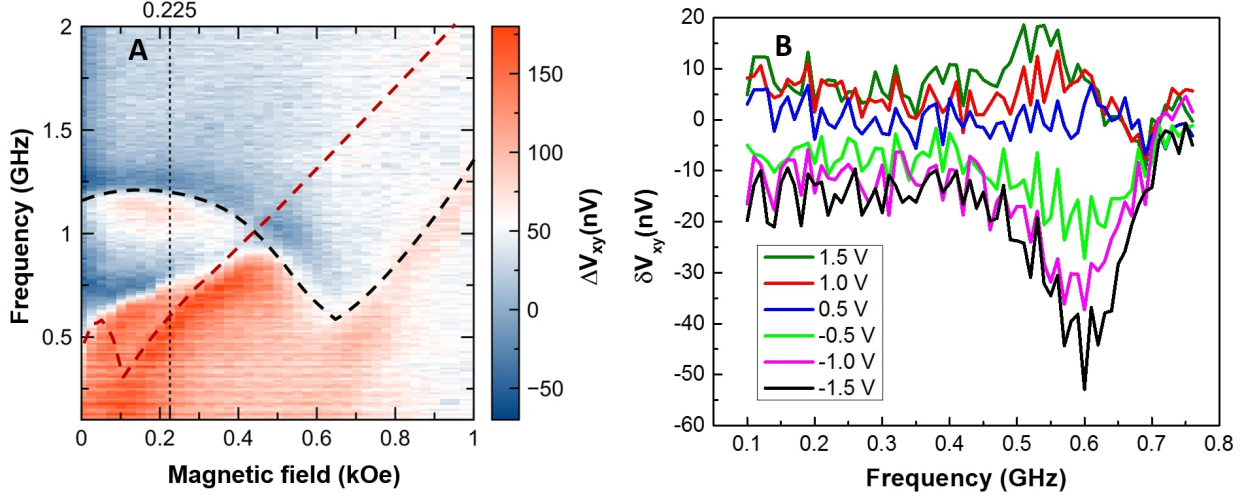


Figure 8.4: **Propagating spin wave spectroscopy**, (A) Variation of anomalous Hall voltage ΔV_{xy} at the right Hall cross due to spin waves arriving from the left Hall cross, measured as a function of spin wave frequency and H_z for the device shown in Fig. 8.1. Dashed lines are guides to the eye showing frequencies of the edge (red) and bulk (black) spin wave eigenmodes of the nanowire. (B) Dependence of the propagating spin wave signal in A on gate voltage $\delta V_{xy}(V_g) = \Delta V_{xy}(V_g) - V_{xy}(0)$ measured at $H_z = 225$ Oe. Negative gate voltage increases magnetic anisotropy barrier under the gate and thereby reduces the amplitude of spin waves of the edge mode arriving to the right Hall cross.

amplitude of the wave arriving to the SW-FET drain. The data in Fig. 8.4(b) indeed reveal that for $V_g < 0$, the amplitude of the edge spin wave arriving to the drain exhibits approximately linear decrease with increasing $|V_g|$. While it is difficult to precisely quantify the gate-induced wave attenuation due to frequency-dependent background in the data in Fig. 8.4(a), it is clear that significant modulation of the wave amplitude is achieved. Indeed, the maximum value of $|\delta V_{xy}(V_g)| = 55$ nV achieved at $V_g = -1.5$ V is a significant fraction of the maximum signal $\Delta V_{xy}(V_g) \approx 150$ nV in Fig. 8.4(a). Since ΔV_{xy} is proportional to spin wave amplitude squared, we estimate that $V_g = -1.5$ V results in greater than 20% reduction of the edge mode amplitude at the drain.

Fig. 8.4(b) shows that $V_g > 0$ weakly affects the propagating spin wave signal. This is not surprising since positive polarity of V_g decreases magnetic anisotropy under the gate and creates a magnetic potential well for the propagating spin waves. Such a well is expected to introduce significant phase shift to a propagating spin wave but has minimal impact on

its amplitude [6]. Our data in Fig. 8.4(b) reveal that the amplitude of propagating spin waves at frequencies just under the bottom of the spin wave dispersion relation is slightly enhanced. This can be explained by the fact that evanescent spin wave in the source region can become propagating in the gate region if its frequency is greater than the bottom of the dispersion relation in the gate region for a given value of $V_g > 0$. We therefore, expect that the amplitude of such evanescent wave in the drain region can be enhanced by $V_g > 0$.

8.4 Micromagnetic Simulations

This system in particular involves propagating spin waves with an external field applied out of plane of the nanowire. Such a configuration is not all that explored in literature, so we employ micromagnetic simulations in this case to actually decipher what kind of modes we are experimentally observing. This project required running a large series of simulations spanning several parameters in order to have our spectral plots (frequency vs H) resemble our experimental data.

8.4.1 Simulation Software and Parameters

Our simulations are carried out in Mumax3 [131] at zero temperature ($T = 0$ K) with defined material parameters: saturation magnetization $M_s = 1500$ emu cm⁻³, Gilbert damping $\alpha = 0.001$, and Landé g-factor $g = 2.1$. We assume an exchange constant $A_{\text{ex}} = 7.5 \times 10^{-7}$ erg/cm

Our simulation geometry consists of $3 \mu\text{m} \times 76 \text{ nm} \times 0.8 \text{ nm}$ ferromagnetic nanowire composed of $2048 \times 32 \times 1$ cells, yielding cell sizes of $1.46 \times 2.37 \times 0.8 \text{ nm}$. We designate an active region 600 nm long in the center to represent the gated region just like the sample. In order to successfully recreate the eigenmodes observed in experiment, we had to explore a param-

eter space of K_{u1} , K_{u2} , DMI, and nanowire width. The chosen parameters will be shown in the next section. Inclusion of DMI was necessary to observe two modes, it has been shown that ultra-thin CoFeB nanowires can have DMI present [127]. Finally, we include absorbing boundary conditions by ramping up the damping near the lengthwise ends of the nanowire. Unlike the previous two chapters, no spin transfer torque is involved here.

8.4.2 Simulation Execution and Analysis

We desire to extract the eigenmode spectra of our nanowire system. So first we must apply an external field H_{app} , and let the system ‘relax’, i.e., reconfigure the magnetization such that it is at an energetic minimum. Once the minimum energy configuration is found, we apply a sinc pulse everywhere just like Eq. (6.6) and store the averaged magnetization response. We increment H_{app} and repeat the simulation. We perform our usual FFT procedure to extract the eigenmode spectra at every field. We choose to FFT the y component of magnetization M_y as it will more clearly display the spin wave dynamics. This is because spin waves in a system where the out of plane direction is equilibrium will exhibit small M_z oscillations. By putting the spectras at every field together we form an f vs H colorplot that makes very clear how the eigenmodes evolve with increasing H_{app} . To elucidate what modes are visible in our eigenmode measurements, we map the spatial profile of modes we see within the active region. This informs us whether the modes have *bulk*, *edge*, or some other more novel structure.

Finally, we simulated and extracted the nanowire spectra when K_{u1} is shifted by a fixed percentage in the active region only. We perform simulations where we fix $H_{app} = 240$ Oe and instead of the sinc pulse apply a small amplitude oscillating field of fixed frequency $h_{CW}(t) = h \sin(2\pi f_{CW}t)$. This emulates the conditions in which our AHE detection of propagating spin waves are conducted at a fixed field and under various gate voltages.

8.5 Simulation Results

8.5.1 Simulated Eigenmode Spectra

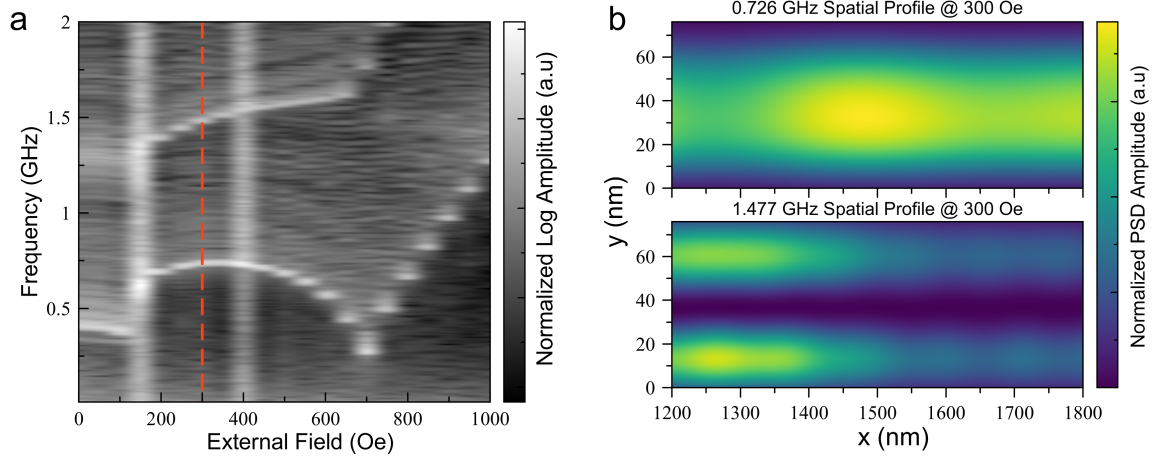


Figure 8.5: **Simulated SWFET eigenmode spectra.** (A) Eigenmode spectra of simulated nanowire with iDMI $D = 8.2 \times 10^{-4} \text{ J/m}^2$, first order PMA $K_{u1} = 1.304 \times 10^6 \text{ J/m}^3$, second order anisotropy $K_{u2} = 1.304 \times 10^4 \text{ J/m}^3$, and nanowire width of 76 nm. (B) Spatial profile of modes visible at 300 Oe (dashed red line) in active region (center 600nm). We confirm that the two modes are bulk (lower frequency) and edge (higher frequency) modes.

For $H_{app} = 240 \text{ Oe}$, we observe two modes at 0.712 GHz and 1.425 GHz which have a bulk and edge spatial profile respectively. The parameters that yielded spectras most similar to our experimental eigenmodes were: iDMI $D = 8.2 \times 10^{-4} \text{ J/m}^2$, first order PMA $K_{u1} = 1.304 \times 10^6 \text{ J/m}^3$, second order anisotropy $K_{u2} = 1.304 \times 10^4 \text{ J/m}^3$, and finally a nanowire width of 76 nm. Fig. 8.5(a) shows the frequency vs H_{app} eigenmode spectra. The two modes are clearly visible and seem to exhibit saturation at around 700 Oe. When we apply a sinc pulse only to one arm of the nano wire and analyze the opposite side, we see the same eigenmode spectra (naturally, since the configuration experiences no physical change). We also observe the higher frequency mode kind of vanishing at very low field ($< 150 \text{ Oe}$). The qualitative features of the two modes deviate at higher fields, eliminating suspicion that they are harmonics. Fig. 8.5(b) shows the corresponding spatial profiles of the two detected modes. We confirm that they are indeed bulk (0.726 GHz) and edge (1.477 GHz) modes.

We also see that the mode profiles have some non-uniformity, possibly due to non-linear dynamics which can lead to some local condensation.

8.5.2 Simulated Gate Effects on Propagating SW Spectra

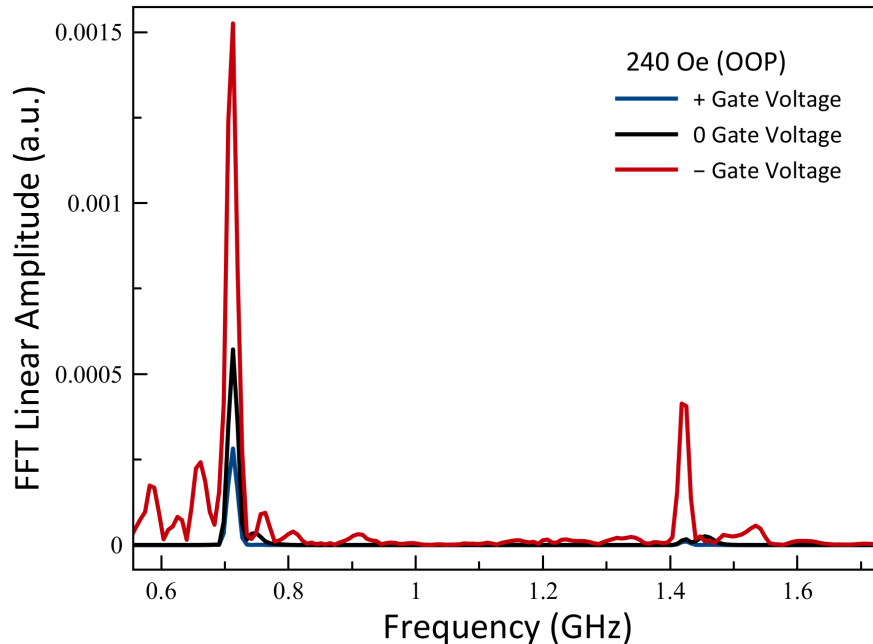


Figure 8.6: **Simulated VCMA effect on propagating SW.** Spin wave spectra ‘measured’ at the drain arm under different K_{u1} values at the gate (to emulate VCMA, increasing K_{u1} corresponds to $-V$ and decreasing K_{u1} to $+V$). External field $H_{app} = 240$ Oe was applied out of plane. We are also using CW driver at the source arm $h_{CW}(t) = h \sin(2\pi f_{CW}t)$ where $f_{CW} = 0.712$ GHz. We observe enhancement in detected spin waves by a factor of ~ 3 for one polarity (red curve) and suppression by a factor of ~ 2 for the other (blue).

Fig. 8.6 shows the simulated effects of VCMA on the detection amplitude of spin waves excited from the source and measured at the drain [108]. We apply an OOP field $H_{app} = 240$ Oe and drive 0.712 GHz continuous wave at the source arm. We observe that for one polarity of the shift there’s a consistent reduction of propagating spin waves (blue curve, where PMA is decreased) maxing out to factor of 0.62 additional loss, while the other polarity there is enhancement of propagating spin waves (red curve) with increased signal

factor of 3.

8.6 Discussion

We find qualitative agreement between simulations and experimental results. Specifically we recover two visible modes in our simulation eigenmode spectra (Fig. 8.5(a)) that are similarly shaped to those in Fig. 8.3. The separated ‘saturation’ fields for the two modes in Fig. 8.3 can be due to some local variation in the anisotropy due to the interface in the active region (like surface pinning from the MgO/Ta), which then will shift the effective field inside and thus make new modes accessible. We have observed in our simulations such an effect where a shift in the active region K_{u1} can introduce new modes on top off the original spectra where there was no change. Other things to consider are nanofabrication related factors such as edge dilution, which can lead to enhanced pinning or roughness related shifts in the spectra, especially for edge modes [89, 31].

The inclusion of iDMI was required in order to observe two modes close enough together in frequency. Our iDMI value of 0.82 mJ/m^2 is much higher than what has been measured in Ta/CoFeB/MgO films (which is usually 1 order of magnitude less, only Pt/CoFeB/MgO has been measured to have $\sim 1 \text{ mJ/m}^2$). Unless the nanowire shape or presence of Ta above the thin MgO somehow enhances some asymmetric exchange within the CoFeB, we attribute our unusually large iDMI to overfitting our simulation parameters to match experiment.

The gate effect simulations (Fig. 8.6) yield good agreement with our propagating spin wave spectroscopy measurements under various gate voltages (Fig. 8.4(b)). In our simulation, when the PMA is reduced (positive gate V), we observe enhanced reduction of spin wave signal at the drain arm that doesn’t change much with continued decreasing shift. Whereas when the PMA is increased (negative gate V), we observe an enhancement of spin wave

dynamics at the detection arm. These two qualitative features match our experimental data in that we observe significant change in one polarity of voltage while experiencing little change in the other polarity. In particular, it corroborates the experimental results collected from AHE detected spin waves.

As of right now, there are only a handful of realizations of magnonic devices that successfully manipulate spin waves via electric field. This work of utilizing VCMA to modulate spin waves motivates towards efficient magnonic logic gates. For example, the phase shift from the reduced PMA in the active region can be engineered to operate as a spin wave logic gate (where the bit information is encoded in the phase), such a device can then be cascaded in a *network* of phase manipulators to form a true spin wave based computer [84].

Chapter 9

Summary and Future Work

In summary, this dissertation has shown and discussed a number of new and exciting approaches to manipulating spin waves and wave dynamics through spin orbit coupling. Spin waves in thin yttrium iron garnet (YIG) films were measured and discovered to be non-reciprocal. The non-reciprocity was characterized and attributed to interfacial Dzyaloshinskii-Moriya interaction between the ferrimagnet and the substrate gadolinium gallium garnet. The insertion of Pt, a large spin orbit coupling material, between the two layers enhances this non-reciprocity by 50%. Observance of non-reciprocity in an ultra low damping film like thin YIG can be utilized to realize scalable passive microwave processing components. Next, the gated Pt/YIG studies reveal however that this system is not ideal for voltage controllable non-reciprocity endowed by the spin-flexo-electric interaction, probably due to YIG having nearly cubic symmetry in its unit cell (centrosymmetric) and thus does not sufficiently polarize in an electric field. The phenomenological constant relating to this effect was extracted. These studies have uncovered new features and contributed to the further understanding of one of the most popular low damping spin wave mediums used both in academia and industry.

Progress in the on-going effort towards utilizing magneto-elastic coupling (which stems from spin orbit interaction) to imprint non-reciprocity onto surface acoustic waves was shown. The most recent devices made in this study showcase newly developed techniques that further the group's nanofabrication capabilities and opens access to more challenging device concepts not considered before. The theory our collaborators Verba et al. [132] have presented draw attention to a more general question of imprinting dispersion features between other quasi-particles. As long as there is non-zero resonant interaction, then this approach is possible. This further motivates new studies aimed to better understand certain coupling mechanisms between different physics and their respective quasi-particle description.

The dimensional crossover study for nanowire spin Hall oscillators showed that increasing wire width past a certain point (when going from quasi-one-dimensional to quasi-two-dimensional) leads to a reduction of overall emitted power. This is because with increasing width there were more modes to compete with each other over the limited influx of angular momentum and thus lower amplitude and phase coherence overall. In other words, there was an increase in non-linear interactions among the modes. The study informs the upper limit for physical dimensions of spin hall oscillators for use in practical applications. Furthermore, it elucidated the mechanisms behind the suppression of coherent auto oscillations with increasing nanowire size.

Next, a novel nanowire spin Hall oscillator with considerably enhanced emitted power was shown. In this system, the energy landscape of the nanowire was manipulated to achieve a state where the energy in plane along the wire was nearly degenerate with out of plane, leading to an *easy*-plane anisotropy that was perpendicular to the polarization of the spin Hall current. This configuration allowed for large angle magnetization dynamics and enhanced coherence in the excited modes. These results provide a new method of achieving high power, easy to fabricate, spin Hall oscillators for a number of practical applications like wireless communications and neuromorphic computing.

Finally, a spin wave field effect transistor was realized. This was achieved via using voltage controlled magnetic anisotropy to modulate spin wave amplitudes travelling through the nanowire. This study adds to the few experimental realizations of electric field controlled magnonic devices. The results in this study will be useful in future efforts of achieving magnonic logic gates or even a true spin wave computer.

Bibliography

- [1] *Spin Current*. Oxford University Press, Jul 2012. ISBN 9780199600380. doi: 10.1093/acprof:oso/9780199600380.001.0001. URL <https://oxford.universitypressscholarship.com/view/10.1093/acprof:oso/9780199600380.001.0001/acprof-9780199600380>.
- [2] Kyongmo An, Daniel R. Birt, Chi-Feng Pai, Kevin Olsson, Daniel C. Ralph, Robert A. Buhrman, and Xiaoqin Li. Control of propagating spin waves via spin transfer torque in a metallic bilayer waveguide. *Physical Review B*, 89(14):140405(R), April 2014. doi: 10.1103/PhysRevB.89.140405.
- [3] K. Ando, S. Takahashi, K. Harii, K. Sasage, J. Ieda, S. Maekawa, and E. Saitoh. Electric Manipulation of Spin Relaxation Using the Spin Hall Effect. *Physical Review Letters*, 101(3):036601, July 2008. ISSN 0031-9007, 1079-7114. doi: 10.1103/PhysRevLett.101.036601.
- [4] Rodrigo Arias and D L Mills. Extrinsic contributions to the ferromagnetic resonance response of ultrathin films. page 3, 2015.
- [5] M. Arora, R. Hübner, D. Suess, B. Heinrich, and E. Girt. Origin of perpendicular magnetic anisotropy in Co/Ni multilayers. *Physical Review B*, 96(2):024401, July 2017. ISSN 2469-9950, 2469-9969. doi: 10.1103/PhysRevB.96.024401.
- [6] Y. Au, M. Dvornik, O. Dmytriiev, and V. V. Kruglyak. Nanoscale spin wave valve and phase shifter. *Applied Physics Letters*, 100(17):172408, April 2012. ISSN 0003-6951. doi: 10.1063/1.4705289. URL <https://aip.scitation.org/doi/10.1063/1.4705289>.
- [7] Can Onur Avci, Ethan Rosenberg, Lucas Caretta, Felix Büttner, Maxwell Mann, Colin Marcus, David Bono, Caroline A. Ross, and Geoffrey S. D. Beach. Interface-driven chiral magnetism and current-driven domain walls in insulating magnetic garnets. *Nature Nanotechnology*, 14(6):561–566, Jun 2019. ISSN 1748-3387, 1748-3395. doi: 10.1038/s41565-019-0421-2. URL <http://www.nature.com/articles/s41565-019-0421-2>.
- [8] Pio Baettig and Tamio Oguchi. Why are garnets not ferroelectric? a theoretical investigation of $\gamma\text{-Fe}_3\text{O}_5$. *Chemistry of Materials*, 20(24):7545–7550, Dec 2008. ISSN 0897-4756, 1520-5002. doi: 10.1021/cm801786h. URL <https://pubs.acs.org/doi/10.1021/cm801786h>.

- [9] I. Barsukov, H. K. Lee, A. A. Jara, Y.-J. Chen, A. M. Gonçalves, C. Sha, J. A. Katine, R. E. Arias, B. A. Ivanov, and I. N. Krivorotov. Giant nonlinear damping in nanoscale ferromagnets. *Science Advances*, 5(10):eaav6943, October 2019. ISSN 2375-2548. doi: 10.1126/sciadv.aav6943.
- [10] Christian Bayer, Jörg Jorzick, Sergej O. Demokritov, Andrei N. Slavin, Konstantin Y. Guslienko, Dmitry V. Berkov, Natalia L. Gorn, Mikhail P. Kostylev, and Burkard Hillebrands. Spin-Wave Excitations in Finite Rectangular Elements. In Burkard Hillebrands and André Thiaville, editors, *Spin Dynamics in Confined Magnetic Structures III*, volume 101 of *Topics in Applied Physics*, pages 57–103. Springer, Berlin, Heidelberg, 2006. ISBN 978-3-540-39842-4. doi: 10.1007/10938171_2.
- [11] L. Berger. Emission of spin waves by a magnetic multilayer traversed by a current. *Physical Review B*, 54(13):9353–9358, October 1996. ISSN 0163-1829, 1095-3795. doi: 10.1103/PhysRevB.54.9353.
- [12] Romuald Bobkowski, Yunlei Li, Robert Fedosejevs, and James N. Broughton. Fabrication of 0.25-um electrode width saw filters using x-ray lithography with a laser plasma source. In *Electron-Beam, X-Ray, EUV, and Ion-Beam Submicrometer Lithographies for Manufacturing VI*, volume 2723, page 393–401. SPIE, May 1996. doi: 10.1117/12.240492. URL <https://www.spiedigitallibrary.org/conference-proceedings-of-spie/2723/0000/Fabrication-of-025-um-electrode-width-SAW-filters-using-x/10.1117/12.240492.full>.
- [13] C. Boone, J. A. Katine, J. R. Childress, J. Zhu, X. Cheng, and I. N. Krivorotov. Experimental test of an analytical theory of spin-torque-oscillator dynamics. *Physical Review B*, 79(14):140404(R), April 2009. ISSN 1098-0121, 1550-235X. doi: 10.1103/PhysRevB.79.140404.
- [14] P M Braganca, B A Gurney, B A Wilson, J A Katine, S Maat, and J R Childress. Nanoscale magnetic field detection using a spin torque oscillator. *Nanotechnology*, 21(23):235202, June 2010. ISSN 0957-4484, 1361-6528. doi: 10.1088/0957-4484/21/23/235202.
- [15] Christophe Caloz, Andrea Alù, Sergei Tretyakov, Dimitrios Sounas, Karim Achouri, and Zoé-Lise Deck-Léger. Electromagnetic nonreciprocity. *Physical Review Applied*, 10(4):047001, Oct 2018. ISSN 2331-7019. doi: 10.1103/PhysRevApplied.10.047001. URL <https://link.aps.org/doi/10.1103/PhysRevApplied.10.047001>.
- [16] Colin Campbell. *Surface acoustic wave devices and their signal processing applications*. Academic Press, Boston, 1989. URL <http://site.ebrary.com/id/10697289>.
- [17] Yi Cao, Guozhong Xing, Huai Lin, Nan Zhang, Houzhi Zheng, and Kaiyou Wang. Prospect of spin-orbitronic devices and their applications. *iScience*, 23(10):101614, Sep 2020. ISSN 2589-0042. doi: 10.1016/j.isci.2020.101614. URL <https://www.ncbi.nlm.nih.gov/pmc/articles/PMC7559259/>.

- [18] Houchen Chang, Tao Liu, Danielle Reifsnyder Hickey, P. A. Praveen Janantha, K. Andre Mkhoyan, and Mingzhong Wu. Sputtering growth of y3fe5o12/pt bilayers and spin transfer at y3fe5o12/pt interfaces. *APL Materials*, 5(12):126104, Dec 2017. doi: 10.1063/1.5013626. URL <https://aip.scitation.org/doi/10.1063/1.5013626>.
- [19] Jen-Ru Chen, Andrew Smith, Eric A. Montoya, Jia G. Lu, and Ilya N. Krivorotov. Spin-orbit torque nano-oscillator with giant magnetoresistance readout. *Communications Physics*, 3(1):1–8, October 2020. ISSN 2399-3650. doi: 10.1038/s42005-020-00454-7.
- [20] Yu-Jin Chen. *Voltage Control of Spin Waves in Nanostructures*. PhD thesis, University of California, Irvine, January 2017.
- [21] A. V. Chumak, V. I. Vasyuchka, A. A. Serga, and B. Hillebrands. Magnon spintronics. *Nature Physics*, 11(6):453–461. ISSN 1745-2481. doi: 10.1038/nphys3347. URL <https://www.nature.com/articles/nphys3347>.
- [22] Andrii V. Chumak, Alexander A. Serga, and Burkard Hillebrands. Magnon transistor for all-magnon data processing. *Nature Communications*, 5:4700, August 2014. ISSN 2041-1723. doi: 10.1038/ncomms5700. URL <https://www.nature.com/articles/ncomms5700>.
- [23] L. J. Cornelissen, J. Liu, B. J. van Wees, and R. A. Duine. Spin-Current-Controlled Modulation of the Magnon Spin Conductance in a Three-Terminal Magnon Transistor. *Physical Review Letters*, 120(9):097702, March 2018. doi: 10.1103/PhysRevLett.120.097702. URL <https://link.aps.org/doi/10.1103/PhysRevLett.120.097702>.
- [24] V. E. Demidov, S. Urazhdin, E. R. J. Edwards, M. D. Stiles, R. D. McMichael, and S. O. Demokritov. Control of Magnetic Fluctuations by Spin Current. *Physical Review Letters*, 107(10):107204, September 2011. doi: 10.1103/PhysRevLett.107.107204.
- [25] V. E. Demidov, S. Urazhdin, A. Anane, V. Cros, and S. O. Demokritov. Spin-orbit-torque magnonics. *Journal of Applied Physics*, 127(17):170901, May 2020. ISSN 0021-8979. doi: 10.1063/5.0007095.
- [26] Vladislav E. Demidov, Sergei Urazhdin, Henning Ulrichs, Vasyl Tiberkevich, Andrei Slavin, Dietmar Baither, Guido Schmitz, and Sergej O. Demokritov. Magnetic nano-oscillator driven by pure spin current. *Nature Materials*, 11(12):1028–1031, December 2012. ISSN 1476-1122, 1476-4660. doi: 10.1038/nmat3459.
- [27] Franz L. Dickert, Peter Forth, Wolf-Eckehard Bulst, Gerhard Fischerauer, and Ulrich Knauer. Saw devices-sensitivity enhancement in going from 80 mhz to 1 ghz. *Sensors and Actuators B: Chemical*, 46(2):120–125, Feb 1998. ISSN 0925-4005. doi: 10.1016/S0925-4005(98)00097-5. URL <https://www.sciencedirect.com/science/article/pii/S0925400598000975>.
- [28] Boris Divinskiy, Sergei Urazhdin, Sergej O. Demokritov, and Vladislav E. Demidov. Controlled nonlinear magnetic damping in spin-Hall nano-devices. *Nature Communications*, 10(1):1–7, November 2019. ISSN 2041-1723. doi: 10.1038/s41467-019-13246-7.

- [29] Michael J. Donahue and D. G. Porter. OOMMF User’s Guide, Version 1.0. Interagency Report NISTIR 6376, National Institute of Standards and Technology, Gaithersburg, MD, September 1999.
- [30] Zheng Duan, Carl T. Boone, Xiao Cheng, Ilya N. Krivorotov, Nathalie Reckers, Sven Stienen, Michael Farle, and Jürgen Lindner. Spin-wave modes in permalloy/platinum wires and tuning of the mode damping by spin Hall current. *Physical Review B*, 90(2):024427, July 2014. ISSN 1098-0121, 1550-235X. doi: 10.1103/PhysRevB.90.024427.
- [31] Zheng Duan, Andrew Smith, Liu Yang, Brian Youngblood, Jürgen Lindner, Vladislav E. Demidov, Sergej O. Demokritov, and Ilya N. Krivorotov. Nanowire spin torque oscillator driven by spin orbit torques. *Nature Communications*, 5(1):5616, December 2014. ISSN 2041-1723. doi: 10.1038/ncomms6616.
- [32] Zheng Duan, Ilya N. Krivorotov, Rodrigo E. Arias, Nathalie Reckers, Sven Stienen, and Jürgen Lindner. Spin wave eigenmodes in transversely magnetized thin film ferromagnetic wires. *Physical Review B*, 92(10):104424, September 2015. ISSN 1098-0121, 1550-235X. doi: 10.1103/PhysRevB.92.104424.
- [33] Randy K. Dumas, E. Iacocca, S. Bonetti, S. R. Sani, S. M. Mohseni, A. Eklund, J. Persson, O. Heinonen, and Johan Åkerman. Spin-Wave-Mode Coexistence on the Nanoscale: A Consequence of the Oersted-Field-Induced Asymmetric Energy Landscape. *Physical Review Letters*, 110(25):257202, June 2013. doi: 10.1103/PhysRevLett.110.257202.
- [34] Sourav Dutta, Sou-Chi Chang, Nickvash Kani, Dmitri E. Nikonov, Sasikanth Manipatruni, Ian A. Young, and Azad Naeemi. Non-volatile clocked spin wave interconnect for beyond-CMOS nanomagnet pipelines. *Scientific Reports*, 5:9861. ISSN 2045-2322. doi: 10.1038/srep09861. URL <https://www.nature.com/articles/srep09861>.
- [35] Mykola Dvornik and Johan Åkerman. Anomalous nonlinearity of the magnonic edge mode. *arXiv:1804.01585 [cond-mat]*, April 2018.
- [36] I. Dzyaloshinsky. A thermodynamic theory of “weak” ferromagnetism of antiferromagnetics. *Journal of Physics and Chemistry of Solids*, 4(4):241–255, Jan 1958. ISSN 0022-3697. doi: 10.1016/0022-3697(58)90076-3. URL <https://www.sciencedirect.com/science/article/pii/0022369758900763>.
- [37] Satoru Emori, Di Yi, Sam Crossley, Jacob J. Wissler, Purnima P. Balakrishnan, Behrouz Khodadadi, Padraic Shafer, Christoph Klewe, Alpha T. N’Diaye, Brittany T. Urwin, Krishnamurthy Mahalingam, Brandon M. Howe, Harold Y. Hwang, Elke Arenholz, and Yuri Suzuki. Ultralow Damping in Nanometer-Thick Epitaxial Spinel Ferrite Thin Films. *Nano Letters*, 18(7):4273–4278, July 2018. ISSN 1530-6984, 1530-6992. doi: 10.1021/acs.nanolett.8b01261.
- [38] Albert Fert, Vincent Cros, and João Sampaio. Skyrmions on the track. *Nature Nanotechnology*, 8(3):152–156, Mar 2013. ISSN 1748-3395. doi: 10.1038/nnano.2013.29. URL <https://www.nature.com/articles/nnano.2013.29>.

- [39] I. Firastrau, D. Gusakova, D. Houssameddine, U. Ebels, M.-C. Cyrille, B. Delaet, B. Dieny, O. Redon, J.-Ch. Toussaint, and L. D. Buda-Prejbeanu. Modeling of the perpendicular polarizer-planar free layer spin torque oscillator: Micromagnetic simulations. *Physical Review B*, 78(2):024437, July 2008. doi: 10.1103/PhysRevB.78.024437.
- [40] T. Fischer, M. Kewenig, D. A. Bozhko, A. A. Serga, I. I. Syvorotka, F. Ciubotaru, C. Adelmann, B. Hillebrands, and A. V. Chumak. Experimental prototype of a spin-wave majority gate. *Applied Physics Letters*, 110(15):152401, April 2017. ISSN 0003-6951, 1077-3118. doi: 10.1063/1.4979840.
- [41] Romain Fleury, Dimitrios L. Sounas, Caleb F. Sieck, Michael R. Haberman, and Andrea Alù. Sound isolation and giant linear nonreciprocity in a compact acoustic circulator. *Science*, 343(6170):516–519, Jan 2014. ISSN 0036-8075, 1095-9203. doi: 10.1126/science.1246957. URL <https://www.science.org/doi/10.1126/science.1246957>.
- [42] R A Gallardo, P Alvarado-Seguel, T Schneider, C Gonzalez-Fuentes, A Roldán-Molina, K Lenz, J Lindner, and P Landeros. Spin-wave non-reciprocity in magnetization-graded ferromagnetic films. *New Journal of Physics*, 21(3):033026, Mar 2019. ISSN 1367-2630. doi: 10.1088/1367-2630/ab0449. URL <https://iopscience.iop.org/article/10.1088/1367-2630/ab0449>.
- [43] S. J. Gamble, Mark H. Burkhardt, A. Kashuba, Rolf Allenspach, Stuart S. P. Parkin, H. C. Siegmann, and J. Stöhr. Electric Field Induced Magnetic Anisotropy in a Ferromagnet. *Physical Review Letters*, 102(21):217201, May 2009. doi: 10.1103/PhysRevLett.102.217201. URL <https://link.aps.org/doi/10.1103/PhysRevLett.102.217201>.
- [44] Chenyang Gao, Cuimei Cao, and Jingze Zhao. Structure and magnetic properties of epitaxial life₅₀8 film with different growth temperatures. *Applied Physics A*, 125(8):566, Jul 2019. ISSN 1432-0630. doi: 10.1007/s00339-019-2850-z. URL <https://doi.org/10.1007/s00339-019-2850-z>.
- [45] N. Gauthier. Magnetic field of an infinite current-carrying ribbon. *American Journal of Physics*, 56(9):819, July 1998. ISSN 0002-9505. doi: 10.1119/1.15456.
- [46] Thomas L. Gilbert. A lagrangian formulation of the gyromagnetic equation of the magnetization field. *Physical Review D*, 100:1243, 1955.
- [47] A. Giordano, M. Carpentieri, A. Laudani, G. Gubbiotti, B. Azzerboni, and G. Finocchio. Spin-Hall nano-oscillator: A micromagnetic study. *Applied Physics Letters*, 105(4):042412, July 2014. ISSN 0003-6951, 1077-3118. doi: 10.1063/1.4892168.
- [48] A. M. Gonçalves, I. Barsukov, Y.-J. Chen, L. Yang, J. A. Katine, and I. N. Krivorotov. Spin torque ferromagnetic resonance with magnetic field modulation. *Applied Physics Letters*, 103(17):172406, October 2013. ISSN 0003-6951, 1077-3118. doi: 10.1063/1.4826927.

- [49] J. Grollier, D. Querlioz, K. Y. Camsari, K. Everschor-Sitte, S. Fukami, and M. D. Stiles. Neuromorphic spintronics. *Nature Electronics*, pages 1–11, March 2020. ISSN 2520-1131. doi: 10.1038/s41928-019-0360-9.
- [50] Zhong-ming Gu, Jie Hu, Bin Liang, Xin-ye Zou, and Jian-chun Cheng. Broadband non-reciprocal transmission of sound with invariant frequency. *Scientific Reports*, 6(1):19824, Jan 2016. ISSN 2045-2322. doi: 10.1038/srep19824. URL <https://www.nature.com/articles/srep19824>.
- [51] Andrea Guarino, Gorazd Poberaj, Daniele Rezzonico, Riccardo Degl’Innocenti, and Peter Günter. Electro–optically tunable microring resonators in lithium niobate. *Nature Photonics*, 1(7):407–410, Jul 2007. ISSN 1749-4893. doi: 10.1038/nphoton.2007.93. URL <https://www.nature.com/articles/nphoton.2007.93>.
- [52] Y. S. Gui, N. Mecking, and C.-M. Hu. Quantized Spin Excitations in a Ferromagnetic Microstrip from Microwave Photovoltage Measurements. *Physical Review Letters*, 98(21):217603, May 2007. doi: 10.1103/PhysRevLett.98.217603.
- [53] A. G. Gurevich and G. A. Melkov. *Magnetization Oscillations and Waves*. CRC Press, Boca Raton, 1996. ISBN 978-0-8493-9460-7.
- [54] Mohammad Haidar, Ahmad A. Awad, Mykola Dvornik, Roman Khymyn, Afshin Houshang, and Johan Åkerman. A single layer spin-orbit torque nano-oscillator. *Nature Communications*, 10(1):2362, May 2019. ISSN 2041-1723. doi: 10.1038/s41467-019-10120-4.
- [55] Orchi Hassan, Rafatul Faria, Kerem Yunus Camsari, Jonathan Z. Sun, and Supriyo Datta. Low-Barrier Magnet Design for Efficient Hardware Binary Stochastic Neurons. *IEEE Magnetism Letters*, 10:1–5, 2019. ISSN 1949-307X, 1949-3088. doi: 10.1109/LMAG.2019.2910787.
- [56] J. Heil, B. Lüthi, and P. Thalmeier. Nonreciprocal surface-acoustic-wave propagation in aluminum. *Physical Review B*, 25(10):6515–6517, May 1982. doi: 10.1103/PhysRevB.25.6515. URL <https://link.aps.org/doi/10.1103/PhysRevB.25.6515>.
- [57] B. Heinrich and J. F. Cochran. Ultrathin metallic magnetic films: Magnetic anisotropies and exchange interactions. *Advances in Physics*, 42(5):523–639, October 1993. ISSN 0001-8732. doi: 10.1080/00018739300101524.
- [58] Axel Hoffmann. Spin Hall Effects in Metals. *IEEE Transactions on Magnetism*, 49(10):5172–5193, October 2013. ISSN 0018-9464, 1941-0069. doi: 10.1109/TMAG.2013.2262947.
- [59] Wenchuang (Walter) Hu, Koshala Sarveswaran, Marya Lieberman, and Gary H. Bernstein. Sub-10 nm electron beam lithography using cold development of poly(methylmethacrylate). *Journal of Vacuum Science & Technology B: Microelectronics and Nanometer Structures Processing, Measurement, and Phenomena*, 22(4):1711–1716, Jul 2004. ISSN 1071-1023. doi: 10.1116/1.1763897. URL <https://avs.scitation.org/doi/abs/10.1116/1.1763897>.

- [60] M. J. Hurben and C. E. Patton. Theory of two magnon scattering microwave relaxation and ferromagnetic resonance linewidth in magnetic thin films. *Journal of Applied Physics*, 83(8):4344–4365, April 1998. ISSN 0021-8979, 1089-7550. doi: 10.1063/1.367194.
- [61] JOHN DAVID JACKSON. 5. JOHN WILEY & SONS, 2021.
- [62] Eva Liskova Jakubisova, Stefan Visnovsky, Houchen Chang, and Mingzhong Wu. Interface effects in nanometer-thick yttrium iron garnet films studied by magneto-optical spectroscopy. *Applied Physics Letters*, 108(8):082403, Feb 2016. ISSN 0003-6951, 1077-3118. doi: 10.1063/1.4942379. URL <http://aip.scitation.org/doi/10.1063/1.4942379>.
- [63] Mahdi Jamali, Jae Hyun Kwon, Soo-Man Seo, Kyung-Jin Lee, and Hyunsoo Yang. Spin wave nonreciprocity for logic device applications. *Scientific Reports*, 3(1):3160, Nov 2013. ISSN 2045-2322. doi: 10.1038/srep03160. URL <https://www.nature.com/articles/srep03160>.
- [64] Emilie Jué, William H. Rippard, and Matthew R. Pufall. Comparison of the spin-transfer torque mechanisms in a three-terminal spin-torque oscillator. *Journal of Applied Physics*, 124(4):043904, July 2018. ISSN 0021-8979. doi: 10.1063/1.5042092.
- [65] V. Kamberský. On ferromagnetic resonance damping in metals. *Czechoslovak Journal of Physics B*, 26(12):1366–1383, Dec 1976. ISSN 1572-9486. doi: 10.1007/BF01587621. URL <https://doi.org/10.1007/BF01587621>.
- [66] A. D. Kent, B. Özyilmaz, and E. del Barco. Spin-transfer-induced precessional magnetization reversal. *Applied Physics Letters*, 84(19):3897–3899, May 2004. ISSN 0003-6951. doi: 10.1063/1.1739271.
- [67] A. Khitun, R. Ostroumov, and K. L. Wang. Spin-wave utilization in a quantum computer. *Physical Review A*, 64(6):062304, November 2001. doi: 10.1103/PhysRevA.64.062304. URL <https://link.aps.org/doi/10.1103/PhysRevA.64.062304>.
- [68] Alexander Khitun and Kang L. Wang. Non-volatile magnonic logic circuits engineering. *Journal of Applied Physics*, 110(3):034306, 2011. ISSN 0021-8979. doi: 10.1063/1.3609062. URL <https://aip.scitation.org/doi/10.1063/1.3609062>.
- [69] Junyeon Kim, Peng Sheng, Saburo Takahashi, Seiji Mitani, and Masamitsu Hayashi. Spin Hall Magnetoresistance in Metallic Bilayers. *Physical Review Letters*, 116(9):097201, February 2016. ISSN 0031-9007, 1079-7114. doi: 10.1103/PhysRevLett.116.097201.
- [70] S. I. Kiselev, J. C. Sankey, I. N. Krivorotov, N. C. Emley, R. J. Schoelkopf, R. A. Buhrman, and D. C. Ralph. Microwave oscillations of a nanomagnet driven by a spin-polarized current. *Nature*, 425(6956):380–383, September 2003. ISSN 0028-0836, 1476-4687. doi: 10.1038/nature01967.

- [71] S. I. Kiselev, J. C. Sankey, I. N. Krivorotov, N. C. Emley, M. Rinkoski, C. Perez, R. A. Buhrman, and D. C. Ralph. Current-Induced Nanomagnet Dynamics for Magnetic Fields Perpendicular to the Sample Plane. *Physical Review Letters*, 93(3):036601, July 2004. doi: 10.1103/PhysRevLett.93.036601.
- [72] I. N. Krivorotov, N. C. Emley, R. A. Buhrman, and D. C. Ralph. Time-domain studies of very-large-angle magnetization dynamics excited by spin transfer torques. *Physical Review B*, 77(5):054440, February 2008. ISSN 1098-0121, 1550-235X. doi: 10.1103/PhysRevB.77.054440.
- [73] V. V. Kruglyak, S. O. Demokritov, and D. Grundler. Magnonics. *Journal of Physics D: Applied Physics*, 43(26):264001. ISSN 0022-3727. doi: 10.1088/0022-3727/43/26/264001. URL <http://stacks.iop.org/0022-3727/43/i=26/a=264001>.
- [74] Lev Davidovich Landau and Evgenii Mikhailovich Lifshitz. On the theory of the dispersion of magnetic permeability in ferromagnetic bodies. 1935.
- [75] B. Lenk, H. Ulrichs, F. Garbs, and M. Münzenberg. The building blocks of magnonics. *Physics Reports*, 507(4):107–136. ISSN 0370-1573. doi:10.1016/j.physrep.2011.06.003. URL <http://www.sciencedirect.com/science/article/pii/S0370157311001694>.
- [76] L. Liu, C.-F. Pai, Y. Li, H. W. Tseng, D. C. Ralph, and R. A. Buhrman. Spin-Torque Switching with the Giant Spin Hall Effect of Tantalum. *Science*, 336(6081):555–558, May 2012. ISSN 0036-8075, 1095-9203. doi: 10.1126/science.1218197.
- [77] Luqiao Liu, Chi-Feng Pai, D. C. Ralph, and R. A. Buhrman. Magnetic Oscillations Driven by the Spin Hall Effect in 3-Terminal Magnetic Tunnel Junction Devices. *Physical Review Letters*, 109(18):186602, October 2012. ISSN 0031-9007, 1079-7114. doi: 10.1103/PhysRevLett.109.186602.
- [78] R. H. Liu, W. L. Lim, and S. Urazhdin. Spectral Characteristics of the Microwave Emission by the Spin Hall Nano-Oscillator. *Physical Review Letters*, 110(14):147601, April 2013. ISSN 0031-9007, 1079-7114. doi: 10.1103/PhysRevLett.110.147601.
- [79] N. Locatelli, V. Cros, and J. Grollier. Spin-torque building blocks. *Nature Materials*, 13(1):11–20, January 2014. ISSN 1476-1122, 1476-4660. doi: 10.1038/nmat3823.
- [80] James Lourembam, Lisen Huang, Bingjin Chen, Jinjun Qiu, Hong Jing Chung, Sherry Lee Koon Yap, Qi Jia Yap, Seng Kai Wong, and Sze Ter Lim. Multi-State Magnetic Tunnel Junction Programmable by Nanosecond Spin-Orbit Torque Pulse Sequence. *Advanced Electronic Materials*, 7(4):2001133, 2021. ISSN 2199-160X. doi: 10.1002/aelm.202001133.
- [81] Chen Luo, Yu Fu, Dong Zhang, Shijun Yuan, Ya Zhai, Shuai Dong, and Hongru Zhai. Temperature dependent coercivity and magnetization of light rare-earth Nd doped permalloy thin films. *Journal of Magnetism and Magnetic Materials*, 374:711–715, January 2015. ISSN 0304-8853. doi: 10.1016/j.jmmm.2014.09.014.

- [82] Rair Macêdo, Arjun S. Kudinoor, Karen L. Livesey, and Robert E. Camley. Breaking space inversion-symmetry to obtain asymmetric spin-wave excitation in systems with nonuniform magnetic exchange. *Advanced Electronic Materials*, 8(1):2100435, Jan 2022. ISSN 2199-160X, 2199-160X. doi: 10.1002/aelm.202100435. URL <https://onlinelibrary.wiley.com/doi/10.1002/aelm.202100435>.
- [83] M. Madami, S. Bonetti, G. Consolo, S. Tacchi, G. Carlotti, G. Gubbiotti, F. B. Mancoff, M. A. Yar, and J. Åkerman. Direct observation of a propagating spin wave induced by spin-transfer torque. *Nature Nanotechnology*, 6(10):635–638, October 2011. ISSN 1748-3395. doi: 10.1038/nnano.2011.140.
- [84] Abdulqader Mahmoud, Florin Ciubotaru, Frederic Vanderveken, Andrii V. Chumak, Said Hamdioui, Christoph Adelman, and Sorin Cotofana. Introduction to spin wave computing. *Journal of Applied Physics*, 128(16):161101, Oct 2020. ISSN 0021-8979. doi: 10.1063/5.0019328. URL <https://aip.scitation.org/doi/10.1063/5.0019328>.
- [85] Hannes Maier-Flaig, Sebastian T. B. Goennenwein, Ryo Ohshima, Masashi Shiraishi, Rudolf Gross, Hans Huebl, and Mathias Weiler. Note: Derivative divide, a method for the analysis of broadband ferromagnetic resonance in the frequency domain. *Review of Scientific Instruments*, 89(7):076101, Jul 2018. ISSN 0034-6748, 1089-7623. doi: 10.1063/1.5045135. URL <http://aip.scitation.org/doi/10.1063/1.5045135>.
- [86] E. J. J. Mallmann, A. S. B. Sombra, J. C. Goes, and P. B. A. Fechine. Yttrium iron garnet: Properties and applications review. *Solid State Phenomena*, 202:65–96, 2013. ISSN 1662-9779. doi: 10.4028/www.scientific.net/SSP.202.65. URL <https://www.scientific.net/SSP.202.65>.
- [87] T. Maruyama, Y. Shiota, T. Nozaki, K. Ohta, N. Toda, M. Mizuguchi, A. A. Tulapurkar, T. Shinjo, M. Shiraishi, S. Mizukami, Y. Ando, and Y. Suzuki. Large voltage-induced magnetic anisotropy change in a few atomic layers of iron. *Nature Nanotechnology*, 4(3):158–161, March 2009. ISSN 1748-3387. doi: 10.1038/nnano.2008.406. URL <http://palgrave.nature.com/nano/journal/v4/n3/full/nnano.2008.406.html>.
- [88] T. McGuire and R. Potter. Anisotropic magnetoresistance in ferromagnetic 3d alloys. *IEEE Transactions on Magnetics*, 11(4):1018–1038, July 1975. ISSN 0018-9464. doi: 10.1109/TMAG.1975.1058782.
- [89] R. D. McMichael and B. B. Maranville. Edge saturation fields and dynamic edge modes in ideal and nonideal magnetic film edges. *Physical Review B*, 74(2):024424, July 2006. ISSN 1098-0121, 1550-235X. doi: 10.1103/PhysRevB.74.024424.
- [90] G. A. Melkov, D. V. Slobodianiuk, V. S. Tiberkevich, G. de Loubens, O. Klein, and A. N. Slavin. Nonlinear Ferromagnetic Resonance in Nanostructures Having Discrete Spectrum of Spin-Wave Modes. *IEEE Magnetics Letters*, 4:4000504–4000504, 2013. ISSN 1949-307X, 1949-3088. doi: 10.1109/LMAG.2013.2278682.

- [91] D. L. Mills and I. E. Dzyaloshinskii. Influence of electric fields on spin waves in simple ferromagnets: Role of the flexoelectric interaction. *Physical Review B*, 78(18):184422, Nov 2008. ISSN 1098-0121, 1550-235X. doi: 10.1103/PhysRevB.78.184422. URL <https://link.aps.org/doi/10.1103/PhysRevB.78.184422>.
- [92] Ioan Mihai Miron, Kevin Garello, Gilles Gaudin, Pierre-Jean Zermatten, Marius V. Costache, Stéphane Auffret, Sébastien Bandiera, Bernard Rodmacq, Alain Schuhl, and Pietro Gambardella. Perpendicular switching of a single ferromagnetic layer induced by in-plane current injection. *Nature*, 476(7359):189–193, August 2011. ISSN 0028-0836, 1476-4687. doi: 10.1038/nature10309.
- [93] S. Mizukami, Y. Ando, and T. Miyazaki. Magnetic relaxation of normal-metal (NM)/80NiFe/NM films. *Journal of Magnetism and Magnetic Materials*, 239(1-3): 42–44, February 2002. ISSN 03048853. doi: 10.1016/S0304-8853(01)00525-X.
- [94] Eric Montoya, Tommy McKinnon, Atieh Zamani, Erol Girt, and Bret Heinrich. Broad-band ferromagnetic resonance system and methods for ultrathin magnetic films. *Journal of Magnetism and Magnetic Materials*, 356:12–20, April 2014. ISSN 03048853. doi: 10.1016/j.jmmm.2013.12.032.
- [95] Eric Montoya, Thomas Sebastian, Helmut Schultheiss, Bret Heinrich, Robert E. Camley, and Zbigniew Celinski. Chapter 3 - Magnetization Dynamics. In Robert E. Camley, Zbigniew Celinski, and Robert L. Stamps, editors, *Handbook of Surface Science*, volume 5 of *Magnetism of Surfaces, Interfaces, and Nanoscale Materials*, pages 113–167. North-Holland, January 2015. doi: 10.1016/B978-0-444-62634-9.00003-5.
- [96] Eric Montoya, Pavlo Omelchenko, Chris Coutts, Nicholas R. Lee-Hone, René Hübner, David Broun, Bret Heinrich, and Erol Girt. Spin transport in tantalum studied using magnetic single and double layers. *Physical Review B*, 94(5):054416, August 2016. ISSN 2469-9950, 2469-9969. doi: 10.1103/PhysRevB.94.054416.
- [97] David Morgan. Surface acoustic wave filters: With applications to electronic communications and signal processing. 2007.
- [98] Tôru Moriya. New mechanism of anisotropic superexchange interaction. *Physical Review Letters*, 4(5):228–230, Mar 1960. doi: 10.1103/PhysRevLett.4.228. URL <https://link.aps.org/doi/10.1103/PhysRevLett.4.228>.
- [99] Tôru Moriya. Anisotropic superexchange interaction and weak ferromagnetism. *Physical Review*, 120(1):91–98, Oct 1960. doi: 10.1103/PhysRev.120.91. URL <https://link.aps.org/doi/10.1103/PhysRev.120.91>.
- [100] Ryan Nakamoto, Bin Xu, Changsong Xu, Hu Xu, and L. Bellaïche. Properties of rare-earth iron garnets from first principles. *Physical Review B*, 95(2):024434, Jan 2017. ISSN 2469-9950, 2469-9969. doi: 10.1103/PhysRevB.95.024434. URL <https://link.aps.org/doi/10.1103/PhysRevB.95.024434>.

- [101] H. Nakayama, M. Althammer, Y.-T. Chen, K. Uchida, Y. Kajiwara, D. Kikuchi, T. Ohtani, S. Geprägs, M. Opel, S. Takahashi, R. Gross, G. E. W. Bauer, S. T. B. Goennenwein, and E. Saitoh. Spin Hall Magnetoresistance Induced by a Nonequilibrium Proximity Effect. *Physical Review Letters*, 110(20):206601, May 2013. ISSN 0031-9007, 1079-7114. doi: 10.1103/PhysRevLett.110.206601.
- [102] Manish K. Niranjana, Chun-Gang Duan, Sitaram S. Jaswal, and Evgeny Y. Tsybal. Electric field effect on magnetization at the Fe/MgO(001) interface. *Applied Physics Letters*, 96(22):222504, May 2010. ISSN 0003-6951, 1077-3118. doi: 10.1063/1.3443658. URL <http://scitation.aip.org/content/aip/journal/apl/96/22/10.1063/1.3443658>.
- [103] A. A. Oliner. *Acoustic Surface Waves*, volume 24 of *Topics in Applied Physics*. Springer Berlin Heidelberg, Berlin, Heidelberg, 1978. ISBN 9783540085751. doi: 10.1007/3-540-08575-0. URL <http://link.springer.com/10.1007/3-540-08575-0>.
- [104] J. P. Park, P. Eames, D. M. Engebretson, J. Berezovsky, and P. A. Crowell. Spatially Resolved Dynamics of Localized Spin-Wave Modes in Ferromagnetic Wires. *Physical Review Letters*, 89(27):277201, December 2002. ISSN 0031-9007, 1079-7114. doi: 10.1103/PhysRevLett.89.277201.
- [105] David M. Pozar. The terminated lossless transmission line. In *Microwave Engineering*, pages 57–60. Wiley, 3rd edition, 2005.
- [106] Matthew R. Pufall, William H. Rippard, György Csaba, Dmitri E. Nikonov, George I. Bourianoff, and Wolfgang Porod. Physical Implementation of Coherently Coupled Oscillator Networks. *IEEE Journal on Exploratory Solid-State Computational Devices and Circuits*, 1:76–84, December 2015. ISSN 2329-9231. doi: 10.1109/JXCDC.2015.2468070.
- [107] Bivas Rana and YoshiChika Otani. Towards magnonic devices based on voltage-controlled magnetic anisotropy. *Communications Physics*, 2(1):1–12, Aug 2019. ISSN 2399-3650. doi: 10.1038/s42005-019-0189-6. URL <https://www.nature.com/articles/s42005-019-0189-6>.
- [108] Bivas Rana, Katsuya Miura, Hiromasa Takahashi, and YoshiChika Otani. Underlayer material dependent symmetric and asymmetric behavior of voltage-controlled magnetic anisotropy in cofeb films. *Journal of Physics: Condensed Matter*, 32(41):414002, Sep 2020. ISSN 0953-8984, 1361-648X. doi: 10.1088/1361-648X/ab99eb. URL <https://iopscience.iop.org/article/10.1088/1361-648X/ab99eb>.
- [109] Graham E. Rowlands and Ilya N. Krivorotov. Magnetization dynamics in a dual free-layer spin-torque nano-oscillator. *Physical Review B*, 86(9):094425, September 2012. ISSN 1098-0121, 1550-235X. doi: 10.1103/PhysRevB.86.094425.
- [110] M. A. Ruderman and C. Kittel. Indirect exchange coupling of nuclear magnetic moments by conduction electrons. *Physical Review*, 96(1):99–102, Oct 1954. doi: 10.1103/PhysRev.96.99. URL <https://link.aps.org/doi/10.1103/PhysRev.96.99>.

- [111] Christopher Safranski, Eric A. Montoya, and Ilya N. Krivorotov. Spin-orbit torque driven by a planar Hall current. *Nature Nanotechnology*, 14(1):27–30, January 2019. ISSN 1748-3395. doi: 10.1038/s41565-018-0282-0.
- [112] R. Sasaki, Y. Nii, Y. Iguchi, and Y. Onose. Nonreciprocal propagation of surface acoustic wave in ni / linbo 3. *Physical Review B*, 95(2):020407, Jan 2017. ISSN 2469-9950, 2469-9969. doi: 10.1103/PhysRevB.95.020407. URL <https://link.aps.org/doi/10.1103/PhysRevB.95.020407>.
- [113] Noriyuki Sato, Robert M. White, and Shan X. Wang. Effect of annealing on exchange stiffness of ultrathin CoFeB film with perpendicular magnetic anisotropy. *Applied Physics Letters*, 108(15):152405, April 2016. ISSN 0003-6951. doi: 10.1063/1.4945039. URL <https://aip.scitation.org/doi/full/10.1063/1.4945039>.
- [114] Noriyuki Sato, Fen Xue, Robert M. White, Chong Bi, and Shan X. Wang. Two-terminal spin-orbit torque magnetoresistive random access memory. *Nature Electronics*, 1(9):508–511, September 2018. ISSN 2520-1131. doi: 10.1038/s41928-018-0131-z.
- [115] Thomas Sebastian, Katrin Schultheiss, Björn Obry, Burkard Hillebrands, and Helmut Schultheiss. Micro-focused Brillouin light scattering: Imaging spin waves at the nanoscale. *Frontiers in Physics*, 3, 2015. ISSN 2296-424X. doi: 10.3389/fphy.2015.00035.
- [116] S. Seki, X. Z. Yu, S. Ishiwata, and Y. Tokura. Observation of skyrmions in a multiferroic material. *Science*, 336(6078):198–201, Apr 2012. ISSN 0036-8075, 1095-9203. doi: 10.1126/science.1214143. URL <https://www.science.org/doi/10.1126/science.1214143>.
- [117] Shawn Yohanes Siew, Eric Jun Hao Cheung, Haidong Liang, Andrew Bettiol, Noriaki Toyoda, Bandar Alshehri, Elhadj Dogheche, and Aaron J. Danner. Ultra-low loss ridge waveguides on lithium niobate via argon ion milling and gas clustered ion beam smoothing. *Opt. Express*, 26(4):4421–4430, Feb 2018. doi: 10.1364/OE.26.004421. URL <http://opg.optica.org/oe/abstract.cfm?URI=oe-26-4-4421>.
- [118] Jairo Sinova, Sergio O. Valenzuela, J. Wunderlich, C. H. Back, and T. Jungwirth. Spin Hall effects. *Reviews of Modern Physics*, 87(4):1213–1260, October 2015. ISSN 0034-6861, 1539-0756. doi: 10.1103/RevModPhys.87.1213.
- [119] A. Slavin and V. Tiberkevich. Nonlinear Auto-Oscillator Theory of Microwave Generation by Spin-Polarized Current. *IEEE Transactions on Magnetism*, 45(4):1875–1918, April 2009. ISSN 0018-9464. doi: 10.1109/TMAG.2008.2009935.
- [120] Denys V. Slobodianiuk, Gennadiy A. Melkov, Katrin Schultheiss, Helmut Schultheiss, and Roman V. Verba. Nonlinear Ferromagnetic Resonance in the Presence of Three-Magnon Scattering in Magnetic Nanostructures. *IEEE Magnetism Letters*, 10:6103405, 2019. ISSN 1949-3088. doi: 10.1109/LMAG.2019.2913132.

- [121] J.C. Slonczewski. Current-driven excitation of magnetic multilayers. *Journal of Magnetism and Magnetic Materials*, 159(1-2):L1–L7, June 1996. ISSN 03048853. doi: 10.1016/0304-8853(96)00062-5.
- [122] Andrew Smith. *Nanowire Spin Hall Oscillators*. PhD thesis, UC Irvine, 2016. URL <https://escholarship.org/uc/item/21q8h0fr>.
- [123] Andrew Smith, Kemal Sobotkiewich, Amanatullah Khan, Eric A. Montoya, Liu Yang, Zheng Duan, Tobias Schneider, Kilian Lenz, Jürgen Lindner, Kyongmo An, Xiaoqin Li, and Ilya N. Krivorotov. Dimensional crossover in spin Hall oscillators. *Physical Review B*, 102(5):054422, August 2020. doi: 10.1103/PhysRevB.102.054422.
- [124] M. Sparks, R. Loudon, and C. Kittel. Ferromagnetic relaxation. i. theory of the relaxation of the uniform precession and the degenerate spectrum in insulators at low temperatures. *Physical Review*, 122(3):791–803, May 1961. doi: 10.1103/PhysRev.122.791. URL <https://link.aps.org/doi/10.1103/PhysRev.122.791>.
- [125] Daniel D. Stancil and Anil Prabhakar. *Spin waves: Theory and applications*. Springer, 2021.
- [126] I. Stasinopoulos, S. Weichselbaumer, A. Bauer, J. Waizner, H. Berger, S. Maendl, M. Garst, C. Pfeiderer, and D. Grundler. Low spin wave damping in the insulating chiral magnet Cu_2OSeO_3 . *Applied Physics Letters*, 111(3):032408, Jul 2017. ISSN 0003-6951, 1077-3118. doi: 10.1063/1.4995240. URL <http://aip.scitation.org/doi/10.1063/1.4995240>.
- [127] Jacob Torrejon, Junyeon Kim, Jaivardhan Sinha, Seiji Mitani, Masamitsu Hayashi, Michihiko Yamanouchi, and Hideo Ohno. Interface control of the magnetic chirality in CoFeB/MgO heterostructures with heavy-metal underlayers. *Nature Communications*, 5(1):4655, Dec 2014. ISSN 2041-1723. doi: 10.1038/ncomms5655. URL <http://www.nature.com/articles/ncomms5655>.
- [128] Jacob Torrejon, Mathieu Riou, Flavio Abreu Araujo, Sumito Tsunegi, Guru Khalsa, Damien Querlioz, Paolo Bortolotti, Vincent Cros, Kay Yakushiji, Akio Fukushima, Hitoshi Kubota, Shinji Yuasa, Mark D. Stiles, and Julie Grollier. Neuromorphic computing with nanoscale spintronic oscillators. *Nature*, 547(7664):428–431, July 2017. ISSN 0028-0836, 1476-4687. doi: 10.1038/nature23011.
- [129] A. A. Tulapurkar, Y. Suzuki, A. Fukushima, H. Kubota, H. Maehara, K. Tsunekawa, D. D. Djayaprawira, N. Watanabe, and S. Yuasa. Spin-torque diode effect in magnetic tunnel junctions. *Nature*, 438(7066):339–342, November 2005. ISSN 0028-0836, 1476-4687. doi: 10.1038/nature04207.
- [130] S. Urazhdin, V. E. Demidov, H. Ulrichs, T. Kendziorczyk, T. Kuhn, J. Leuthold, G. Wilde, and S. O. Demokritov. Nanomagnonic devices based on the spin-transfer torque. *Nature Nanotechnology*, 9(7):509–513, July 2014. ISSN 1748-3387, 1748-3395. doi: 10.1038/nnano.2014.88.

- [131] Arne Vansteenkiste, Jonathan Leliaert, Mykola Dvornik, Mathias Helsen, Felipe Garcia-Sanchez, and Bartel Van Waeyenberge. The design and verification of MuMax3. *AIP Advances*, 4(10):107133, October 2014. ISSN 2158-3226. doi: 10.1063/1.4899186.
- [132] Roman Verba, Ivan Lisenkov, Ilya Krivorotov, Vasil Tiberkevich, and Andrei Slavin. Nonreciprocal Surface Acoustic Waves in Multilayers with Magnetoelastic and Interfacial Dzyaloshinskii-Moriya Interactions. *Physical Review Applied*, 9(6):064014, June 2018. doi: 10.1103/PhysRevApplied.9.064014.
- [133] Roman Verba, Vasil Tiberkevich, and Andrei Slavin. Wide-band nonreciprocity of surface acoustic waves induced by magnetoelastic coupling with a synthetic antiferromagnet. *Physical Review Applied*, 12(5):054061, Nov 2019. ISSN 2331-7019. doi: 10.1103/PhysRevApplied.12.054061. URL <https://link.aps.org/doi/10.1103/PhysRevApplied.12.054061>.
- [134] K. Vogt, F. Y. Fradin, J. E. Pearson, T. Sebastian, S. D. Bader, B. Hillebrands, A. Hoffmann, and H. Schultheiss. Realization of a spin-wave multiplexer. *Nature Communications*, 5:3727. ISSN 2041-1723. doi: 10.1038/ncomms4727. URL <https://www.nature.com/articles/ncomms4727>.
- [135] Kai Wagner, Andrew Smith, Toni Hache, Jen-Ru Chen, Liu Yang, Eric Montoya, Katrin Schultheiss, Jürgen Lindner, Jürgen Fassbender, Ilya Krivorotov, and Helmut Schultheiss. Injection locking of multiple auto-oscillation modes in a tapered nanowire spin Hall oscillator. *Scientific Reports*, 8(1):16040, December 2018. ISSN 2045-2322. doi: 10.1038/s41598-018-34271-4.
- [136] Xuhui Wang, Gerrit E. W. Bauer, and Axel Hoffmann. Dynamics of thin-film spin-flip transistors with perpendicular source-drain magnetizations. *Physical Review B*, 73(5):054436, February 2006. ISSN 1098-0121, 1550-235X. doi: 10.1103/PhysRevB.73.054436.
- [137] Tayyab Waqar and Sezgin Ersoy. Design and analysis comparison of surface acoustic wave-based sensors for fabrication using additive manufacturing. *Journal of Nanomaterials*, 2021:e5598347, Jun 2021. ISSN 1687-4110. doi: 10.1155/2021/5598347. URL <https://www.hindawi.com/journals/jnm/2021/5598347/>.
- [138] Joel K. W. Yang and Karl K. Berggren. Using high-contrast salty development of hydrogen silsesquioxane for sub-10-nm half-pitch lithography. *Journal of Vacuum Science & Technology B: Microelectronics and Nanometer Structures Processing, Measurement, and Phenomena*, 25(6):2025–2029, Nov 2007. ISSN 1071-1023. doi: 10.1116/1.2801881. URL <https://avs.scitation.org/doi/full/10.1116/1.2801881>.
- [139] Mohammad Zahedinejad, Himanshu Fulara, Roman Khymyn, Afshin Houshang, Mykola Dvornik, Shunsuke Fukami, Shun Kanai, Hideo Ohno, and Johan Åkerman. Memristive control of mutual spin Hall nano-oscillator synchronization for neuromorphic computing. *Nature Materials*, 21(1):81–87, January 2022. ISSN 1476-4660. doi: 10.1038/s41563-021-01153-6.

- [140] Steven S.-L. Zhang, Ezio Iacocca, and Olle Heinonen. Tunable Mode Coupling in Nanocontact Spin-Torque Oscillators. *Physical Review Applied*, 8(1):014034, July 2017. doi: 10.1103/PhysRevApplied.8.014034.
- [141] Xufeng Zhang, Tianyu Liu, Michael E. Flatté, and Hong X. Tang. Electric-field coupling to spin waves in a centrosymmetric ferrite. *Physical Review Letters*, 113(3):037202, Jul 2014. ISSN 0031-9007, 1079-7114. doi: 10.1103/PhysRevLett.113.037202. URL <https://link.aps.org/doi/10.1103/PhysRevLett.113.037202>.
- [142] X. Zheng and Y. Zhou. Theory and Applications of Spin Torque Nano-Oscillator: A Brief Review. *Solid State Phenomena*, 232:147–167, June 2015. ISSN 1662-9779. doi: 10.4028/www.scientific.net/SSP.232.147.
- [143] Jian Zhu, J. A. Katine, Graham E. Rowlands, Yu-Jin Chen, Zheng Duan, Juan G. Alzate, Pramey Upadhyaya, Juergen Langer, Pedram Khalili Amiri, Kang L. Wang, and Ilya N. Krivorotov. Voltage-Induced Ferromagnetic Resonance in Magnetic Tunnel Junctions. *Physical Review Letters*, 108(19):197203, May 2012. doi: 10.1103/PhysRevLett.108.197203. URL <http://link.aps.org/doi/10.1103/PhysRevLett.108.197203>.

Appendix A

Appendix

A.1 Micromagnetic Simulations Through UCI's RCIC

While we have our own simulation computers with some power to run micromagnetic simulations, the freely accessible computation resources in UCI's High Performance Cluster should not be ignored. Here are some notes, tips, and tricks for those who want to utilize it. In my experience, I was able to execute *hundreds* of simulations over literal hours when the cluster was not under heavy load, trying to do something like that on our lab PCs would have taken months. Note that some code snippets will have breaks in them that are for formatting with the document, but in the actual code are not line breaks.

The UCI High Performance Cluster 3 (HPC3) is a massive computational hub that is openly accessible to UCI students and faculty to run expensive calculations and simulations. More information about the cluster specs can be found at <https://rcic.uci.edu/hpc3/hpc3-cluster-specs.html>. The key hardware for us are the 52 Nvidia V100 GPU's available on the cluster, these GPUs are *insanely* fast compared to even the Nvidia TESLA K40c that we have in the office.

All referential information regarding the cluster is found <https://rcic.uci.edu/index.html>. Any information not found in this document is likely to be found there. Otherwise you can email the RCIC folks to get specific help.

Fortunately, RCIC already has a beginner's guide:

<https://rcic.uci.edu/hpc3/beginner-guide.html>

I highly recommend reading through that page, some notes I have regarding some things they talk about:

- Vim and emacs have a steep-ish learning curve when it comes to editing files on the cluster. But if you see yourself using text editors for programming and stuff in the future frequently, it is well worth learning at least the basics. For fast changes, you can simply use nano. However if vim or emacs isn't your thing it may be better to use your own editor locally for the scripts and programs you will write and then transfer them over once you finish (transferring files are covered in the beginner-guide).
- `rsync` is very handy to make file transfers be streamlined, it effectively checks if there are any differences between the source and destination sync directories and then pulls the changed/new files.
- Aliases are your best friend, you can utilize them to make day to day things on the cluster considerably faster/easier.
- I personally liked using the linux subsystem on my windows computers, this is because I also use the linux subsystem for python programs (easier to set-up as opposed to windows).
- The guide is quite good, everything in it should be read and referenced when you may have simple questions.

A.1.1 Setting-up Mumax3 on the cluster:

Setting up mumax3 for your account is quite straightforward, you only need to download and transfer in the appropriate version of mumax3 into your HPC3 home directory. The version depends on which nvidia driver the HPC3 uses for their GPU's, you can check this by running:

```
nvidia-smi
```

And noting the nvidia driver version

The current version that we use (7/21/2022): mumax3.10_linux_cuda10.1

You can download mumax3.10 at <https://mumax.github.io/download.html>

Once downloaded, transfer the tar file to your hpc3 home and untar it there.

A.1.2 Running Mumax3 Jobs on the Cluster

Running simulations are done via scheduling a 'job' to the slurm scheduler. What we do is write a **jobscript** that executes the simulation when it is permitted to run.

A jobscript that runs a single simulation looks like this (with additional commenting):

```
#!/bin/bash

#SBATCH --job-name=mx3-single           ## Name of the job.
#SBATCH -A amanatuk                    ## account to charge
#SBATCH -p free-gpu                     ## partition/queue name
#SBATCH --nodes=1                       ## (-N) number of nodes to use
#SBATCH --ntasks=1                     ## (-n) number of tasks to launch
#SBATCH --cpus-per-task=1               ## number of cores the job needs
```

```

#SBATCH --error=slurm-\%J.err          ## error log file
#SBATCH --gres=gpu:V100:1              ## request use of 1 gpu

# Run command hostname and save output to the file out.txt

# For logging gpu driver and version
nvidia-smi

# Required for mumax3 to run properly
module load cuda/10.1.243

# mx3 filename to run (doesn't include mx3 extension)
mx3_name=Easy_Plane_SHO_v9-10-2f_jc_-z_idc_2.4646_ku1_3.1617_gfact_LONGRUN

# Move the working directory to the area I
# want to run the sim (the mx3 sim will be here too)
cd /pub/amanatuk/simsdata/mumax3/EasySHO/BATCH_RUNS/

# Execute simulation
srun ~/mumax3.10_linux_cuda10.1/mumax3 {mx3_name}.mx3

# When finished it 'move's the original mx3 into the output folder
mv {mx3_name}.mx3 {mx3_name}.out/

# Also move the slurm jobscript into the output folder as well
mv "$(readlink -f $0)" {mx3_name}.out/

# SPECIFIC TO THIS SIM (outputs 5000 ovf's), go inside the directory.
cd {mx3_name}.out/

# archive all the ovf into a single tar file
tar -czvf ovf_files.tar.gz m*.ovf

# deletes the ovfs after they have been archived

```

```
rm -r m*.ovf
```

All you need is any working mx3 file (even one that worked on your computer) and place it in the desired working directory on the hpc3, be sure to make the necessary changes in your jobscript copy to work within your space.

Finally, to queue the job: `sbatch slurm_script`

And you should see it queued when you check your queued jobs

A.1.3 Checking Job Status

You can check the status of your queued jobs by running:

```
squeue -u amanatuk (here you would replace amanatuk with your hpc3 username)
```

What I like to do is use the watch feature to constantly monitor job statuses:

```
watch -d squeue -u amanatuk
```

(watch -d runs the following commands every 2 seconds and highlights any changes in the output)

A.1.4 Useful Aliases

Aliases are like user defined shortcuts, any string of commands you are repeatedly having to execute can be shortened to an alias, this is incredibly useful and save a bunch of time. I will be writing some aliases I use, they will be specific to my account and computer but it should be clear what needs to be adapted to fit your context.

To log in:

```
alias hpc3asmishu="ssh -X amanatuk@hpc3.rcic.uci.edu"
```

If you have a local directory you want synchronized with a directory on the cluster:

```
alias hpc3\_sync\_mydir="rsync -av --progress  
↔ amanatuk@hpc3.rcic.uci.edu:/pub/amanatuk/simsdata/  
↔ /mnt/d/Mishu/Documents/mylocalsimsdata/"
```

Some shortcuts when working inside the cluster:

```
alias mumax3="/data/homezvol2/amanatuk/mumax3.10\_linux\_cuda10.1/mumax3"  
alias checkspace='quota -s amanatuk 2>/dev/null;dfsquotas amanatuk "dfs2 dfs3"  
alias checkbank='sbank balance statement'  
alias checkfile sizes='ls -l --block-size=G'  
alias watchjobs='watch -d squeue -u amanatuk'  
alias ovftopng='~/mumax3.10_linux_cuda10.1/mumax3-convert'
```

A.1.5 Batch Execution of Mumax3 Simulations

If you need to run a large amount of simulations in parallel, you will first need a template `.mx3` file, a python script that generates your batch of simulations, and finally a slurm job script to queue them all up.

The main idea is as follows, in your template `.mx3` file you input unique keywords where you want to procedurally vary the parameters (so for example where you set the external field you would place `$H_EXTERNAL`), the python script then goes through the template, replaces the keywords with the desired parameters, and saves it as a new file with the run number somewhere in the file name. Finally, the job script uses its internal counting parameter to

run the simulation with the same run number.

```
1  /*
2  * VCMA SW FET Nanowire simulations, Mishu / 2019
3  * Simulate  $f(H)$  in OOP external field
4  * Uses CW excitation to probe specific eigenmodes with VCMA (ku1 modulated) gate
5  */
6
7  DisableSlonczewskiTorque = true
8  DisableZhangLiTorque = true
9
10 /* Geometry */
11 length := 3.0e-6 // meters
12 width := 76 * 1e-9 // meters
13 thickness := 0.8e-9
14 active_length := 600e-9
15 lead_length := 500e-9 // meters, size of excitation/detection region
16
17 Nx := 2048
18 Ny := 32
19 Nz := 1
20
21 print(Nx, Ny, Nz)
22
23 setgridsize(Nx, Ny, Nz)
24 setcellsize(length/Nx, width/Ny, thickness/Nz)
25
26 nanowire := cuboid(length, width, thickness)
27 active_region := cuboid(active_length, width, thickness)
28 source_region := cuboid(lead_length, width, thickness)
29 setgeom(nanowire)
30 defregion(0, nanowire)
31 defregion(1, active_region)
```

```

32 // excitation/detection arms placed outside of active region, 500nm large, know it is
   ↪ centered at 0,0,0 and shifted
33 // by half of the active region + half of the 500nm to be adjacent but not overlap
34 defregion(2, source_region.Transl((active_length + lead_length)/2, 0, 0))
35 defregion(3, source_region.Transl(-(active_length + lead_length)/2, 0, 0))
36 saveas(geom, "Nanowire_structure")
37 save(regions)
38
39 /** Material Parameters **/
40 // Add references here
41 Msat = 1500e3 // 1500 emu/cm3
42 alphaFree := 0.01 // For f(H) sinc
43 alpha = alphaFree
44 Aex = 7.5e-12 // pJ/m 15.0e-12
45
46 Ku1_SI := 1.027 * 1.27e6 // J/m3 reference??
47 Ku1 = Ku1_SI
48 Ku1_active := $KU1_PERCENT * Ku1_SI
49
50 Ku2_SI := 1.4 * 1.25e4 // J/m3 (found using FH curves)
51 Ku2 = Ku2_SI
52 Ku2_active := 0.95*Ku2_SI
53 anisU = vector(0.001, 0.002, 1)
54
55 g_fct := 2.1
56 mu_B := 9.2740091523E-24
57 h_bar := 1.05457173E-34
58 GammaLL = (mu_B / h_bar) * g_fct
59 /** Adding DMI in to see effects **/
60 Dind = 8.2e-4 // J/m2
61
62 // Active region difference in Ku1?
63 Ku1.setregion(1, Ku1_active)

```

```

64 //Ku2.setregion(1, Ku2_active)
65
66
67 lex := sqrt(Aex.GetRegion(1) / (0.5 * mu0 * pow(Msat.GetRegion(1), 2)))
68 print(Aex.GetRegion(1), Msat.GetRegion(1))
69 print(lex) //exchange length using aex, msat
70
71
72 /** End Material Parameters **/
73
74 /**
75                 Absorbing boundary conditions
76                 Done by ramping up alpha near the ends of the wire (x-axis)
77 */
78 tmp:=0.0
79 for b:=0 ; b<=19 ; b++){
80     defregion(b+4,
81     xrange(length/2-(20-b)*20e-9,
82     length/2-(19-b)*20e-9).add(xrange(-length/2+(19-b)*20e-9,
83     ↪ -length/2+(20-b)*20e-9)))
84     tmp=exp((b+1)/10)
85     print(tmp)
86     alpha.setregion(b+4,alphaFree*tmp)
87 }
88 saveas(alpha, "alpha")
89 /** End Absorbing boundary conditions **/
90
91 /* Set Material Parameters After Region Def */
92 //save(Msat)
93 //save(Aex)
94 //save(Ku1)
95

```

```

96  /*
97  Regions:
98  0) nanowire
99  1) active_region
100 2) source rf
101 3) drain rf
102 */
103 tableadd(m.region(3))
104 tableadd(m.region(2))
105 tableadd(B_ext.region(1))
106 tableadd(B_ext.region(2))
107
108 /* f(H) Settings */
109 // Set to work for batch sims (HPC3)
110 // Settings in Oersted, program takes TESLA!!!
111 // Field must be OOP, sinc pulse should be perp to external field and easy axis.
112
113 H_app := $H_APP //0e
114
115 theta_H := 0.1 //degrees from z-axis
116 phi_H := 89.9 //degrees from x-axis
117
118
119 /* Continuous Wave Excitation Settings */
120 f_set := 0.712 * 1.0e9 //Hz
121 f_cut := 20.0e9 //Hz for sampling rate (~ 2x probing frequency)
122 t_cut := 1 / f_cut
123 f_samp := 2 * f_cut
124 t_samp := 1 / f_samp
125
126 omega_cut := 2 * pi * f_set // Called omega_cut but actually should be omega_set
127
128 timestep := t_samp //25.0e-12

```

```

129 timestep = 5e-12
130 totaltime := timestep*30000.0 /// 10*t_cut//50.0e-9 + 10*t_cut
131 print("t_step =", timestep)
132 print("t_total =", totaltime)
133 print("Nfreq =", totaltime/timestep)
134 print("Nskip =", 10*t_cut/timestep)
135
136 /* START SIM */
137
138
139 // Saturation done by setting m uniform in B_ext direction
140 maxdt = 0
141 m = uniform(sin(theta_H*pi/180)*cos(phi_H*pi/180),
142 ↔ sin(theta_H*pi/180)*sin(phi_H*pi/180), cos(theta_H*pi/180))
143
144 // Relax at set field converted to Tesla
145 B_app := H_app/1e4
146 Bx := B_app*sin(theta_H*pi/180)*cos(phi_H*pi/180)
147 By := B_app*sin(theta_H*pi/180)*sin(phi_H*pi/180)
148 Bz := B_app*cos(theta_H*pi/180)
149
150 B_ext = vector(Bx, By, Bz)
151
152 print("Set field: ", B_ext)
153 filename := sprintf("B_set_%.1f.ovf", B_app)
154 saveas(B_ext, filename)
155 Relax()
156
157 // Save relaxed State
158 filename = sprintf("Relaxed_%.1f.ovf", B_app)
159 saveas(m, filename)
160

```

```

161 // Check damping values
162 print("alpha region 0: ", alpha.region(0))
163 print("alpha region 1: ", alpha.region(1))
164 print(Bx, By, Bz)
165
166 // Sinc excitation, along all axes
167 // sinc(x) returns sin(x)/x, we use x = 2pi*f_cut*t
168 Amp := 5/1e4 // Tesla
169
170 /**
171 B_ext.SetRegion(0, vector(
172     Bx + Amp*sin(theta_H*pi/180)*cos(phi_H*pi/180)*sinc(omega_cut*(t-20*t_cut)),
173     By + Amp*sin(theta_H*pi/180)*sin(phi_H*pi/180)*sinc(omega_cut*(t-20*t_cut)),
174     Bz + Amp*cos(theta_H*pi/180)*sinc(omega_cut*(t-20*t_cut)) ) )
175 ***/
176
177 B_ext.SetRegion(2, vector(
178     Bx + Amp*sin(theta_H*pi/180)*cos(phi_H*pi/180)*sin(omega_cut*(t)),
179     By + Amp*sin(theta_H*pi/180)*sin(phi_H*pi/180)*sin(omega_cut*(t)),
180     Bz + Amp*cos(theta_H*pi/180)*sin(omega_cut*(t)) ) )
181
182 print(B_ext.region(0))
183 print(B_ext.region(1))
184
185 tableautosave(timestep)
186 //autosave(m,timestep)
187 run(totaltime)/(50e-9 + 10*t\_cut)

```

And an example python script is as follows:

```
"""
    Description: (Amanatullah 'Mishu' Khan)

    Modified to use for sweeping loop steps for
    faster turnaround in hpc3

    NOTE: template m3 must have $VARNAME placeholders
    matching that of substitute dict below
    -> don't forget to drop the loop brackets!
"""
from string import Template
import numpy as np
import os

# specify the values for which we want to generate the scripts
# specify filename, this script must be in the same place as template

### UNITS OF De
start_happ = 240
end_happ = 240
steps_happ = 0

### UNITS OF var2 (PERCENT)
start_var2 = .98
end_var2 = 1.02
steps_var2 = 40

happ_values = np.linspace(start_happ, end_happ, steps_happ+1)
var2_values = np.linspace(start_var2, end_var2, steps_var2+1)
```

```

print('ARRAY OF PARAMETERS:\n')
print('HAPP ARRAY:\n', happ_values)
print('VAR2 ARRAY:\n', var2_values)
print('RUN COUNT:\t', len(happ_values)*len(var2_values))

input('Confirm these parameters then key enter, otherwise ctrl+c')

template_file = "BATCH_mishu_swfet_fH_simple_cluster_run.mx3"
base_filename = "swfet_fH_simple_cluster_"

# read template script
with open(template_file,'r') as f:
    scripttmpl = Template(f.read())

run_num = 1
for happ in happ_values:

    for var2 in var2_values:

        # write the script for each combination of field and var2 value
        script = scripttmpl.substitute(dict(H_APP=happ, KU1_PERCENT=var2))
        scriptfile = base_filename + "happ_%.1f_ku1_percentage_%.3f__run%.3g.mx3" % (happ,
        ↪ var2, run_num)
        with open(scriptfile,'w') as f:
            f.write(script)
        print(scriptfile)
        run_num += 1

print('ARRAY OF SCRIPTS HAVE BEEN MADE')
print('YOU MUST UPDATE THE TASK NUMBER OF RUNS IN THE SBATCH FILE')

```

A.1.6 Queuing the Slurm Script Job

Finally, the slurm script that queues up all the jobs is:

```
#!/bin/bash

#SBATCH --job-name=sw26-1          ## Name of the job.
#SBATCH -A amanatuk                ## account to charge
#SBATCH -p free-gpu                ## partition/queue name
#SBATCH --nodes=1                  ## (-N) number of nodes to use
#SBATCH --ntasks=1                 ## (-n) number of tasks to launch
#SBATCH --cpus-per-task=1          ## number of cores the job needs
#SBATCH --error=slurm-%J.err       ## error log file
#SBATCH --gres=gpu:V100:1          ## request use of 1 gpu
#SBATCH --array=1-41               ## number of array tasks
                                   ## $SLURM_ARRAY_TASK_ID iterates the number

# Run command hostname and save output to the file out.txt

nvidia-smi
module load cuda/10.1.243
dirname=/pub/amanatuk/simsdata/mumax3/SWFET_Sims/2022sims/\
SWFET_v26-1-fine_local_CW_rf_0.712GHz_with_gate_2400e/

# Move to sim directory
cd ${dirname}

# Move job script to it
if [ $SLURM_ARRAY_TASK_ID -eq 1 ]
then
    cp "$(readlink -f $0)" .
fi
```

```

# Run job, if it finishes, move mx3 file into it, you'll need to check remaining mx3's
#         to see which jobs need to be repeated (by modifying --array to run those)
srun ~/mumax3.10_linux_cuda10.1/mumax3 *run$SLURM_ARRAY_TASK_ID.mx3
mv *run$SLURM_ARRAY_TASK_ID.mx3 *run$SLURM_ARRAY_TASK_ID.out/

```

A.2 Post-processing Simulation Output Data

A.2.1 FFT Processing Of Series of Mumax3 Output Directories

This script crawls through filtered directories and post processes them. You can effectively replace the core fast fourier transform bit of the code with whatever you desire to do to process each directory.

```

from mpl_toolkits.mplot3d import Axes3D
from scipy.interpolate import griddata
from scipy.interpolate import interp1d
import matplotlib.pyplot as plt
import numpy as np
import pandas as pd
import re
import os
import glob

"""
Amanatullah 'Mishu' Khan

Bases fft from 2D_colorplot_from_mumaxtable_with_slicer_v3.py
Directory crawling and other features pulled from batch-output-ao-plotter_amplitude.py

Code looks at a number of directories looped over using batch mumax3 scripts

```

used in hpc3 for faster turnaround.

It goes into each directory with it's table.txt, does fft of it, and spits out an fft_table.txt in the same directory.

Another python script will iterate through these to do 2D plots and whatnot.

```
"""  
  
# Filename related parameters, these are for regex  
# Use regexr.com for help in getting proper regex  
searchtoken1 = 'idc_([+-]?[\d.\d]+)'  
searchtoken2 = 'ku1_([+-]?[\d.\d]+)'  
token1_var = 'idc'  
token2_var = 'ku1'  
directory_template = 'Easy_Plane_SHO_v9-10-2f_jc_-z*.out'  
↔ '#Easy_Plane_SHO_v9-10-2f_jc_-z*.out'  
file_to_fft = 'table.txt'  
  
# Apply Blackman filter to reduce spectral leakage, check wikipedia for more info  
debug = True # Additional printouts  
use_bm_filter = True # If false applies no window  
interp_timestep = 5e-12 # Should set same as timestep in mumax3  
skip_steps = 0e-9/interp_timestep # To cut off transients if table from t=0  
column_to_fft = 5 # Column with m(t) data (0 indexed)  
column_of_components = [5, 6, 7] # Columns of x, y, z data to process for Mvect  
  
##### End User Inputs #####  
  
def cmpkey(text, token):  
    return float(re.findall(token, text)[0])  
  
searched_directory_list = glob.glob(os.path.join(os.getcwd(),
```

```

                                                    directory_template))

execpath = os.getcwd()

def get_column_label(path_to_file, index_of_column):
    # var is named fields, this is the "h" part of usual fh plot
    column_extract = pd.read_table(path_to_file, nrows = 3)
    # get rid of the first # and space
    column_extract.columns = column_extract.columns.str.replace('# ', '')
    col_label = column_extract.columns[index_of_column].replace(r' \(.*\)', '').replace('
    ↪ ()', '').replace('.', '') # cleanup
    col_label = re.sub(r' \(.*\)', '', col_label) # cleanup 2 since above one is dumb af
    return col_label

directory = []
for dirs in searched_directory_list:
    try:
        if not os.path.exists(execpath + '/' + dirs + '/' + file_to_fft):
            print(dirs, 'Does not have', file_to_fft, 'skipping!')
            continue
        directory.append((dirs, cmpkey(dirs, searchtoken1), cmpkey(dirs, searchtoken2)))

        # directory.append((dirs, cmpkey(dirs.replace('p', '.'))))
        # print(list(map(float, re.findall(searchtoken,
        #                                     dirs.replace('p', '.'))))
    except Exception as e:
        print('Pulling directory vars failed!\n Reason: ', e)
        pass

for l in directory:
    print(l)

```

```

input('Is the list correct?')

xyz_data = []
d_index = 0
# Loads in the data that we want to fft
for d in directory:
    filename = execpath + '/' + d[0] + '/' + file_to_fft
    print("FFTING: ", filename)
    # Extract column name using pandas subroutine
    column_name = get_column_label(filename, column_to_fft)

    # loaded in as data[0] = t, data[1] = mx, etc..
    data = np.loadtxt(filename, unpack=True)
    tslice = data[0]
    mslice = interp1d(tslice, data[column_to_fft])
    mslice_squared = interp1d(tslice, np.square(data[column_to_fft]))

    mvect = np.sqrt(np.square(data[column_of_components[0]]) +
        ↪ np.square(data[column_of_components[1]]) +
        ↪ np.square(data[column_of_components[2]]))

    t_steps = int((tslice[-1] - tslice[0])/interp_timestep)
    t = np.linspace(tslice[0], tslice[-1], t_steps)

    # Debug
    if debug:
        print(tslice[0], tslice[-1], len(tslice), t_steps, len(mslice(t)), '\t',
            ↪ max(mslice(t)))

    FFTlength = len(mslice(t)) - int(skip_steps) if(int(skip_steps) < len(mslice(t)))
    ↪ else len(mslice(t))
    FFTstart = int(skip_steps) if (int(skip_steps) < len(mslice(t))) else 0

```

```

print('FFT length (N-k):', FFTlength)
print('Skipping (k) steps:', FFTstart, '=', interp_timestep*FFTstart, 'seconds')

# Applies blackman spectral filter
window = np.blackman(FFTlength) if use_bm_filter else 1
mslice_remove_offset = mslice(t) - np.mean(mslice(t))
mslice_squared_rem_off = mslice_squared(t) - np.mean(mslice_squared(t))

# Generate linear and log scale fft, applies window, takes absolute value, keeps
↳ positive frequency portion of fft output.
fft_linear = np.abs(np.fft.fft(mslice_remove_offset[-FFTlength:]*window))*
↳ (2.0/FFTlength)
fft_linear = fft_linear[0:int(FFTlength/2)]
fft_log = np.log10(np.abs(np.fft.fft(mslice_remove_offset[-FFTlength:]*window))*
↳ (2.0/FFTlength))
fft_log = fft_log[0:int(FFTlength/2)]
fft_squared_linear = np.abs(np.fft.fft(mslice_squared_rem_off[-FFTlength:]*window))*
↳ (2.0/FFTlength)
fft_squared_linear = fft_squared_linear[0:int(FFTlength/2)]
fft_squared_log =
↳ np.log10(np.abs(np.fft.fft(mslice_squared_rem_off[-FFTlength:]*window))*
↳ (2.0/FFTlength))
fft_squared_log = fft_squared_log[0:int(FFTlength/2)]

# Generate frequency axis in units of GHz
frequencies = np.fft.fftfreq(FFTlength, d = interp_timestep)[0:int(FFTlength/2)]/1e9
filename = execpath + '/' + d[0] + '/' + 'fft_' + file_to_fft
print('Saved fft to: ', filename)

# Save fft data as a new table
datahdr = ('Frequency(GHz)',
          column_name + '_fft_linear',
          column_name + '_fft_log',
          column_name + '_squared_fft_linear',

```

```

        column_name + '_squared_fft_log')
np.savetxt(filename, np.transpose(np.array([frequencies,
                                           fft_linear,
                                           fft_log,
                                           fft_squared_linear,
                                           fft_squared_log])),
           newline = '\n', header = '\t'.join(map(str, datahdr)))

datahdr = ('t(s)', 'Mvect')
filename = filename = execpath + '/' + d[0] + '/' + 'Mvect_table.txt'
print('Saved mvect to: ', filename)
np.savetxt(filename, np.transpose(np.array([tslice, mvect])),
           newline = '\n', header = '\t'.join(map(str, datahdr)))

```

A.2.2 Generating Colorplots from Simulation Data

Additionally, a similar structure can be adopted to organize the data in a digestible format, in the script below I compile a series of generated fft's to form a color plot that yields valuable insight into the data:

```

from mpl_toolkits.mplot3d import Axes3D
from scipy.interpolate import griddata
from scipy.interpolate import interp1d
import matplotlib.pyplot as plt
import numpy as np
import pandas as pd
import re
import os
import glob

"""

```

Amanatullah 'Mishu' Khan

Directory crawling and other features pulled from batch-fft-the-tables.py

Code looks at a number of directories looped over using batch mumax3 scripts used in hpc3 for faster turnaround.

It goes into each directory, reads in the fft_table.txt, and processes as the user → desires, in this case it will generate color plots and flattened 3d maps.

pseudo code is as follows:

scan for appropriate directories

for each dir:

read in the fft data

map it to vars extracted from directory

map flattened data to same vars as a separate tuple

for each set of tuples made from the data crawling:

for each fixed var1 (or var2):

generate 2d colorplot for each var2 (or var1)

save fftmatrix in new folder for each fixed var1 (or var2)

generate flattened data of all colormaps together (also a colormap)

save this flattened data matrix in same directory

generated frequency extracted version of flattened data

save this data matrix as well

To do:

Address cplot z scale to truncate below min cutoff frequency (now only cuts off above → max)

Save raw matrix data alongside png's for magicplot import (easier to adjust and → analyze)

```

"""
##### Directory Inputs #####
# Filename related parameters, these are for regex
# Use regexr.com for help in getting proper regex
searchtoken1 = 'idc_([+-]?[\d.\d]+)'
searchtoken2 = 'ku1_([+-]?[\S.]+)_'
token1_var = 'Idc'
token1_var_units = 'mA'
token2_var = 'Ku1'
token2_var_units = 'ergs/cm^2'
directory_template = 'Easy_Plane_SHO_v9-10-2f_jc_-z*out'
file_to_process = 'fft_table.txt'

column_to_process = 2                # Column with fft data (0 indexed)

##### Plotting Inputs #####
# 2D colorplots from fixing each var1/var2
y_axis_range_max = 4.0
y_axis_range_min = 0.1
number_of_cplot_levels = 100

#####
# 2D 'flattened' colorplot from extracting max amplitude from every fft
flatten_threshold = -5

title = 'Eigenmode max amp phase plot (IDC)'
z_label = 'Log Amplitude (a.u.)'
z_label_from_yaxis = 'Frequency (GHz)'
# If this is false it'll do 3d plot
contour_plot = True

# Removes this many rows from beginning of data before flattening
# Useful mainly when removing dc leakage in fft (artificial maximum at 0 f)

```

```

truncate_range = 1

# If true, returns the y axis where the max is found (like f in fft)
# when false, simply extracts the maximum value across slice
flatten_to_yaxis = False

##### End User Inputs #####

def cmpkey(text, token):
    return float(re.findall(token, text)[0])

searched_directory_list = glob.glob(os.path.join(os.getcwd(),
                                                directory_template))

execpath = os.getcwd()

def get_column_label(path_to_file, index_of_column):
    # var is named fields, this is the "h" part of usual fh plot
    column_extract = pd.read_table(path_to_file, nrows = 3)
    # get rid of the first # and space
    column_extract.columns = column_extract.columns.str.replace('# ', '')
    col_label = column_extract.columns[index_of_column].replace(r'\(.*\)', '').replace('
    ↪ ()', '').replace('.', '') # cleanup
    col_label = re.sub(r'\(.*\)', '', col_label) # cleanup 2 since above one is dumb af
    return col_label

directory = []
for dirs in searched_directory_list:
    try:
        if not os.path.exists(execpath + '/' + dirs + '/' + file_to_process):
            print(dirs, 'Does not have', file_to_process, 'skipping!')

```

```

        continue
    directory.append((dirs, cmpkey(dirs, searchtoken1), cmpkey(dirs, searchtoken2),
        ↪ cmpkey(dirs, 'run([+-]?[\d.\d]+).out')))

        # directory.append((dirs, cmpkey(dirs.replace('p', '.'))))
    # print(list(map(float, re.findall(searchtoken,
    #                                     dirs.replace('p', '.'))))))
except:
    print('Encountered an error trying to find\t', dirs)
    pass

# Sort by the run order, this makes the colorplots come out correctly
directory = sorted(directory, key=lambda item: item[3])

for l in directory:
    print(l)
input('Is the list correct?')

data_matrix = []
xyz_flattened = []
d_index = 0
# Loads in the fft data that we want to process
for d in directory:
    filename = execpath + '/' + d[0] + '/' + file_to_process
    # Extract column name using pandas subroutine
    column_name = get_column_label(filename, column_to_process)
    print("Processing:\t", filename)
    print("Extracting:\t", column_name)
    # loaded in as data[0] = t, data[1] = mx, etc..
    data = np.loadtxt(filename, unpack=True)
    frequency = data[0]

```

```

max_from_slice = max(data[column_to_process][truncate_range:])
# Flatten to just raw maximum
if not flatten_to_yaxis:
    flattened_data = (d[1], d[2], max_from_slice)
# Otherwise flatten to the frequency where max is found
# If max amplitude is below threshold, set to 0
else:
    if max_from_slice < flatten_threshold:
        flattened_data = (d[1], d[2], 0)
    else:
        flattened_data = (d[1], d[2], data[0][np.where(data[column_to_process] ==
↪ max_from_slice)[0]])
xyz_flattened.append(flattened_data)
fft_tuple = (d[1], d[2], frequency, data[column_to_process])
data_matrix.append(fft_tuple)
if d_index == -1:
    break # For debugging
d_index += 1

# Iterating over tuple list to extract axes
var1_axis = np.unique([stuff[0] for stuff in data_matrix])
var2_axis = np.unique([stuff[1] for stuff in data_matrix])

pd_data = pd.DataFrame(data_matrix, columns=[token1_var, token2_var, "frequency",
↪ "fft"])
f_pd = pd.DataFrame(frequency, columns=['frequency'])
print(pd_data)

# Makes colorplots with fixed var1's
for var1 in var1_axis:
    break #Since FH, these may not yield much
    temp_xyz = []
    cplot_data = pd_data[pd_data[token1_var] == var1]

```

```

frequency_cut = len(f_pd[f_pd['frequency'] < y_axis_range_max])
fftmatrix = np.vstack([d for d in cplot_data["fft"]]).T[:frequency_cut]
frequency = frequency[:frequency_cut]
# For cplot
fft_max = fftmatrix.max()
fft_min = fftmatrix.min()
fft_step = round((fft_max-fft_min)/number_of_cplot_levels, 20)
lvls = np.arange(fft_min, fft_max+fft_step, fft_step)
# Plotting
plt.subplot(1, 1, 1)
#print(cplot_data[token2_var].shape, frequency.shape, fftmatrix.shape)
cplot = plt.contourf(cplot_data[token2_var].to_numpy(), frequency, fftmatrix,
↳ levels=lvls)
plt.ylim([y_axis_range_min, y_axis_range_max])
plt.xlabel(token2_var + '(%s)' % (token2_var_units))
plt.ylabel('frequency (GHz)')
plt.title('%s with %s fixed at %s %s' % (column_name, token1_var, str(var1),
↳ token1_var_units))
cbar = plt.colorbar()
cbar.ax.set_ylabel('Amplitude')
cplot_image_name = 'Easy_Plane_SHO_v9-10-2f_jc_-z_*.out'.replace('*', '%s_%s' %
↳ (token1_var, str(var1)))
plt.savefig(cplot_image_name.replace('.out', '.png'))
print('Saved ', cplot_image_name.replace('.out', '.png'))
# Cleanup for next plot
plt.clf()

# NOTE MAKE SURE THE PD IS ORDERING BY VAR2 IN THIS LOOP
# Makes colorplots with fixed var2's
for var2 in var2_axis:
    temp_xyz = []
    cplot_data = pd_data[pd_data[token2_var] == var2]

```

```

#print(cplot_data)
frequency_cut = len(f_pd[f_pd['frequency'] < y_axis_range_max])
fftmatrix = np.vstack([d for d in cplot_data["fft"]]).T[:frequency_cut]
frequency = frequency[:frequency_cut]

# For cplot

fft_max = fftmatrix.max()
fft_min = fftmatrix.min()
fft_step = round((fft_max-fft_min)/number_of_cplot_levels, 20)
lvls = np.arange(fft_min, fft_max+fft_step, fft_step)

# Plotting
plt.subplot(1, 1, 1)
#print(cplot_data[token1_var].shape, frequency.shape, fftmatrix.shape)
cplot = plt.contourf(cplot_data[token1_var].to_numpy(), frequency, fftmatrix,
↳ levels=lvls)
plt.ylim([y_axis_range_min, y_axis_range_max])
plt.xlabel(token1_var + '(%s)' % (token1_var_units))
plt.ylabel('frequency (GHz)')
plt.title('%s with %s fixed at %s %s' % (column_name, token2_var, str(var2),
↳ token2_var_units))
cbar = plt.colorbar()
cbar.ax.set_ylabel('Amplitude')
cplot_image_name = 'Easy_Plane_SH0_v9-10-2f_jc_-z_*.out'.replace('*', '%s_%s' %
↳ (token2_var, str(var2)))
plt.savefig(cplot_image_name.replace('.out', '.png'))
print('Saved ', cplot_image_name.replace('.out', '.png'))

# Cleanup for next plot
plt.clf()

# Flattened colorplot plotting
x, y, z = zip(*xyz_flattened)
z = list(map(float, z))

grid_x, grid_y = np.mgrid[min(x):max(x):100j, min(y):max(y):100j]

```

```

grid_z = griddata((x, y), z, (grid_x, grid_y), method='nearest')

# Makes and saves it.
fig = plt.figure()
if contour_plot:
    ax = fig.add_subplot(111)
    grid_extent = [grid_x.min(), grid_x.max(), grid_y.min(), grid_y.max()]
    cplot = ax.imshow(grid_z.T, extent=grid_extent, aspect='auto', origin='lower')
    cbar = fig.colorbar(cplot, ax=ax)
    cbar.set_label(z_label if not flatten_to_yaxis else z_label_from_yaxis)
else:
    ax = fig.gca(projection='3d')
    ax.plot_surface(grid_x, grid_y, grid_z, cmap=plt.cm.Spectral)

plt.title(title)
plt.xlabel('%s (%s)' % (token1_var, token1_var_units))
plt.ylabel('%s (%s)' % (token2_var, token2_var_units))
if not flatten_to_yaxis:
    cplot_image_name = 'Easy_Plane_SH0_v9-10-2f_jc_-z_*.out'.replace('*', '%s_%s_%s' %
        ↪ (token1_var, token2_var, 'FLATTENED'))
else:
    cplot_image_name = 'Easy_Plane_SH0_v9-10-2f_jc_-z_*.out'.replace('*', '%s_%s_%s' %
        ↪ (token1_var, token2_var, 'FLATTENED_yaxis'))
plt.savefig(cplot_image_name.replace('.out', '.png'))

plt.show()

```

A.2.3 Animating Mumax3 Data In Blender

I wrote a script that allows the animation studio Blender (free and open source) to take in the *table.txt* output from Mumax3 and generate an animation of \mathbf{M} vs t . In principle this script can be adapted to do whatever desired per data point in the imported file. I present this code to showcases how powerful scripting can be in representing data in compact, meaningful, and digestible ways such as videos.

```
import bpy
import numpy as np
import bmesh

# Loads in table.txt which holds the averaged mx, my, mz, and time step outputs from
↳ micromagnetic simulation
# Generates the spline curves that draw the planar projections of the M trajectory
# Makes the M arrow point along the trajectory by locking the arrow z-axis to always
↳ point at a zero emitting light point source.
# Point source is updated every frame t to new x,y,z
# Scaling of the arrow is set by the vector magnitude.

# Requires the arrow to already be drawn and set to originate from 0, 0, 0
# Backgrounds and other things are not affected.

filename = 'D:\\Mishu\\Documents\\Krivorotov Labs\\Python Stuff\\RCIC SIM
↳ FILES\\EPSHO\\EPSHO_v9-10-2f-BATCH-v8_linear_calculated_tdep\\' +
↳ 'Easy_Plane_SH0_v9-10-2f_jc_-z_idc_2.4424_ku1_3.1614__run61.out\\table.txt'
data = np.loadtxt(filename, unpack=True)

x = data[5][0:2860]
y = data[6][0:2860]
z = data[7][0:2860]
t = data[0][0:2860]
```

```

vector_xyz = np.vstack((x, y, z))

#Need to reset spline objects, ignore the time text curve object
try:
    for crv in bpy.data.curves:
        if crv != bpy.data.curves['time text']:
            bpy.data.curves.remove(crv)
    for stuff in bpy.app.handlers.frame_change_pre:
        bpy.app.handlers.frame_change_pre.remove(stuff)
except:
    pass

# M path and projection planes
m_curve = bpy.data.curves.new('m_curve', 'CURVE')
m_curve.dimensions = '3D'
spline = m_curve.splines.new(type='NURBS')
m_spline = bpy.data.objects.new('m_spline', m_curve)
bpy.context.scene.collection.objects.link(m_spline)

xy_curve = bpy.data.curves.new('xy_curve', 'CURVE')
xy_curve.dimensions = '3D'
spline = xy_curve.splines.new(type='NURBS')
xy_spline = bpy.data.objects.new('xy_spline', xy_curve)
bpy.context.scene.collection.objects.link(xy_spline)

yz_curve = bpy.data.curves.new('yz_curve', 'CURVE')
yz_curve.dimensions = '3D'
spline = yz_curve.splines.new(type='NURBS')
yz_spline = bpy.data.objects.new('yz_spline', yz_curve)
bpy.context.scene.collection.objects.link(yz_spline)

zx_curve = bpy.data.curves.new('zx_curve', 'CURVE')

```

```

zx_curve.dimensions = '3D'
spline = zx_curve.splines.new(type='NURBS')
zx_spline = bpy.data.objects.new('zx_spline', zx_curve)
bpy.context.scene.collection.objects.link(zx_spline)

#establish objects to animate
print('\n\n\n')
m_vect_focal_point = bpy.data.objects['rotation focal point']
m_vect_arrow = bpy.data.objects['ARROW']
m_spline = bpy.data.objects['m_spline']
time_text = bpy.data.objects['time text']
scene = bpy.data.scenes['Scene']

def recalculate_text(scene):
    frame_num = scene.frame_current
    time_text.data.body = "t = %.2f" % (t[frame_num]*1e9) + ' ns'

#remove previous animation frames
for stuff in bpy.data.objects:
    if stuff != bpy.data.objects['Camera']:
        stuff.animation_data_clear()
#m_vect_focal_point.animation_data_clear()
#m_vect_arrow.animation_data_clear()
#m_spline.animation_data_clear()
#m_curve.animation_data_clear()
#xy_spline.animation_data_clear()
#xy_curve.animation_data_clear()
#yz_spline.animation_data_clear()
#yz_curve.animation_data_clear()

```

```

#zx_spline.animation_data_clear()
#zx_curve.animation_data_clear()

#some prepping of objects
m_spline.data.bevel_depth = 0.01
xy_spline.data.bevel_depth = 0.01
yz_spline.data.bevel_depth = 0.01
zx_spline.data.bevel_depth = 0.01

m_spline.data.materials.append(bpy.data.materials['m spline'])
xy_spline.data.materials.append(bpy.data.materials['xy spline'])
yz_spline.data.materials.append(bpy.data.materials['yz spline'])
zx_spline.data.materials.append(bpy.data.materials['zx spline'])

mesh = m_vect_arrow.data
v_edge_tot = [0] * len(mesh.vertices)
maxedges = 0
maxvert = None
for edge in mesh.edges:
    for vert in edge.vertices:
        v_edge_tot[vert] += 1
        count = v_edge_tot[vert]
        if count > maxedges:
            maxedges = count
            maxvert = vert

vert = mesh.vertices[maxvert]

m_vect_focal_point.location = [x[0],y[0],z[0]]
m_vect_arrow.scale = [0.05, 0.05, 1.0]
m_vect_arrow.dimensions = [0.16,0.16,1]
orig_scale = m_vect_arrow.scale.copy()

```

```

for i in range(0, len(x)):

    m_vect_focal_point.location = [x[i],y[i],z[i]]
    m_vect_arrow.scale = orig_scale*np.linalg.norm([x[i],y[i],z[i]])
    bpy.context.view_layer.update()
    m_vect_focal_point.keyframe_insert('location', frame=i)
    m_vect_arrow.keyframe_insert('scale', frame=i)

    # Draw path of vector tip in 3d
    vector_tip = list(m_vect_arrow.matrix_world @
    ↪ bpy.data.objects['ARROW'].data.vertices[maxvert].co)
    bevel_end = float((i+1.0)/len(x))
    print(vector_tip)

    m_spline.data.splines[0].points.add(1)
    m_spline.data.splines[0].points[-1].co = (vector_tip + [1.0])
    m_curve.bevel_factor_end = bevel_end
    m_curve.keyframe_insert('bevel_factor_end', frame=i)

    xy_spline.data.splines[0].points.add(1)
    xy_spline.data.splines[0].points[-1].co = ([vector_tip[0], vector_tip[1], -1] +
    ↪ [1.0])
    xy_curve.bevel_factor_end = bevel_end
    xy_curve.keyframe_insert('bevel_factor_end', frame=i)

    yz_spline.data.splines[0].points.add(1)
    yz_spline.data.splines[0].points[-1].co = ([-1, vector_tip[1], vector_tip[2]] +
    ↪ [1.0])
    yz_curve.bevel_factor_end = bevel_end
    yz_curve.keyframe_insert('bevel_factor_end', frame=i)

    zx_spline.data.splines[0].points.add(1)

```

```

zx_spline.data.splines[0].points[-1].co = ([vector_tip[0], 1, vector_tip[2]] +
↳ [1.0])
zx_curve.bevel_factor_end = bevel_end
zx_curve.keyframe_insert('bevel_factor_end', frame=i)

#time_text.data.body = "t = %.2f" % (t[i]*1e9) + ' ns'
#print(time_text.data.body)
#time_text.keyframe_insert('body', frame=i)

bpy.data.scenes['Scene'].frame_end = len(x) + 1
bpy.app.handlers.frame_change_pre.append(recalculate_text)
#print(orig_scale, np.linalg.norm([x[i],y[i],z[i]]),
↳ orig_scale*np.linalg.norm([x[i],y[i],z[i]]))

```

A.3 Electron Beam Lithography Notes

Often times there are some niche issues or subtle things that arise when using the EBL system at LEXI Magellan. I will document some notes I had regarding them.

round(-1) error

Sometimes NPGS will throw the above error and prematurely end the writing procedure, this seems to happen if your pattern overextends beyond the original image window. Reducing the zoom factor in your NPGS runfile can prevent this from happening.

Defocusing from beam swapping

If you are writing an array of devices and are repeatedly swapping from low current to high current, the beam may gradually lose focus from switching, it is very obvious when switching to very big currents then back. You can mitigate this by first writing all of the fine features in an array with the lowest current first, then switching to the next lowest current and writing those patterns, and finally switch to the largest current to do the leads. This also saves some time as the SEM will not have to keep switching between currents. It can be done in NPGS as follows:

- Duplicate the original entity that writes the array, e.g. if there are three layers to your write, there should be three copies.
- Set the first array entity to SKIP all other layers aside from the first one.
- The second array entity similarly will skip the first layer and third onwards.
- The third would skip layer 1 and layer 2.
- Make sure that all three entities have the same parameters, especially the appropriate dosages and beam current indices.
- Make sure that all other arrays aside from the first have 0,0 for the **XY Move to Pattern Center** field.

It is useful to use the office NPGS's "Simulate Writing" command to make sure your runfile is executing properly.

DAC Drifting

If your layer has a lot of features that need to be carefully spaced (like fingers in an interdigital transducer), the DAC that controls the e-beam such that your pattern is written can have some non-zero drifting as it writes, this is most notable when it writes one half of a pattern, jumps elsewhere, and finally comes back to finish. I have observed this drift to be on the order of 100 nm, which can ruin devices Fig. A.1.

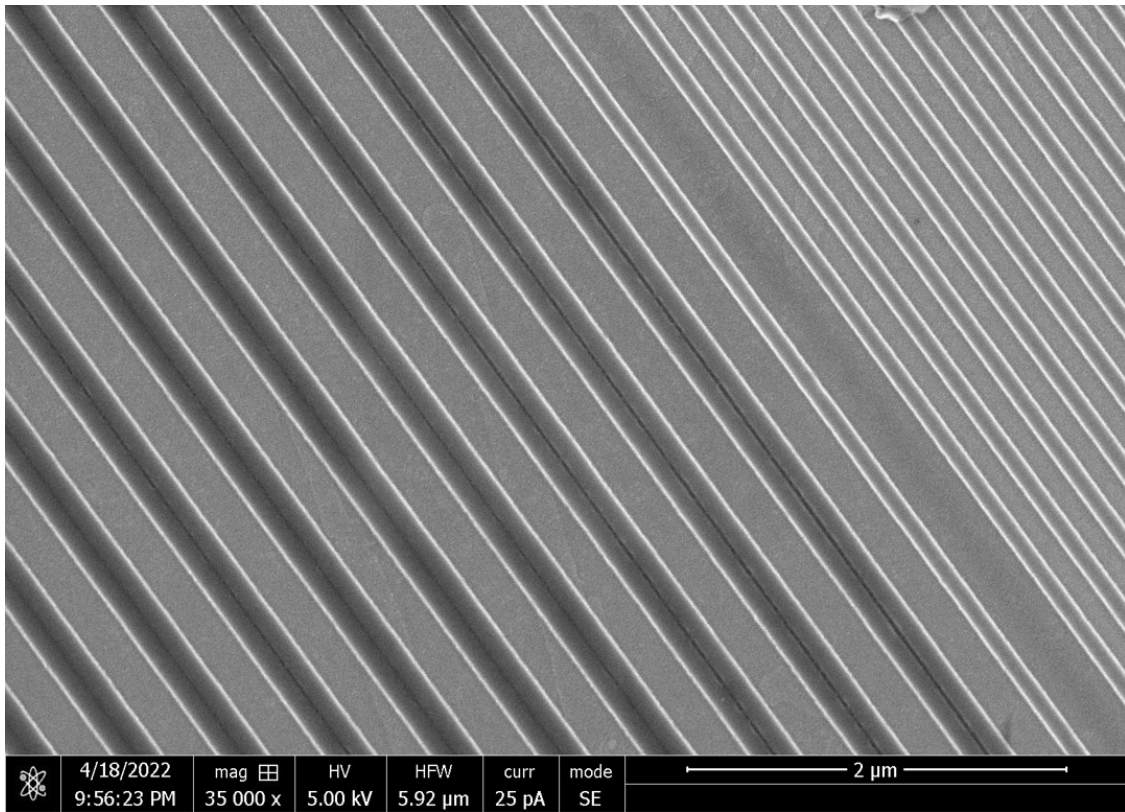


Figure A.1: **DAC drift leading to overlap** Darker structures are supposed to be spaced identically to the bright structures on the right. NPGS wrote half of the grating at the beginning and wrote the other half at the end. Due to the drift, they ended up overlapping.

You can make NPGS guarantee writing pieces of a pattern in one continuous fashion by grouping those pieces into a ‘cell’ in layout editor. I have seen however that if the pattern is too large, it will split writing it no matter what. I suggest maybe breaking it into parts and using the write simulation to see how it writes until you’re satisfied.